Spectroscopic Study of the Absorption Properties of Ozone and Methane for use in the Remote Sensing Applications

Dissertation

zur Erlangung des Grades

Doktor der Naturwissenschaften

am Fachbereich Physik

der Universität Bremen

vorgelegt von

Dipl.– Phys. Victor Gorshelev

Bremen, Dezember 2014

Institut für Umweltphysik (IUP), Universität Bremen

Universität Bremen

iup

1 Gutachter: Prof. Dr. John Burrows

2 Gutachter: Prof. Dr. Justus Notholt

Datum des Kolloquiums: 23.04.2015

Contents

Introduction

Monitoring of the atmospheric composition of the Earth is essential for studying the processes occurring in different layers of the atmosphere and, consequently, for air quality control and the climate change prediction. Important international treaties and recommendations are often based on the analysis of the environmental observations. The most well known examples are the 1989 Montreal Protocol, restricting the use of certain chlorofluorocarbons causing the depletion of the ozone layer, and the 1999 Kyoto Protocol, setting obligations on the industrialized countries to limit the emissions of greenhouse gases.

The most important conclusions are based on the data from the long-term global observations. Monitoring of this kind helps to improve the understanding of the atmospheric physics and chemistry and detect the trends and changes in the parameters of the atmosphere. Nowadays this data is coming from both space- or airborne instruments and ground based monitoring networks. It is worth noting that not only every device has a limited operational lifetime, but also the characteristics of the detectors installed in each instrument tend to degrade with time. Thus, measurements made during every mission must be as precise as possible, and on the other hand there should be a possibility of a transition (in terms of congruous data interpretation and dataset cross-reference) between data from preceding missions to consequent ones. Since the beginning of the satellite observation programs in early 1970s, over 120 satellites dedicated to remote sensing and the Earth sciences have been launched, thus providing over four decades of the global systematic observation data.

The atmosphere consists mostly of nitrogen N_2 (~78%), oxygen O_2 (~21%) and argon Ar (~1%), which are well-mixed components with constant concentration ratios over altitude. Water vapour is the next most abundant component, mainly present in the lower atmosphere. The rest of the species contribute less than 0.04% and are often referred to as the *trace gases*. Although it is safe to assume that major atmospheric constituents have not changed much in the last millions of years, minor constituents have changed dramatically. Variances in the concentration of some of the trace gases (like CO_2, O_3, CH_4, nitrogen oxides N_xO_y, man-made chlorofluorocarbons, etc.) and their distribution are extremely important and have undeniable influence on the air quality, planetary climate and life on Earth in general.

Both natural processes and the anthropogenic activities have a serious influence on the atmospheric composition. Reliable observation systems are therefore needed in order to produce a realistic estimate of the composition variability and identify main processes driving the change.

The ozone (O_3) and the methane (CH_4) are among the most important trace gases. They play crucial role in the physical and chemical processes in the atmosphere, like formation of the protective stratospheric ozone layer or contribution to the greenhouse effect by absorption of the solar radiation (by both ozone and methane) or radiation re-emitted by the Earth's surface. Another important factor is that both ozone and methane concentration and distribution

changes serve as the important markers of the anthropogenic influence on the environment.

Satellite-borne remote sensing instruments dedicated to the atmospheric observations mostly operate within the wavelength range of the solar spectrum. Depending on the goals of a mission, instruments can perform observations in ultraviolet, visible, and different regions of the infrared part of the spectrum.

While some instruments designed for the remote sensing applications are more universal than the others, majority of them are often dedicated to perform a certain set of measurements (which mostly means that the spectra are recorded within particular wavelength "windows" or "channels"), allowing to monitor a limited number of the atmospheric constituent species. In this case, the atmospheric composition is derived after processing the spectra acquired by the satellite-borne instruments. Most methods utilize the fitting of the observed and synthetic spectra. Modelled spectra are produced based on the preliminary assumptions of approximate concentrations, temperatures and altitude distribution of the trace gases. Minimization of discrepancy between these spectra, among other things, provides more accurate information on the concentrations of the constituent species. These methods require a precise knowledge of the electromagnetic radiation absorption characteristics of the different atmospheric gases in a wide spectral range, as well as the temperature and pressure dependences of these parameters. The uncertainties in these tabulated spectral data lead to the uncertainties in the resulting retrieved concentrations and distribution profiles of atmospheric gases.

Most of the modern instruments operate in the ultraviolet, visible and infrared parts of the spectrum between 250 nm and 1000 nm for ozone observations. For methane detection, infrared regions of the spectrum around 1,6 μm or 2,4 μm are mostly used. Despite the fact that different research groups have been analysing the absorption spectra of both ozone and methane with a lot of scrutiny for decades, there still is a room for improvement of the quality of the data. Consequently, the new detailed spectroscopic data would allow to further increase the quality of the atmospheric observations.

Demand for an updated and improved (in terms of uncertainties and parameterization capabilities) spectroscopic data for ozone and methane from the remote sensing community was a major motivating factor for this study.

This work is dedicated to the experimental research and analysis of the absorption spectra of ozone and methane and is structured as follows:

1. In the first section, along with the general information about the scale and structure of the atmosphere, importance of ozone and methane for the planetary climate and the environment in general is discussed. An overview of the chemical and the physical processes responsible for the formation, distribution and removal of these species from the atmosphere is presented. Some of the instruments used for the atmospheric monitoring are mentioned, as well as several methods of the satellite spectra processing.

2. Section two covers the basics of the molecular spectroscopy applicable to this research and the experimental methods used: in particular, Fourier-Transform absorption spectroscopy. Main phenomena responsible for the specific features of the ozone and methane spectra and their temperature and/or pressure dependences are discussed. An overview of the relevant spectroscopic datasets is provided for both ozone and methane. And finally, the overall goal of this work is set: acquisition of the new high-quality broadband spectra and corresponding data processing and the methods of achieving this goal.

3. Section three provides the description of the experimental setups used to measure the absorption spectra at various temperature and pressure combinations. One should note that the ozone spectrum in the considered wavelength region is continuous with quite broad features, whereas the methane spectrum consists of resolved lines and unresolved multiplets. Therefore, several different configurations of the experimental equipment were used for measurements, as well as different approaches towards the spectra processing were utilized.

4. Section four is dedicated to the analysis of the acquired experimental spectra of ozone. New data is compared with the results reported earlier by other groups. Also, the overall data quality analysis and absorption cross-section temperature dependence is performed.

5. Section five reports on the results of the measurement campaign and corresponding data processing of methane absorption spectra. Again, the quality of the new data is assessed and comparisons with previously available datasets are performed. In addition, some results of the test retrievals (performed by collaborating teams) based on the updated line parameters are presented.

6. Section six is dedicated to discussion of the achieved goals and the overall conclusions.

1. Atmospheric composition and chemistry

In the beginning, it is important to make a short summary of some basic concepts of the atmospheric structure, composition and chemistry. In this section, along with the general information on the subject, focus will be made on the processes responsible for production and destruction of the two atmospheric species of particular interest for this study – ozone and methane. Also, a brief overview of some remote sensing methods and instruments used for the observation of the ozone and methane will be given.

1.1. Stratification

The Earth's atmosphere is characterized by the temperature and pressure changes with height. The pressure within the planetary atmosphere follows the barometric law and decreases approximately exponentially as a function of altitude. Average temperature variation with altitude, also displaying characteristic profile, is the basis for distinguishing the layers of the atmosphere.

The atmosphere is conventionally separated into four regions, very distinctive in their structure, thermodynamics, photochemistry and dynamics. This stratification is best reflected by the atmospheric vertical temperature profile, whose inflection points are used to distinguish the four regions (Figure 1.1).

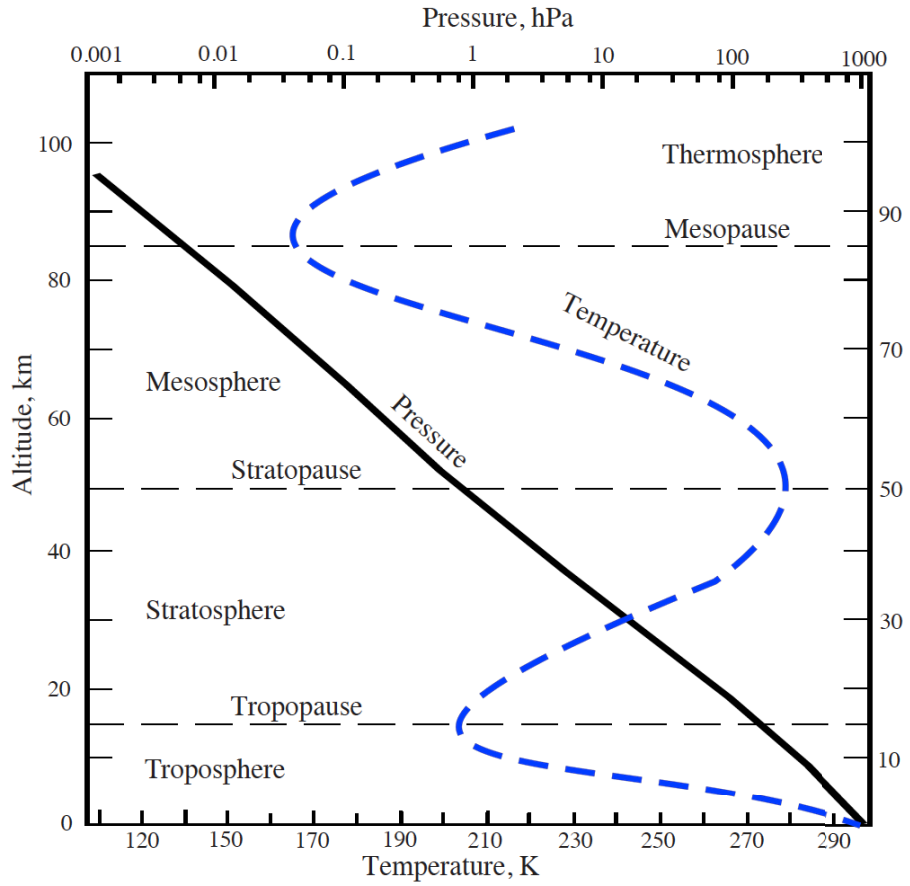

Figure 1.1. *Stratification of the atmosphere.*

Characteristic variation of the temperature and the total pressure (log scale on top) with altitude.

The atmospheric thermal structure is ultimately defined by a combination of dynamic and radiative transfer processes. Starting at the sea level, the atmospheric layers and the boundaries separating them are divided as follows:

-*Troposphere,* extending from the sea level up to the *tropopause*, a boundary layer which is situated between 8 km at high latitudes and 15 km at the equator. Although the troposphere makes up a small fraction of the atmosphere's total height, it comprises about 75% of its total mass. It contains the bulk of atmospheric water vapour, the majority of clouds and is the layer where most of the precipitation happens, which provides an important mechanism for removing pollutants from the atmosphere. The troposphere is heated from the Earth's surface, which absorbs solar radiation and releases heat back up in the infrared part of the spectrum. Air temperature in this region decreases linearly with altitude, at a lapse rate of 5 to 7 K/km. The tropopause marks the end of this linear temperature decrease. The word troposphere means “turning sphere”, reflecting the fact that convection dominates over radiative transfer in this region. Warm air masses travel upwards to the tropopause, carrying water vapour and forming the clouds as they cool down. Troposphere is in contact with the Earth’s surface and interacts directly with other environmental subsystems, like the biosphere, the hydrosphere, the cryosphere, the lithosphere, and most importantly, with the human habitat.

-*Stratosphere,* extending from the tropopause to the *stratopause,* a boundary layer at about 45 - 55 km altitude, is a very stable environment where heat transfer is mainly radiative and vertical mixing is slow. Stratosphere is the region where the bulk of the atmospheric ozone is formed. The ozone absorbs ultra-violet part of the spectrum of the incoming solar radiation. As a result, the stratosphere heats up and has a positive temperature gradient, reaching 271 K at the stratopause at approximately 50 km altitude.

-*Mesosphere,* extending from the stratopause to the *mesopause*, a boundary layer at about 80 - 90 km altitude. As the ozone heating diminishes, temperature gradient continues to fall linearly in the mesosphere up to the mesopause, the coldest point in the atmosphere.

-*Thermosphere,* extending from the mesopause, is the region which is radically different from the three underlying layers of the atmosphere. Temperature gradient reverse is a result of the absorption of short-wavelength radiation by N_2 and O_2. The *ionosphere* is the region including upper mesosphere and thermosphere where solar radiation ionizes the molecules and atoms, forming the plasma that interacts with the Earth’s magnetic field.

1.2. Spatial and temporal scales of the atmospheric processes

The Earth’s atmosphere is a complicated dynamical system, where gaseous constituents are continuously being exchanged with the oceans and the biosphere. Cycles that atmospheric gases participate in involve a number of physical and chemical processes. The lifetime cycle (or biogeochemical cycle) of an element or a compound refers to the transport of the species between

atmospheric, oceanic, biospheric, and land realms, the amounts contained in the different reservoirs, and the exchange rate between them.

Atmospheric trace gases can be produced as a result of:

- chemical processes within the atmosphere;
- volcanic exhaust;
- biological activity;
- radioactive decay;
- anthropogenic activities.

Removal of the gases from the atmosphere happens mainly due to:

- chemical reactions in the atmosphere;
- biological activity;
- physical processes in the atmosphere (like particle formation);
- deposition and uptake by the oceans and land masses.

Depending on the responsible removal process, the residence time of a species introduced into the atmosphere ranges from seconds to millions of years.

Over their lifespan in the atmosphere, most (excluding the especially inert ones) species participate in some form of chemical reactions. Two major mechanisms responsible for chemical alteration exist:

- photochemical reactions (photodissociation of molecules through interaction with photons of sufficient energy present in sunlight);
- conventional chemical reactions (dominating mechanism, when two molecules interact and undergo a chemical reaction to produce new species).

It is not uncommon for products appearing during the reactions leading to removal (also called "sink") of some species to be the source for other atmospheric species.

The atmosphere can be thought of as a huge chemical reactor with continuously happening multiple reactions. Species are being introduced and removed over strongly varying temporal and spatial scales, spanning over eight orders of magnitude (Figure 1.2).

Atmospheric species lifetimes (the average time that a molecule resides in the atmosphere before removal) are in the range between t < 1s for the most reactive free radicals, to many years for the most stable molecules. Each species can also be attributed characteristic spatial transport scale, with small characteristic scales for short-lived molecules vs. global scales for long-lived species ($t \sim$ several years). For example, the hydroxyl radical (OH) with a lifetime of less than 0.01 s has a spatial transport scale of only about 1 cm, whereas methane (CH_4) with its lifetime of about 10 years is more or less uniformly mixed globally.

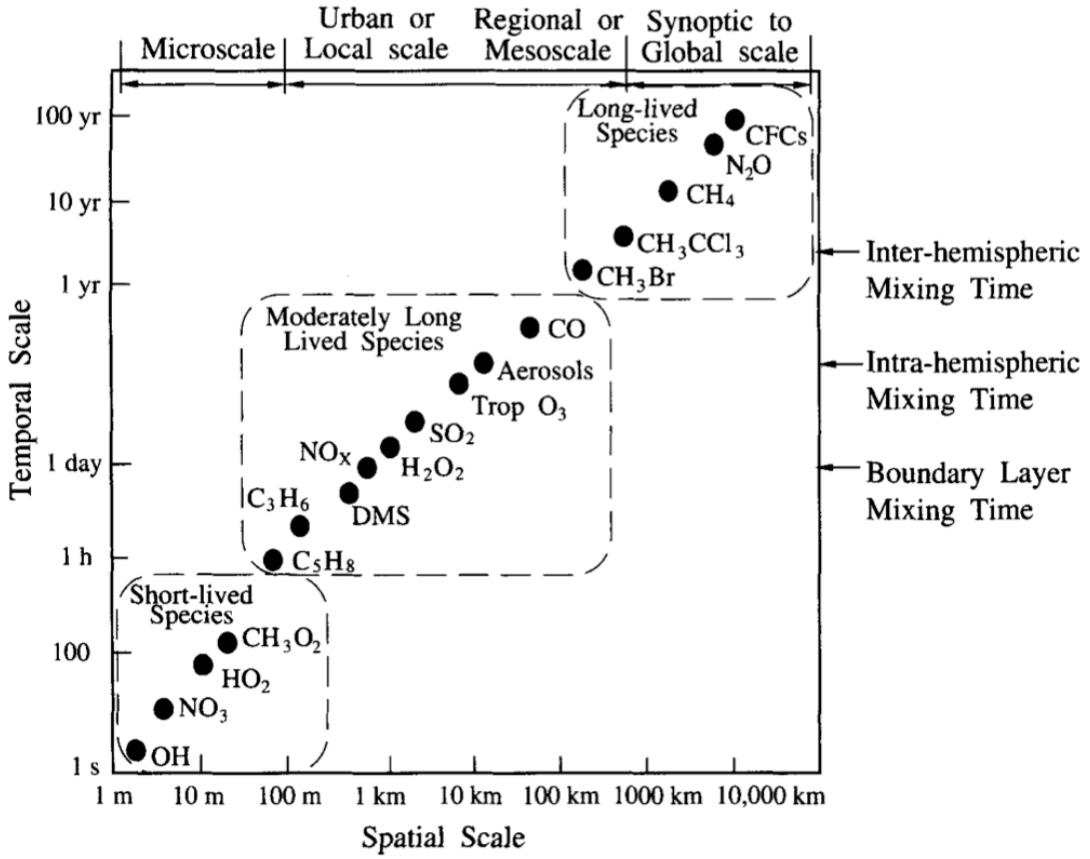

Figure 1.2. *Diagram representing temporal and spatial scale of some atmospheric species lifetime*
Image source: ***/Seinfeld, Pandis, 2006/***

1.3. Atmospheric constituents

1.3.1. General considerations

Along with the major constituents - O_2, N_2, and Ar, comprising about 99%, virtually every element of the periodic table is found in the atmosphere (Table 1.1).

Mixing ratio, or mole fraction, is a convenient unit used in atmospheric chemistry to describe the abundance, defined as the ratio of the amount (or mass) of the substance in a given volume to the total amount (or mass) of all constituents in that volume. Corresponding units are ppXv or ppXm, X being the multiplier: ppm- parts per million, ppb- parts per billion, etc., and v or m, often omitted, refer to volume or mass fraction.

Table 1.1. *Mixing ratios of some atmospheric gases in dry air*

Gas	Mixing ratio (mol/mol)
Nitrogen (N_2)	0.78
Oxygen (O_2)	0.21
Argon (Ar)	0.0093
Carbon dioxide (CO_2)	$365*10^{-6}$/ 365 ppm
Neon (Ne)	$18*10^{-6}$/ 18 ppm
Ozone (O_3)	$0.01\text{-}10*10^{-6}$/ 0.01-10 ppm
Helium (He)	$5.2*10^{-6}$ / 5.2 ppm
Methane (CH_4)	$1.8*10^{-6}$ / 1.8 ppm
Krypton (Kr)	$1.1*10^{-6}$/ 1.1 ppm
Hydrogen (H_2)	$500*10^{-9}$/ 0.5 ppm
Nitrous oxide (N_2O)	$320*10^{-9}$/ 0.32 ppm

Atmospheric species are commonly classified according to the chemical composition into the following major groups:

- *Sulphur-containing compounds*, the principal ones being hydrogen sulphide (H_2S), dimethyl sulphide (CH_3SCH_3), carbon disulphide (CS_2), carbonyl sulphide (OCS), and sulphur dioxide (SO_2).
- *Nitrogen-containing compounds*. Nitrogen is an essential nutrient for all living organisms. The important nitrogen-containing trace species in the atmosphere are nitrous oxide (N_2O), nitric oxide (NO), nitrogen dioxide (NO_2), nitric acid (HNO_3), and ammonia (NH_3). The sum of NO and NO_2 is usually designated as NO_x. More details on the atmospheric nitrogen cycle are presented in Table 1.1 and Appendix A.1.
- *Carbon-containing compounds*. Nomenclature of these molecules is vast, and detailed review goes beyond the scope of this section. However, it is

worth mentioning the most significant species like carbon mono- and dioxides CO and CO_2 (major contributor to greenhouse effect), methane CH_4 (the most abundant hydrocarbon in the atmosphere), volatile organic compounds (or VOCs, a plethora of vapour-phase atmospheric organics).

- *Halogen-containing compounds* or *halocarbons*. These can be subdivided into several categories: *chlorofluorocarbons* (*CFCs,* containing carbon, chlorine, and fluorine atoms), *hydrochlorofluorocarbons* (*HCFCs,* containing atoms of hydrogen, in addition to carbon, chlorine, and fluorine), *hydrofluorocarbons* (*HFCs,* containing atoms of hydrogen, in addition to carbon and fluorine), *halons* - bromine-containing halocarbons.
- *Particulate matter (aerosols),* which may come from natural sources, such as windborne dust, sea spray, volcanoes, and from anthropogenic activities, such as combustion of fuels. Aerosol particles range in size from a few nanometers to tens of micrometers. Particles are eventually removed from the atmosphere either through dry deposition at the Earth's surface or incorporation into cloud droplets during the formation of precipitation (wet deposition). Residence times of particles in the troposphere vary only from a few days to a few weeks.

Another important group of chemicals playing key roles in the atmospheric chemistry is *free radicals*, participating in the oxidation and further transformation of species released in the atmosphere by natural or anthropogenic activity. Free radicals (for example, hydroxyl OH, hydroperoxyl HO_2, chlorine Cl, chlorine monoxide ClO, etc.) have an unpaired electron in the outer valence shell, making them especially reactive. Hydroxyl can be considered as the “cleaner” of the atmosphere, removing trace gases and pollutants (OH radical scavenges hydrocarbons and organic molecules by capturing the hydrogen atom to form water). The state of "air pollution" is defined as the condition when substances that result from anthropogenic activities are present at concentrations sufficiently higher above normal levels.

This classification is not exclusive, while many species may belong to several groups simultaneously due to their chemical composition (like most halogens containing carbon atoms).

Virtually all species react with OH and other radicals, rendering the chemistry of the troposphere a complicated and interconnected system. Some basic interactions are illustrated here with Figure 1.3 and later in Section 1.3.2 with Figure 1.9.

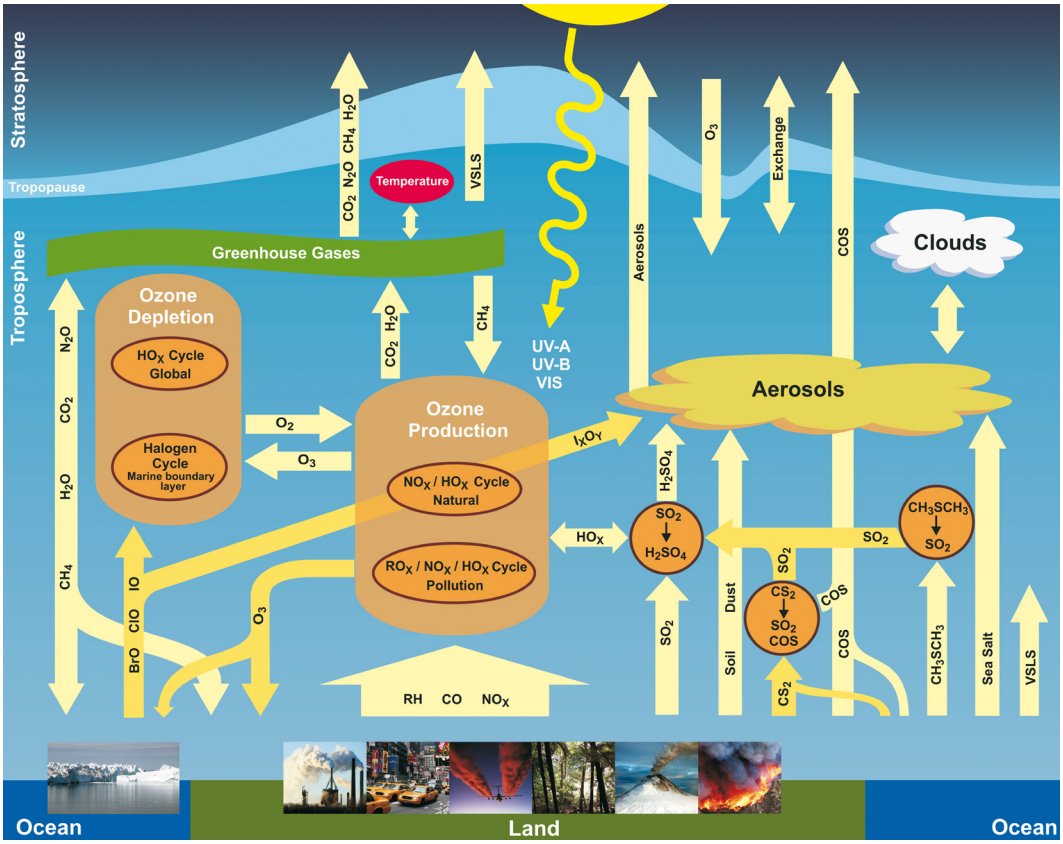

Figure 1.3. *A schematic diagram, depicting the complex chemical and physical interactions in the troposphere. The Earth's surface is a natural and anthropogenic source of volatile organic compounds, VOC (also shown as RH), CO, NOx and other species. Aerosols are produced by physical and chemical processes. Species are removed from the troposphere by deposition to the surface or transport up to the stratosphere.*

Image source: J.P. Burrows and S. Noel, IUP, Bremen

Eventually, all chemical processes in the troposphere result in the formation of more stable, oxidized products such as CO_2, various organic acids and nitrogen products, which result from the reactions involving nitric oxide, NO, NO_2, and many others. These are then extracted from the troposphere by both wet and dry deposition or by transport into the stratosphere, where they can be photolysed by UV radiation.

Development of scientific instruments over the last decades has enabled identification of atmospheric trace species down to levels of about 1 ppt by volume. Observations have shown that the composition of the atmosphere is changing on the global scale. Analysis of both modern measurements and inspection of air trapped in bubbles in the ice cores provide a record of dramatic, global increases in the concentrations of gases such as CO_2, methane (CH_4), nitrous oxide (N_2O), and various halogen-containing compounds.

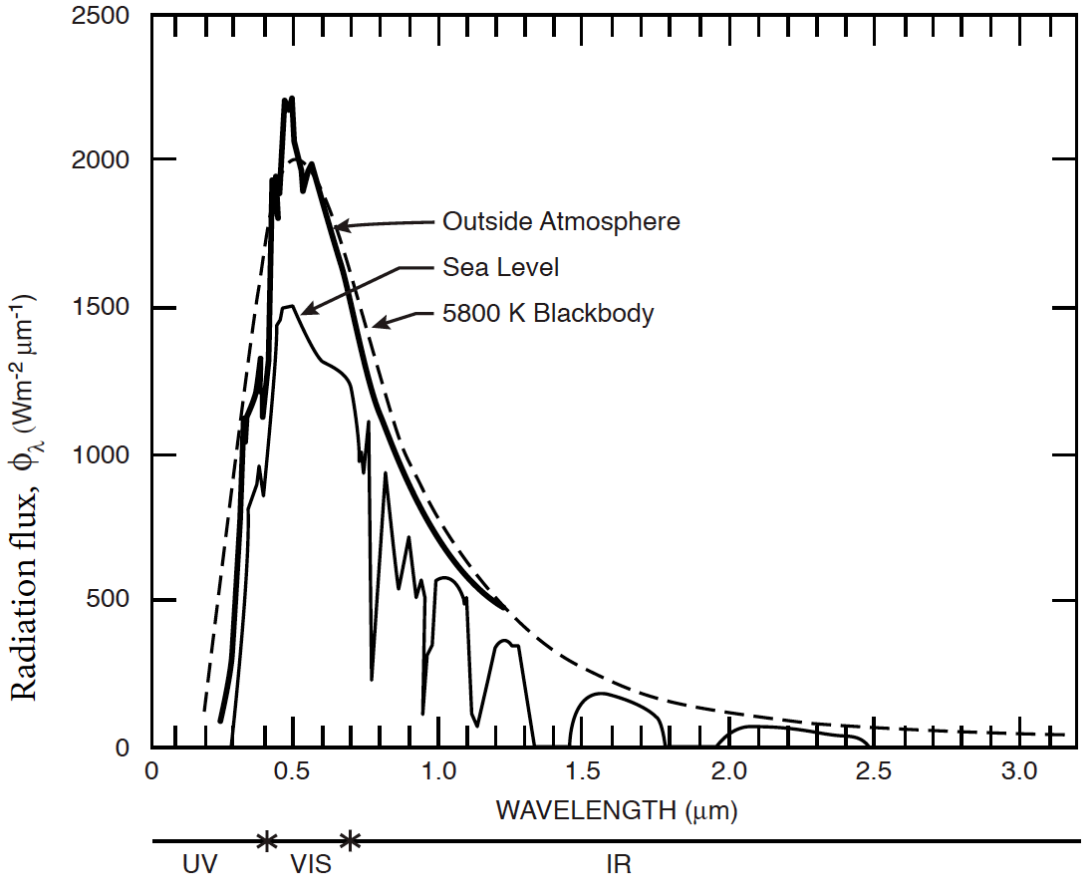

Figure 1.4. *Solar radiation spectrum outside the atmosphere (characteristic for blackbody with temperature 5800K) and at sea level after interacting with atmospheric species.*

The influx of solar radiation (Figure 1.4) and rotation of the Earth are the main drivers of cyclic chemical reaction in the atmosphere.

The species mentioned earlier, along with ozone, are greenhouse gases: they absorb infrared radiation from the Earth's surface and re-radiate a portion of this radiation back, the outcome being so-called “greenhouse effect”. This results in an increase of the average atmospheric temperature by several degrees Celsius, causing the global warming, which is the subject of major environmental and political concerns.

There are four apparent greenhouse gases that can be ranked by the percentage of contribution to greenhouse effect ***/Kiehl et al., 1997/***: water vapour ~36-70%, carbon dioxide ~9-26%, methane ~4-9%, and ozone ~3-7%. The latter two species are of particular interest for this study.

To quantify the amount of the radiation absorbed, a special term called global-warming potential (GWP) is used, signifying the ratio of the amount of heat trapped by a certain mass of the gas relative to this of carbon dioxide. The GWP depends on spectral location of its absorbing wavelength, on absorption of infrared radiation by the given species (the greater infrared radiation absorption

is, the larger is the GWP) and on atmospheric lifetime of the species (the longer atmospheric lifetime is, the bigger is the GWP). For instance, the GWP_{100} of methane over 100 years is 28, which means that if the same mass of methane and carbon dioxide were introduced into the atmosphere, that methane will trap 28 times more heat than the carbon dioxide over the next 100 years ***/IPCC, 2007/***.

There are numerous severe impacts of the global warming:

- sea level rise, leading to beach erosion, coastal wetland loss and loss of low-lying territories;
- water resource change (precipitation pattern shift; increases instances of heavy precipitation; new burdens on water capture, storage and distribution system);
- effects on agriculture (changes in the length of growing season, growth of undesirable plant species);
- effects on air quality (increase in reaction rates and concentrations of certain of atmospheric species e.g. increase in O_3 in urban areas; change in how pollutants are dispersed; more droughts, wider spread of forest fire, worsened air quality);
- impact on human health (respiratory problems affected by air quality change);
- effect on biodiversity (some species may grow too quick and overshoot their reproductive period - e.g. reef coral; forest could be devastated if the rate of climate change outpaced the rate at which forest species could migrate; change in the pattern of ocean current).

1.3.2. Species of interest: Ozone O_3

Being a reactive oxidant produced naturally in trace amounts in the Earth's atmosphere, ozone is present at higher concentrations in the upper atmospheric layers than close to the ground. Majority of the Earth's atmospheric ozone (~90%) resides in the stratosphere.

Molecular oxygen O_2 completely absorbs all radiation shorter than λ = 240 nm, photodissociating into two oxygen atoms as a result (see absorption spectrum in Figure 1.5). The atmosphere is virtually transparent at wavelengths λ > 240 nm with respect to O_2.

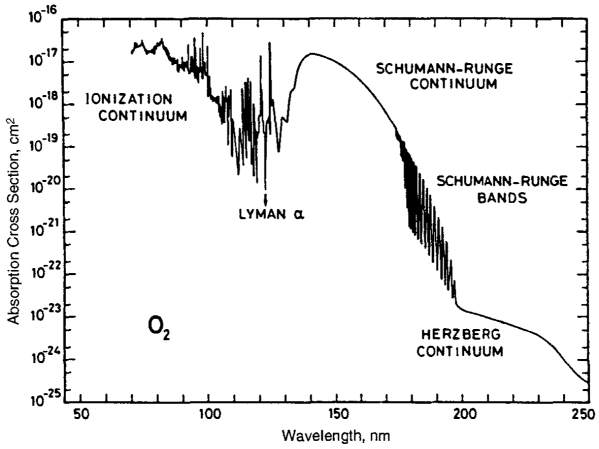

Figure 1.5. *Molecular oxygen (O_2) absorption cross-section. Image source:* **/Seinfeld, Pandis, 2006/**

Figure 1.6 shows the O_2 photodissociation rate as a function of altitude. Starting from 30 km and up to over 80 km, absorption in the Herzberg continuum, Schumann-Runge bands and Schumann-Runge continuum consequently dominates the photodissociation, see Figure 1.5 for details on wavelength ranges corresponding to the bands.

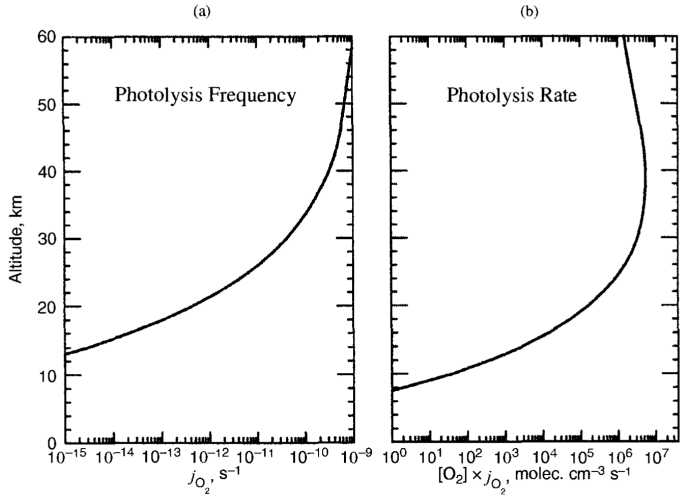

Figure 1.6. *Photodissociation rate of O_2. Image source:* **/Seinfeld, Pandis, 2006/**

As it will be shown in the next section, oxygen photodissociation is the starting point in the stratospheric ozone production cycle.

Stratospheric ozone absorbs virtually all the biologically harmful UV radiation between 210 and 290 nm, along with the so-called UV-B wavelength range 290-320 nm (Figure 1.7). Ozone always dissociates when it absorbs a visible or UV photon. Photodissociation of O_3 in the visible region, the so-called Chappuis band (430-740 nm), is the major source of ground state O atoms in the stratosphere.

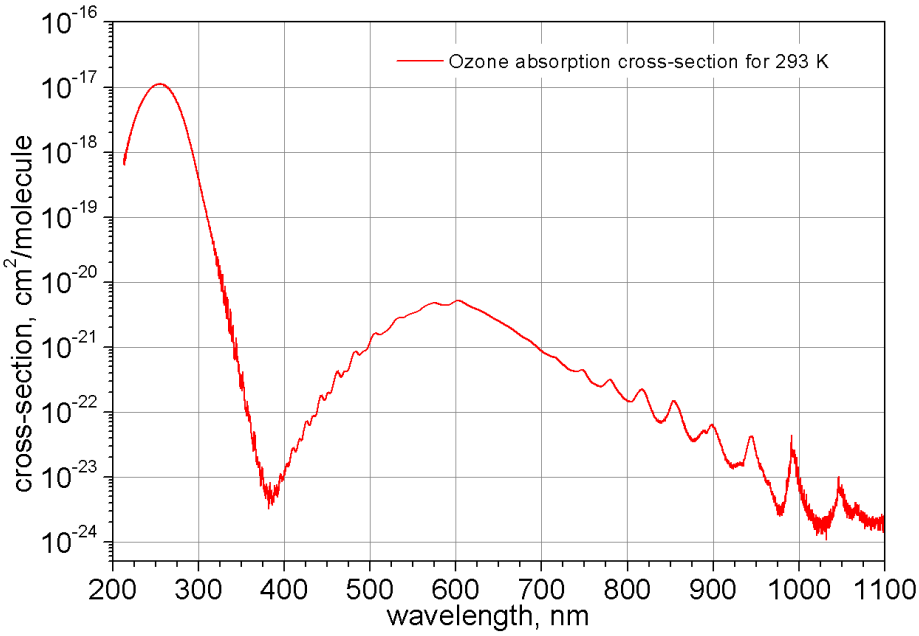

Figure 1.7. *Ozone absorption cross-section.*

Figure 1.8 gives an example of the stratospheric ozone concentration profile, with apparent peak around 20-30 km altitude.

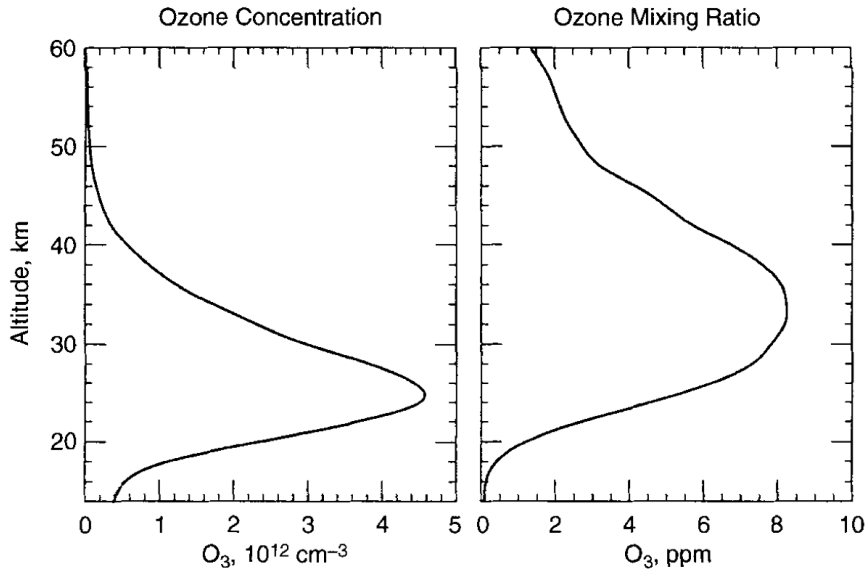

Figure 1.8. *Example of stratospheric ozone profile. Note that molecular concentration and mixing ratio peak at different altitudes.*

Image source: **/Seinfeld, Pandis, 2006/**

Ozone is also present in smaller amounts in the troposphere, with natural mixing ratios in the range of 10-40 ppb, versus the peak stratospheric values over 10,000 ppb (10ppm). However, naturally occurring tropospheric ozone accounts for about 10-15% with respect to the atmospheric total. Ozone enters the troposphere via exchange with the stratosphere. It is also created by the catalytic photochemically induced chain reactions involving the oxidation of VOCs and the oxides of nitrogen, NO and NO_2. In the troposphere ozone acts as a greenhouse gas, and is a necessary source of oxidation.

Anthropogenically-emitted substances have the potential to deplete the natural levels of stratospheric ozone, and at the same time, lead to ozone increases in the troposphere. Increase of the UV-B reaching the Earth's surface can lead to more frequent incidences of skin cancer. However, ozone is considered toxic and harmful for the human health and vegetation when present at elevated concentrations in the troposphere. It is therefore beneficial to decrease tropospheric ozone levels by controlling the ozone precursors - hydrocarbons and nitrogen oxides.

The Chapman mechanism and relevant chemical cycles

At the tropopause, the temperature profile described in the Section 1.1 changes, increasing with altitude throughout the stratosphere due to increase of ozone concentration. The amount of stratospheric and mesospheric ozone is determined by a set of photochemical transformations involving ozone and molecular oxygen.

The series of reactions described below, named the "Chapman cycle" after Sydney Chapman, who first considered it in 1930's, is the main mechanism responsible for ozone production in the stratosphere (above ~ 30 km altitude). Solar UV radiation of wavelengths less than 240 nm dissociates molecular oxygen (see Figure 1.5, 1.6):

$$O_2 + h\nu_{(\lambda<240\ nm)} \rightarrow O + O \qquad (1.1)$$

The oxygen atoms then react with O_2 in the presence of a third body M (N_2 , O_2, or O_3 molecule) to produce ozone molecule O_3:

$$O + O_2 + M \rightarrow O_3 + M \qquad (1.2)$$

Ozone formed in this reaction strongly absorbs radiation in the 210-320 nm range (Figure 1.7). Depending on the wavelength of the absorbed photon, O_3 photodissociates back to O_2 and either ground-state atomic oxygen O:

$$O_3 + h\nu_{(430\ nm<\lambda<740\ nm)} \rightarrow O + O_2 \qquad (1.3)$$

or the first electronically excited state of atomic singlet-D oxygen, $O(^1D)$:

$$O_3 + h\nu_{(200\ nm<\lambda<300\ nm)} \rightarrow O(^1D) + O_2 \qquad (1.3')$$

The photodissociation of O_3 at altitudes below about 30 km is governed mainly by absorption in the Chappuis bands (reaction (1.3)), whereas above ~30 km, absorption in the Hartley bands (200-300 nm) dominates (reaction (1.3')).

Oxygen atoms produced in reaction (1.3) just recombine with O_2 to form O_3 with the release of heat (reaction (1.2)), thus rendering the absorption of radiation by O_3 a conversion mechanism of light into heat without any net loss of ozone. Energy is also released from reaction (1.2). If two oxygen atoms meet, they react to form one oxygen molecule O_2.

UV photons in reaction (1.3') have sufficient energies to produce excited states of both O [$O(^1D)$] and O_2 [O_2 ($^1\Delta$)]. Relaxation of the $O(^1D)$ to ground-state atomic oxygen occurs by collision with third body molecule M (N_2 or O_2):

$$O(^1D) + M \rightarrow O + M$$

or by reaction with water molecule

$$O(^1D) + H_2O \rightarrow 2\ OH$$

Finally, O and O_3 react to reform two O_2 molecules:

$$O + O_3 \rightarrow O_2 + O_2 \qquad (1.4)$$

The Chapman cycle is responsible for generating a steady-state concentration of O_3 in the stratosphere. The net amount of ozone in the stratosphere is determined by a balance between production by solar radiation and removal. The concentration of O atoms is very low; therefore the removal rate is slow.

O_3 production rates are the highest at about 40 km altitude at the equator, whereas ozone concentrations peak at northern latitudes. The stratospheric O_3 concentrations are at maximum in areas remote from those where O_3 is being produced, meaning that the lifetime of stratospheric O_3 is longer than the time needed for the transport to occur. Typical transport timescale from the equator to the poles in the stratosphere is about 3-4 months.

Atmospheric species contribute to ozone destruction if they are present in excessive concentrations or are being regenerated in catalytic cycles. A complicated and interconnected system of such cycles (as, for example, in Figure 1.9) involving nitrogen oxides, hydrogen radicals, chlorine and bromine is the main driver of ozone production or destruction.

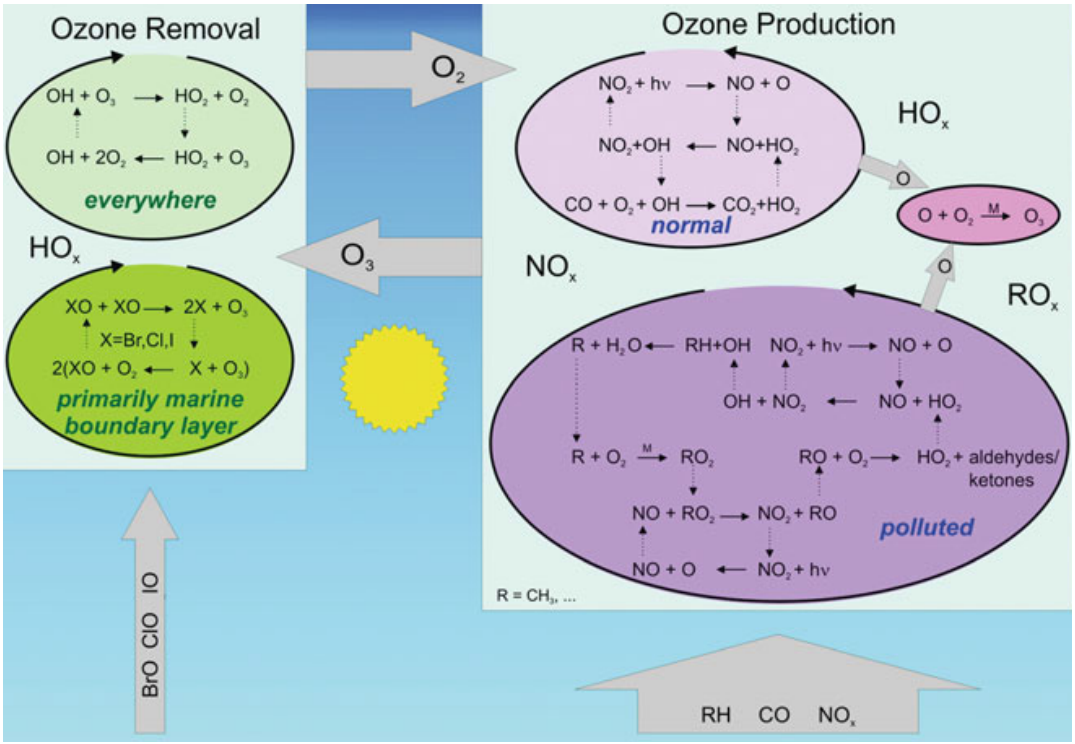

Figure 1.9. *Some of the chemical processes involved in the production and removal of tropospheric ozone.*

Image source: J.P. Burrows and S. Noel, IUP, Bremen.

Chemistry of these cycles was first closely investigated in the early 1970s by **/Crutzen, 1970/** and **/Johnston**, **1971/**. Different cycles dominate at different altitudes in the atmosphere.

Reactive nitrogen compounds NOx (a sum of NO + NO_2) are produced in the stratosphere from N_2O, which is released by biospheric microbial activity and does not participate in tropospheric chemistry. Important reactions relevant for atmospheric nitrogen cycles are presented in Table 1.1.

The species of HO_X family (OH + HO_2) are also the key participants in atmospheric chemistry reactions; the most important cycles are listed in Table 1.2.

Several diagrams and tables relevant for the atmospheric chemistry processes are available in Appendix A.1.

Table 1.1. *Several important reactions of the NO_X cycle*	
Reactions	***Comments***
$N_2O + h\nu \rightarrow N_2 + O(^1D)$ (1.5) $N_2O + O(^1D) \rightarrow NO + NO$ (1.6a) $\rightarrow N_2 + O_2$ (1.6b)	Main source of NOx ($NO + NO_2$)
NO_X cycle 1: $NO + O_3 \rightarrow NO_2 + O_2$ (1.7) $NO_2 + O \rightarrow NO + O_2$ (1.8) Total: $O_3 + O \rightarrow O_2 + O_2$	Conversion of odd oxygen ($O_3 + O$) to even oxygen (O_2) (most effective in the upper stratosphere, where O atom concentrations are highest)
$NO_2 + h\nu \rightarrow NO + O$ (1.9) $O + O_2 + M \rightarrow O_3 + M$ (1.10)	Competing mechanism to (1.8)
NO_X cycle 2: $NO + O \rightarrow NO_2 + O_2$ (1.11) $NO_2 + O \rightarrow NO_3 + O_2$ (1.12) $NO_3 + h\nu \rightarrow NO + O_2$ (1.13) Total: $O_3 + O_3 \rightarrow O_2 + O_2 + O_2$	Cycle that does not require O atoms and therefore is more important in the lower stratosphere
$NO_3 + h\nu \rightarrow NO_2 + O$ (channel a) $\rightarrow NO + O_2$ (channel b)	Photolysis of NO_3

Table 1.2. *Several important reactions of the stratospheric HO_X cycle*	
Reactions	***Comments***
$O_3 + h\nu \rightarrow O(^1D) + O_2$	O_3 photolysis *(200 nm<λ<300 nm)*
$O(^1D) + H_2O \rightarrow OH + OH$ $O(^1D) + CH_4 \rightarrow OH + CH_3$	~ 90% of OH produced ~ 10% of OH produced
$HO_2 + NO \rightarrow NO_2 + OH$	Interconversion between OH and HO_2
$NO_2 + h\nu \rightarrow NO + O$	NO_2 photolysis, followed by:
$O + O_2 + M \rightarrow O_3 + M$	
$HO_2 + O \rightarrow OH + O_2$ $HO_2 + O_3 \rightarrow OH + O_2 + O_2$	Odd oxygen removal
$OH + O_3 \rightarrow HO_2 + O_2$	Regeneration of HO_2
HO_X cycle 1: $OH + O_3 \rightarrow HO_2 + O_2$ $HO_2 + O \rightarrow OH + O_2$ Total: $O_3 + O \rightarrow O_2 + O_2$	Catalytic ozone-depletion cycle #1
HO_X cycle 2: $OH + O_3 \rightarrow HO_2 + O_2$ $HO_2 + O_3 \rightarrow OH + O_2 + O_2$ Total: $O_3 + O_3 \rightarrow O_2 + O_2 + O_2$	Catalytic ozone-depletion cycle #2

The ozone hole

Although the OH and NO species are naturally present in the stratosphere, anthropogenic activity has perturbed the balance and modified the catalytic destruction cycles. The most well known examples are the emissions of chlorofluorocarbons (CFCs) and halons, which greatly increased the chlorine (Cl) and bromine (Br) concentrations. A single Cl or Br atom can catalyse tens of thousands of decomposition reactions prior to its removal from the stratosphere.

The results is the global loss of ozone in the upper stratosphere and the late winter and springtime removal of ozone in the lower atmosphere **/Farman et al., 1985/**. Observations unveiled almost complete disappearance of ozone in the Antarctic stratosphere during the austral spring (Antarctic ozone hole), and somewhat less dramatic decreases over the Arctic and over the northern and southern midlatitudes. The threat of the further severe reduction of O_3 concentrations due to anthropogenic activity resulted in the 1985 Vienna Convention for the Protection of the Ozone Layer and its 1987 Montreal protocol, which banned certain human-made ozone depleting substances (ODSs).

In analogy to global warming potential (GWP) (Section 1.3.1), ozone depletion potential (ODP) is used to quantify the relative contributions of various ODSs to ozone layer depletion. It relates the amount of stratospheric ozone destroyed by the release of a unit mass of a chemical at Earth's surface to the amount destroyed by the release of a unit mass of chlorofluorocarbon 11, CFC-11 ($CFCl_3$). Figure 1.10 provides historical data and forecast of emissions of certain ODSs.

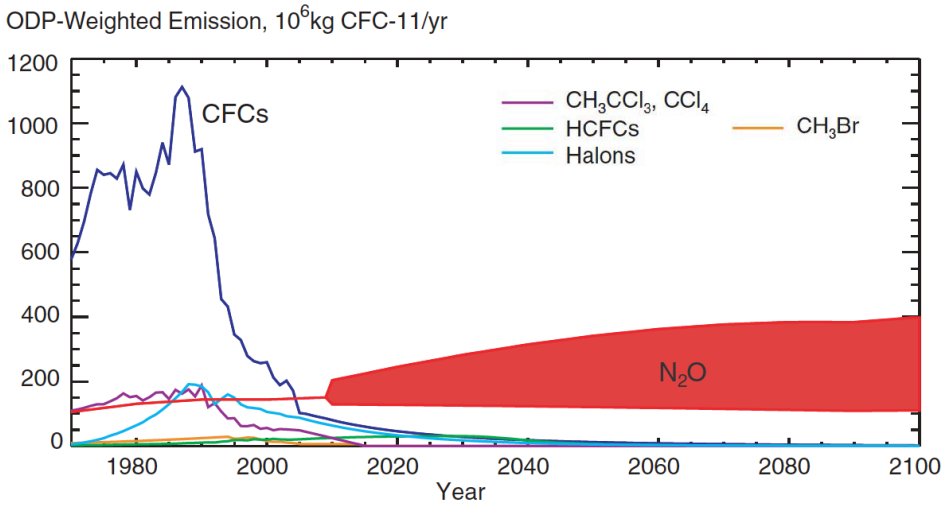

Figure 1.10. *Historical and projected ODP-weighted emissions of the most important ODSs*

Image source: adapted from **/Ravishankara et al., 2009/**.

The importance of anthropogenic modification of the nitrogen cycle and the resultant bacterial increase in the production of nitrous oxide (N_2O) from soils has also been recognized **/Ravishankara et al., 2009/**. N_2O is long lived in the troposphere, and after transport to the stratosphere, it reacts with excited oxygen atoms $O(^1D)$ to produce nitric oxide NO, which participates in the most important O_3 catalytic destruction cycle (see Table 1.1). At the same time, while stratospheric ozone levels have been decreasing, tropospheric concentrations in the northern hemisphere have been building up.

1.3.3. Species of interest: Methane CH_4

Methane is the most abundant hydrocarbon in the atmosphere and the third major contributor to the greenhouse effect (see section 1.3.1). With GWP_{100} of about 28 and observed trends of the atmospheric mixing ratios change, methane is a subject of constant global monitoring.

Reconstruction of historical concentrations of CO_2 and CH_4 was made possible via analysis of air taken from bubbles trapped in the ice core samples obtained in Antarctica and Greenland, where it was preserved for hundreds of years. CO_2 and CH_4 concentrations remained almost unchanged in the period from roughly 10,000 years ago until 300 years ago, with mixing ratios in the order of 260 ppm and 700 ppb. At around 1700s, the CH_4 levels started to increase, and about 100 years ago levels of both CO_2 and CH_4 began grow especially fast, with CH_4 mixing ratios reaching the present day value of ~1800 ppb.

The alarming rate of the atmospheric methane increase since pre-industrial era is attributed to human activity - combustion of fossil fuels (coal and oil) for energy and transportation, industrial and agricultural activities, biomass burning, and deforestation.

Direct atmospheric measurements of CH_4 of sufficient spatial coverage to calculate global annual means began around 1980 (Figure 1.11).

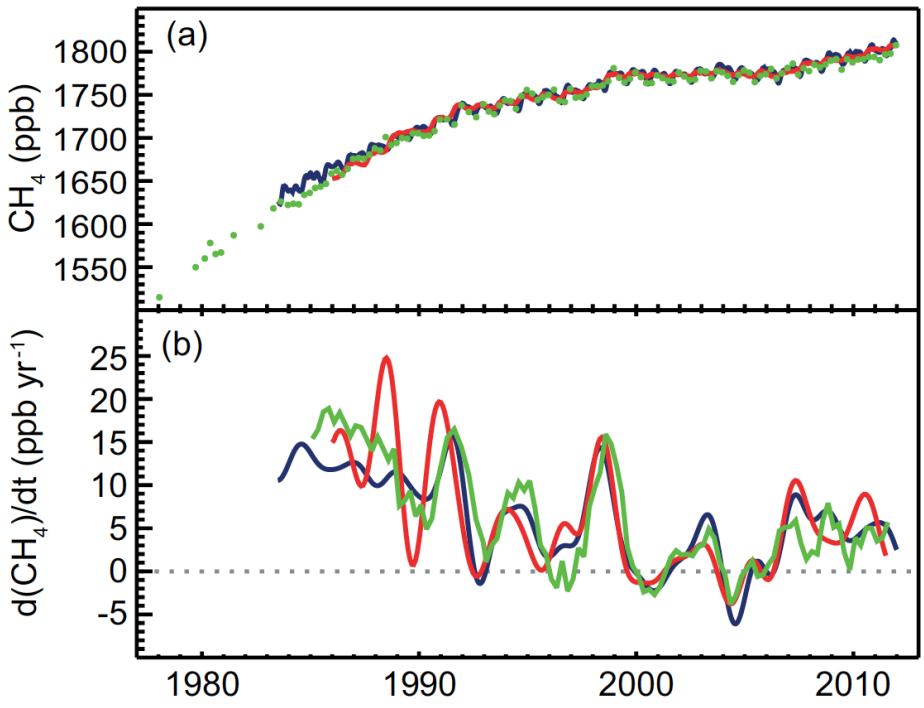

Figure 1.11. *(a) Globally averaged CH_4 dry-air mole fractions from UCI (green), AGAGE (red), and NOAA/ESRL/GMD (blue)*

(b) Instantaneous growth rate for globally averaged atmospheric CH_4 (colour code as in (a)).

Image source: **/IPCC, 2013/**.

The net rate of CH_4 emissions is generally estimated from three approaches:

- extrapolation from direct flux measurements and observations;
- process-based modelling (*bottom-up* approach);
- inverse modelling (*top-down* approach).

Bottom-up approaches are used to attribute the decadal budgets to individual processes emitting CH_4. When the bottom-up approach is used to extrapolate the emissions to larger scales, uncertainty results from the inherent large temporal and spatial variations of fluxes and the limited range of observational conditions.

Top-down inversions rely on the spatially distributed, temporally continuous observations of concentration, and in some cases isotopic composition in the atmosphere, which allows to distinguish emissions per source type. The top-down method also includes aircraft and satellite observations.

The latest Intergovernmental Panel on Climate Change report (***/IPCC, 2013/***) provides the methane budget based on both top-down and bottom-up data. Table 1.3 gives the breakdown of methane sources and sinks for three recent decades.

The sources of CH_4 at the surface of the Earth can be *thermogenic* (natural emissions of fossil CH_4 from geological seepages, geothermal vents and mud volcanoes, emissions caused by leaks from fossil fuel extraction and use) and *pyrogenic* (incomplete burning of fossil fuels and plant biomass in both natural and anthropogenic fires). *Biogenic* CH_4, produced from organic matter under low oxygen conditions by fermentation processes of methanogenic microbes, may also come from both natural sources (wetlands, termites and to a small extent, the ocean) and anthropogenic emissions: rice agriculture, livestock, landfills, waste treatment, man-made lakes and wetlands.

Anthropogenic activity accounts for 50-65% of total CH_4 emissions. Fluctuations of CH_4 release from natural wetlands are the main drivers of the global annual variability of CH_4 emissions.

A significant geological stock ($2*10^6$ to $9.3*10^6$ $Tg(CH_4)$) of CH_4 exists in the form of methane clathrate deposits in shallow ocean sediments and permafrost soils. These hydrates are stable at low temperature and high pressure. Warming or pressure changes could render some of these hydrates unstable, potentially releasing CH_4 into soil, ocean and atmosphere (***/IPCC, 2013/***).

The major CH_4 sinks are the oxidation by OH in the troposphere, biological oxidation in drier soil, and loss to the stratosphere. Additional sink is presumably oxidation by Cl in the marine atmospheric boundary layer. The decline in the growth rate of atmospheric CH_4 concentration until 2009 shows no clear correlation with change in sink strengths. This trend has continued since 1993, and the reduction in the CH_4 growth rate has been suggested to be a consequence of source stabilization and the approach of the global CH_4 budget towards steady state. On the example of the year 2011 (Table 1.3), the estimated imbalance of +14 $Tg(CH_4)yr^{-1}$ between the current sources and sinks of CH_4 indicates that methane is accumulating in the atmosphere.

Table 1.3. *Global CH_4 budget for the past three decades and 2011.*
Values correspond to the mean of the cited references and not always equal (max-min)/2
Uncertainties are listed using minimum and maximum of each published estimate for each decade.
Source: ***/IPCC, 2013/*** *and references therein*

Tg (CH_4) yr^{-1} mean [min–max]	1980–1989		1990–1999		2000–2009	
	Top-Down	Bottom-Up	Top-Down	Bottom-Up	Top-Down	Bottom-Up
Natural sources	**193 [150–267]**	**355 [244–466]**	**182 [167–197]**	**336 [230–465]**	**218 [179–273]**	**347 [238–484]**
Natural wetlands	**157 [115–231]**	**225 [183–266]**	**150 [144–160]**	**206 [169–265]**	**175 [142–208]**	**217 [177–284]**
Other sources	**36 [35–36]**	**130 [61–200]**	**32 [23–37]**	**130 [61–200]**	**43 [37–65]**	**130 [61–200]**
Freshwater		40 [8–73]		40 [8–73]		40 [8–73]
Wild animals		15 [15–15]		15 [15–15]		15 [15–15]
Wildfires		3 [1–5]		3 [1–5]		3 [1–5]
Termites		11 [2–22]		11 [2–22]		11 [2–22]
Geological (incl. oceans)		54 [33–75]		54 [33–75]		54 [33–75]
Hydrates		6 [2–9]		6 [2–9]		6 [2–9]
Permafrost		1 [0–1]		1 [0–1]		1 [0–1]
Anthropogenic sources	**348 [305–383]**	**308 [292–323]**	**372 [290–453]**	**313 [281–347]**	**335 [273–409]**	**331 [304–368]**
Agriculture and waste	**208 [187–220]**	**185 [172–197]**	**239 [180–301]**	**187 [177–196]**	**209 [180–241]**	**200 [187–224]**
Rice		45 [41–47]		35 [32–37]		36 [33–40]
Ruminants		85 [81–90]		87 [82–91]		89 [87–94]
Landfills and waste		55 [50–60]		65 [63–68]		75 [67–90]
Biomass burning	**46 [43–55]**	**34 [31–37]**	**38 [26–45]**	**42 [38–45]**	**30 [24–45]**	**35 [32–39]**
Fossil fuels	**94 [75–108]**	**89 [89–89]**	**95 [84–107]**	**84 [66–96]**	**96 [77–123]**	**96 [85–105]**
Sinks						
Total chemical loss	**490 [450–533]**	**539 [411–671]**	**515 [491–554]**	**571 [521–621]**	**518 [510–538]**	**604 [483–738]**
Tropospheric OH		468 [382–567]		479 [457–501]		528 [454–617]
Stratospheric OH		46 [16–67]		67 [51–83]		51 [16–84]
Tropospheric Cl		25 [13–37]		25 [13–37]		25 [13–37]
Soils	**21 [10–27]**	**28 [9–47]**	**27 [27–27]**	**28 [9–47]**	**32 [26–42]**	**28 [9–47]**
Global						
Sum of sources	**541 [500–592]**	**663 [536–789]**	**554 [529–596]**	**649 [511–812]**	**553 [526–569]**	**678 [542–852]**
Sum of sinks	**511 [460–559]**	**567 [420–718]**	**542 [518–579]**	**599 [530–668]**	**550 [514–560]**	**632 [592–785]**
Imbalance (sources - sinks)	**30 [16–40]**		**12 [7–17]**		**3 [–4–19]**	
Atmospheric growth rate	**34**		**17**		**6**	

Global top-down	**2011 (IPCC)**
Burden (Tg CH_4)	**4954±10**
Natural sources	**202±35**
Anthropogenic sources	**354±45**
Total sources	**556±56**
Atmospheric sinks	**542±56**
Atmospheric increase	**14±3**

Atmospheric chemistry of methane

Reaction with the hydroxyl radical (OH) is the main loss channel for CH_4 (as well as for many HFCs and HCFCs) and the largest term in the global CH_4 budget.

The atmospheric lifetime against reaction with OH is defined as the time required for it to turn over the entire CH_4 atmospheric burden:

$$\frac{4954\ \text{Tg}}{518\ \text{Tg/yr}} = 9.5\ \text{years}.$$

The lifetime of methane is varied by its abundance in the atmosphere. Increase of CH_4 concentration leads to the longer atmospheric lifetime. Therefore, trends and annual variability in OH concentration significantly impact the understanding of changes in CH_4 emissions.

The principal oxidation reaction of CH_4 is:

$$CH_4 + OH \xrightarrow[O_2]{} CH_3O_2 + H_2O \qquad (1.14)$$

↳ main product: methyl peroxy radical CH_3O_2

CH_3O_2, the product of reaction (1.14) can react with NO, NO_2, HO_2 radicals. The reaction with NO leads to the methoxy radical (CH_3O) and NO_2:

$$CH_3O_2 + NO \xrightarrow[O_2]{} HCHO + HO_2 + NO_2 \qquad (1.15)$$

CH_3O_2 with HO_2 forms methyl hydroperoxide (CH_3OOH):

$$CH_3O_2 + HO_2 \rightarrow CH_3OOH + O_2 \qquad (1.16)$$

which photodissociates or reacts with OH:

$$CH_3OOH + h\nu \rightarrow CH_3O + OH \qquad (1.17)$$

$$CH_3OOH + OH \rightarrow H_2O + CH_3O_2 \qquad (1.18a)$$

$$\rightarrow H_2O + CH_2OOH \qquad (1.18b)$$

↳ main products: HCHO + OH

With tropospheric lifetime of about 2 days, CH_3OOH and has a significant impact on the methane oxidation chain: reactions (1.15) - (1.18b) lead to creation and loss of a variety of radicals. In the end, the OH is regenerated, and a molecule of formaldehyde (HCHO) is formed.

HCHO, a first-generation oxidation product of CH_4 and many other hydrocarbons, undergoes two main reactions in the atmosphere, photolysis

$$HCHO + h\nu \rightarrow H + CHO$$

fast reaction: ↳ $HCO + O_2 \rightarrow HO_2 + CO$ (1.19a)

or, concisely: $HCHO + h\nu \xrightarrow[O_2]{} 2\ HO_2 + CO$ (1.19b)

$$\rightarrow H_2 + CO \qquad (1.19c)$$

and reaction with OH

$$HCHO + OH \rightarrow HCO + H_2O \qquad (1.20a)$$

$$\text{fast reaction: } \downarrow\ HCO + O_2 \rightarrow HO_2 + CO \qquad (1.19a)$$

or, concisely: $$HCHO + OH \xrightarrow[O_2]{} HO_2 + CO + H_2O \qquad (1.20)$$

Almost every CH_4 molecule is converted to HCHO with relatively short lifetime (~8 hours). Both photolysis and OH reaction of HCHO lead to formation of CO, the principal product of methane oxidation. CO is converted to CO_2 within several month to complete the CH_4 oxidation chain (see Appendix A.1 for details). The overall $CH_4 \rightarrow CO_2$ sequence is shown in Figure 1.12.

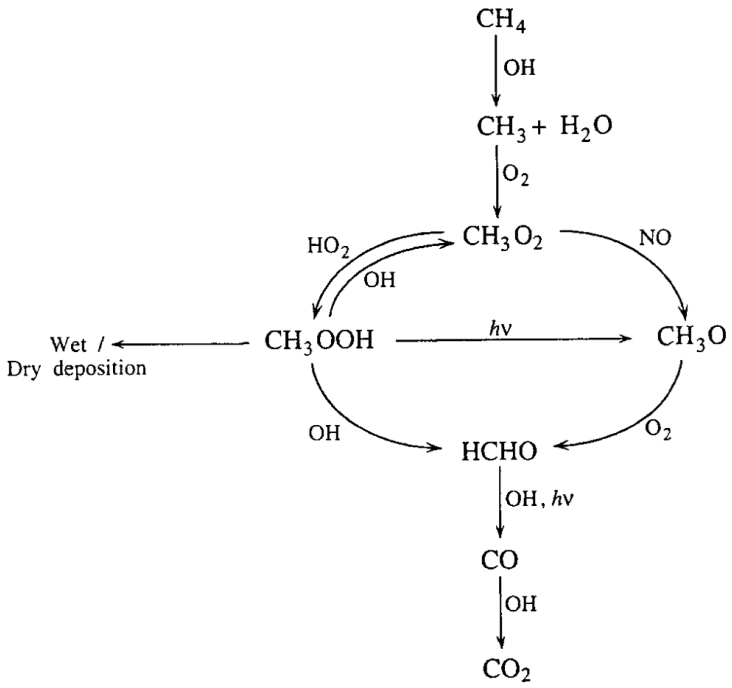

Figure 1.12. *CH_4 oxidation chain*

Image source: adapted from **/Seinfeld, Pandis, 2006/**.

Methane oxidation is linked to ozone production via peroxy radicals HO_2 and CH_3O_2, appearing in reactions (1.14), (1.18a), (1.15), (1.19b) and oxidation of CO by OH (see Table A.2 in the Appendix A.1):

$$CO + OH \xrightarrow{O_2} CO_2 + HO_2$$

Peroxy radicals react with NO to form NO_2:

$$HO_2 + NO \rightarrow OH + NO_2$$

$$CH_3O_2 + NO \rightarrow CH_3O + NO_2$$

The resulting NO_2 photodissociates as in (1.19)+(1.10), see Table 1.1:

$$NO_2 + h\nu \rightarrow NO + O \quad (1.9)$$

$$O + O_2 + M \rightarrow O_3 + M \quad (1.10)$$

Assuming the extreme case, when NO_x levels are sufficiently high that the peroxy radicals react exclusively with NO and formaldehyde HCHO is removed via photolysis only, summing all reactions yields the following net reaction for conversion of CH_4 to CO_2:

$$CH_4 + 10\ O_2 \rightarrow CO_2 + H_2O + 5\ O_3 + 2\ OH$$

so that five O_3 molecules appear per one reacted CH_4 Molecule. This never happens in the atmosphere, since all the competing reactions were neglected in the estimate.

In contrast, in an atmosphere depleted of NO_x so that CH_3O_2 reacts by (1.16), and assuming that CH_3OOH reacts by (1.18b) and CH_2O reacts by (1.19a), summing all reactions in the mechanism yields:

$$CH_4 + 3\ OH + 2\ O_2 \rightarrow CO_2 + 3\ H_2O + HO_2$$

where no O_3 is produced and two HO_x molecules are consumed. This emphasizes the critical role of NO_x for maintaining O_3 and OH concentrations in the troposphere.

In both cases, the oxidation of methane in stratosphere is a source of stratospheric water vapor.

The reaction of methane with free chloride produces chloromethane and hydrochloric acid. This process is called free radical halogenation.

$$CH_4 + Cl_2 \rightarrow CH_3Cl + HCl \quad (1.21)$$

1.4. Remote sensing of O_3 and CH_4

Monitoring of the Earth's climate system is based on direct physical and biogeochemical measurements and remote sensing from ground stations, satellites and other platforms. These methods provide a comprehensive view of the variability and long-term changes in the atmosphere, the ocean, the cryosphere, and the land surface, and allow estimate the influence of natural and anthropogenic activities on global climatic processes.

Global-scale instrumental observations began in the mid-19th century for temperature and other variables, with more comprehensive and diverse sets of observations available starting from 1950 (Figure 1.13). Reconstructions based on paleoclimate-dated samples provide a longer-term context, extending records for some parameters to hundreds to millions of years ago.

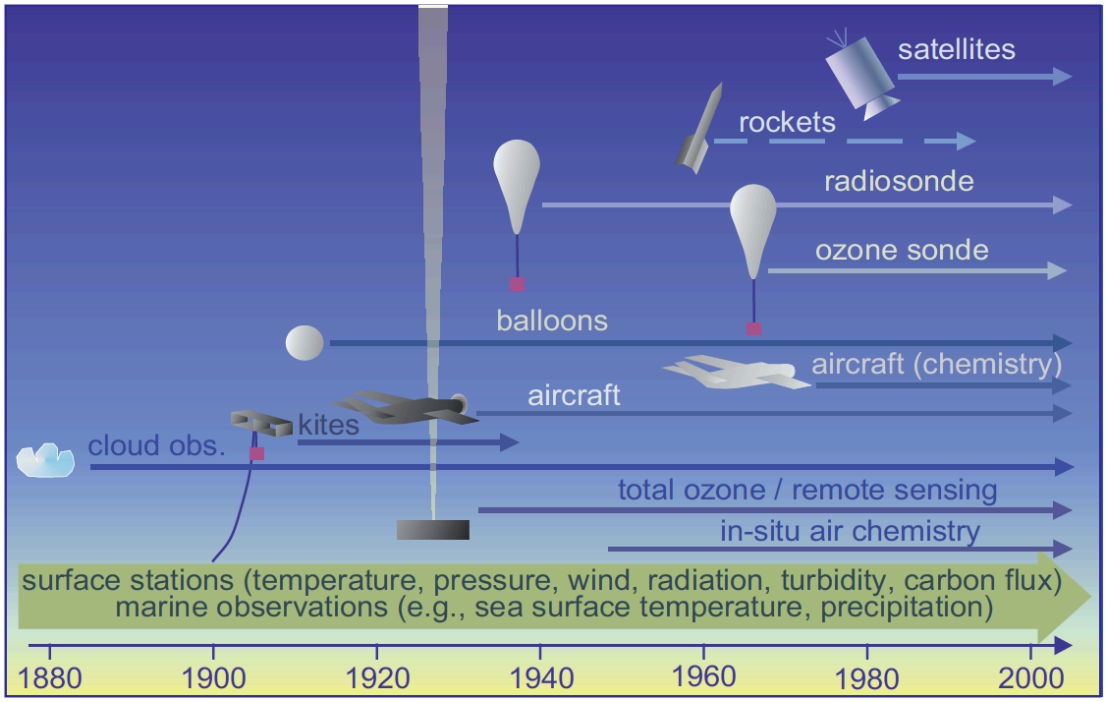

Figure 1.13. *Evolution of the environmental observation instrumentation, parameters, and scales*

Improved understanding and systematic monitoring of the Earth's climate requires the observations of various atmospheric, oceanic and terrestrial parameters and therefore has to rely on various technologies. Some tools are ground based, measuring spectra of the transmitted and scattered radiation at the same location more or less continuously. Identical instruments installed at different location form ground-based networks. Other sensors are orbiting the Earth on board of the satellites, providing global coverage with characteristic time and spatial resolution. In addition, in-situ measurements made by instruments installed on ships, buoys, ocean profilers, aircraft and balloons provide useful information on the mid-scale time and spatial resolution. During

recent years, new monitoring systems have increased the number of observations by orders of magnitude, with measurements made at locations not available before. Parallel to this, tools to analyse and process the data have been developed and enhanced to deal with the increase of information and to provide a more comprehensive view of the Earth's climate. More non-instrumental (proxy) data have been acquired to provide a more detailed picture of climate changes in the past.

The goal of the long-term observations is to monitor temporal changes in the atmospheric composition and chemistry. Of a special interest are trends in stratospheric and tropospheric ozone mixing ratios, atmospheric amounts of ODSs, GHG concentrations (CO_2, CH_4, and N_2O), and trends in aerosol properties **/Burrows et al, 2011/**.

Atmospheric species exhibit an enormous range of spatial and temporal variability, which depends on their lifetime. Long-lived species can be characterized through measurements at strategically located sampling sites around the globe, allowing to adequately assess their spatial distribution and temporal trends. As species lifetimes become shorter, their spatial and temporal variations become more significant. Characterization of the spatial and temporal distribution of atmospheric components in urban sites requires dozens of measurement spots per hundreds of square kilometres.

Delivered information reflects both total amounts of the species in the atmosphere and vertical profile of the species distribution.

The majority of the data has been coming in increasing quantities from the satellites (Figure 1.14). Data quality improvement comes from more advanced instrument design or from more accurate correction in the ground-station processing.

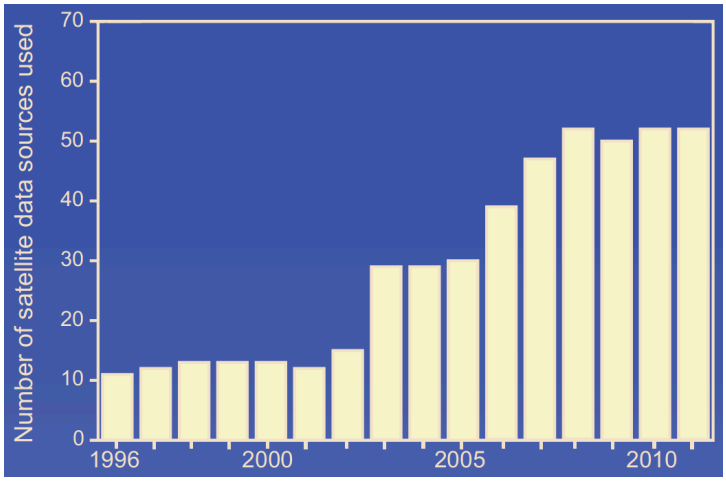

Figure 1.14. *Increase of the data coming from the satellite-borne instruments*

Below is a brief description of some instruments relevant for the ozone and methane observations.

1.4.1. Ground based instruments

The earliest instrument used to measure both total column and profiles of O_3 in the atmosphere is the Dobson spectrophotometer, developed in 1920's by Gordon Dobson.

Using direct or scattered sun- and moonlight, the spectrometer measures the UV light intensity at pairs of wavelengths that are strongly absorbed and weakly absorbed by ozone (for example, 305 nm and 325 nm). Thus, by measuring the relative intensities of suitably selected pair wavelengths with the Dobson instrument, it is possible to determine how much ozone is present in a vertical column of air extending from ground level to the top of the atmosphere in the vicinity of the instrument. The result is expressed in Dobson Units (DU), a thickness of a layer of pure ozone at standard temperature and pressure (STP). One Dobson unit corresponds to a layer of 0.01 mm of ozone if all the ozone in the column was to be brought to STP (P=1013.25 hPa, T=273°K) **/WMO, 2008/.**

If Dobson spectrophotometer observations are made on the clear zenith sky during a one-half day, and observed instrument N values are plotted vs. time, a maximum in the N values is observed to occur shortly after sunrise or before sunset. This reversal (or "Umkehr") in the plotted curve is related to the effective scattering height in the atmosphere of the wavelengths on which observations are made. Coupled with information on standard ozone profiles and a knowledge of the total ozone amount, the Umkehr data can be analyzed to yield the ozone vertical distributions that reveal changes in ozone associated with day-to-day weather conditions as well as with seasonal and long-term trends.

In 1957, the international ozone commission facilitated the development of a global network of the Dobson spectrophotometer instruments for O_3 measurements.

During the 1970's, the Brewer instrument was developed. It is based on the same measurement principle as the Dobson instrument, but uses more state-of-the-art technology, from multi-wavelength operation and high stray light rejection to measurement automation and tracking.

The Dobson and the Brewer spectrometers have been the most widely used, as they are the standard instruments for the Global Atmosphere Watch (GAW) program of the WMO, and remain one of the main sources of information about long-term ozone changes, trend analyses, and identification of possible natural or anthropogenic influences on atmospheric composition.

Other instruments such as ozonometers and hand-held sun-photometers, also make measurements of the total ozone. A balloon flight with instruments measuring in-situ ozone can be analyzed for total ozone as well. The results from these instruments can be compared to the Dobson results to detect problems. Various instruments have their own set of assumptions and approximations that have to be understood, but the results from these instruments and from the Dobson instrument should "track" – the actual level may not be the same, but the changes in the measured ozone will be the same direction and magnitude. If the relationship between the Dobson and another instrument changes abruptly, then

both instruments should be investigated. As the other instruments have an independent calibration schemes and scales, the Dobson instrument should not be calibrated to the other instrument, and vice versa.

Ozone total column measurements based on the Dobson method are strongly affected by aerosols and pollutants in the atmosphere, which also absorb solar radiation at UV wavelengths.

Total Carbon Column Observing Network (TCCON) is a network of ground-based Fourier Transform Spectrometers measuring the high-resolution spectrum of sunlight transmitted through the atmosphere in the near-infrared spectral region. From these spectra, accurate and precise column-averaged abundance of CO_2, CH_4, N_2O, HF, CO, H_2O, and HDO are retrieved. Data from the individual stations provide information on regional carbon sources and sinks (Figure 1.15).

Figure 1.15. *Current 22 TCCON locations (red dots) and future stations (blue squares).*

TCCON data are used to validate the spectroscopic parameters for orbiting instruments. One of the primary advantages of TCCON spectra is that they reflect real atmospheric conditions that include simultaneous absorption by all trace gases present in the Earth's atmosphere.

Currently there are several GHG observation campaigns running in parallel from the land and the sea surface sites and aircraft. There are also continuous measurements from baseline observatories and tall tower provided by NOAA (Global Greenhouse Gas Reference Network). Globally, however, the network of surface measurements for the major greenhouse gases is still very sparse with large continental areas remaining poorly monitored. This is especially true for the tropical regions, where strong convection transports emissions aloft resulting in generally very low signals at remote marine observation sites. Therefore, satellite measurements with quasi-global coverage provide a very attractive complement to the surface network. Satellite observations combined with the modelling can add important missing global information on regional methane sources and sinks required for the better climate prediction.

1.4.2. Satellite borne instruments

Soon after the beginning of space era in 1958, global observations of the amounts and distributions of atmospheric trace constituents were initiated by the Soviet Union and USA space agencies. The European space program evolved relatively slower until the discovery of the ozone hole, which boosted the development of European remote sounding instrumentation.

Modern global monitoring of the atmosphere is possible with high precision and spatial resolution of up to several kilometers. The observations are available on the long term basis using combinations of the remote sensing instruments of several generations. Remote sensing instruments detect the solar radiation (as well as light from moon and stars) transmitted, backscattered and reflected from the Earth's atmospheric layers and surface.

Trace gases have characteristic absorption at different wavelength regions from ultraviolet (UV) to infrared (IR) and the thermal infrared (TIR), and instruments are designed to operate at specific ranges (called "channels") of the electromagnetic spectrum (Figure 1.16). This allows to monitor numerous atmospheric species: O_3, O_2, NO_2, N_2O, BrO, OClO, SO_2, H_2CO_2, CO, CO_2, CH_4, H_2O, etc.

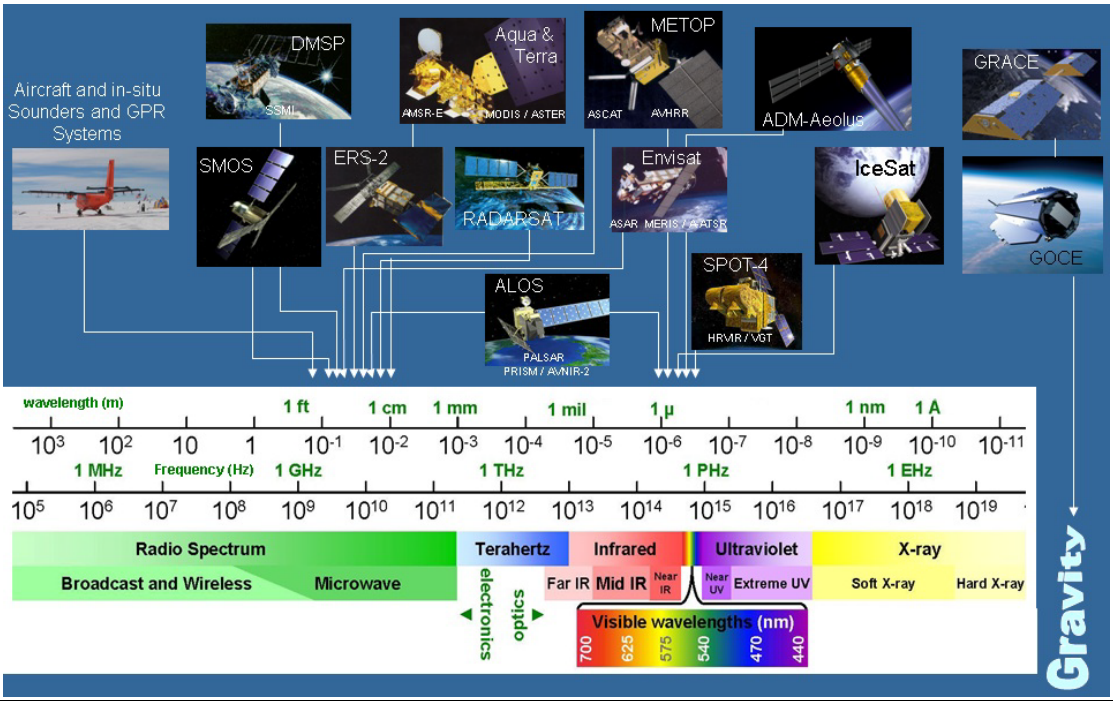

Figure 1.16. *Operational wavelength of some remote sensing instruments.*

Remote sensing instruments that provide data suitable for various types of applications can be characterized by the **wavelength bands** used for acquisition, **spatial resolution**, the **coverage area** and the **temporal coverage**, i.e. how frequent a given location on the Earth's surface is scanned, and the **viewing**

geometry. An overview of the classification is presented in Table 1.4.

Table 1.4. *Classification of remote sensing instruments*

By spatial resolution	- Low resolution systems (1 km or more); - Medium resolution systems (100 m to 1 km); - High resolution systems (5 m to 100 m); - Very high-resolution systems (5 m or less).
By viewing geometry	- Nadir (downwards towards the surface of the Earth, sunlight reflected from the Earth's surface and the atmosphere is analyzed) - Limb (light scattered from the Earth's rim at different tangent altitudes) - Occultation (observing the light of the rising or setting sun, moon, or stars through the atmosphere at different tangent altitudes)
By spectral regions used in data acquisition	- Optical imaging systems (include visible, near infrared, and shortwave infrared systems); - Thermal imaging systems; - Synthetic aperture radar (SAR) imaging systems.
Optical/thermal imaging systems: by the number of spectral bands used	- Monospectral or panchromatic (single wavelength band, grayscale image) systems; - Multispectral (several spectral bands) systems; - Superspectral (tens of spectral bands) systems; - Hyperspectral (hundreds of spectral bands) systems.
SAR systems: by the combination of frequency bands and polarization modes	- Single frequency (L-band, or C-band, or X-band); - Multiple frequency (Combination of two or more frequency bands); - Single polarization (VV, or HH, or HV); - Multiple polarization (two or more polarization modes).

Detailed consideration of over a hundred of satellites carrying remote sensing instruments launched since the early 1970s would require a separate publication and is beyond the scope of this work.

A concise overview of some instruments relevant to methane and ozone remote sensing is presented in Figure 1.17 and Table 1.5.

Table 1.5. *Several remote sensing instruments relevant for O_3 and CH_4 observations.*

Instrument	Targeted Species	Comments
TOMS (Total Ozone Monitoring Spectrometer)	O_3	measurements at near-UV
OMI (Ozone Monitoring Instrument)	O_3	measurements in 290-500 nm range, observing in nadir viewing geometry
OSIRIS (Optical Spectrograph and Infra-Red Imaging System)	O_3 + other species	measurements in 274-810 nm range, single line of sight scanned through a range of tangent altitudes
SBUV (Solar Back Scattered Ultraviolet)	O_3	measurements at near-UV
SAGE (Stratospheric Aerosol and Gas Experiment)	O_3 + other species	measurements at selected wavelengths in the visible and near IR
GOSAT (Greenhouse gases Observing SATellite)	CH_4 + other species	measurements with the Thermal- and Near-infrared Sensors for carbon Observation Fourier Transform Spectrometer (TANSO-FTS)
SCIAMACHY (Scanning Imaging Absorption spectrometer for Atmospheric CHartographY)	O_3, CH_4 + other species	measurements in 240-700 nm range, backscattered and reflected radiation in alternate limb and nadir viewing geometry and solar and lunar occultations;
GOME (Global Ozone Monitoring Experiment) GOME 2	O_3	measurements in 232-793 nm range, backscattered radiation
MIPAS (Michelson Interferometer for Passive Atmospheric Sounding)	O_3, CH_4 + other species	detection of limb emission spectra
Sentinel 4 Sentinel 5	O_3 + other species	nadir spectral measurements of backscattered radiation
GOMOS (Global Monitor of Ozone by Stellar occultation)	O_3	measurements in the visible and NIR range, stellar occultation
LRIR (Limb Radiance Inversion Radiometer) LIMS (Limb Infrared Monitor of the Stratosphere)	O_3 + other species	remote sounding in the thermal infrared
SMR (Sub Millimeter Radiometer)	O_3	measuring mm-range emission
ATMOS (Atmospheric Trace MOlecule Spectroscopy)	O_3 + other species	solar occultation measurements
ILAS (Improved Limb Atmospheric Spectrometer) IMG (Interferometric Monitor for Greenhouse gases)	O_3 + other species	nadir and limb sounding infrared instrument
MLS (Microwave Limb Sounder) MAS (Microwave Atmospheric Sounder)	O_3 + other species	millimeter and sub-millimeter wave radiometry
MERLIN (Methane Remote Sensing LIDAR Mission)	CH_4	LIDAR sounding at two nearby laser wavelengths

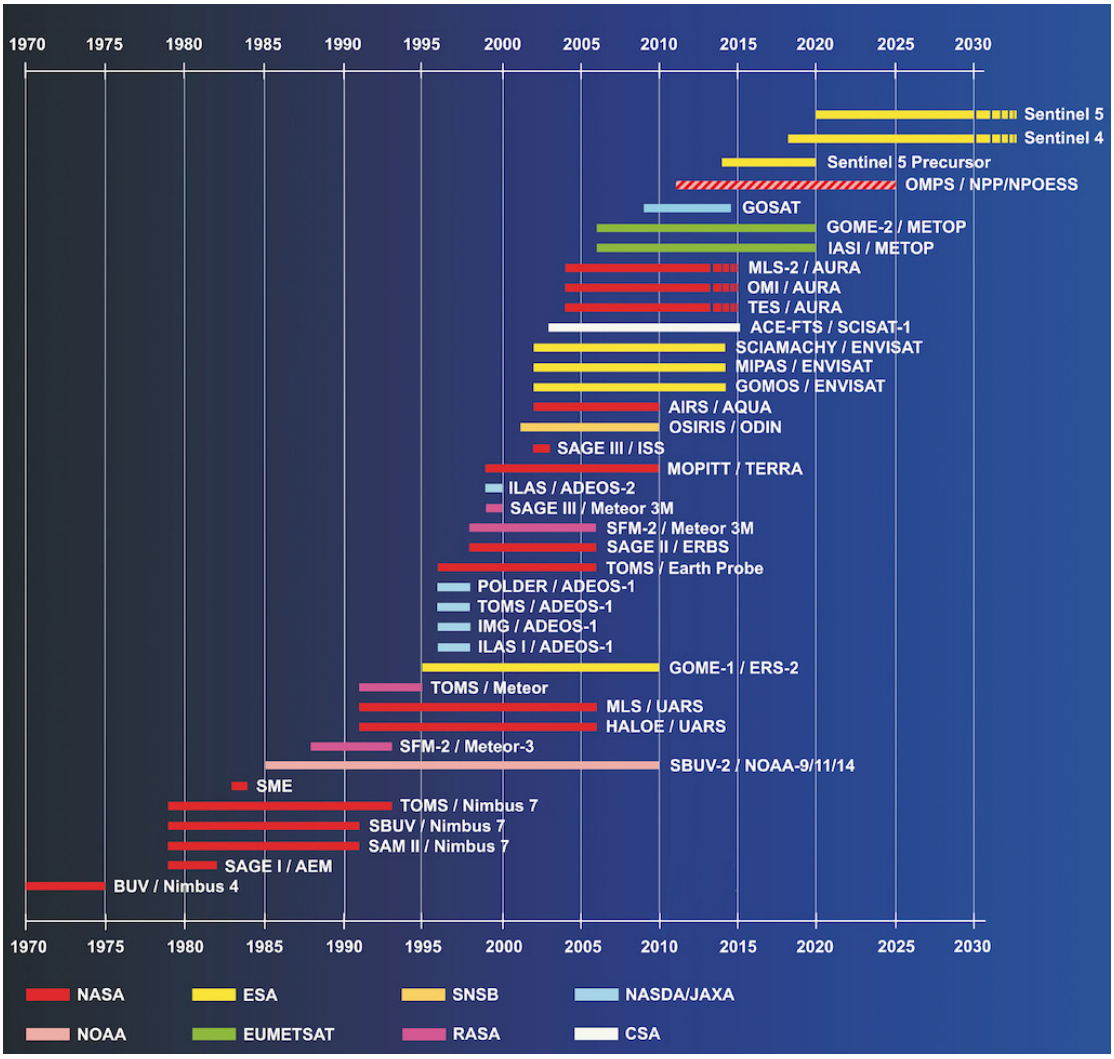

Figure 1.17. *Satellite-borne remote sensing instruments: a look back and a perspective.*
Image source: DLR-IMF

1.4.3. Retrievals and databases

While remote sensing instruments constantly supply the raw observation data as images, spectra or other formats of recorded signal, it is the consequent processing on the ground that provides the actual values of interest to the scientific community. This processing, in general called retrieval, involves several stages of the data manipulation, transformation and interpretation.

Spectra from the orbiting satellite-borne spectrometers are obviously different from those obtained in the controlled laboratory environment: absorption features of all trace gases present during the observation in instrument's line of sight overlap and form a complicated spectrum (see Figure 1.4). For calculation of the species total column (a measure of the total amount of species contained

in a column of atmosphere from ground level upwards) or vertical distribution, different retrieval algorithms are developed. Among other input information, these algorithms require the knowledge on the instrumental slit function (in case of data from spectrometers) and characteristic absorption spectra of the species within the considered spectral range. The latter are directly related to the spectral signatures obtained by the remote sensing instrument.

One of the important steps of various retrieval algorithms is modeling of absorption spectra of constituent species. The iterative process of minimization of discrepancy between the resulting synthetic spectra (or their derivative products) and the observed ones allows to make relatively precise estimates of the species concentration and their vertical distribution.

In general terms, modelling of absorption spectrum of particular species relies on the basic relation describing attenuation of light passing through the absorbing medium (Beer-Lambert law, discussed in Section 2.6) and the knowledge of absorption characteristics of the species at particular wavelength. These characteristics may be represented as the absorption cross-sections (when species demonstrate continuous absorption spectra) and the absorption line parameters (in case of spectra consisting of separate lines), see Section 2.x. Nowadays, numerous databases containing the absorption parameters of majority of atmospheric species exist.

One of the examples of powerful analytical method to study the atmosphere is the Differential Optical Absorption Spectroscopy (DOAS) **/Perner and Platt, 1979/**. Within the DOAS approach, trace gases are identified using their distinct absorption structures in the UV-visible spectral range. Only narrowband spectral features (high frequency constituents) are analysed, whereas the broadband structures (low frequency constituents) are approximated by a polynomial. The examples of low frequency components are variations caused by cloud cover or light scattering by molecules and aerosols and that are difficult to quantify.

This approach is especially beneficial for the observation of species that show significant and structured absorption in the UV-visible wavelength range. As it will be demonstrated in Section 2.5, ozone has very distinguishable spectral features in the 320-350 nm wavelength range. The 325-335 nm spectral region was selected for remote sensing retrievals as suitable to derive the total O_3 column using differential optical absorption spectroscopy (DOAS) or a modified DOAS approach **/Burrows et al., 1999b/**. Standard DOAS derives the O_3 column by fitting the slant column absorption using a reference absorption cross-section at the instrument's spectral resolution to the measured sun-normalized radiance. The DOAS approach has been successfully applied to SCIAMACHY, GOME-2, and OMI data as well (**/Bovensmann et al., 1999/**, **/Veefkind and de Haan, 2002/**).

Other species for which the concentrations are being successfully retrieved with DOAS method are NO_2, BrO, HCHO, CHOCHO, H_2O, OClO, as well as many greenhouse gases **/Buchwitz et al., 2000b/.**

As it will be discussed in Section 2, ozone spectrum in the UV-NIR spectral region is presented by continuum absorption, characterized by the value of the

absorption cross-section. Methane spectrum has a different structure, mostly consisting of isolated spectral lines and manifolds (unresolved groups of lines), which also often form groups called bands. Both the absorption cross-sections and the line parameters can demonstrate dependence on conditions which species are considered at, namely the partial pressure and the temperature.

1.5. Summary

Atmosphere is a complicated dynamic system, where multiple interconnected chemical (involving formation, transformation and destruction of species) and physical processes occur simultaneously. Being driven by the influx of the solar radiation, planetary rotation and interaction with the Earth's surface, these processes define the environment humanity exists in.

Technological progress of humanity within the last few hundred years appears to have an undeniable influence on the atmospheric chemistry in particular (the ozone hole due to perturbation of the ozone creation-destruction cycle by man-made gases), and the planetary climate in general (global warming due to anthropogenically-driven increase of greenhouse gases in the atmosphere).

Global environmental monitoring therefore has an enormous significance. Detection of changes in the parameters, keeping track of trends and variations of the atmospheric species concentration and distribution is facilitated by the global long-term observations. The most effective and reliable way to perform the necessary measurements nowadays is by remote sensing using the orbiting instruments.

Algorithms used to process the data delivered by the satellite instruments and retrieve the concentration profiles, total columns, and spatial distribution patterns of the atmospheric species rely, among other things, on the "boundary conditions" - spectroscopic data characterising the absorption properties of trace gases. Errors and uncertainties in this data introduce biases in the retrievals and decrease the reliability of the results.

Ozone and methane are among the most important atmospheric species. Remote sensing of these species suffers from the errors in the spectroscopic data used in the retrieval algorithms.

Although numerous spectroscopic datasets based on laboratory measurements and theoretical considerations exist today, there still is a room for improvement of the quality of the data. Particular issues related to the ozone and methane spectroscopic data will be considered in more detail in Section 2.5.

Advances in development of the experimental instruments and theoretical methods (and consequently, modelling algorithms) allow to produce spectroscopic parameters with better uncertainties.

Demand for the high-quality spectroscopic data for remote sensing applications was the main motivation for this work.

2. Molecular spectroscopy: theoretical background and datasets

Spectroscopy is an essential method to study the physical properties of matter by analysis of the electromagnetic radiation absorbed, emitted or scattered by the atoms and molecules, which can be in gaseous, liquid or solid forms. Advances in quantum mechanics and the experimental techniques and instrumentation over the last century allowed for dramatic progress in spectroscopy.

Every molecule has its own unique fingerprint - a characteristic absorption (emission) spectrum, which is used to identify the species in remote sensing applications. As it will be demonstrated, molecular spectra are subject to variation depending on the local parameters like the temperature, (partial) pressure and presence of other species.

This section revises the selected physical concepts concerning the molecular energy levels and transitions and some of the spectral line broadening mechanisms. The basics of the absorption spectroscopy and principal considerations of dispersion-based and the Fourier Transform spectrometers are provided.

Also, this section contains a brief overview of the several modern databases widely used in the remote sensing algorithms for ozone and methane retrievals. Reference data availability, sources and uncertainties are discussed for ozone cross-sections and methane line parameters.

2.1. Levels and transitions

Electromagnetic radiation can be characterised either in terms of the wavelength or frequency. Conventionally the wavelength λ [nm/μm] is used in the UV-VIS-NIR, the wavenumber $\tilde{\nu}$ [cm^{-1}] in the NIR-MIR-FIR, and the frequency ν [MHz/GHz] in the microwave regions, Figure 2.1. These units are related as:

$$\tilde{\nu} = \frac{\nu}{c} = \frac{1}{\lambda}$$

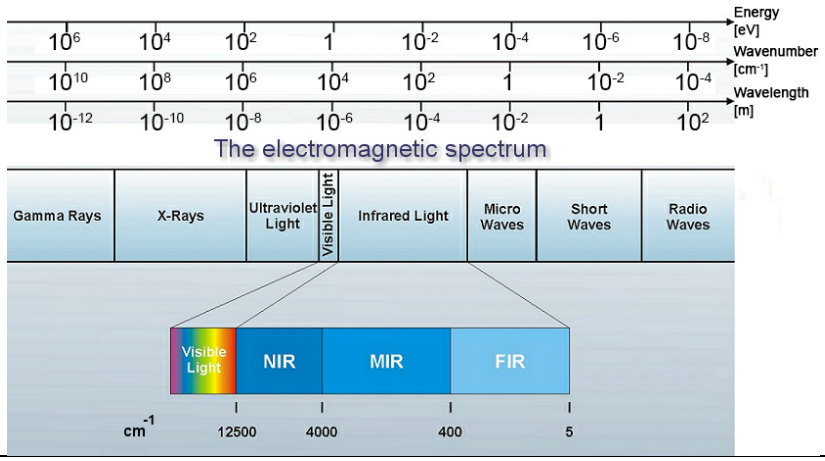

Figure 2.1. *Electromagnetic spectrum*

According to the quantum mechanics, atoms and molecules can exist in certain discrete states that are different with respect to the electron configuration, angular momentum, parity and energy. Transitions between different energy states are associated with the absorption and emission of the electromagnetic radiation by the molecule. The actually observed resulting spectrum may consist of both individual lines corresponding to specific transitions and continuous bands, depending on the density of transitions on wavelength scale and typical Doppler widths.

The use of the word "line" to describe an experimentally observed transition goes back to the early days of observations of visible spectra with spectroscopes. In those instruments, the lines observed in, for example, the spectrum of a sodium flame are images, formed at various wavelengths, of the entrance slit. Although modern observations are usually in the form of a plot of some measure of the intensity of the transition vs. wavelength, frequency or wavenumber, peaks in such a spectrum are referred to as "lines".

Using somewhat simplified approach, the full energy state a molecule can be divided into electronic, rotational, and vibrational constituents:

$$E = E_{vib} + E_{rot} + E_{elec} \tag{2.1}$$

The simplest way describe the vibrational energy state is to consider an example of a diatomic molecule. The bond between the two atoms in a diatomic molecule can be viewed as a spring, which, as the internuclear distance *r* changes from the equilibrium value r_e, exerts a force that tends to restore atoms to the equilibrium position. Such a system, assuming the parabolic shape of the potential energy curve, is approximated by a harmonic oscillator. For the vibrational motion of a harmonic oscillator, the vibrational energy term is given by:

$$E_{vib} = \hbar\omega \left(v + \frac{1}{2}\right) \tag{2.2}$$

where $\hbar = \frac{h}{2\pi}$, *h* is the Plank constant $h=6.626\times10^{-34}$ *J·s,* ω is the angular frequency ($\omega = 2\pi \cdot \nu$), v is a vibrational quantum number (v = 0,1,2,…), so that energy levels of the ideal oscillator are equally spaced (Figure 2.2 a-b).

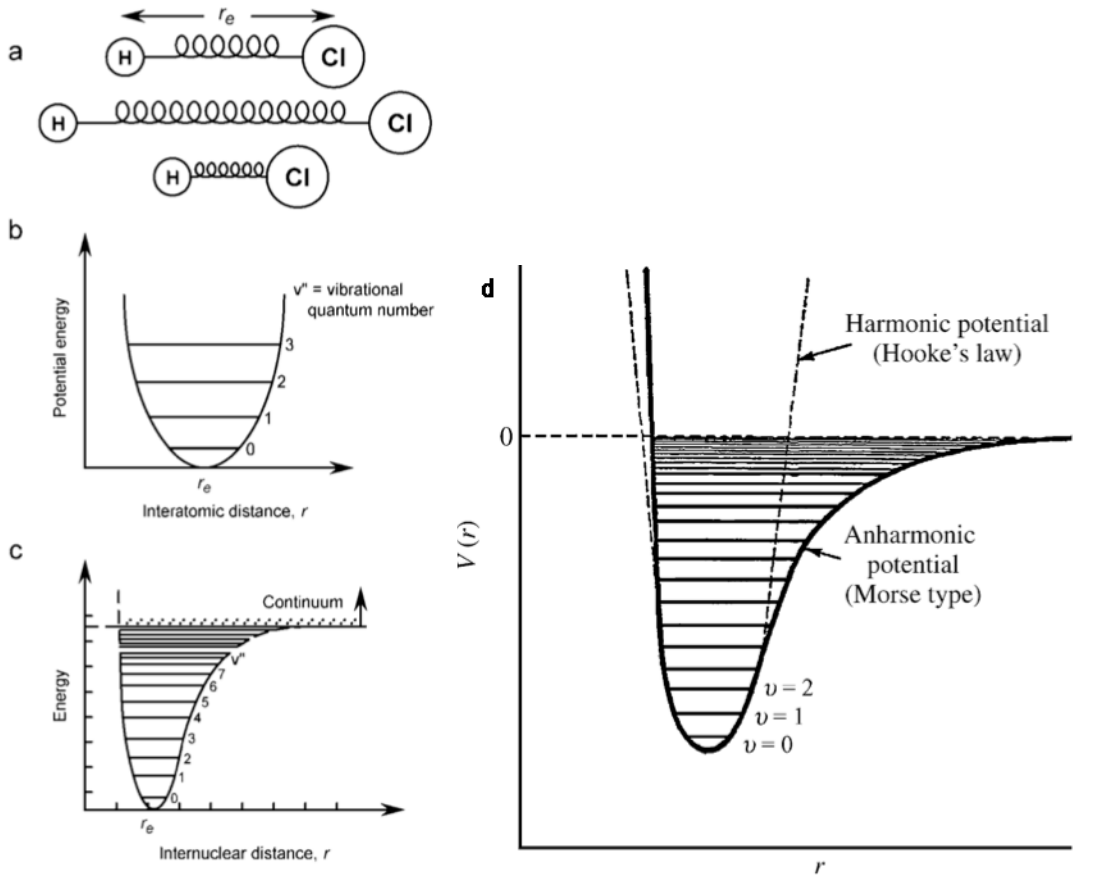

Figure 2.2. *(a) Vibration of heteronuclear diatomic molecule (HCl) (b) potential energy of an ideal harmonic oscillator, and (c) an anharmonic oscillator described by the Morse function (d)*

This idealized approximation is valid for low vibrational energy levels only. For real molecules, the potential energy rises sharply at small values of *r*, whereas for large *r* the bond stretches until it ultimately breaks and the dissociation occurs. The real potential is not symmetric (Figure 2.2c,d). The energy of vibrational transition is on the order of 0.1 eV, with the corresponding wavelengths in the IR spectral range. Because the vibrational energy level spacing is relatively large (typically of the order of 10^3 cm^{-1}) compared to the thermal energy, most molecules at room temperature are in their lowest vibrational energy level and light absorption normally occurs from v = 0.

A selection rule (transition rule) formally constrains the possible transitions of a system from one state to another. Selection rules have been derived for electronic, vibrational, and rotational transitions. The strength or energy of the interaction between a charge distribution and an electric field depends on the dipole moment of the charge distribution in a molecule.

To obtain the strength of the interaction that causes transitions between states (each characterized by its wave function), the transition dipole moment integral is used rather than the dipole moment. If transition dipole moment integral is zero, then the interaction energy is zero and no transition occurs or is possible between the two states. Such a transition is said to be forbidden (electric-dipole

forbidden). If transition dipole moment integral is large, then the probability of a transition is large **/Herzberg, 1988/**.

For a purely vibrational transition, the selection rule requires the change of the dipole moment during the vibration. This oscillating dipole moment produces an electric field that can interact with the oscillating electric and magnetic fields of the electromagnetic radiation. Heteronuclear diatomic molecules such as NO, HCl, and CO absorb infrared radiation and undergo vibrational transitions, contrary to homonuclear diatomic molecules such as N_2 and 0_2, whose dipole moments remain constant during vibration.

Thus, the vibrational transitions occur for $\Delta v = \pm 1, \pm 2, \pm 3, \ldots$. For the harmonic oscillator, only the transitions with $\Delta v = \pm 1$ are allowed (fundamental modes). The anharmonicity of the real molecules leads to weaker overtone transitions with $\Delta v = \pm 2, \pm 3, \pm 4, \ldots$. For linear diatomic molecules only one mode of vibration is possible (stretching of the bond length). For polyatomic molecules, several modes of vibration are possible, resulting in changes of the bond lengths and angles between the bonds (Figure 2.3a)

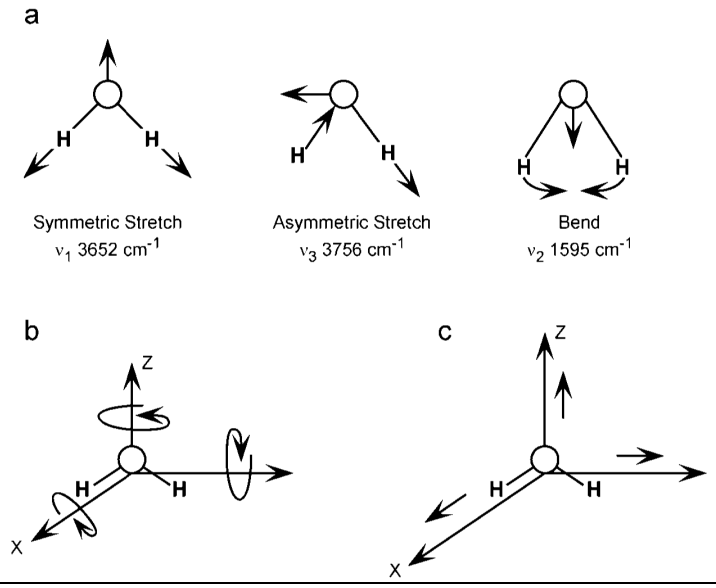

Figure 2.3. *(a) Internal vibrations of the bonds in the H_2O molecule, (b) rotational motion of H_2O, and (c) translation of the H_2O molecule.*

For a given electronic configuration and a given vibrational level (v value), it is also possible to discriminate the rotation of the molecule with respect to particular axis (Figure 2.3b). The rotational energy is given as:

$$E_{rot} = B \cdot J \cdot (J + 1) \qquad (2.3)$$

$$B = \hbar^2 / 2\Theta$$

where B is the rotational constant of a molecule (assumed to be a rigid rotator with constant internuclear distances) for a particular rotation mode, connected

with the moment of inertia Θ for the given rotational axis, and J is the rotational quantum number (J = 0, 1, 2,…). Again, this approximation is limited to small values of J, since bond lengths of real polyatomic molecules are subject to stretching due to the centrifugal force, resulting in increase of Θ for higher J values.

The difference in the angular momentum quantum number of initial and final states is given as $\Delta J = \pm 1$, since the photon exchanged with the atom or molecule has a spin of unity. The rotational transition can be observed when ΔJ = 0, ±1. The transitions are denoted as P-branch (ΔJ = -1), and R-branch (ΔJ = +1). For Q-branch transitions, observed simultaneously with an electronic transition, ΔJ = 0.

The energy difference between two consecutive rotational states ($\Delta J = +1$) is:

$$\Delta E_{rot} = E_{J+1} - E_J = B[\,(J+1)(J+2) - J(J+1)\,] = 2B(J+1)$$

The spacing between rotational energy levels increases with J. Energy level spacings are small compared to those of vibrational transitions, typically of the order of 10 cm^{-1} (10^{-3} eV) in the lower levels; this corresponds to absorption in the microwave region. The resulting observed sequence of rotational transitions (called "band") consists of a series of equally spaced lines.

At room temperature conditions, the thermal energy available is sufficient to populate the energy levels above J = 0.

The E_{elec} component characterizes the energy of excited electronic configurations of the molecule. Energy difference ΔE associated with electronic transitions is of the order of 1 eV, corresponding to wavelengths in the visible or UV parts of the spectrum. The change in the electronic energy may occur simultaneously with the changes in vibrational and rotational energy (molecular bond length and interaction potential changes with the electronic configuration). As a result, observed electronic transitions may have a vibrational structure with a rotational "fine structure".

Electronic states notation arises from the symmetry group theory, and involves consideration of the angular momentum of the molecules (electronic and rotational) and their electronic spin. The detailed explanation of concept is available in classical monograph by **/Herzberg, 1988/**.

The energy levels are thus described by a sum of the corresponding terms:

$$E = E_{elec} + \hbar\omega\left(v + \frac{1}{2}\right) + B \cdot J \cdot (J+1) \qquad (2.4)$$

Real molecular spectra have a complex structure and involve electronic, vibrational-rotational (also called ro-vibrational) and pure rotational transitions at typical ambient temperatures. The simple example for transitions between two vibrational levels v´´=0 and v´=1 belonging to the same electronic energy level and separated in the rotational levels J´´ and J´ is shown in Figure 2.4.

The photon energy of allowed transitions is given by the difference of energy of two consecutive states:

$$\Delta E = E(\mathrm{v}', J') - E(\mathrm{v}'', J'') =$$
$$= \hbar\omega\left(\mathrm{v}' + \tfrac{1}{2}\right) + B' \cdot J' \cdot (J'+1) - \hbar\omega\left(\mathrm{v}'' + \tfrac{1}{2}\right) + B'' \cdot J'' \cdot (J''+1) \qquad (2.6)$$

Assuming $B' \approx B'' = B$, $\Delta v = +1$

$$\Delta E = \frac{\hbar\omega}{2} + B \cdot \left(J' \cdot (J'+1) - J'' \cdot (J''+1)\right) \qquad (2.6a)$$

and for P, R and Q branches

$\Delta J = +1$,	$J'=J''+1$,	$\Delta E \approx h\nu_0 + 2B \cdot (J''+1)$	
$\Delta J = -1$,	$J'=J''-1$,	$\Delta E \approx h\nu_0 - 2B \cdot J''$	(2.6b)
$\Delta J = 0$,	$J'=J'$,	$\Delta E = h\nu_0 + (B' - B'')J' \cdot (J'+1)$	

Schematically, P, Q and R branches are shown in Figure 2.4. Since difference between rotational constants is not very big, components of the Q-branch spectral lines are closely spaced. The Frank-Condon principle defines intensity distribution in the branches **/Herzberg, 1988/**.

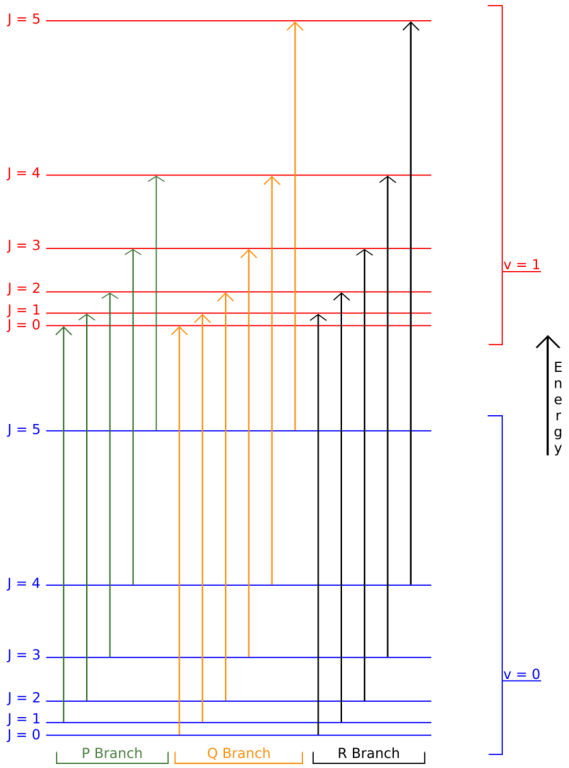

Figure 2.4. *An energy level diagram showing some of the transitions involved in the IR ro-vibrational spectrum of a linear molecule*

Resolved ro-vibrational molecular spectra are of particular interest for remote sensing applications because they allow to distinguish constituents due to their characteristic spectral features.

Homonuclear molecules (like N_2 and O_2) do not have strong absorption features in the thermal infrared, making the atmosphere virtually transparent for sunlight

in this region. In contrast, heteronuclear diatomic molecules and most polyatomic molecules have strong resolved rotational spectral features in the IR, which makes this range useful for spectroscopic observations.

The principles considered above for diatomic molecules are generally valid for polyatomic molecules, but their spectra are far more complicated.

Nonlinear polyatomic molecules consisting of n atoms have three rotational constants with respect to the principal axes and 3n-6 vibrational degrees of freedom (3n-5 for linear polyatomic molecules). The resulting spectrum may contain multiple absorption bands, as well as overtone bands ($\Delta v > 1$) and combination bands (absorptions corresponding to the sum of two or more of the fundamental vibrations).

2.2. Spectral line broadening and line shape profiles

Spectroscopic observations consider the result of interaction of the electromagnetic radiation with an ensemble of atoms or molecules present at certain temperature conditions and concentration (pressure).

In a simplified notation, a line in the spectrum is related to the statistical distribution of individual acts of emission or absorption acts by constituent molecules. Several mechanisms considered below define the broadening width and shape of spectral lines. The contribution of the line-broadening process is usually estimated by the half width at half maximum (HWHM) of the resulting line profile.

Approximation of the shape of the broadened line by a certain profile is, among other things, necessary for the correct modelling of the absorption spectra in atmospheric retrieval algorithms.

2.2.1. Natural broadening

Natural broadening is explained in terms of the classical electrodynamics, where it is a consequence of the finite lifetime of the excited state due to the spontaneous emission.

An excited atom or molecule is considered as system with an oscillating dipole moment. The energy of this system will decrease exponentially with time due to the emission of electromagnetic radiation:

$$E(t) = E_{ex} e^{-\delta t} \tag{2.7}$$

where δ is a damping constant, and $\tau = 1/\delta$ is the time that energy is decayed to 1/e of its initial value.

Further consideration yields the resulting line profile of a naturally-broadened spectral line at frequency ν_0, which is described by Lorentz function (normalized to the unity area):

$$g_{nat}(\gamma,\nu) = \frac{1}{\pi}\frac{\gamma_{nat}}{(\nu-\nu_0)^2+(\gamma_{nat})^2} \quad (2.8)$$

where natural line width $\gamma_{nat} = \frac{1}{2\pi\tau}$ depends on the lifetime of the excited state of the molecule, but not directly on the wavelength of the emitted or absorbed radiation.

For transitions in the visible spectral range performed by isolated molecules, the natural line widths are in the order of 0.01pm ($0.6*10^{-3}$ cm^{-1}).

2.2.2. Doppler broadening

Doppler broadening is a result of the Doppler effect, which is the shift in detected frequency of the signal from a source moving toward or away from the detector. Assuming the thermal motion with Maxwellian distribution of molecular velocities along the line of sight of the observer, the resulting broadened profile of spectral line at frequency ν_0 is described by the Gaussian function (normalized to the unity area):

$$g_D(\nu) = \sqrt{\frac{ln2}{\pi}}\frac{1}{\gamma_D}\, exp\left(-ln2\frac{(\nu-\nu_0)^2}{\gamma_D^2}\right) \quad (2.9)$$

where

$$\gamma_D = \frac{\nu_0}{c}\sqrt{ln2\frac{2kT}{m}} \quad (2.10)$$

is the Doppler HWHM, k is the Boltzmann constant, m is the molecular mass; for a given line position γ_D depends on the gas temperature and molecule mass only.

For transitions in the visible spectral range, the typical Doppler line widths are in the order of 1 pm (0.06 cm^{-1}).

2.2.3. Pressure broadening

Pressure broadening, or collisional broadening, is the consequence of close interactions of the molecules. Collisions perturb the excited state of the molecule when intervals between the collisions are comparable to the lifetime of the excited state. The decreased lifetime of the state creates an increased uncertainty in photon energy, broadening the spectral line.

The line profile resulting from pressure broadening is also Lorentzian as in (2.8):

$$g_p(\gamma,\nu) = \frac{1}{\pi}\frac{\gamma_p}{(\nu-\nu_0)^2+(\gamma_p)^2} \quad (2.11)$$

with characteristic values of pressure broadened width γ_p of about 1 pm (0.06 cm^{-1}) at normal conditions.

The amount of pressure broadening depends not only on the frequency of the collisions, which is proportional to the speed of the molecule and the density of gas. Also, probability of energy state perturbation depends on the kind of the

collision partner molecule: of particular interest are the self-broadening (collision partner is of the same species) and the air-broadening.

From kinetic theory of gases considerations, the pressure-broadened line HWHM γ_p of a gas species at partial pressure p_{self} in mixture with air at total pressure p and temperature T can then in general be expressed as:

$$\gamma_p(p,T) = \left[\gamma_{air}(p_{ref},T_{ref})\cdot(p-p_{self}) + \gamma_{self}(p_{ref},T_{ref})\cdot p_{self}\right]\cdot\left[\frac{1}{p_{ref}}\right]\cdot\left[\frac{T_{ref}}{T}\right]^{\frac{1}{2}} \quad (2.12)$$

where $\gamma_{air/self}(p_{ref},T_{ref})$ are the pressure broadening coefficients at some reference pressure p_{ref} and temperature T_{ref}.

2.2.4. Voigt profile

The line shape in presence of both Doppler and pressure broadening is given by the Voigt function, which is a convolution of the Lorentz and the Gaussian profiles g_D and g_p:

$$g_V(v) = \int_{-\infty}^{+\infty} g_D(v',\gamma_D)\, g_p(v-v',\gamma_p)dv' \quad (2.13)$$

or:

$$g_V(v) = \frac{1}{\gamma_D}\sqrt{\frac{ln2}{\pi}}\frac{y}{\pi}\int_{-\infty}^{+\infty}\frac{\exp(-t^2)}{y^2+(x-t)^2}dt, \qquad here\ y = \frac{\gamma_L}{\gamma_D}\sqrt{\frac{ln2}{\pi}ln2},\ x = \left[\frac{(v-v_0)}{\gamma_D}\right]\sqrt{ln2}$$

Figure 2.5 demonstrates the relation between the three described line shape profiles for hypothetical case when $\gamma_L = \gamma_D = 1$.

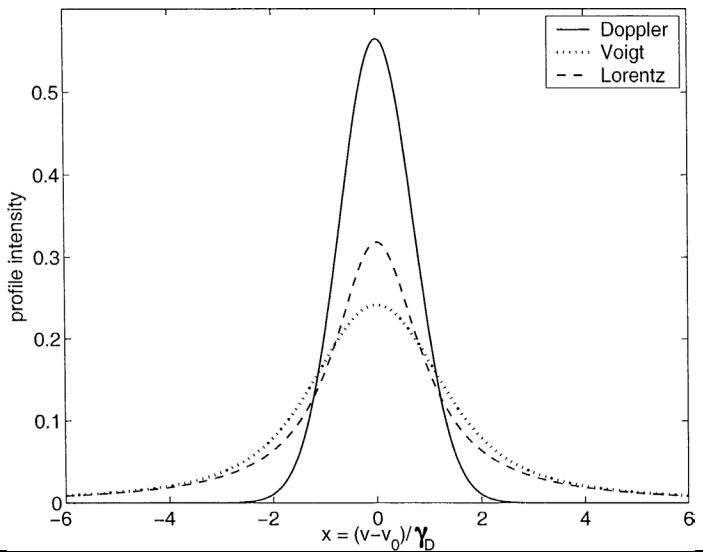

Figure 2.5. *Modelled normalized Lorentz (dashed line), Doppler (solid line), and the corresponding Voigt (dotted line) profiles for the case $\gamma_L = \gamma_D = 1$.*

For gaseous atmospheric species, natural line half-width γ_{nat} is always much smaller than γ_D and γ_p; the latter two are comparable at lower pressures, with γ_p becoming the dominating broadening mechanism as the pressure becomes higher. The maximum of the line shape is inversely proportional to the line width. For the same line widths, the maximum of a Gaussian profile is slightly higher than a Lorentz profile. Considering the wavelength dependence of line half-widths, Doppler broadening is usually negligible in the microwave and far IR regions, becoming noticeable in the near IR, and dominating in the UV. In the visible and UV spectral range Doppler broadening is comparable to pressure (Lorentzian) broadening.

2.2.5. Non-Voigt line shapes

The broadening mechanisms listed above are based on certain assumptions and simplifications. Generally, the actually observed spectra can be modeled using these line profiles relatively well. Additional finer effects exist that also influence the broadening of spectral lines (**/Hartmann et al., 2008/** and references therein).

Several collision phenomena, especially noticeable in high-resolution spectra, may distort the "classical" Voigt profiles: Dicke narrowing **/Dicke, 1953; Galatry, 1961; Rautian, 1967/,** speed-dependent broadening and shifting **/Berman, 1972/**, and line mixing **/Gordon et al., 1971/**:

- ***Dicke narrowing*** results from a constriction of the inhomogeneous Doppler distribution due to velocity-changing collisions responsible for mass diffusion. It is most apparent at low to moderate pressures as is found in the upper atmosphere **/Pine, 1992, 1997/** yielding deviations from the Voigt profile of a few percent near the line center. The relationship of the velocity-changing collision rate to the macroscopic diffusion constant is only approximate and may require an extra parameter for each transition **/Pine, 1992, 1997; Pine et al., 2000, 2003/**.

- ***Speed dependent broadening and shifting*** is a consequence of the finite range of the intermolecular potential yielding a collision cross section that depends on the relative kinetic energy. It affects the line profile at pressures throughout the atmosphere and is difficult to distinguish from Dicke narrowing at lower pressures. However, it persists at higher pressures where it has been observed to yield spectral deviations on the order of 1% in the P and R branches of the v_3 band of methane **/Pine et al., 2000 /**. A comparable study of the Q branch exhibited no speed-dependent spectral signatures **/Pine et al., 2003/**.

- **Line mixing** results from the interference between overlapping transitions coupled by rotationally inelastic collisions. For the complex methane spectrum, it causes deviations of tens of percent from linearly superimposed profiles at higher pressures, representative of the troposphere. If overlap and coupling are weak, line mixing can be treated as a first-order dispersive correction **/Pine et al., 2000, 2003/** for each

transition with one extra parameter per line. However, in the case of strong overlap and coupling, a more complete description of the "relaxation" matrix is required, along with a numerically intensive inversion procedure.

Since these phenomena often occur simultaneously, a number of generalized profiles have been introduced, combining Dicke narrowing with speed dependence **/Ciurylo et al., 2001/**, Dicke narrowing with line mixing **/Pine, 1997/** and all three **/Ciurylo et al., 2000/.** Each of these line shape anomalies have been observed for methane **/Pine, 1992, 1997; Pine et al., 2000 2003/**.

Furthermore**, /Brault et al., 2003/** report that CO self-broadened spectra show systematic residuals on the order of 1% when fitted by a conventional Voigt profile. Using the speed dependent Voigt (sVoigt) profile instead of Voigt and Lorentz profiles decreases these residuals (Figure 2.6). The excellent fit to the speed dependent dispersive Voigt profile throughout the pressure range studied (266-533 mbar) indicated that the Dicke narrowing contribution is difficult to quantify. Dicke narrowing would be expected to be more prominent at lower pressures; line mixing, and speed averaging effects at higher pressures. Though the investigation was limited to self-broadening in the v=2←0 band of CO, previous studies of gas broadening in other bands yielded similar line profiles. A very recent study by **/Wójtewicz et al., 2013/** of twelve CO transitions near 1.6 μm confirms the appropriateness of the speed dependent line profile and the difficulty to distinguish between the Dicke narrowing and speed dependence contributions.

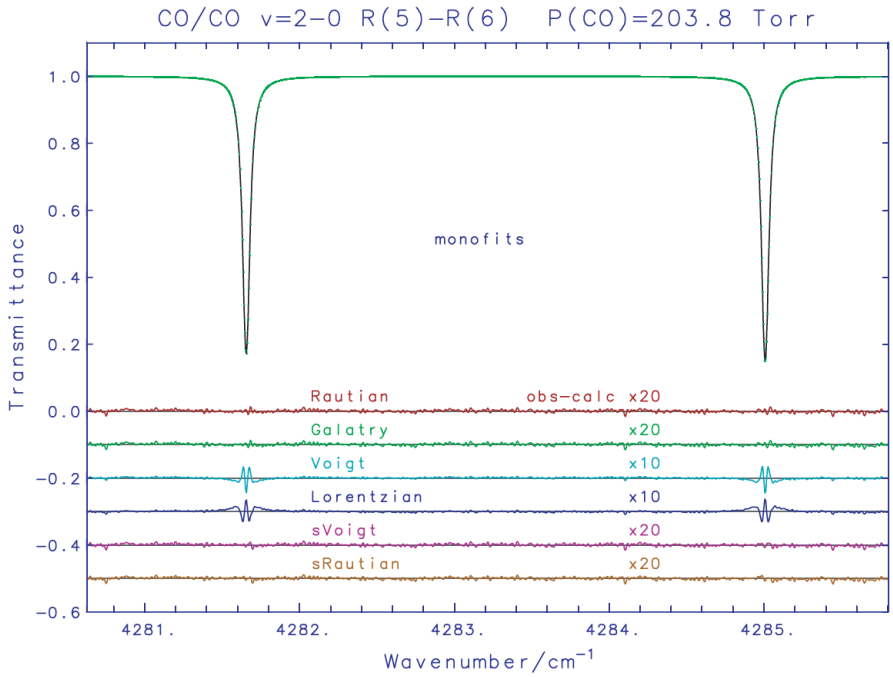

Figure 2.6. *Line shape analysis for the CO self-broadened spectrum from* ***/Brault et al., 2003/.***

2.2.6. Broadening coefficients and other line parameters

As it was mentioned earlier, several approaches exist to describe the mechanisms influencing spectral line broadening and approximate observed line shapes.

For the purposes of this study, formalism adopted in the HITRAN spectroscopic database (see Section 2.5.2) is relevant.

General dependence of the pressure-broadened line half-width provided by equation (2.12) is slightly modified in the HITRAN notation. Here, the pressure broadened line half-width $\gamma(p, T)$ of a Lorentz profile for species at partial pressure p_{self} [atm] in a gas at pressure p [atm], temperature T [K] and is calculated as:

$$\gamma_p(p,T) = \left[\gamma_{air}(p_{ref},T_{ref}) \cdot (p - p_{self}) + \gamma_{self}(p_{ref},T_{ref}) \cdot p_{self}\right] \cdot \left[\frac{T_{ref}}{T}\right]^n \quad (2.14)$$

In this equation:

- γ_{air} and γ_{self} are the air-broadened and the self-broadened half-widths at half maximum (HWHM) [cm^{-1}/atm] at reference temperature T_{ref} = 296 K and reference pressure p_{ref} = 1 atm. These parameters are transition and foreign gas dependent ("foreign gas" stands for all other species in the considered sample). The air-broadening coefficients are calculated as a sum of the broadening by nitrogen and oxygen:

$$\gamma_{air}=0.79 \cdot \gamma_{N2} + 0.21 \cdot \gamma_{O2} \quad (2.15)$$

- n is the coefficient of temperature dependence of the pressure broadened half-width, which is assumed to be transition dependent, rather than fixed at classical value of 0.5.

Further minor effect, which is also important for high spectral resolution observations, is the shift of the line center as a function of total pressure **/Ben-Reuven et al., 1963/.**

HITRAN provides information on the air-broadened pressure shift δ [cm^{-1}/atm] at T_{ref} = 296 K, p_{ref} = 1 atm, of the line transition frequency $\nu_{\eta\eta}$:

$$\nu_{\eta\eta}^{*}=\nu_{\eta\eta} + \delta(p_{ref}) \cdot p \quad (2.16)$$

This parameter is also transition dependent, with typically values a few 0.001 cm^{-1}/atm.

Another spectroscopic parameter included in HITRAN and relevant for description of a line profile is the line intensity S.

The spectral line intensity describes the probability of transition between two energy levels. The intensity is defined here for a single molecule. Radiative

transfer theory for the two states *n, n'* of a vibrational-rotational system defines the spectral line intensity [cm/molecule] at T_{ref} = 296 K as:

$$S_{nn'} = \frac{h\nu_{nn'}}{c}\frac{n_n}{N}\left(1 - \frac{g_n}{g_{n'}}\frac{n_{n'}}{n_n}\right)B_{nn'}$$

where $B_{nn'}$ is the Einstein coefficient for absorption, n_n and $n_{nn'}$ are the populations of the lower and upper states respectively, g_n and $g_{n'}$ are the state statistical weights, and N is the molecular number density (**/Rothman et al., 1998/, /Herzberg, 1988/**).

The Einstein coefficient $B_{nn'}$ is related to the weighted transition-moment squared $\Re$ (Debye^2 = 10^{-36} ergs cm^3):

$$\Re_{nn'} = \frac{3h^2}{8\pi^3}B_{nn'}\times 10^{36}$$

Assuming local thermodynamic equilibrium (LTE), the population distribution between states is governed by Boltzmann statistics at the ambient temperature. This allows us to write

$$S_{nn'}(T_{ref}) = \frac{8\pi^3}{3hc}\nu_{nn'}\frac{I_a g_n \exp\left(\frac{-c_2 E_n}{T_{ref}}\right)}{Q(T_{ref})}\left[1 - exp\left(\frac{-c_2\nu_{nn'}}{T_{ref}}\right)\right]\Re_{nn'}\times 10^{-36} \qquad (2.17)$$

where $S_{nn'}$ is weighted according to the natural terrestrial isotopic abundances, I_a is the natural terrestrial isotopic abundance, c_2 is the second radiation constant $c = hc/k = 1.4388$ *cm·K*, E_n is the lower state energy [cm^{-1}], and $Q(T_{ref})$ is the total internal partition at reference temperature. *Q(T)* is used to determine how molecules in LTE are distributed among the various energy states at particular temperatures (**/Rothman et al., 1998/**).

Figure 2.7 illustrates the considerations above.

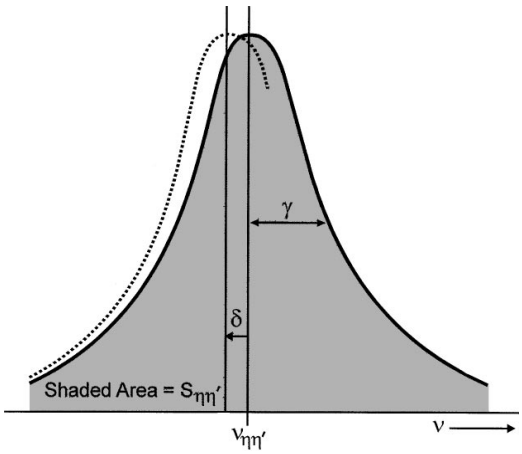

Figure 2.7. *Schematic of fundamental spectroscopic parameters of a line transition in HITRAN. The dotted line refers to a perturbed transition with a negative δ* ***/Rothman et al., 1998/****.*

Line parameters $\nu_{\eta\eta}$, $S_{nn'}$, γ_{air}, γ_{self}, n and δ, provided in HITRAN, allow to calculate the profile of an absorption line using Voigt line shape function g_V at a wide range of temperatures and pressures.

2.3. Basics of the absorption spectroscopy

As it was mentioned earlier, every molecule has a distinct absorption or emission spectrum. In order to exploit this quality in remote sensing applications (and many other fundamental and applied purposes), a detailed knowledge of spectral information of the species is needed.

Both extensive experimental laboratory data and theoretical framework is required to describe the governing physical processes and build the comprehensive numerical models reproducing observed spectra.

Absorption spectroscopy is an essential experimental technique used to characterize the interaction of radiation with matter.

2.3.1. Beer-Lambert law

The method of absorption spectroscopy is based on the Beer-Lambert law, which describes the attenuation of the light intensity transmitted through the absorbing medium.

For gaseous species with observed unresolved continuous absorption spectrum in a considered region (like ozone in the range from UV to IR), the Beer-Lambert law can be written as:

$$I(\lambda) = I_0(\lambda) \int_0^L e^{(-n(T,p,l)*\sigma(\lambda,T))} dl \qquad (2.18)$$

Here $I_0(\lambda)$ is the light intensity in the absence of absorbing molecules (background), n is the absorbing gas number density, which is generally a function of temperature T, pressure p, and the position l along the beam path, L is the total length of the absorbing medium and σ [cm^2/molecule] is the wavelength dependent (and normally also temperature dependent) absorption cross-section.

For species with absorption spectrum consisting of resolved isolated rotational-vibrational bands (like methane in the IR), an alternative form is more convenient:

$$I(\tilde{\nu}) = I_0(\tilde{\nu}) \int_0^L e^{(-\mathrm{S}(\tilde{\nu})*\mathrm{g}(\tilde{\nu})*n(T,p,l)*)} dl \qquad (2.19)$$

Here $\tilde{\nu}$ is the wavenumber [cm^{-1}], and cross-section σ is substituted by the product of the line shape function g[cm] and line intensity S[$cm/molecule$]. The line shape function describes the broadened line profile and depends on the broadening parameters considered earlier.

In a laboratory environment it is possible to control the experimental conditions with very high precision, so that the number density n[cm^{-3}] is assumed to be homogeneously distributed along the absorption path of a known length L[cm]. Knowing other parameters, such as T and p, the value of n can be established from the ideal gas law ($p=nk_BT$).

In this case, equation (2.18) can be transformed as:

$$A(\lambda)=1 - I/I_0 = 1- exp[- \sigma(\lambda)\cdot L \cdot n] \qquad (2.20)$$

where A is the unitless absorbance. The unitless value

$$OD(\lambda) = \ln(I_0/I) = \sigma(\lambda) \cdot L \cdot n \tag{2.21}$$

is known as the *optical density*.

Equation (2.19) becomes

$$A(\tilde{\nu}) = 1 - I/I_0 = 1 - \exp[- S(\tilde{\nu}) \cdot g(\tilde{\nu}) \cdot L \cdot n] \tag{2.22}$$

with corresponding expression for optical density:

$$OD(\tilde{\nu}) = \ln(I_0/I) = S(\tilde{\nu}) \cdot g(\tilde{\nu}) \cdot L \cdot n \tag{2.23}$$

Generally, line parameters can be derived numerically from the experimental absorption spectra. Naturally, it is desirable that the measurements resolution is comparable with or better than the characteristic width of the line shape, determined by the dominating broadening mechanism.

Relative cross-sections are represented by the optical density (2.21). *Absolute cross-sections* can be found from the optical density if species concentration, temperature and absorption path length are known.

Alternatively, in case of ozone spectra, measurements performed at selected wavelengths with a special attention to control of the experimental parameters are often used to calibrate the relative cross-sections. This approach is also applied in cases when relative cross-sections of one research group are calibrated with the external reference values. In this case, however, uncertainties in the reference data propagate into the calibrated spectra (see Section 2.5.1).

2.4. Relevant measurement techniques

Numerous instruments and experimental approaches are available for spectroscopic measurements. Following sections provide a short overview of the two methods relevant for this study. Further details on spectra measurement techniques are available in **/Hollas, 1988/** or **/Griffiths, Haseth, 2007/**.

2.4.1. Fourier transform spectroscopy

Fourier transform spectroscopy (FTS) is a measurement technique that is used to produce the high-resolution spectra in a wide spectral range, applied especially successfully for the investigations in the visible through thermal infrared.

Theorized over 130 years ago, Fourier spectrometers become feasible only with the development of fast and efficient semiconductor detectors capable of operating in a wide spectral range, and computers required to perform numerical calculations of the Fourier transformations.

Some basic underlying principles of Fourier spectroscopy will be demonstrated below for an idealized instrument. The Fourier transform spectrometer (FTS) has the optical scheme of a Michelson-type interferometer. The main components of the Fourier transform spectrometer are shown in Figure 2.8.

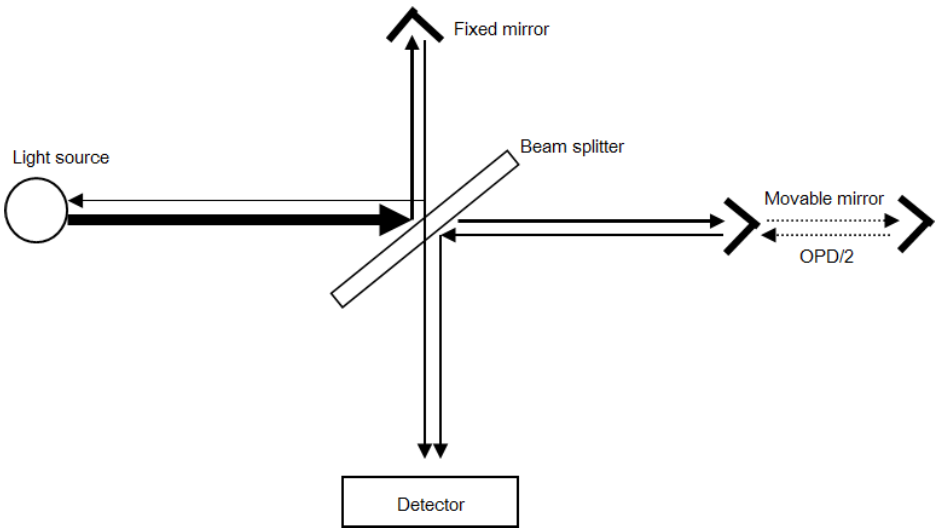

Figure 2.8. *The principle optical layout of a Fourier Transform Spectrometer*

The light is separated into two beams by the half-transparent mirror (beam splitter), with 50% of the incident radiation transmitted to a movable mirror and the other 50% reflected to a fixed mirror. Both beams are then reflected back by the mirrors. Due to the difference in the distance travelled by each beam (called optical path difference, OPD), they arrive at the beam splitter with a certain time difference and interfere. Half of the recombined beam is transmitted to the light

source and half is reflected to a detector. The OPD is precisely varied via translation of the movable mirror (a process called "scanning"), and resulting variable interference signal is recorded and digitized. Normally the movable interferometer mirror is scanned with a constant velocity V (cm/s). Alternatively, mirror is positioned at equally spaced points for fixed short periods and stepped rapidly between these points (a step-scan).

The variation in the intensity of the beam passing to the detector as a function of the path difference ultimately yields the spectral information in a Fourier transform spectrometer.

Within the plane wave approximation, the incident light can be considered as a wave E_{inc} with amplitude $E_{0\,inc}$, for monochromatic light modulated by harmonic function $e^{i(kx-wt)}$ with the wave vector k, angular frequency ω, the position x and time t:

$$E_{inc}(k,t) = E_{0\,inc}e^{i(kx-\omega t)}$$

The superposition, or interference of the two beams mentioned earlier can thus be described as:

$$E = E_1 + E_2 = E_0(e^{i(kx_1-\omega t)} + e^{i(kx_2-\omega t)}) = E_0 e^{-i\omega t}(e^{ikx_1} + e^{ikx_2})$$

Which for intensity $I = |E|^2$ gives:

$$I = E_0^2(e^{ikx_1} + e^{ikx_2})(e^{-ikx_1} + e^{-ikx_2}) = E_0^2(1 + 1 + e^{ik(x_1-x_2)} + e^{-ik(x_1-x_2)})$$
$$= 2E_0^2(1 + \cos(k(x_1 - x_2)))$$

With $\delta = (x_1 - x_2)$ being the optical path difference, and defining $B(\tilde{\nu}) = 2E_0^2$ as spectral energy at wavenumber $\tilde{\nu} = \frac{k}{2\pi}$, the resulting signal $I(\delta)$ at the detector would be a periodic function of the OPD for monochromatic light.

$$I(\delta) = B(\tilde{\nu})(1 + \cos(2\pi\tilde{\nu}\delta))$$

For wideband light sources (like the ones used in the laboratories, or the Sun), the signal at the detector of the interferometer for every OPD δ is a superposition of the interferences of the different frequencies:

$$I(\delta) = \int_0^{+\infty} B(\tilde{\nu})\,(1 + \cos(2\pi\tilde{\nu}\delta))d\tilde{\nu} \qquad (2.24)$$

The interferogram $I(\delta)$ in (2.24) is a sum of a constant (called DC) term $B(\tilde{\nu})$ and varying AC term $B(\tilde{\nu})\cos(2\pi\tilde{\nu}\delta)$. The DC term in the interferogram is the intensity of the incident radiation (remembering that for an ideal beamsplitter half of the incident radiation will be reflected back to the source), and the AC term contains all the spectral information of the incident signal.

Usually, only the AC component $I(\delta) = \int_0^{+\infty} B(\tilde{\nu})\cos(2\pi\tilde{\nu}\delta)\,d\tilde{\nu}$ is important in spectrometric measurements, and is generally referred to as the interferogram.

Since $\cos(2\pi\tilde{\nu}\delta)$ is an even function, the interferogram should be symmetrical about the zero OPD for a perfectly aligned ideal instrument.

To restore the *frequency domain* signal $B(\tilde{\nu})$ from the *time domain* signal $I(\delta)$, the Fourier transformation is applied to $I(\delta)$.

An integral Fourier transformation *FT* of a function *f(x)* and inverse Fourier transform FT^{-1} are defined as

$$FT\big(f(x)\big) = F(y) = \int_{-\infty}^{+\infty} f(x)\, e^{i2\pi xy} dx \qquad (2.25)$$

$$FT^{-1}\big(F(y)\big) = f(x) = \frac{1}{2\pi}\int_{-\infty}^{+\infty} F(y)\, e^{-i2\pi xy} dy$$

Taking into account the Euler´s relation $e^{i2\pi xy} = \cos 2\pi xy + i \sin 2\pi xy$

and the fact that for an even function (*f(x)=f(-x)*)

$$\int_{-\infty}^{+\infty} f(x)\, sinx\, dx = 0$$

$$\int_{-\infty}^{+\infty} f(x)\, cosx\, dx = 2\int_{0}^{+\infty} f(x)\, cosx\, dx$$

the equation (2.25) becomes

$$F(y) = 2\int_{0}^{+\infty} f(x) \cos 2\pi xy\, dx \qquad (2.26)$$

The interference signal *I(δ)* can be expressed as *F(y)* in (2.26), and the inverse Fourier transform *f(x)* being the spectrum *B(ṽ)* of the incident radiation.

Assuming the even nature of *I(δ)* (see above), a Fourier transformation of the recorded AC term of the interferogram (omitting numerical factors) is:

$$I(\delta) = \int_{0}^{+\infty} B(\tilde{\nu}) \cos(2\pi\tilde{\nu}\delta)\, d\tilde{\nu}$$

$$B'(\tilde{\nu}) = \int_{0}^{+\infty} I(\delta) \cos(2\pi\tilde{\nu}\delta)\, d\delta$$

The necessary numerical manipulations of the digitized interferogram signal are offloaded to the computer (or embedded hardware) controlling the spectrometer, presenting the measured spectra in a conventional intuitive form.

There are many more details concerning the particular hardware implementations and limitations. The amplitude of the interferogram as observed after the detection and amplification is proportional not only to the intensity of the source but also to the beamsplitter efficiency, detector response, and the amplifier characteristics. Signal processing methods are also used to counter the issues caused by finite length of the interferograms as a consequence of finite OPD (typical values of OPD for high-resolution spectrometers are on the order of a few meters).

To achieve the high accuracy in determination of the OPD, a stabilized He-Ne laser is added into the interferometer as internal reference source. The laser beam parallels the signal path through the interferometer and produces its own interferogram at a separate detector. This signal is used as an extremely accurate measure of the optical path difference.

The resolution or the ideal Fourier spectrometer depends on the maximal OPD of the scan:

$$\Delta\tilde{\nu} = \frac{1}{\delta_{max}}$$

Finite aperture diameter causing non-parallel radiation flux and other optical imperfections limit the achievable resolution. For non–ideal instruments further

deviations have to be expected due to the wavelength dependence of the index of refraction, thickness differences of the beam splitter, misaligned mirrors, etc.

2.4.2. Dispersion spectroscopy

Unlike in a Fourier spectrometer, which utilizes the separation of electromagnetic radiation components in *time domain*, dispersion of light by a prism or a diffraction grating is the phenomenon utilized to *spatially* split the constituent wavelengths of the electromagnetic radiation. The dispersed light is then imaged to the plane where an array of detectors or other form of sensors is located.

Nowadays prisms have been largely superseded by diffraction gratings as dispersing elements, but they still have uses in spectroscopy.

Optical properties of a prism are demonstrated in Figure 2.9.

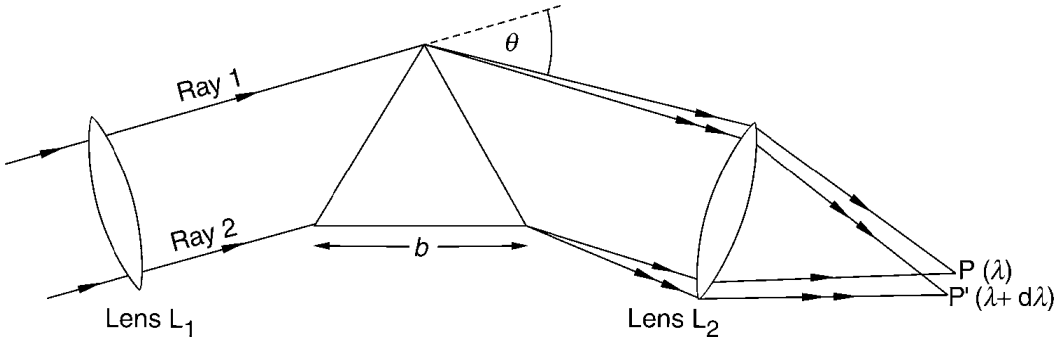

Figure 2.9. *Dispersion by a prism*

One face of a prism with base length b is filled with radiation from a broadband light source made parallel by lens L_1. The prism disperses and resolves the radiation, which is focused by the lens L_2 onto a detector plane. For observably separated wavelengths λ and $\lambda+d\lambda$, the obtained resolution is $d\lambda$ (or the corresponding interval for frequency $d\nu$ or wavenumber $d\tilde{\nu}$).

The resolving power R of a dispersing element is defined as

$$R = \frac{\lambda}{d\lambda} = \frac{\nu}{d\nu} = \frac{\tilde{\nu}}{d\tilde{\nu}} \qquad (2.27)$$

For a prism with a face fully illuminated by the incident flux, resolving power is

$$R = b\frac{dn}{d\lambda}$$

Here n is the refractive index of the prism material. For high resolving power $dn/d\lambda$ should be large, which happens near a wavelength where the material absorbs radiation. For glass, absorption occurs near $\lambda < \sim 360$ nm and, therefore, the resolving power is greatest in the blue and violet regions. Quartz absorbs at $\lambda < \sim 185$ nm and its resolving power is greatest in the 200-300 nm region and rather low in the visible.

If, as in Figure 2.9, P(λ) and P′ (λ+$d\lambda$) are a distance *dl* apart then the linear dispersion is defined as $dl/d\lambda$ whereas the angular dispersion is defined as $d\theta/d\lambda$, where θ is the angle shown.

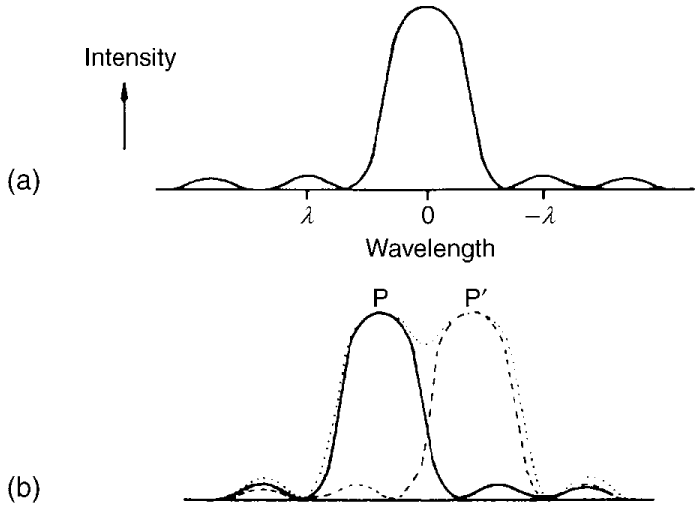

Figure 2.10. *(a) Diffraction pattern produced by a narrow slit. (b) The Rayleigh criterion for resolution*

If a narrow entrance slit is placed in front of lens L_1 in Figure 2.9, a diffraction pattern from the image of the slit is formed in the detector plane with intensity minima at ±λ, ±2λ,... from the central maximum (Figure 2.10a). Rayleigh criterion suggests that the images P and P′ (Figure 2.9) are considered "just resolved" when the two diffraction patterns overlap such that the principal maximum of the diffraction pattern of P falls on the first minimum of the diffraction pattern of P′ and vice versa (Figure 2.10b).

A line in a spectrum is an image of the entrance slit formed at a particular wavelength, the image being a diffraction pattern as in Figure 2.10a. Therefore, resolution of the dispersing element is reduced as the slit is widened. On the other hand, if reducing slit width below certain value does not result in reduced observed line width (even though the dispersing element is capable of higher resolution), then the line width is likely to be limited by pressure or Doppler broadening.

A diffraction grating consists of a series of parallel grooves ruled on a clear glassy or reflecting base. The surface may be plane or concave, the latter type able to focus as well as disperse and reflect the light falling on it.

Figure 2.11 demonstrates the diffraction pattern of broadband light falling at 90^0 to the surface of a reflection grating G.

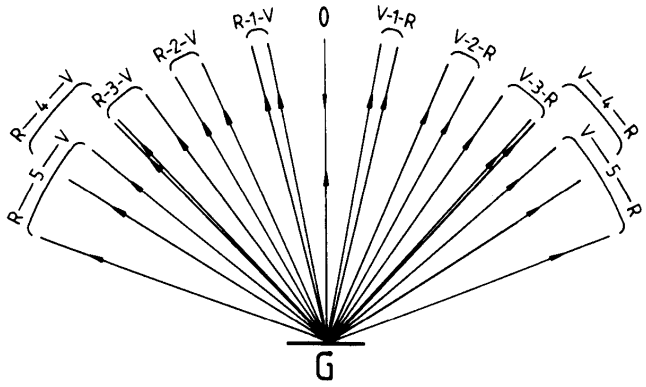

Figure 2.11. *Diffraction orders from a plane reflection grating G; R indicates the red end of the spectrum; V indicates the violet end of the spectrum; the central number is the order of diffraction*

The general equation for diffraction by a grating is:

$$m\lambda = d(\sin i + \sin\theta)$$

where i and θ are the incidence and reflection angles, both measured from the normal to the surface, d is the groove spacing, λ is the wavelength, and m (= 0; 1; 2; ...) is the order of diffraction.

For normal incidence

$$m\lambda = d \cdot \sin\theta$$

The angular dispersion produced by the grating is

$$\frac{d\theta}{d\lambda} = \frac{m}{d \cdot \cos\theta} \qquad (2.28)$$

Equation (2.28), illustrated by Figure 2.11, shows that angular dispersion increases with the order, the dispersion shown being from violet (V) to red (R) in each order.

The resolving power R (equation (2.27)) of a grating (provided that all grooves are illuminated) is given by

$$R = mN \qquad (2.29)$$

where N is the total number of grooves. Equations (2.28) and (2.29) demonstrate that for high resolution (and high dispersion) applications as high order as possible should be used. However, in higher orders there is an increasing problem of overlapping of adjacent orders (Figure 2.11). Filtering or pre-dispersion of the incident light with a small prism or grating allows to deal with this problem. This approach is utilized in the Echelle spectrometer (Section 3.3.1).

2.5. Spectroscopic features of ozone and methane

2.5.1. Ozone molecule

The O_3 absorption spectrum in the region 200-1100 nm comprises four absorption bands, conventionally referred to as Hartley band (between ~200-300 nm), Huggins band (between ~300-360 nm), Chappuis band (between ~430-740 nm), and weak Wulf band (between ~750-1000 nm) with more or less pronounced structures, resulting from the intra-molecular vibrational dynamics (Figure 2.12).

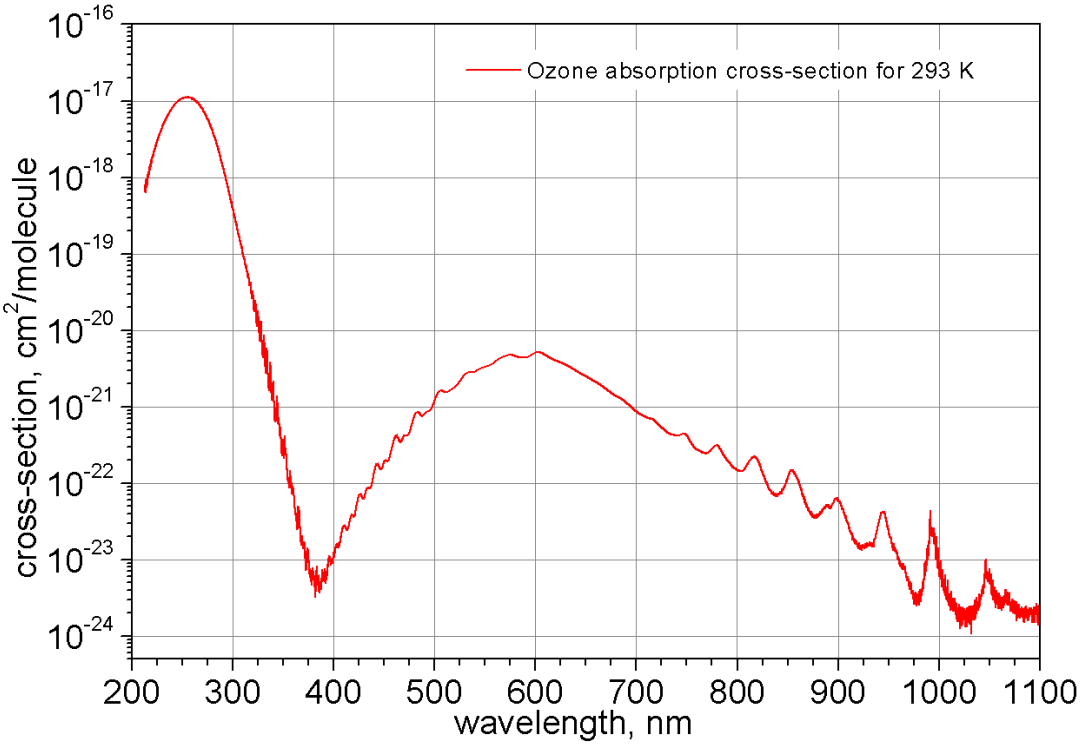

Figure 2.12. *Ozone absorption cross-section.*

Quantum mechanical dynamics calculations of the O_3 potential energy surfaces (4-dimensional for the case of nonlinear triatomic molecule) explain the principle features of the O_3 spectrum in the UV/visible/NIR wavelength regions **/Banichevich et al., 1993; Grebenshchikov et al., 2007; Schinke and McBane, 2010/**. The assignment of the absorption bands from the nine electronic states was comprehensibly illustrated using the one-dimensional cuts through the potential energy surfaces in **/Grebenshchikov et al., 2007/**. Quantum mechanical modelling of the O_3 molecule has the potential to produce a noise-free absorption cross-sections and line parameters (Figure 2.13.1).

However, because of the relatively high density of low-lying states and coupling effects, the quality of the *ab initio* calculations is still inferior to experimental

data accuracy. Results of numerous experimental studies can be found, for example, in the online spectral database of gaseous molecules of the Max–Planck Institute for Chemistry in Mainz (MPI) **/Keller-Rudek and Moortgat, 2013/**, which contains data obtained by more than forty teams covering the different spectral regions and temperatures.

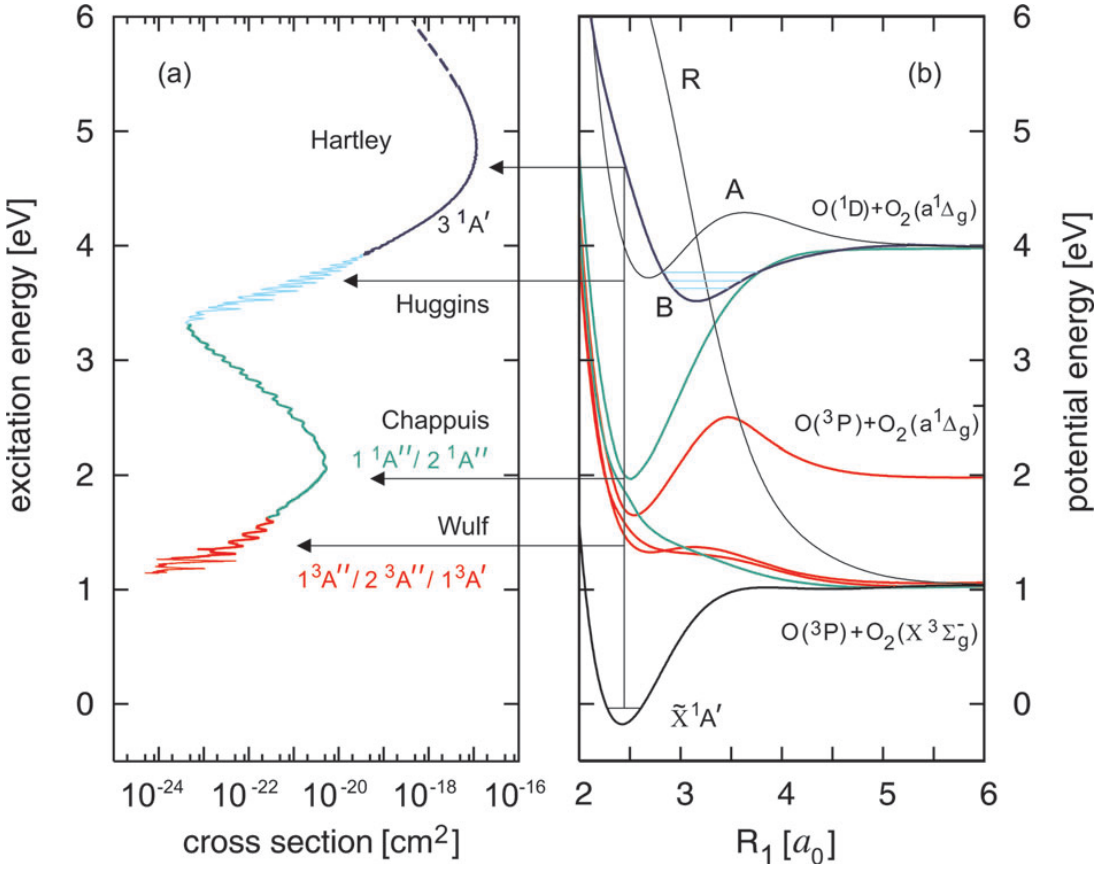

Figure 2.13.1. *(a) The measured absorption cross-section (in cm2; logarithmic scale) of ozone as function of the excitation energy.*

(b) One-dimensional cuts through the potential energy surfaces relevant for the photodissociation of ozone. R1 is one of the O–O bond lengths; the other one is fixed at R2=2.43 a_0 and the bond angle is α=117^0. E=0 corresponds to $O_3(\tilde{X})$ in the ground vibrational state (zero point energy). A, B, and R indicate the three (diabatic) ^{1}A states relevant for the Hartley and Huggins bands. The horizontal arrows illustrate the electronic assignments of the absorption bands. Colour coding in (a) and (b) stresses the relation between the absorption bands and the underlying electronic states.

Image source: **/Grebenshchikov et al., 2007/**

Accurate information on the temperature dependence of the absorption cross-sections (Figure 2.13.2) is vital for the retrievals of the ozone profiles and columns from UV, visible and near infrared spectra measured by the modern remote sensing instruments. The origin of the temperature dependence of the ozone absorption cross section arises from changes in the population distribution in the rotational-vibrational states of the ground electronic state.

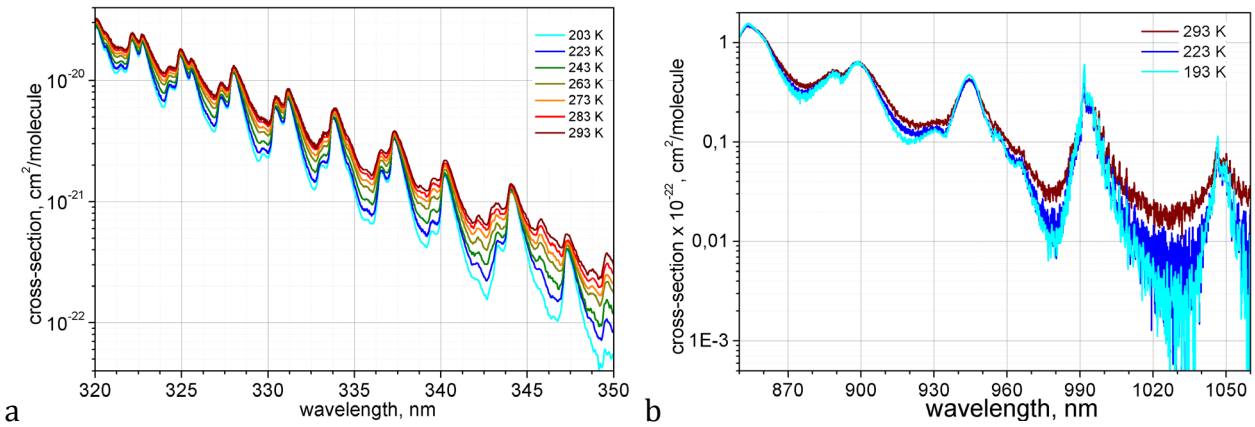

Figure 2.13.2. *Characteristic temperature dependence in the Huggins (a) and Wulf (b) bands*

The features and structure of the ozone absorption spectra and their changes with temperature were subject of extensive studies, mainly stimulated by ozone remote sensing applications **/Barnes and Mauersberger, 1987; Brion et al., 1993; Bogumil et al., 2003, Burkholder and Talukdar, 1994; Burrows et al., 1999; Malicet et al., 1989; Malicet et al., 1995; Paur and Bass, 1984; Voigt et al., 2001/**.

The Hartley absorption band in the UV consists of a very broad continuum with series of narrow peaks superimposed near the absorption maximum. At the maximum of the Hartley band around 254 nm, the temperature variation is in the range of 0.5% - 1% from 203 to 273 K **/Barnes and Mauersberger, 1987; Malicet et al., 1989/**.

The temperature variation in the Huggins band is strongly wavelength dependent with differences up to 70% and 30% for minimum and maximum of the spectral feature around 335 nm **/Brion et al., 1993; Malicet et al., 1995; Paur and Bass, 1984/**, which makes this region especially important for ozone retrievals.

The Chappuis absorption band in the visible wavelength range consists of a continuum with a series of peaks superimposed on the "blue" side of the spectrum. Weak temperature dependence below 1% was found for absorption cross sections on the top of the band **/Burkholder and Talukdar, 1994/**. The continuum of the visible is extended in the near-infrared (NIR) wavelength region, and on this extension the structure is superimposed.

The Wulf absorption band in NIR exhibits temperature dependence similar to the Huggins band, but typical cross-sections values are about 10^{-3} of those in the Huggins band.

2.5.2. Methane molecule

In addition to being a research subject from the standpoint of the atmospheric sciences, methane is one of the most important molecules in chemistry and physics.

Starting out with its structural models and its chemical bonding, CH_4 molecule has become a prototype for the study of multidimensional potential energy hypersurfaces **/Marquardt and Quack, 1998/** in relation to quantum dynamics of polyatomic molecules. Methane has also been a prototype for kinetic studies of bond fission reactions and their theory, and for molecular spectroscopy **/Marquardt and Quack, 1998/**. In conjunction with full dimensional methods for calculating energy levels of polyatomic molecules, spectroscopy may be used for their refinement. New development in experimental methods renewed the interest in methane: high-resolution Fourier transform spectroscopy of CH_4 isotopologues is applied in bulk and to supersonic jet samples in studies of the intramolecular vibrational redistribution **/Quack, 1990/**.

The second most abundant methane isotopologue, $^{13}CH_4$, is observed in the Earth's atmosphere with approximately 1% natural abundance. The ratio $^{13}C/^{12}C$ is important since it is linked to the formation process of methane and therefore allows to trace CH_4 sources.

The methane molecule has a tetrahedral symmetry in its ground state and is, therefore, a spherical top rigid rotor. The Coriolis and anharmonic interactions in the CH_4 molecule combine to reduce the rotational degeneracy of the vibration-rotation levels and cause the absorptions to consist of blended manifolds of lines.

Tetrahedral molecules (the XY_4) have four normal modes of vibration according to the symmetry of the associated normal coordinates **/Herzberg, 1988/**: the ν_1–mode, a non–degenerate symmetric XY–stretching vibration (A_1 symmetry), the ν_2–mode, a double-degenerate XY–bending vibration (E symmetry) and two triple-degenerate modes, the ν_3–mode, a XY–stretching vibration (F_2 symmetry) and the ν_4–mode, a XY–bending vibration (F_2 symmetry) (see Figure 2.14 and Table 2.1).

Table 2.1. *Fundamentals for the normal modes of $^{12}CH_4$, $^{13}CH_4$ and $^{12}CD_4$*

Assignment		Term values, cm^{-1}		
		$^{12}CH_4$	$^{13}CH_4$	$^{12}CD_4$
Level	symmetry $\Gamma(T_d)$	$\tilde{E}$	$\tilde{E}$	$\tilde{E}$
ν_1	A_1	2916.481145	2915.442036	2101.3824
ν_2	E	1533.332635	1533.492779	1091.6516
ν_3	F_2	3019.493283	3009.545581	2260.0797
ν_4	F_2	1310.761268	1302.780778	997.8711

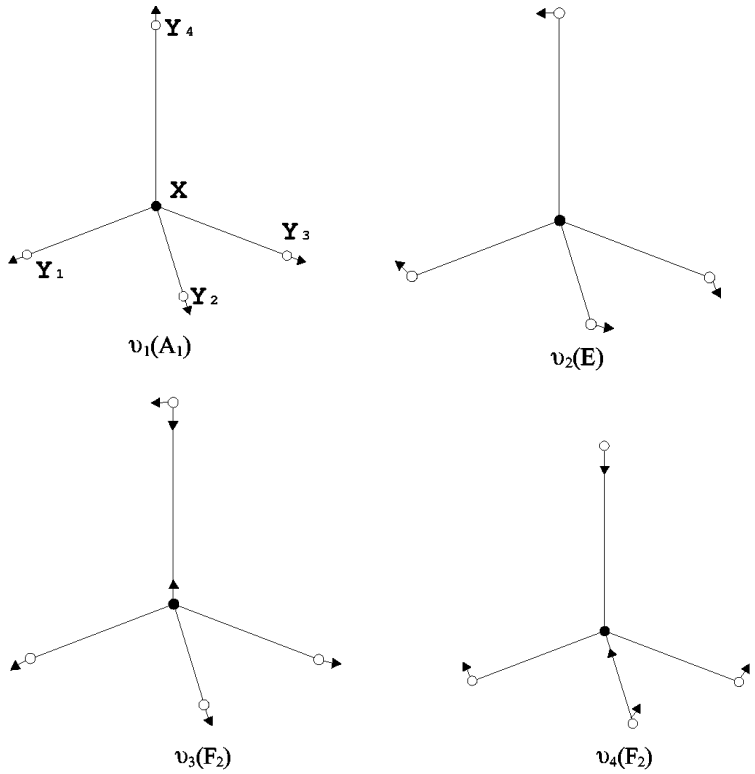

Figure 2.14. *Normal modes of vibration of tetrahedral XY_4 molecules.*

The four normal mode frequencies ν_k, (k=1,..., 4) for the methane isotopologues satisfy an approximate relation

$$\nu_1 \approx 2\nu_2 \approx \nu_3 \approx 2\nu_4$$

For the excited overtone and combination states this results in groups of close–lying vibrational bands, the polyads.

Each combination band (4–tuple of vibrational quantum numbers $(\nu_1, \nu_2, \nu_3, \nu_4)^t \in N^4$) is assigned to a polyad P_n according to the conventional equivalence relation

$$(\nu_1,\nu_2,\nu_3,\nu_4) \in P_n \Leftrightarrow (\nu_1,\nu_2,\nu_3,\nu_4)(2,1,2,1)^t = n$$

The superscript t denotes transposition. The vector $(2,1,2,1)^t$ is referred to as the polyad structure of methane, which applies similarly to many other tetrahedral XY_4 molecules. Conventionally, the polyads P_n are numbered with increasing energy starting with $n = 0$ for the ground state monad, $n = 1$ for the dyad etc. The Greek prefix indicates the number of levels in the polyad. For $n > 0$ the number $(n + 1)$ gives the number of levels with pure bending character and $(n/2 + 1)$ for even n the number of levels with pure stretching character.

Figure 2.15 presents the $^{13}CH_4$ polyad energy level scheme, which applies similarly to XY_4 molecules, with the scale of the ordinate specific for X and Y. Table 2.2 lists the polyads for $^{13}CH_4$, where the overlap of polyads becomes very significant above 12000 cm^{-1}.

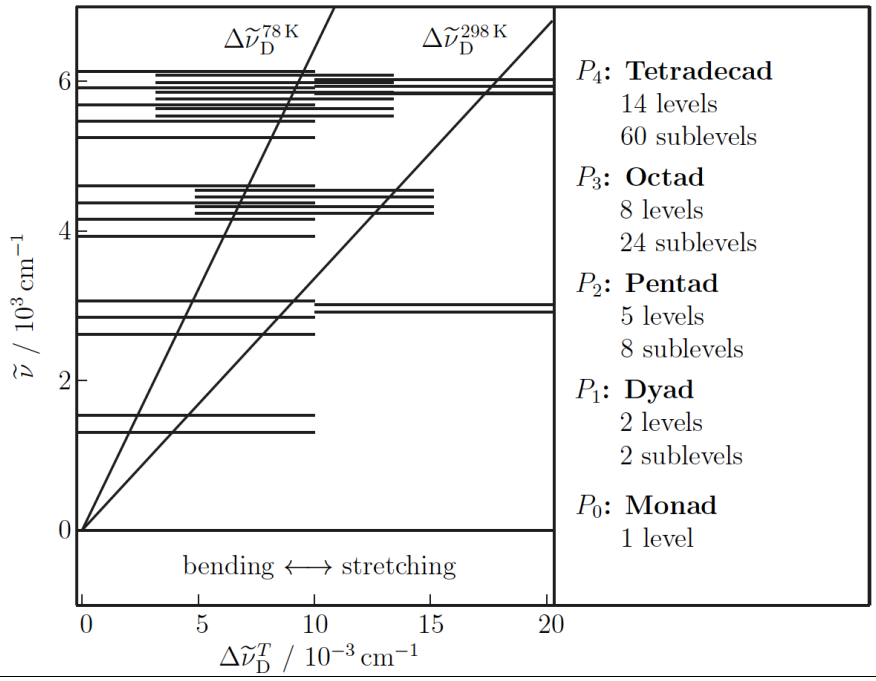

Figure 2.15. *The polyad scheme of methane $^{13}CH_4$ up to 6000 cm^{-1} .*

The vibrational levels on the left are positioned according to their stretching and bending character. The Doppler FWHMs in the 0–6500cm^{-1} region are indicated by line diagonals for T=80 K and T=298 K. The polyad nomenclature is given on the right, indicating the number of levels and sub-levels in each polyad

Table 2.2. *The vibrational polyads of methane on the example of $^{13}CH_4$. For $^{12}CH_4$ and $^{13}CD_4$ the lower ($n\cdot\tilde{E}(v_4)$) and the upper ($n\cdot\tilde{E}(v_2)$) limits of the polyad P_n can be estimated from the term values of the fundamentals as summarized in Table 2.1.*

Polyad nomenclature		Range, cm^{-1}	Levels	Sublevels	IR–active
P_n	**Notation**				
P_0	Monad	0	1	1	0
P_1	Dyad	1300–1500	2	2	1
P_2	Pentad	2600–3100	5	9	3
P_3	Octad	3900–4600	8	24	8
P_4	Tetradecad	5200–6200	14	60	20
P_5	Icosad	6500–7700	20	134	43
P_6	Triacontad	7800–9300	30	280	90
P_7	Tetracontad	9100–10800	40	538	169
P_8	Pentacontakaipentad	10400–12300	55	996	313

The spectral region of interest for this work (1625-1685 nm or 5935–6154 cm^{-1}) belongs to the 2v3 band (see Figure 2.16).

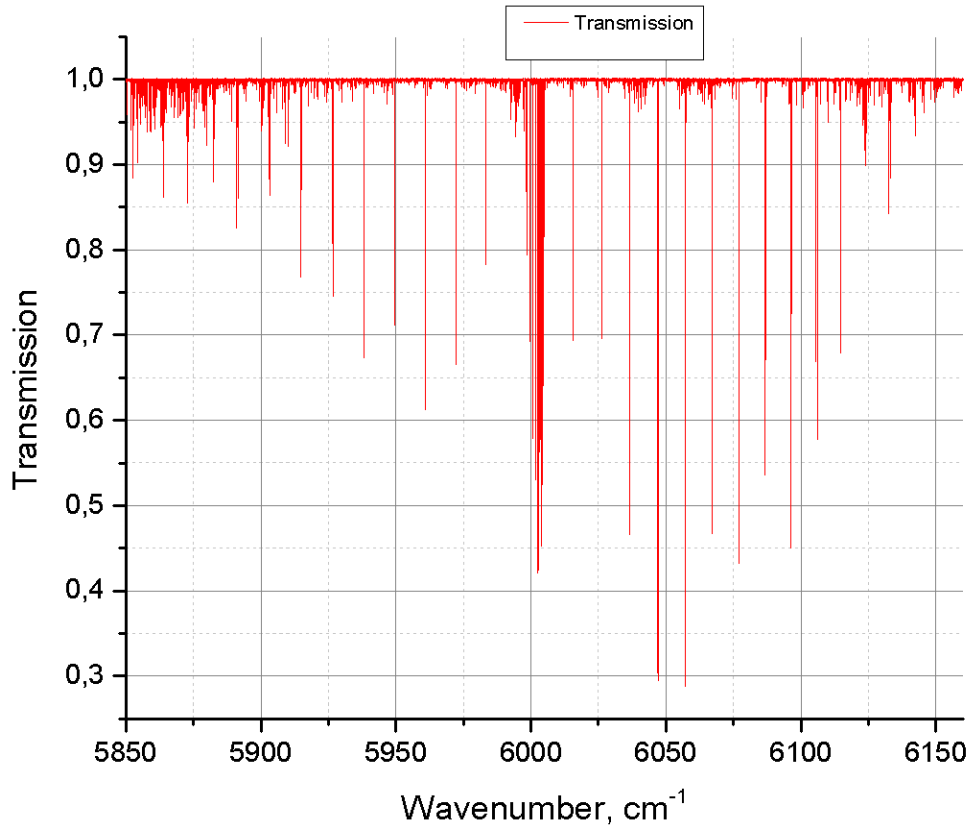

Figure 2.16. *Methane transmission spectrum near 2v3 band around 6000cm^{-1} (T=293 K)*

The 2v3 band at 6000 cm^{-1} was assigned by **/Fox, 1962/** and later interpreted by **/Bobin, 1972/**. Lists of assigned lines in *P, Q* and *R* branches for the two main isotopologues is given in Appendix 2 (from HITRAN 2008 edition) **/Rothman et al., 2009/**).

2.6. Spectroscopic datasets

Numerous datasets are used nowadays as the reference data for remote sensing retrievals. These databases provide information on the absorption line parameters for species with resolved rotational-vibrational structures (see Section 2.2.6), absorption cross-sections for molecules with very dense unresolved spectra, and sometimes aerosols parameters (such as refractive indices).

2.6.1. Ozone-related data

The remote sensing instruments used to retrieve the O_3 amounts and distributions have individual and unique slit functions, which vary as a function of wavelength. Spectral resolution and bandwidths of the instruments vary and often change over the different spectral windows or channels. The task of comparing the different data sets and creating a consolidated and consistent data set for the remote sensing or in situ measurement of atmospheric O_3 becomes especially challenging when different techniques and reference data for cross-sections are used.

The O_3 absorption cross-sections determined experimentally from the pioneering works dated as early as 1932 up to the most recent studies in the solar spectral range have been collected, collated and made available in the extensive online spectral atlas of gaseous molecules of the Max-Planck Institute for Chemistry, Mainz **/Keller-Rudek and Moortgat, 2013/**. This atlas contains the contributions of more than forty teams, covering both different spectral regions and temperatures.

A review by **/Orphal, 2003/** investigated the broadband O_3 absorption cross-sections, obtained by the different groups during the decades up to 2003. Partly based on this review, the NASA Panel for Data Evaluation compiled a data set in 2011, which was derived from different sources and covered the spectral region from 122 nm up to 827.5 nm for two temperatures **/NASA, 2011/**.

Following is a short overview of the several datasets currently used in modern remote sensing applications and for comparisons in this study. For historical reasons, the datasets are often referred to by the names of the leading author that provided the particular data.

Bass and Paur

The high-resolution broadband data obtained by Bass and Paur (abbreviated as BP) **/Bass and Paur, 1984; Paur and Bass, 1984/** using the Ebert type scanning monochromator are included in the standard O_3 total column and profile retrievals using ground-based (Brewer **/Komhyr and Evans, 2008/** and Dobson **/Scarnato et al., 2009/**) and satellite spectrometers (SBUV **/NOAA, 2007/**, TOMS **/McPeters et al., 1998/**, and in the OMI retrievals **/Veefkind and de Haan, 2002/**).

These data are also included in the 2008 version of the high-resolution transmission molecular absorption database HITRAN **/Rothmann et al., 2009/**; however, it has been noted that a wavelength shift must be applied to obtain optimal results in the Huggins band. In addition, this dataset is limited to the spectral region 245 - 343 nm and the lowest temperature available is 203 K.

Brion, Malicet, Daumont

The high-resolution broadband data obtained by the Reims team of Brion, Malicet, Daumont (abbreviated as BMD) using a Czerny Turner type monochromator **/Brion et al., 1993; Brion et al., 1998; Daumont et al., 1992; Malicet et al., 1995/** are available for the spectral range 195 - 830 nm at room temperature and for the reduced spectral range 194.5 - 520 nm for several lower temperatures down to 218 K. These data are adopted for most recent SBUV version 8.6 retrievals **/Bhartia et al., 2012/** and updated OMI retrievals.

Voigt et al.

The high-resolution temperature-dependent broadband cross-sections obtained previously by a team at the University of Bremen by means of Fourier-transform spectroscopy in the range 230 - 830 nm were recorded at five temperatures **/Voigt et al., 2001/** using the total sample pressures of 100 and 1000 mbar to inspect the possible pressure effect.

Bogumil et al.

The low-resolution broadband cross-sections obtained by the IUP University of Bremen team using original satellite flight models (FM) spectrometers (SCIAMACHY, GOME and GOME-2 FM3 (**/Bogumil et al., 2003/, /Burrows et al., 1999a/, /Chehade et al., 2012/**) provided pre-flight information about the performance of the instruments. In addition, they are unique source of reference spectral data, otherwise not available. These datasets have the advantage that prior knowledge of instrumental slit functions is not needed if used in the ozone retrieval with the same flight-model. However, transformation of these datasets for use with other instruments (having similar but different instrument functions) is not straightforward as the sampling is limited. Currently the **/Bogumil et al., 2003/** dataset is used for retrievals of the SAGE II, SAGE III **/McCormick et al., 1989/** and OSIRIS **/OSIRIS, 2012/** spectra in addition to SCIAMACHY.

/Weber et al. 2011/ investigated the impact of absorption cross-section choice on total O_3 retrieval applied to GOME, SCIAMACHY, and GOME2 and discussed the issues associated with resolution matching, wavelength shifts, and scalings. As a consequence the ozone cross-section data for GOME2 FM3 and SCIAMACHY (as reported by **/Bogumil et al., 2003/**) have been adjusted as reported by **/Chehade et al. 2012, 2013/**.

Single-wavelength data

Absolute cross-sections measurements have been performed at selected wavelengths in the absorption minimum between the Huggins and Chappuis bands and in the Wulf band by **/Axson et al., 2011/**, **/Anderson and Mauersberger, 1992/**, **/Enami et al., 2004/** and **/El Helou et al., 2005/**. They provide additional information for the spectral regions where existing broadband datasets demonstrate strong disagreement or only a single broadband measurement is available. Measurements by **/El Helou et al., 2005/** and **/Barnes and Mauersberger, 1987/** were performed at all temperatures using pure ozone, while data by **/Enami et al., 2004/** were scaled using Hearn's value at 253.65 nm.

Table 2.3 provides an overview of the most relevant ozone cross-sections in the UV, visible, and near IR available at more than one temperature. Typical accuracies of 2-3% are reported in the spectral regions with strong absorption (maximum of Hartley, Huggins, and Chappuis bands) for all literature data.

Table 2.3. *Characteristics of the datasets on ozone absorption cross-sections.*

Dataset	**T, K**	**Wavelength, nm**
Barnes et al., 1987	195, 221, 237, 253, 273, 297, 318	253.65
El Helou et al., 2005	144, 175, 223, 225, 291, 293 150, 222, 294 150, 222, 294	543.7, 594.3, 604.8, 612.1, 633 748.7, 779.4, 817.2, 853.2, 898.3, 944.3, 991.8, 1046.8
Enami et al., 2004	215, 245, 260, 273, 298 214, 245, 273, 296	762.07 764.47
Bogumil et al., 2003	203, 223, 243, 273, 293	230 – 1084
Burkholder et al., 1994	220, 240, 260, 280, 295	407 – 762
Burrows et al., 1999	202, 221, 241, 273, 293	231 – 794
Bass and Paur (BP), 1984	203, 223, 246, 276, 280 Polynomial coefficients	245 – 340 245 – 343
Brion, Malicet, and Daumont (BMD), 1989 -1998	218 228, 243, 273 295 Polynomial coefficients	195 – 650 195 – 520 195 – 830 195 – 520
Voigt et al., 2001	203, 223, 243, 280, 293	230 – 851

More details on these datasets can be found in the review by **/Orphal, 2003/.**

Among the datasets available at high spectral resolution (below 0.1 nm), only the data from Brion, Malicet, and Daumont team were obtained from absolute measurements. Unfortunately, these data are only available for temperatures down to 218 K and for limited spectral regions only. The measurements by **/Bass, Paur, 1984/** were scaled to Hearn's value at 253.65 nm at room

temperature **/Hearn, 1961/** and in turn used for scaling the broadband low-resolution data by **/Bogumil et al., 2003/**. Low-resolution data by **/Burrows et al., 1999/** were measured absolutely using the titration method at 293 K and scaled at all temperatures assuming the invariant integrated optical densities. The integrated absorption cross-sections of **/Burrows et al., 1999/** were later used for absolute scaling of the broadband high-resolution data by **/Voigt et al., 2001/**. Measurements by **/Burkholder, Talukdar, 1994/** were normalized using the absolute absorption cross sections of **/Anderson and Mausberger, 1992/** measured at five specific wavelengths near the peak of the Chappuis band at 298 K.

Broadband datasets are available as original experimental data at selected temperatures and as wavelength dependent temperature coefficients from a quadratic polynomial fit (Section 4.2.2.2). **/Liu et al., 2007/** derived polynomial coefficients from the BMD data at four temperatures excluding the 273 K data. Polynomial coefficients obtained from BP measurements are included in the HITRAN 2008 **/Rothman et al., 2009/**.

Despite the high quality, the datasets mentioned above do not meet the demands on the resolution, spectral coverage and availability at different temperatures, needed for modern remote sensing instruments. There is an obvious lack of consistent and consolidated data on O_3 absorption cross-sections.

2.6.2. Methane-related data

HITRAN

Already mentioned in earlier sections, HITRAN (**Hi**gh Resolution **Tran**smission Molecular Absorption Database) is the one of the most widely used databases. It is a compilation of spectroscopic parameters that a variety of software products use to predict and simulate the transmittance and emission of light in the atmosphere. The database is a long-running project started by the Air Force Cambridge Research Laboratories (AFCRL) in the late 1960's in response to the need for detailed knowledge of the infrared properties of the atmosphere. HITRAN is updated on a regular basis, including contributions of new and improved data provided by renowned research groups.

Presented below are the highlights of some important features of the HITRAN database with focus on methane line parameters relevant for this study.

HITRAN format for line parameters

The format of the parameters for each spectral line, equivalent to a record in the database, is presented in Table 2.4. Along with the line position (vacuum wavenumber) and the line intensity (blue), HITRAN provides information on four pressure-broadening coefficients for resolved lines (red), which allows to reconstruct the pressure-broadened line profile (see Section 2.2.6).

Table 2.4. *HITRAN format for transition parameters*

Parameter	Meaning	Comments or units
M	Molecule number	HITRAN chronological assignment
I	Isotopologue number	Ordering by abundance
ν	Vacuum wavenumber	cm^{-1}
S	Intensity	$cm^{-1}/(molecule\ cm^{-2})$ at 296K
A	Einstein A-coefficient	s^{-1}
γ_{air}	**Air-broadened half-width**	**HWHM @ 296K (in $cm^{-1}atm^{-1}$)**
γ_{self}	**Self-broadened half-width**	**HWHM @ 296K (in $cm^{-1}atm^{-1}$)**
E''	Lower-state energy	cm^{-1}
η_{air}	**T - dependence for γ_{air}**	**Unitless**
δ_{air}	**Air pressure induced line shift**	**cm^{-1} atm^{-1} at 296K**
V'	Upper-state "global" quanta	
V''	Lower-state "global" quanta	
Q'	Upper-state "local" quanta	
Q''	Lower-state "local" quanta	
I_{err}	Uncertainty indices	Accuracy for 6 critical parameters
I_{ref}	Reference indices	References for 6 critical parameters
*	Flag	Availability of data for line mixing
g'	Statistical weight of upper state	
g''	Statistical weight of lower state	

The critical point for the modern retrievals is the knowledge of the accuracy of the spectroscopic parameters. If available in the source data, HITRAN provides uncertainties for the following six transition parameters: intensity, line position, air pressure induced line shift, air- and self-broadened half-widths and temperature dependence (along with references to source publications). The codes for these uncertainties as they are given in HITRAN are listed in Table 2.5.

Table 2.5. *Uncertainty codes adopted for HITRAN*

Line position and air pressure-induced shift, cm^{-1}		**Intensity, air- and self-broadening half-widths and temperature-dependence**	
Code	**Uncertainty range**	**Code**	**Uncertainty range**
0	≥1 or Unreported	0	Unreported or unavailable
1	0.1 - 1	1	Default or constant
2	0.01 – 0.1	2	Average or estimate
3	0.001 – 0.01	3	≥20%
4	0.0001 – 0.001	4	10% - 20%
5	0.00001 - 0.0001	5	5% - 10%
6	Better than 0.00001	6	2% - 5%
		7	1% - 2%
		8	Better than 1%

Especially important are the broadening parameters, influencing the profile of observed lines.

The uncertainties codes for the pressure broadening coefficients for CH_4 are presented on lower panels in Figure 2.17**,** comparing the two versions of the HITRAN database (2008 and 2012)**.** HITRAN 2012 has been improved and

extended compared to the HITRAN 2008. However, for most lines the uncertainty is either larger (worse) than 20% or is roughly estimated or averaged.

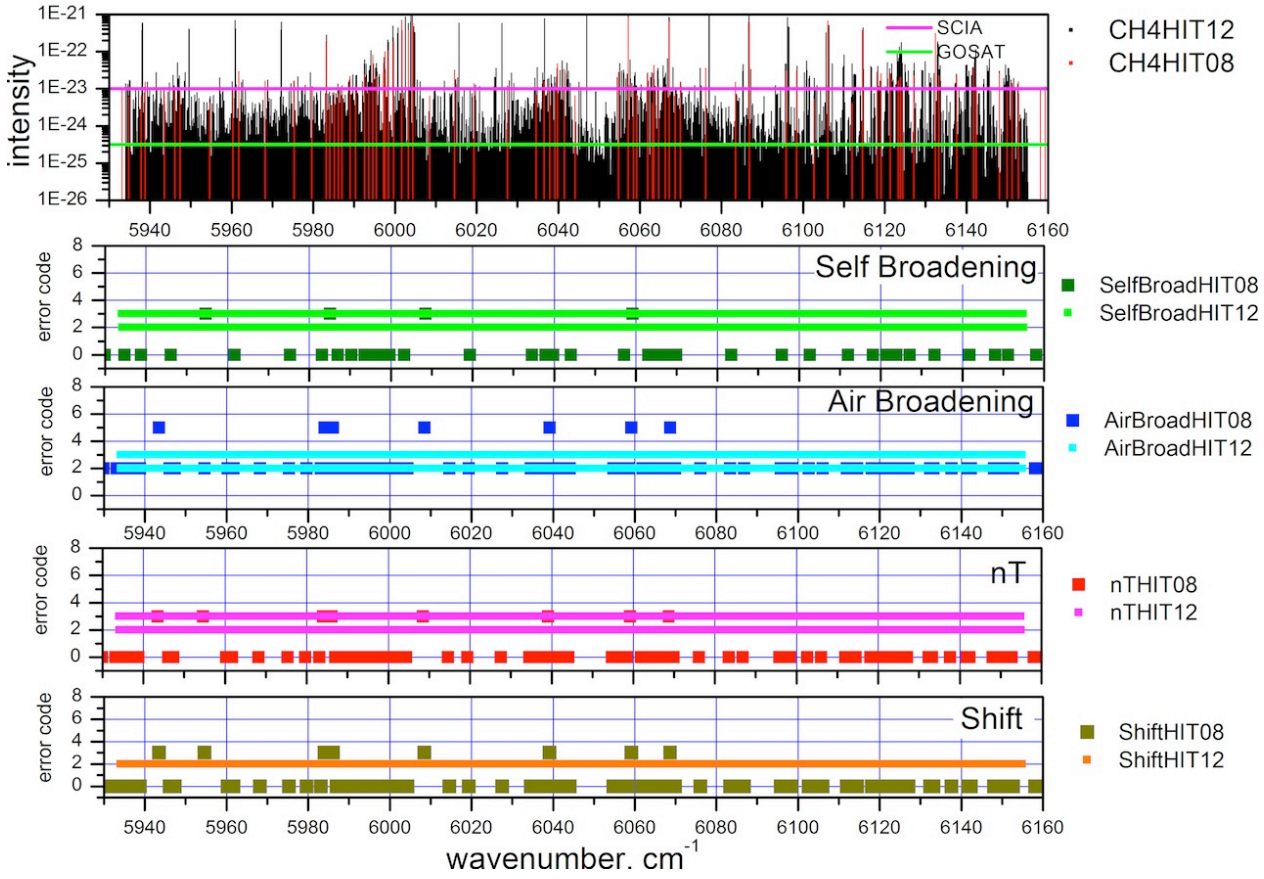

Figure 2.17. *Upper panel - spectral windows of SCIAMACHY, OCO and GOSAT and line intensities of CH_4 taken from the HITRAN 2008 and 2012. Lower panels - HITRAN 2008 uncertainty codes for broadening coefficients: self- and air-broadening, temperature dependence and pressure shift for CH_4*

HITRAN format for cross-sections

The HITRAN database provides information on the absorption cross section for some species in selected spectral regions. UV cross-section for a number of molecules were introduced in the 2004 edition of HITRAN **/Rothman et al., 2005/**. They were intended to represent the most useful data for analysis of the atmospheric measurements, including the ground-based and satellite-borne spectroscopic measurements of the atmosphere **/Chance, 2005/**.

Cross-section data for each molecule is placed in a separate file, containing sets of temperature and pressure pairs. Set headers provide information to programs reading the data and include reference to the source data.

HITRAN database evolution for CH_4 near 6000 cm^{-1}

Updates of the data included in the HITRAN database from the early 1990ties to the most recent version are described by **/McClatchey et al., 1973/, /Rothman et al., 1992, 1998, 2003, 2005, 2009/**, **/Brown, 2005/, /Brown et al., 1992, 2003, 2013/.** Evolution of the database for the region around 6000 cm^{-1} since 1986 is summarized in the Table 2.6.

Table 2.6. *Evolution of information and data sources in the course of HITRAN database upgrades for CH_4 line parameters around 6000 cm^{-1}*

Line positions and intensities	**Air-broadened half-widths**	**Self-broadened half-widths**	**Temperature dependence**	**Pressure shift, cm^{-1}/atm**
HITRAN 1986, /Rothman et al, 1987/				
/Husson et al, 1986/ /Fox et al., 1980/ /Margolis, 1973/	/Tejwani et al., 1974/	-	three different values according to symmetry, /Varanasi et al., 1983/	-
HITRAN 1991-1992 /Brown et al., 1992/				
/Margolis 1988/	/Margolis 1988/, /Brown et al., 1992/	scaled air-broadened values	mean value 0.75 for all lines.	- 0.008
HITRAN 1996, HITRAN 2000-2001 /Brown et al., 2003/ HITRAN 2004 /Rothman et al., 2005/, /Brown, 2005/				
Same as before				
HITRAN 2008 /Rothman et al., 2009/				
5860-6180 cm^{-1}: line positions from /Margolis 1988/, line intensities from /Frankenberg et al., 2008b/	5860-6180 cm^{-1} from /Frankenberg et al., 2008b/	Same as before	5500-5860 cm^{-1}: 0.75 for most lines. 5860-6180 cm^{-1}: 0.85 unless direct measurements were available /Lyulin et al., 2009/	5500-5860 cm^{-1}: same as before 5860-6180 cm^{-1}: Line-by-line, /Frankenberg et al., 2008b/
HITRAN 2012 /Brown et al., 2013/				
/Zolot et al., 2013/, /Campargue et al., 2012b/, /Campargue et al., 2012a/ /Lyulin et al., 2010/	Averaged widths by J (assigned/estimated from empirical lower-state energy) for 6799 lines Updated algorithm of /Brown et al., 1992/ (averaging by J, C and DJ)	Updated algorithm from /Brown et al., 1992/ (averaging by J, C and ΔJ)	/Brown et al., 2003/	Calculated using empirically derived approximation: *shift* = -2×10^{-6} × (*line position*).

In the first original report by **/McClatchey et al., 1973/** the *J*- and *T*-dependence of methane line widths were taken from the results of **/Varanasi, 1971/** and **/Tejwani and Varanasi, 1971/**. The only measured values of air-broadened CH_4 half-widths were those for multiples of v_3 and $2v_3$ at 295 K: 0.061 cm^{-1} atm^{-1} for *J*=1-5 and 0.048 $cm^{-1}atm^{-1}$ for *J*=15-17.

The 1986 HITRAN compilation contained only 142 lines of $^{12}CH_4$, and 93 lines of $^{13}CH_4$ calculated for the $2v_3$ bands in the 5897-6107 cm^{-1} region. An error in

band intensity (which existed since the first edition) has been corrected by multiplying the intensities by 2.5 to conform to the measurements by **/Margolis, 1973/.** In **/Margolis, 1973/**, the line strength of the manifolds of the $2\nu_3$ band have been measured for the *P, Q* and *R* branches up to *J*=10 (*J*=9 for the R branch), using the high resolution (0.06 cm^{-1}) spectra taken with a Jarrell-Ash Co. Ebert-Fastie type 1.8 m spectrometer.

The parameters of the $^{13}CH_4$ $2\nu_3$ band have been added using isotopically scaled intensities of the $^{12}CH_4$ prediction **/Fox et al., 1980/**. The accuracies of the parameters were thought to be 0.005 - 0.020 cm^{-1} for positions and 5 - 20% for intensities. Air broadened half-widths were determined from the calculated O_2- and N_2-broadened half-widths of **/Tejwani et al., 1974a/** corrected to 296 K.

In **/Margolis, 1988/**, the positions and strengths of more than 2000 methane absorption lines have been measured in the 5500–6180-cm^{-1} spectral region, using the high resolution (0.01 cm^{-1}) spectra recorded at room temperature (296 K) with a Fourier transform spectrometer. In the following work, **/Margolis, 1990/,** the strengths of more than 1600 lines of CH_4 have been measured in the spectral interval between 5500 and 6150 cm^{-1} at room and lower temperatures. The energy of the lower state of the transition was found empirically from the variation of the measured strengths using the temperature dependence of the methane partition function and the Boltzmann factor for the energy level populations. The average measured uncertainty in *J* is 20%.

Based on the work of **/Margolis, 1988, 1990/**, a significant amount of new data became available in the HITRAN editions from 1991 and 1992 as described in **/Brown et al., 1992/**. The updated line list between 5500 and 6185 cm^{-1} was extended to cover ~2000 experimental positions and line intensities. While only 3% of the lines were assigned (to $2\nu_3$ at 6000 cm^{-1} and $2\nu_4+\nu_3$ near 5640 cm^{-1}), many of the lower state energies were determined empirically using the cold sample spectra **/Margolis, 1988, 1990/**.

Compared to the 1986 edition, the $2\nu_3$ band intensity effectively increased by 11% and substantial Herman-Wallis factor was applied to the *P* and *R* branch lines. Because only the strongest lines of $^{13}CH_4$ were measured, the new experimental and old predicted values were merged, using measurements where available, and scaling the old prediction in proportion to the change in the $^{12}CH_4$ band strength and Herman-Wallis factor. The $^{13}CH_4$ lines with intensities greater than $4\cdot10^{-24}$ $cm^{-1}/(molecule\cdot cm^{-2})$ were generally taken from the experimental values.

For air-broadened widths, the empirical mean values for $^{12}CH_4$ **/Rinsland et al., 1988/** obtained for the ν_4 and ν_2 bands were tabulated to provide widths as a function of *J* and symmetry *C (=A,F,E)* for transitions with known assignments. The uncertainties associated with this tabulation exceed the experimental accuracy (±20%) because the dependence of the width on transition quantum numbers is ignored. For $^{13}CH_4$, a value of 0.95 times the mean values for $^{12}CH_4$ were used. In the range from 3900 to 6186 cm^{-1}, the widths of the unassigned lines with empirically determined lower states were taken, using the effective *J"* calculated from the lower state energy *E"* and assuming that the lines were all *F*-symmetry species. The widths of the remaining unassigned lines were set to a

default value of 0.055 cm^{-1}/atm. For CH_3D, the default value of 0.060 cm^{-1}/atm was used.

For self-broadened line widths, the air-broadened values were scaled to provide "*a crude estimate*" as a function of *J* and *C (=A,F,E).* The scaling factors were tabulated from the ratio of self-broadened values **/Ballard et al., 1986/** to corresponding air-widths **/Rinsland et al., 1988/** for 53 transitions in the 1310-1370 cm^{-1} region. The mean ratio of self- to air-broadened half-widths was 1.37 (±0.09), with scatter rather from the transition quantum number dependence than the measurement error. The widths of unassigned lines above 3900 cm^{-1} with empirically measured lower state energies were determined by computing the effective *J"* and assuming the *F*-symmetry of the species. For unidentified lines, the value of 0.075 cm^{-1}/atm was used. All estimated self-broadened half-widths were rounded to the nearest 0.001 cm^{-1}/atm. The CH_3D lines were set to a default value of 0.08 cm^{-1}/atm. The uncertainties associated with the estimates are thought to be ±25%.

In the 1986 edition, the temperature dependence of the half-width *n* was set to three different values according to the symmetry of the species, using the results of **/Varanasi et al, 1983/**. However, other studies did not confirm this conclusion, so for the 1991 and 1992 editions, a mean value of 0.75 has been selected for all lines.

Pressure shifts of methane in air were implemented for the first time in the 1991-1992 edition. For the region near 6000 cm^{-1}, the default value of -0.008 cm^{-1}/atm was given as an estimate based on the mean value obtained in the spectral region.

In general, methane data in the 1991-1992 HITRAN edition for the wavenumber region 5500-6180 cm^{-1} contained only the empirical values with experimental lower states, with self-broadened widths extrapolated from few measurements. No changes for the region around 6000 cm^{-1} were done in the 1996 and 2000-2001 editions **/Brown et al., 2003/**. The set of CH_4 spectral line parameters contained in the HITRAN 2004 database for this region was still not complete **/Brown et al., 2005/**. Some of the parameters, in particular, the broadening and shifting parameters were still obtained by the extrapolations from the measurements performed for lower frequency regions.

In the 2008 HITRAN edition **/Rothman et al., 2008/** for the spectral region near 6000 cm^{-1}, values for the line positions were taken from **/Margolis, 1988/** similar to the previous editions. Line intensities for the 5860–6180 cm^{-1} region are the data retrieved by **/Frankenberg, et al., 2008b/** on the base of the work of **/Margolis, 1988/**. Weak lines with intensities less than 10^{-24} cm^{-1}/(molecule cm^{-2}) at 296 K were still missing between 5500 and 6180 cm^{-1}.

New values for air broadening were inserted from 5860 to 6184 cm^{-1} which are scaled N_2-broadening from **/Frankenberg, et al., 2008b/**. Between 5560 to 5860 cm^{-1} a few hundred values for γ_{air} were entered as they were obtained by **/Lyulin et al., 2009/** within the work on the GOSAT line list.

As can be seen from the Table 2.6, the methane self-broadening coefficients in the spectral region near the 6000 cm^{-1} have received little attention for a while.

This lack of direct measurements has presented a problem in creating good databases. The HITRAN 2008 values are based on an estimated values from **/Brown, 1992/**. Meanwhile, new data became available from the GOSAT line list study **/Lyulin et al., 2011/**, which are partly included in the 2012 HITRAN edition.

The same is relevant to the pressure induced shift δ. In HITRAN 2008, for most of the transitions up to 5860 cm^{-1}, estimated default values similar to those used in HITRAN 2000 **/Brown et al., 2003/** and 2004 **/Brown, 2005/** were used if there were no direct measurements of the half-widths and pressure shifts **/Predoi-Cross et al., 2005, 2006/**; the exceptions were approximately 4000 measured or theoretically predicted broadening coefficients inserted on a line-by-line basis. The shifts for 5860-6180 cm^{-1} were taken from **/Frankenberg et al., 2008b/** on line-by-line basis.

Temperature dependence n was set to a default constant (0.75 below 5860 cm^{-1} or 0.85 above 5860 cm^{-1}) unless direct measurements were available **/Lyulin et al., 2009/**. Since the release of the HITRAN 2008 edition, new data became available from **/Lyulin et al., 2011/**.

Only a few investigations were dedicated to the study of spectroscopic parameters of the isotopologues $^{13}CH_4$ (~1.11% abundance) and CH_3D (0.06% abundance), especially at low temperature **/Martin et al., 2010/, /Walrand et al., 1996/.** Most of the parameters for the CH_3D were retained from HITRAN 2004. Because the $^{13}CH_3D$ was detected in the Titan's atmosphere, this species was added to the database for the first time.

HITRAN 2008 considered the new mid- and near-IR parameters to be preliminary and therefore, rather conservative accuracies were set, especially for temperature dependence and shifts coefficients; this certainly indicated that additional laboratory and theoretical studies were needed.

The new compilation of parameters was released by the joint team of spectroscopists around mid-2013 **/Brown et al., 2013/**. The somewhat belated database version is named HITRAN 2012.

The HITRAN 2012 compilation includes the new global analyses and measurements for $^{12}CH_4$, $^{13}CH_4$ and $^{12}CH_3D$. With a minimum intensity at 296 K set to 10^{-37} [cm^{-1}/(molecule*cm^{-2}] for the far-IR and down to 10^{-29} for the mid- and near-IR, the methane database increased from 290091 lines in HITRAN 2008 to 659848 lines (80% of which belong to the main isotopologue).

Contributors to the CH_4 data included in the HITRAN 2012 are listed in Table 2.6 and presented schematically in Figure 2.18, using the codes and references provided by the database and the HITRAN documentation page. In the near-IR above 5550 cm^{-1}, the compilation is based on empirical measurements. Prior laboratory results were replaced with the extensive new FTIR (5550-5852 cm^{-1}), Differential Absorption Spectroscopy (DAS) and Cavity Ring Down Spectroscopy (CRDS) (5852-7912 cm^{-1}) measurements. Ground state J- values for nearly half of the measured lines in this range were obtained, either by confirming the quantum assignments of analyses or by using the spectra at 80 K and 296 K. Available pressure-broadening measurements from HITRAN 2008 were

transferred into the new compilation, but 99% of the lines were given crudely-estimated coefficients. High accuracy line positions were inserted for the stronger P, Q and R branch transitions of $2v_3$ at 1.66 μm.

According to Figure 2.18, the line positions and intensities were mostly taken from **/Campargue et al., 2012b/** for the $^{12}CH_4$ and **/Lyulin et al., 2010/** for $^{13}CH_4$. Data for some lines are taken from **/Zolot et al., 2013/** and **/Campargue et al., 2012a/**. The four broadening parameters are obtained using calculations and estimations based on the updated algorithm described in **/Brown et al., 1992/** and lower-state energy values.

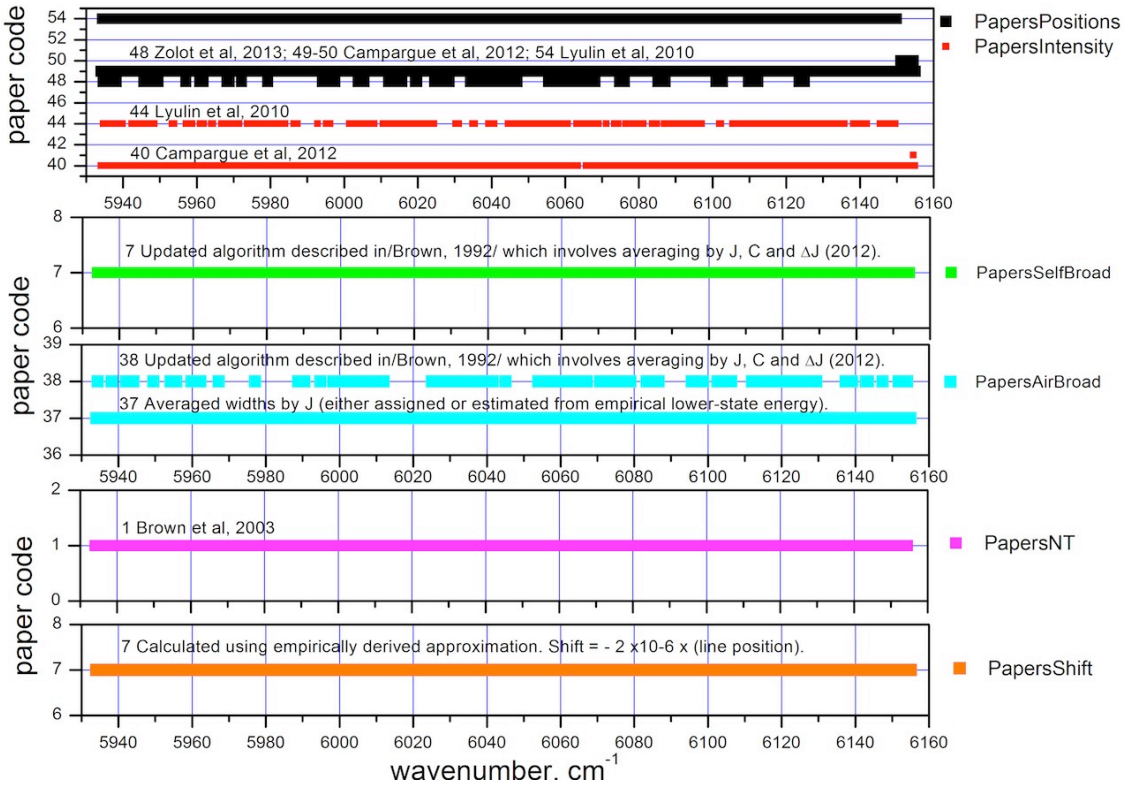

Figure 2.18. *Publications contributing to HITRAN 2012 for CH_4. From top to bottom: line positions and line intensities, self- and air-broadening, temperature dependence and pressure shift.*

Other relevant data

In addition to studies that contributed directly to the HITRAN database editions, recent research activity was also focused specifically on the $2v_3$ band. Some of it involves broadband FTIR spectroscopy and covers nearly the whole 5500-6180 cm^{-1} region for the goals of the atmospheric remote sensing applications. Another approach, based on the narrow-band high-resolution tunable diode laser spectroscopy (TDLS), is applied to investigate the strongest CH_4 features available in a spectral region relatively free of water absorption influence and other interferences: single lines (*R0* and *R1*) and manifolds *R3* and *R4*.

Some of the studies on the pressure broadening parameters are summarized in the Table 2.7 and considered in the following pages.

Tunable diode laser spectroscopy (TDLS)

/Zeninari et al., 2001/ performed measurements of the line shape parameters of the *R3* triplet of the $2\nu_3$ band using a TDLS with an absorption White cell for low pressure and a photoacoustic cell for high pressure. The broadening and the shift coefficients were obtained while varying the pressure of different perturbing gases: air and noble gases (He, Ne, Ar, Kr, and Xe).

/Kapitanov et al., 2007/ used a two-channel opto-acoustic diode laser spectrometer to investigate the $2\nu_3$ band in the region 6080-6180 cm^{-1} with resolution of about $3x10^{-4}$ cm^{-1}. Results on the *R3* triplet broadening and shift by SF_6, N_2, and air are supplement for the data from **/Zeninari et al., 2001/.** The absorption spectrum was recorded at the temperature of 295 K, methane pressure of 95 mbar and perturbing gases pressure of 0 to 1000 mbar. Overall, about 600 absorption lines were investigated. The pressure dependence of the shift on all perturbers was found to be linear with probability of 0.99 and the shift coefficient was found to be negative within the considered pressure range.

/Dufour et al., 2003/ used TDLS to study the broadening and (Dicke) narrowing parameters of the *R0* line perturbed by N_2, O_2 and He at different pressures (27 - 400 mbar), and *R3* manifold perturbed by N_2, Ar and He at 67 - 667 mbar. Data were analysed using the soft- and hard-collision models; line mixing effects were considered.

/Gharavi et al., 2005/ used TDLS for the measurement of the line strengths and collision-broadened half-widths of CH_4 perturbed by CO_2, N_2, H_2O, CH_4, and CO as a function of temperature and pressure for *R3* and *R4* manifolds. A three-, five- and six-parameter model for the analysis of absorption line parameters was used.

/Menard-Bourcin et al., 2007/ applied a method based on the measurements of the depopulation rates of rotational levels in the $2\nu_3$ vibrational state of $^{12}CH_4$ by a pump-probe technique. This method allows to obtain the depopulation rate coefficient of a well defined ro-vibrational level with a selected tetrahedral symmetry species *A, E, F* whereas, in line width measurements, the determination of the broadening coefficient for each tetrahedral component of a multiplet is not straightforward. Furthermore, for self-collisions, rotational depopulation rates can be measured at low temperature while the pressure above which methane condenses is too low to measure the pressure broadening accurately.

Table 2.7. *Studies related to the pressure broadening parameters*

	Method	Range, cm^{-1}	Parameters	Perturbing gases
Darnton et al., 1973		*P2, R0, R1*	self-broadening temperature dependence	CH_4
Margolis, 1988, 1990	FTS	5500-6180	line positions; line strength	
Zeninari et al., 2001	TDLS	*R3*	broadening coefficients; shifts	Air, He, Ne, Ar, Kr, Xe
Dufour et al., 2003	TDLS	*R0, R3*	broadening parameters; narrowing (Dicke) parameters; line mixing effects	N_2, O_2, He, Ar
Gharavi et al., 2005	TDLS	*R3, R4*	line strengths; broadening coefficients; self-broadening	N_2, CO_2, H_2O, CH_4, CO
Kapitanov et al., 2007	TDLS	6080-6180 *R3*	broadening; shift	Air, N_2, SF_6
Menard-Bourcin et al., 2007	Optical pumping	*P2, R0, R1*	depopulation rates of rot. levels, broadening coefficients; temperature dependence	N_2, CH_4
Frankenberg et al., 2008	FTS	5860-6184	line strengths; broadening coefficients; shift; temperature dependence	N_2
Lyulin et al., 2009	FTS	5550-6236	broadening coefficients; shift; temperature dependence	N_2, O_2
Campargue et al., 2012	CRDS-DAS	5550 - 7912	line positions and intensities	

High-resolution broadband spectroscopy

WKLMC line list

Another available line list for the 5852–7919 cm^{-1} region was created using the differential absorption spectroscopy (DAS) and tunable diode cavity-ring-down spectroscopy (CRDS) methods **/Campargue et al., 2012a,b/**, **/Campargue et al., 2013a,b/**. This dataset is refered to as "WKLMC", according to the authors' surnames (**W**ang, **K**assi, **L**eshchishina, **M**ondelain, **C**ampargue). The "final" version of the empirical lists for CH_4 at 80 K and 296 K was created by combining the WKMC list **/Campargue et al., 2012/** with new results obtained by DAS in the $2v_3$ region at 5852–6183 cm^{-1} **/Campargue et al., 2013b/**. Two empirical lists for CH_4 at 296 K and 80 K in "natural" abundance are provided for the atmospheric and planetary applications respectively. They include the isotopologue identification ($^{12}CH_4$, $^{13}CH_4$ and CH_3D) and the lower state energy level, E_{emp}, derived from the ratio of the line intensities measured at 296 K and 80 K. The 296 K list includes 55262 absorption lines. The 80 K list is made relevant for a wider range of temperatures by including 30282 lines observed

only at 296 K, with corresponding lower state energy values chosen to make them below the detectability limit at 80 K. Overall, the 80 K list includes 73225 absorption lines. For the two temperatures, the list is provided in HITRAN format.

Frankenberg et al.

In their study, **/Frankenberg et al., 2008b/** used the high resolution (0.01 cm^{-1}) spectra obtained using Bruker HR Fourier Transform spectrometer (FTS) in the Institute of Environmental Physics in Bremen. As was mentioned above, shifts and air-broadening coefficients reported by **/Frankenberg et al., 2008/** were included in the HITRAN database 2008.

The analysis done by **/Frankenberg, et al., 2008b/** was based on a limited number of measurements. Only four mixtures of CH_4 with N_2 at room temperatures were investigated; details on the experimental set-up and mixtures are given in Section 5.1**.**

/Frankenberg et al., 2008b/ applied a multispectrum nonlinear constrained least squares method based on optimal estimation to derive the spectroscopic parameters by simultaneously fitting the laboratory spectra at different ambient pressures. Each line was treated separately, even for multiplets, and no cross-correlations between the lines were assumed. A standard Voigt line shape was used and the Jacobian of the transmission with respect to shift and broadening coefficients computed analytically, as explained in **/Schreier, 1992/** and references therein.

/Frankenberg, et al., 2008b/ performed fitting of the relative line intensities, but strictly constrained to the **/Margolis, 1988/** values given in HITRAN 2004, permitting only small deviations. The integrated column density of methane was determined using a fit covering the isolated *R0* and *R1* transitions. For the final determination of spectral parameters, **/Frankenberg, et al., 2008b/** kept the cell column densities fixed. Thereby the line strengths retrieved in their study were linked to the *R0* and *R1* strengths given in HITRAN 2004 **/Margolis, 1988/**.

Prior pressure shifts are all reset to –0.011 cm^{-1} atm^{-1} as **/Kapitanov et al., 2007/** reported this pressure shift for the *R3* triplet. **/Frankenberg, et al., 2008b/** adapted prior broadening coefficients from measurements in the fundamental by **/Pine et al, 1992, 1997/**. Self-broadening was neglected since the CH_4 volume mixing ratio in the cell was 2% at most. Temperature dependence was fixed at 0.85 for the whole 5860-6184 cm^{-1} range.

/Frankenberg et al., 2008b/ report several unsolved and open issues. They point out that the temperature dependence of pressure broadening requires further research for most transitions. While HITRAN attributes a temperature exponent of 0.75/0.85 universally in the considered spectral ranges, **/Darnton et al, 1973/** and **/Gharavi et al., 2005/** find values ranging between 0.83 and 0.93 for *R0-R4* in the $2v_3$ branch. At 243 K, this might already lead to discrepancies in the broadening coefficient of up to 3% (temperature exponent 0.75 vs. 0.9).

GOSAT line list

Several papers by the joint Russian-Japanese team (Lyulin, Nikitin, Perevalov, Morino, Yokota, Kumazawa, Watanabe) are connected with the elaboration of the GOSAT line list. Based on the extensive experimental studies using the infrared Fourier spectrometer, the first version of CH_4 spectral line list in support of the GOSAT mission was prepared in 2008 but has not been published. In **/Lyulin et al., 2009/,** a slightly modified version of the first GOSAT methane spectral line list has been presented. The paper by **/Lyulin et al., 2009/** is devoted to the study of the broadening and shifting of the methane spectral lines in the 5550–6236 cm^{-1} range by N_2 and O_2 as foreign gases. The paper **/Nikitin et al., 2009/** is devoted to the assignment of $^{13}CH_4$ lines in this region. The next paper **/Nikitin et al., 2010/** presents GOSAT-2009 line list in the region 5550-6236 cm^{-1} in HITRAN format. Finally, the paper by **/Lyulin et al., 2010/** describes enhanced investigation of the self-broadening and self-induced shift parameters in the 5556-6166 cm^{-1} region, contributed to the GOSAT 2009 lines list.

The high-resolution measurements (0.005 cm^{-1}) of **/Lyulin et al., 2009, 2011/** and **/Nilitin et al., 2009, 2010/** significantly extended the conditions range of **/Frankenberg et al., 2008b/.** The absorption spectra of mixtures of CH_4 with N_2 and O_2 were recorded at different partial pressures for three temperatures (240, 267, and 296 K). Details on the gas mixtures used in **/Lyulin et al., 2009/** and **/Nikitin et al., 2010/** are given in Section 5.1.

In that experiment, the wavenumber scale has been calibrated using the CH_4 line positions taken from the HITRAN 2004 database. In the fitting procedure, initial values of the line positions and line intensities, as well as the line assignments, were taken from **/Wegner et al., 1998/** and **/Nikitin et al., 2010/.** The spectral line parameters were retrieved using the multispectrum fitting procedure in which a nonlinear least-squares methods was applied simultaneously to the spectra recorded under the various experimental conditions: the spectral line parameters were fitted simultaneously to six spectra recorded at a given temperature.

To retrieve the parameters of the overlapped lines of the *J*-manifolds of the $2\nu_3$ (F_2) band theoretically predicted line positions and intensities were used as initial values in the fits. When the results of the fit of the line intensities differed considerably (15–20%) from the theoretical ones, either a line position or a line intensity of one of the lines of a manifold was fixed.

The line width and line shift were calculated using the following equations:

$$\gamma = \gamma_{CH_4} p_{CH_4} + \gamma_x p_x$$

$$\delta = \delta_{CH_4} p_{CH_4} + \delta_x p_x$$

where γ_{CH4}, p_{CH4}, and γ_X, p_X are widths and partial pressures of the methane and a broadening gas and δ_{CH4}, and δ_X are shifts by methane and a broadening gas.

The output of the fits produces values for line position, line intensity, self-broadening, self-shifting coefficients, buffer gas broadening, and temperature

exponents were obtained for each selected line for three temperatures (296, 267, and 240 K).

As a results of the described studies, a list of the spectral line parameters has been generated in HITRAN 2008 format for the 5550–6236 cm^{-1} region with an intensity cut off at 4×10^{-26} cm/molecule at 296 K. The list contains 10917 lines, with only 2918 completely assigned lines and 1576 lines with partial assignment of the lower state (*J*- value). For these lines **/Nikitin et al., 2010/** give the energy of the lower state.

The values of the line positions and line intensities presented in the GOSAT 2009 list are retrieved as a result of the work described in **/Nikitin et al., 2010/**. The fitted line positions and line intensities do not differ considerably from the initial values: the line intensities obtained in the results of the fits at all three temperatures agree within 1% of the initial values. The agreement between the HITRAN 2008 and GOSAT 2009 line positions is on average within 0.001 cm^{-1}. The root mean square of the residuals between HITRAN 2008 and GOSAT values of the line intensities is 4.8%.

Majority of the obtained air-broadening coefficients agree with those of HITRAN 2004 within 10%, but there are cases for which the residuals exceed 10% and reach 40%. In GOSAT list the values of the air-broadening and air-shifting coefficients for the *J*- manifold of the strongest $2\nu_3(F_2)$ band of $^{12}CH_4$ were obtained as result of the direct measurements. The coefficients of additional 446 lines have been calculated using the results of the direct measurements of the broadening and shifting by N_2 and O_2 **/Lyulin et al., 2009/**. As a default mean value, the value of γ_{air}=0.0600 cm^{-1} atm^{-1} for the air-broadening coefficients is recommended.

The recovered self-broadening coefficients vary from 0.040 to 0.120 cm^{-1} atm^{-1} at 296 K and they are in a reasonable agreement with the values by **/Predoi-Cross et al., 2005/** for the 4100-4635 cm^{-1}. The self-broadening coefficients of 406 lines contained in GOSAT line list were measured in **/Lyulin et al., 2011/**. As a default value for the self-broadening coefficient its mean value of γ_{self} = 0.0770 cm^{-1} atm^{-1} is recommended.

The transition-averaged ratio γ_{O2}/γ_{N2} is commonly used to predict the O_2 or air broadened half-widths in the CH_4 molecule. This ratio was found to be nearly constant for the same band: the transition-averaged ratio for the ν_3 band was found to be equal to 0.937 **/Pine, 1992/,** 0.943 **/Pine et al, 2003/,** 0.976 **/Antony, et al., 2008/**. There is a good agreement of broadening coefficients for both O_2 and N_2 buffer gases as well as for their ratios between values obtained by **/Lyulin et al., 2009/** and those measured in **/Mondelain et al., 2005/** for the ν_2+ ν_4 band.

The shifting coefficients vary in a rather large range from line to line. Averaged values of the N_2- and air-shifting coefficients are close to the observed values for the *R3* manifold of the $2\nu_3$ (F_2) band published by **/Dufour et al., 2003/**, **/Kapitanov, et al., 2007/** and **/Zerninari et al., 2001/**, respectively. For the generation of the CH_4 line list in the 5550-6236 cm^{-1} region, recommended mean values of the shifting coefficients at 296K for the cases when a measured value is

unknown is -10.933 [$10^{-3}cm^{-1}$] for air and -11.0034 and -10.529 for N_2 and O_2 respectively.

The values of the exponents of the temperature dependence of the air-broadening coefficients by **/Lyulin et al., 2009/** differ considerably from the default values used in the HITRAN 2004 database for this molecule in the studied region. The average values obtained for the temperature exponent of the N_2-broadening coefficient at 296 K is close to the values measured in **/Darnton, et al., 1973/** and **/Gharavi, et al., 2005/** for five lines of the $2v_3$ band and to the values measured in **/Predoi-Cross, et al., 2005/** for four lines of v_3 band. The temperature dependence of the temperature exponents for both N_2 and O_2 buffer gases was observed. **/Lyulin et al., 2009/** and **/Nikitin et al., 2010/** suggest to use as a default value n=0.85 at 296 K.

2.7. Summary

Retrieval methods used to infer the mixing ratios and distributions of atmospheric trace gases in the spectral range from UV to thermal infrared rely on the molecular absorption spectroscopic data. Uncertainties in these "boundary conditions" directly influence the error budget of the retrieved concentrations (reaching up to several percent).

For example, three low-resolution databases on the ozone absorption cross-sections were obtained using the satellite flight model (FM) spectrometers GOME, GOME-2 and SCIAMACHY prior to launch. Several problems were detected using these data:

- SCIAMACHY total O_3 retrieval (using SCIAMACHY FM reference spectra) were 5% higher than GOME (with GOME FM reference spectra) in the range 325-335 nm;
- GOME-2 total O_3 retrieval (using GOME-2 FM) is 9% higher than calculated with resolution adjusted GOME FM.

There are discrepancies between the ozone amounts obtained by other instruments as well. Scientific community also detected other numerous problematic issues with the various ozone databases, such as poor signal-to-noise ratio at certain wavelengths, insufficient information on the temperature dependence and insufficient spectral resolution.

For methane retrievals one of the central problems is connected with limited information on the broadening parameters of the spectral lines.

Although a large quantity of the reference data is available nowadays, there is still a room for improvement of the quality of the data.

Spectroscopic laboratory measurements are the essential source of data that, along with theoretical research, can help to improve the uncertainties of the values reported in the datasets.

For the purposes of this study, several modern databases relevant for ozone and methane were analysed.

Criteria for the choice of a preferred ozone absorption cross-section dataset have been a subject of vigorous discussions within the O_3 observing community.

The necessity to measure small changes in stratospheric and tropospheric O_3 defines strict requirements on the accuracy of the O_3 absorption cross-sections used in retrievals from remote sensing instruments. Besides, accurate measurements are very useful for the assessment of the structure, potential energy diagram, and electronic states of ozone.

The following demands of the reliable ozone dataset can be highlighted:

- the spectral resolution of the cross-sections should be at least one order of magnitude better than the instrumental bandwidths of modern spectrometers or interferometers used in remote sensing;
- the spectral region measured needs to be sufficiently wide to include spectral channels and windows of as many instruments as possible to provide consistency across the various retrievals;
- data should be available for an adequate temperature range corresponding to that observed in the atmosphere.

The state-of-the-art methane line parameter database in the spectral region around 1.6 μm critical for retrievals prior to the start of this work was HITRAN 2008 **/Rothman et al., 2009**/. Nevertheless, as already noted by **/Frankenberg et al., 2008b/**, further improvements are expected to result in even lower uncertainty of the inferred line parameters. This includes more accurate laboratory measurements covering a broader range of conditions, such as the more relevant temperatures instead of only room temperature. It has been also identified that the satellite CH_4 retrievals **/Schneising et al., 2009/**, **/Frankenberg et al., 2008a/** in the 1.6 μm spectral region as used by SCIAMACHY/ENVISAT **/Bovensmann et al., 1999/** and TANSO/GOSAT **/Kuze et al., 2009/** would very likely benefit from the improved spectroscopic line parameters of methane.

In this context, the goals of the presented study can be formulated and summarized.

To produce a new reliable ozone absorption cross-sections dataset, the laboratory measurement campaign and corresponding data analysis need to be performed.

The new ozone cross-sections should have the best possible accuracy in order to serve as a useful new reference data set.

Analysis of temperature dependence and temperature parameterization of the resulting absorption cross-sections should be provided, along with an extensive comparison with the major reference datasets previously available.

For the purposes of improvement of methane spectroscopic data, laboratory measurements of absorption (or transmittance) spectra in the 1.6 μm IR region have to be carried out.

These spectra need to be processed by the specially designed software, allowing to determine the CH_4 absorption line broadening parameters (as defined by the HITRAN format).

The resulting dataset needs to be analysed and compared with the previously available reference data.

Assessment of the implication of the improved methane line parameters for the satellite XCH_4 retrievals using SCIAMACHY and GOSAT will also be performed.

3. Experimental set-ups

Acquisition of high quality spectra is an essential part of any experimental research dedicated to the improvement of the spectroscopic data. Numerous techniques exist today, allowing to perform the necessary measurements. However, there is no single universal approach: every method has intrinsic limitations due to the complicated nature of the considered spectra or capabilities of the hardware used.

Equipment available at the Molecular Spectroscopy Laboratory in the University of Bremen was suitable for the purposes of this study and met the demands to the quality of the measured spectra.

Two measurements campaigns were completed:

- dedicated to acquisition of ozone absorption spectra necessary for absorption cross-section evaluation in the 213–1100 nm spectral range;
- dedicated to acquisition of methane absorption spectra necessary for line parameters investigation near 1.6 μm.

In both cases, the temperatures of the investigated gas mixtures were varied in a wide range between 193 K and 296 K.

The experimental set-ups comprise a number of important subsystems that are responsible for creating and maintaining the controlled environment in the experimental cell. Knowledge of temperature, pressure, chemical composition of considered gas mixtures and stabilization of the mentioned parameters is as critical as recording the spectra with target resolution and sufficient signal-to-noise ratio.

This section reviews the laboratory setups used for the absorption measurements in the ultraviolet (UV 213–400 nm), visible (VIS 400–700 nm), near infrared (NIR 700–1100 nm), and IR spectral region around 1.6 μm (6000 cm^{-1} in the units conventionally used in infrared spectroscopy).

The experimental setups can be in general divided into several major constituent component groups: experimental cells, gas supply systems, the spectrometers and the light sources.

3.1. Experimental cells and temperature stabilization

Two cells used during the absorption measurements are demonstrated in Figure 3.1. Both cells are cylindrical double-jacketed quartz vessels with a total length of 140 cm and an inner diameter of 5 cm.

Depending on the required absorption path length, different optical configurations are possible. Both flanges accommodating White-type **/White, 1942/** optics (for multipass alignment) and transparent evacuated quartz windows (for single- or double pass arrangement) were used, resulting in various effective lengths. One of the cells features an additional orthogonal pass in the middle for measurements of strong ozone absorption in the UV (path length of 5 cm).

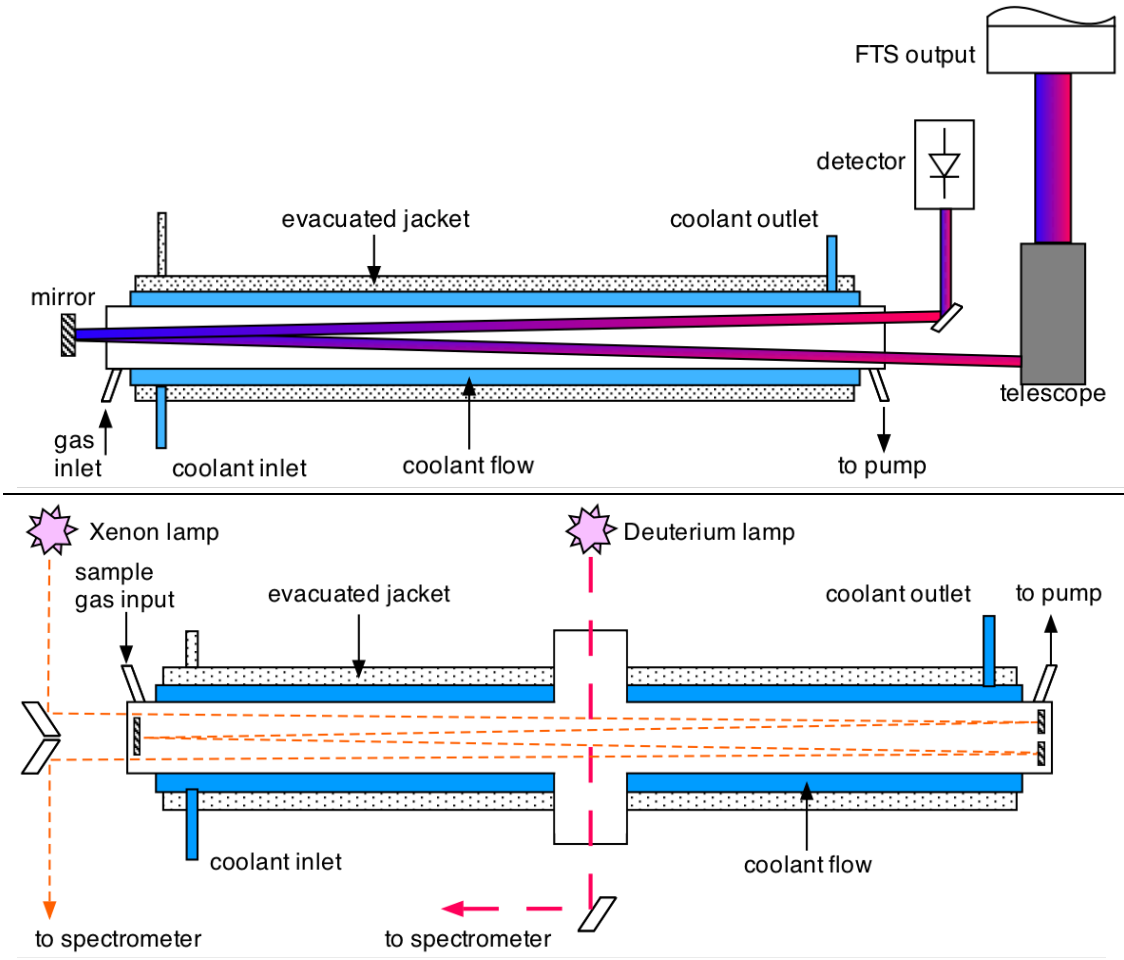

Figure 3.1. *Absorption cells.*
Upper panel: absorption cell coupled to the Fourier transform spectrometer.
Lower panel: absorption cell with White optics coupled to the Echelle spectrometer.

A layer of flowing ethanol insulated from the ambient air by the evacuated outer jacket surrounds the inner volume of the cells. The outer surfaces are additionally wrapped in aluminium foil and insulating foam. Stable cell temperatures from 296 K down to 193 K were maintained by the special thermostat systems responsible for the ethanol cooling and circulation (Haake Phoenix CT90W cryostat). The temperature was measured using the internal cryostat sensors and external platinum (Pt-100) sensors, the latter being installed inside the cells at both ends.

The cryostats were capable of limiting the temperature statistical fluctuations to less than ±0.3 K for all temperatures. The calibration of the internal sensors of the thermostats was verified using several alcohol thermometers. An agreement to within 1 K or better was found over the full range of operational temperatures.

Several Pt-sensors were used to assess the gas temperature homogeneity inside the cell and in the cell jacket, which was found to be within 1%. To exclude possible offsets of the Pt-sensors readings due to contact with the cell walls, the gas temperature was additionally estimated by means of an independent spectroscopic non-intrusive method using the absorption by the oxygen A-band at 760 nm. This method is based on the comparison of the measured O_2 absorption spectrum with the synthetic spectra calculated for different temperatures using the line parameters from the HITRAN 2008. The algorithm involves an iterative fitting of the rotational structure of the A-band using the dependence of line intensities on rotational temperature. The output is the mean over the cell temperature. The accuracy of the HITRAN parameters for O_2 is about 1% and the signal-to-noise of the oxygen absorption spectrum was better than 1%.

The Pt-sensors, the cryostat internal sensor, and spectroscopic measurements both in the static and flowing gas regime were found to agree within 1 – 3 K for almost all temperatures, resulting in an uncertainty of 0.3 – 1.5% for the whole range of the temperatures. The rotational temperature estimation mentioned above is shown in Figure 3.2 as a function of the temperature measured by the cryostat sensor. A relative uncertainty of 1.5% can be taken as the upper limit for the temperature-related uncertainty (also shown in Figure 3.2 for convenience).

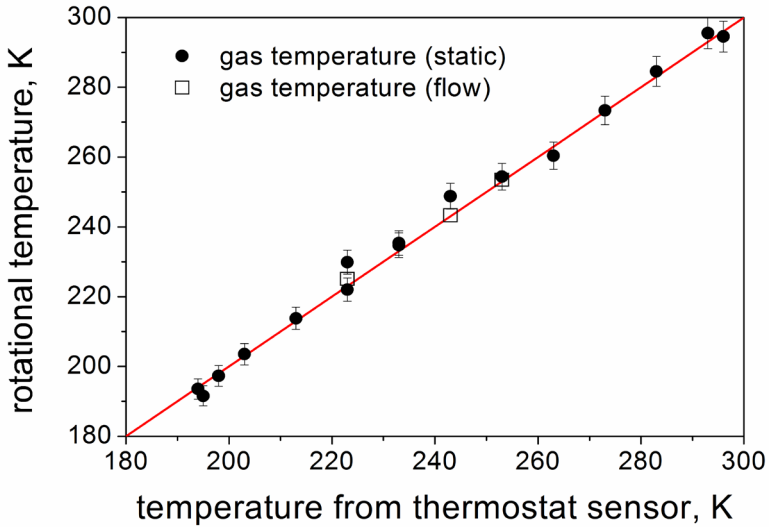

Figure 3.2. *Correlation between the rotational temperature derived from the oxygen A-band and the temperature obtained using cryostat sensor (symbols).*

These assessments were initially performed during ozone measurement campaign, but the results and uncertainties estimates remain valid for methane measurements as well.

3.2. Gas supply system

Nowadays, gases of high chemical purity and isotopic composition are available for the experimental demands. For the purposes of this study, bottles of O_2, CH_4, N_2 and dry synthetic air (0.79/0.21 N_2/O_2 mixture) were connected to the laboratory gas distribution system.

For both measurement campaigns, the gas supply and evacuation systems included the following components:

- the rotary vane and turbomolecular pumps, allowing to maintain necessary low pressure for the purposes of flow regimes and cell evacuation to pressures below 0.01 mbar;
- pressure gauges (MKS Baratron 722A series) for pressure monitoring;
- flow controllers (MKS Instruments) allowing to set the desired gas flow rate in a wide range from a few sccm to several slm (sccm and slm stand for "standard cubic centimetre/liter per minute", where standard conditions are room temperature and pressure);
- precision valves installed in important points of the pipelines, allowing to regulate the pressure in controlled volumes and isolate them when needed.

The total pressure and flow rate in the experimental cell is defined by a combination of supply (set by flow controller) and pumping rates (determined by valve setting).

Since ozone is a powerful oxidizer, it might cause damage to the gas system components (specifically, pumps). Therefore, ozone destroyer (a vessel with a platinum-coated heated wire causing catalytic ozone decomposition) was installed in the pipeline between the cell and the pump.

Several specific features of gas mixture preparation are considered below.

3.2.1. Ozone production and decay

Ozone is an unstable molecule, and for laboratory experiments it has to be produced on site from pure oxygen using the ozone generator. The principle internal element of the ozone generator is a coaxial cylindrical vessel where electrical discharge causes the dissociation of the oxygen molecules in collisions with accelerated electrons. Further recombination of $O+O_2$ yields the O_3 molecule.

To achieve the O_3 concentrations in the range needed for experimental purposes, several ozone generators were available. Efficiency of a particular device ranges from 1 to 10% depending on parameters like discharge voltage, gas pressure and flow rate. The gas pressure in the ozone generators and the whole oxygen supply system was kept at about 1.5 bar, which corresponds to the optimal regime of the ozone generator efficiency and allows to avoid gas dilution in the event of leaks. During all the experiments, the leak rate in the cell was below 0.04 mbar/hour.

Collisions with other molecules and surfaces cause the decay of ozone molecules.

In the available quartz cell with White optics (installed inside), the ozone concentration falls by 10% after 10-12 hours at room temperatures. The ozone decay rate at temperatures below 243 K is at least one order of magnitude slower.

Several sample preparation methods were used for the ozone cross-section measurements:

- Flow regime, when for a given oxygen flow rate, the performance of the ozone generator was adjusted, resulting in the ozone-oxygen mixture with ozone content in the range from 0 to 10%. The resulting optical density spectra were scaled via concatenation with the absolutely calibrated spectra (see Section 4.1.2).
- Static mode, when the cell was filled with pure ozone to a certain pressure and sealed on both ends. The resulting optical density spectra were scaled based on the observation of pressure change of the ozone-oxygen mixture due to ozone dissociation (see Section 4.1.2).

For the ozone measurements performed in flow regimes, a system was equipped with pre-cooling unit to ensure the efficient cooling of the oxygen-ozone mixture, which spent only limited time in the absorption cells, to target temperatures. The pre-cooler is a 10-meter long pipe fitted into the thermostat vessel. The length of the pipeline exposed to ambient air is approximately 50 cm. Such an arrangement, with proper thermal insulation, reduces the ozone-oxygen mixture heating on its way from the cooler to the cell. The inner surface of the pipe was passivized in order to suppress the catalytic ozone destruction.

Ozone cold trap

Measurements using pure ozone for all temperatures were performed for two spectral regions: in the UV near the in the Huggins band and in the VIS-IR region around 450-750 nm in the Chappuis band.

In these experiments, O_3 was extracted from the ozone-oxygen mixture flow supplied by the ozone generator with a quartz trap immersed in a Dewar vessel with liquid nitrogen (Figures 3.3 and 3.4). This method takes advantage of the difference in the boiling temperatures of oxygen and ozone (oxygen has lower boiling temperature and is easily pumped away from the trap whereas condensed ozone is collected on the bottom of the trap immersed in the liquid nitrogen). After sufficient quantity of ozone is collected in the trap, the latter is warmed up and the evaporating ozone is allowed to flow through the Teflon tube of about 1 m length into the cell, which was preliminarily evacuated down to the lowest possible pressure and then disconnected from the pump. This method was used by several groups **/Griggs, 1968/**, **/Molina & Molina, 1986/**, **/Yoshino, Freeman, Esmant, & Parkinson, 1988/**.

The disadvantage of this method is that an extreme caution is required in handling of the mixture, since the liquid and solid phases of ozone can explosively decompose. For safety reasons, the absolute pressure of ozone was

limited by 50 mbar, allowing to perform measurements with pure ozone only in selected regions of the ozone cross-section spectra (Section 4.1).

Since ozone tends to decay significantly at temperatures above 243 K on the time scale of the typical measurement, some pressure reading corrections were made based on the continuous observation of the total pressure and stoichiometry condition, i. e. from $2O_3 \rightarrow 3O_2$.

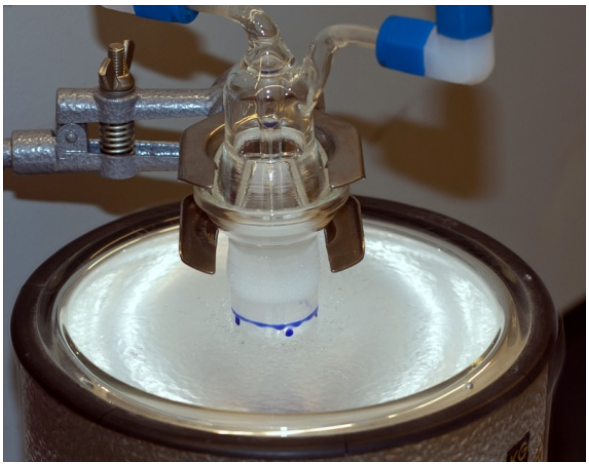

Figure 3.3. *Liquid nitrogen (LN_2) trap.*

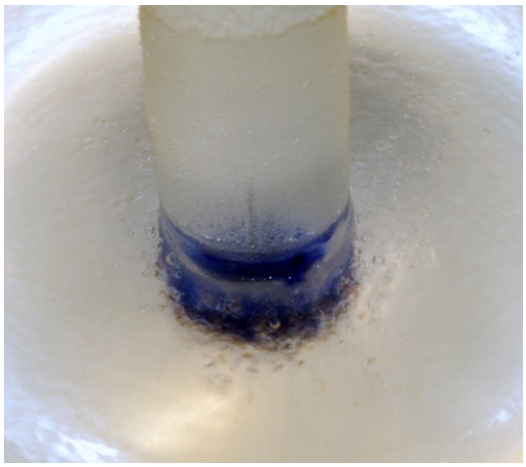

Figure 3.4. *Liquefied ozone in the LN_2 trap.*

3.2.2. Methane mixture preparation

In their research, **/Frankenberg et al., 2008b/** pointed out the importance of uniformity of the considered gas mixtures, which requires a specific routine of the sample preparation. This approach was adopted for the purposes of CH_4 absorption spectra measurements.

Methane mixtures with buffer gases were prepared under careful control of the mixing in the absorption cell. To achieve this, the filling procedure was divided in three steps: at first, the pre-evacuated (below 0.01 mbar) cell was filled with the buffer gas to about half the target pressure; then a portion of methane corresponding to the desired partial pressure was supplied, and at last the remaining portion of buffer gas was added to reach the final pressure.

3.3. Spectrometers

Two instruments were available to record the absorption spectra: the ESA 4000 Echelle grating spectrometer from LLA Berlin, and the IFS 120/125 HR Fourier transform spectrometer from Bruker (further referred to as Echelle and FTS). Both devices provided high wavelength accuracy and adequate signal-to-noise ratio over the entire optical spectral range (see Table 3.1).

3.3.1. Echelle spectrometer

The light coupled to the Echelle spectrometer with a quartz UV-transparent optical fiber is collimated with a pair of slits (Figure 3.5). Dispersion on the orthogonally positioned prism and grating creates a two-dimensional pattern of spaced diffraction orders with high order number that would otherwise overlap (see Section 2.4.2).

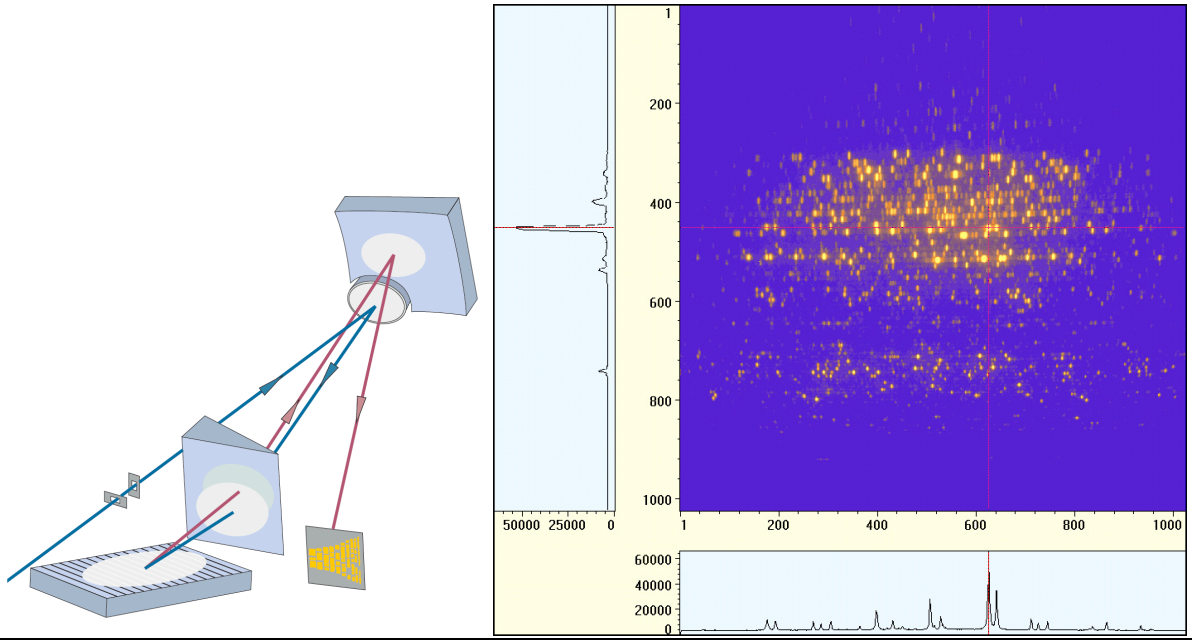

Figure 3.5. *Echelle spectrometer optical scheme and spectrum formation principle*

This pattern is imaged on the acquisition system of the spectrophotometer – an intensified charge-coupled device (ICCD), digitized, transferred to the computer running the controlling software, processed and converted from the *X-Y-I* array (*X*- and *Y*- coordinates of a pixel with intensity *I* on a 1024x1024 sensor) to a conventional intensity vs. wavelength form.

Depending on the signal intensity, spectra can be recorded within a very short period compared to FTS scan times (see Table 3.1), which makes an enhanced averaging and good signal-to noise ratio possible. The drifts of the background (I_0, see Section 2.3.1) due to the lamp intensity variations were reduced by making measurements both before and after the absorption spectrum acquisition. Typically, spectra were reproducible within <0.5%.

The Echelle spectrometer has a changing linear dispersion per pixel (24 μm) as a function of wavelength, being 0.005 nm, 0.010 nm and 0.019 nm at 200, 400 and 780 nm, respectively. The wavelength sampling interval is 0.01 nm.

Thus, the Echelle spectrometer is capable of recording the UV/VIS spectrum from 213 nm to 830 nm with a spectral resolution as high as ~ 0.02 nm FWHM at

300 nm. The wavelength calibration is very stable and ensures the accuracy as good as 0.005 nm. Resolution and wavelength calibration were tested using the Hg and Cd lamps and atomic lines positions listed by the National Institute of Standards and Technology (NIST). The accuracy of the wavelength calibration of the Echelle spectrometer with respect to the manufacturer's pre-calibration was found to be about 0.001-0.005 nm, which is close to the dispersion limit (0.005 nm per pixel in UV/VIS), see Figure 3.6.

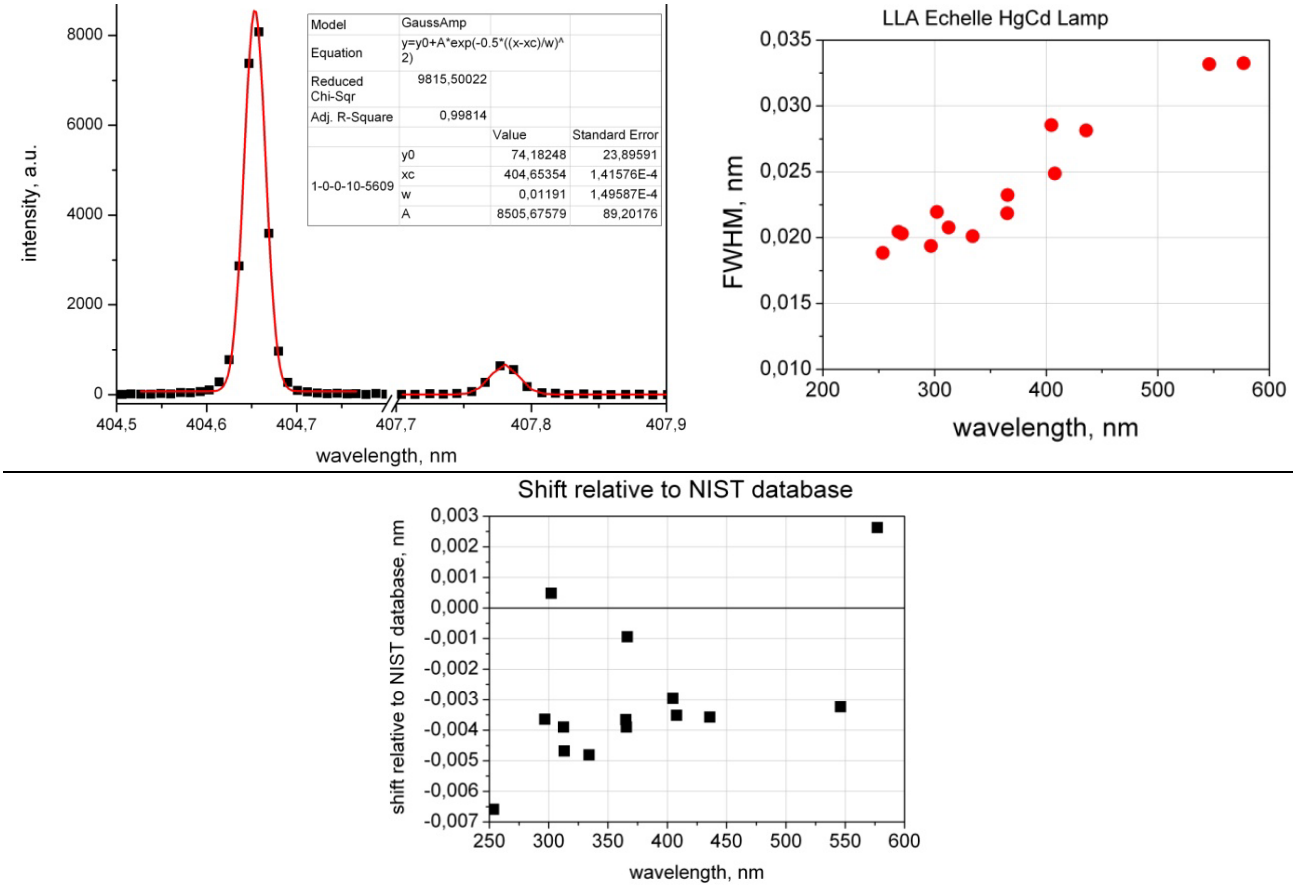

Figure 3.6. *Upper left: Hg lamp lines and Gaussian fits used to determine the instrumental FWHM for wavelength calibration.*

Upper right: FWHM of HgCd lamp lines as measured with the Echelle spectrometer.

Lower: Wavelength shifts of the HgCd lamp lines measured with the Echelle spectrometer relative to the line positions given by NIST.

The Echelle spectrometer delivered data on the air wavelength scale, which was converted into vacuum wavelength scale using the Edlen's equation **/Edlen, 1966/**:

$$(n-1)_{standard} = (\lambda_{vac}/\lambda_{air} - 1)_{standard} =$$

$$= 8{,}34213 \cdot 10^{-5} + \frac{2{,}406030 \cdot 10^{-2}}{130 - \frac{10^6}{\lambda^2}} \cdot + \frac{1{,}5997 \cdot 10^{-4}}{38{,}9 - \frac{10^6}{\lambda^2}} \qquad (3.1)$$

In measurements utilizing the Echelle spectrometer, the optical scheme is classical for an absorption experiment. The light from the external light sources enters the cell after the adjusting optics (system of lenses and mirrors). It is possible to arrange either a single or multiple (4 and more) passes along the cell, or a single pass through the short cross-path. Upon leaving the cell, the light is coupled into the optical fiber of the Echelle spectrometer (Figure 3.7).

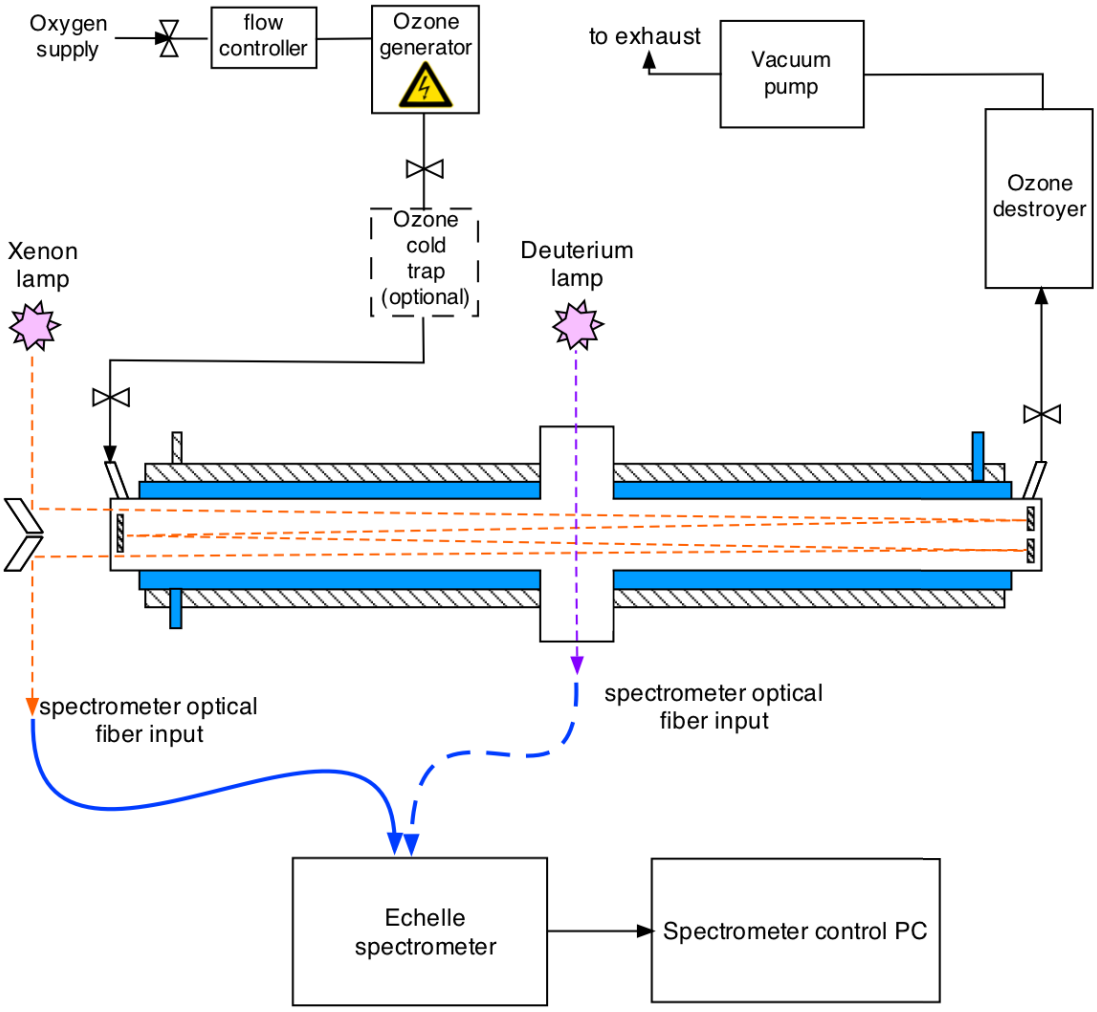

Figure 3.7. *Experimental setup with Echelle spectrometer*

3.3.2. Bruker IFS 120/125 HR spectrometer

The Bruker IFS-120HR is a Fourier transform spectrometer widely used for the spectroscopic measurements (see Section 2.4.1). The IFS-120HR instrument available in the laboratory was upgraded to electronics and some optical parts of a subsequent IFS-125HR device between the O_3 and CH_4 campaigns.

Optical arrangement utilized in measurements with the Bruker FTS was somewhat different from the conventional schemes, because the absorption path is too long to place the absorption cell and the detector in the dedicated spectrometer sample/detector compartments.

The light from the FTS internal source is guided outside through the special exit port (Figure 3.8). After adjustment with the telescope, the beam enters the experimental cell (Figure 3.1).

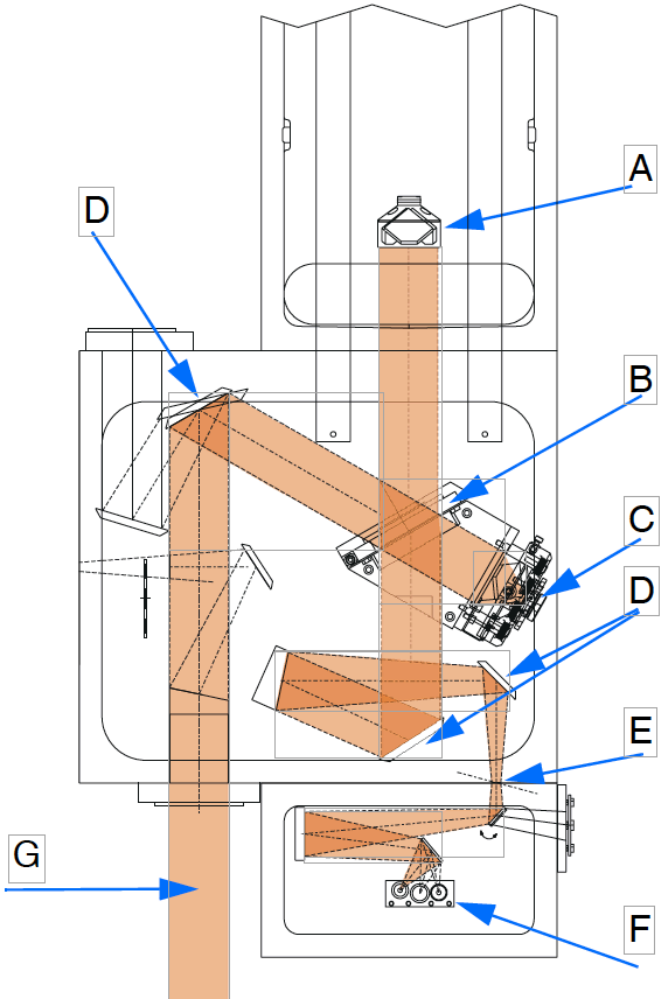

Figure 3.8. *Internal optical scheme of the Bruker spectrometer*

A- scanner with movable retroflecting mirror, B- beam splitter, C- fixed retroflecting mirror, D- folding mirror, E- input aperture, F- selectable sources, G- beam coming from spectrometer

To avoid the etalon effect (periodic structure observed on the spectra, see Section 5.1.3), the output FTS window is wedged (has non-parallel surfaces). All optical elements inside the FTS and the telescope have special coating enhancing the transmittance in the UV-VIS. Depending on the measured spectral range, quartz or CaF_2 beam splitters were used for UV-VIS and NIR-IR regions, respectively. It was possible to arrange a single or double pass through the cell.

Upon leaving the cell, the light is focused on the external detector connected to the FTS. Several semiconductor detectors (GaP, Si and InGaAs) having optimal sensitivity in the visible and infrared spectral regions were used for the measurements. More information on the FTS setup can be found in Table 3.1 and in **/Voigt et al., 2001/**.

The wavelength scale of the FTS is calibrated with an internal stabilized He-Ne laser. The extreme linearity in the laser wavelength registration is sufficient to calibrate the entire spectrum.

The Bruker FTS was used for the ozone absorption spectra measurements in the spectral regions 290-350 nm and 450-1100 nm with a resolution of 1 cm^{-1} (corresponds to a FWHM of 0.01 nm at 300 nm and 0.1 nm at 1000 nm, see Figure 3.9). The internal instrument compartment was not evacuated, and the wavenumber scale delivered by FTS was shifted due to air refraction. As well as for spectra produced by Echelle spectrometer, FTS ozone absorption spectra were converted to the vacuum wavelength scale according to equation (3.1).

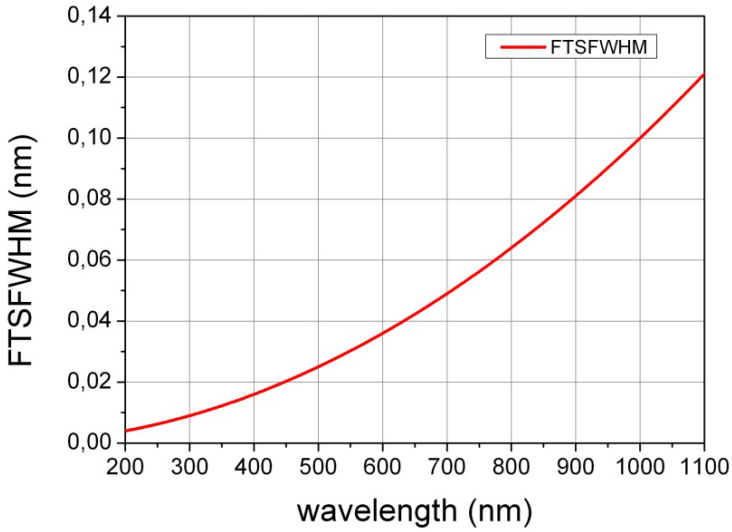

Figure 3.9. *The FTS resolution of 1 cm^{-1} recalculated in [nm] units*

There were some additional limitations during the ozone-related measurements in selected spectral regions:

- The optical scheme of the instrument contains a large number of optical surfaces (Figure 3.8), resulting in very small light throughput in the UV region and poor signal-to-noise ratio for wavelength shorter than 290 nm.
- Possible multipass options are restricted to single or double pass due to the geometry of the spectrometer/telescope optics. Therefore, measurements of the weak cross-sections in the region around 380 nm (hereafter referred to as 'bottom') have very poor signal-to-noise ratio due to the very low optical density.

The measurements of the methane absorption spectra around 1.6 μm were all performed on the experimental setup with the Bruker FTS.

The instrument compartment was kept evacuated to pressures below 1 mbar, so that the air refraction was negligible and the resulting spectra were calibrated to the vacuum wavenumber scale.

Depending on the considered wavelength region, several different light sources were used for optimization of the system efficiency: deuterium (D_2) and xenon (Xe) super quiet gas discharge lamps in the UV-VIS and tungsten filament (W) lamp in the VIS-IR-NIR.

Table 3.1 summarizes the particular details of the experimental setups used during both the ozone- and methane-related measurement campaigns.

Table 3.1. *Main parameters of the setups used for O_3 and CH_4 absorption spectra measurement campaigns.*

	Setup 1: UV-VIS	**Setup 2: VIS-NIR**	
	O_3 campaign	**O_3 campaign**	**CH_4 campaign**
Spectrometer	Echelle	FTS	
Light source	Xe and D_2 lamps	Xe and W lamps	W lamp
Detector	ICCD	Si or GaP photodiodes	InGaAs photodiode
Resolution, FWHM	0.02 nm at λ = 300 nm	0.02 nm at λ = 300 nm 0.2 nm at λ = 1000 nm	0.01 cm^{-1}
Wavelength region	213 < λ_{air}< 600 nm conversion to λ_{vac} according to Elden's formula (3.1)	300 < λ_{air} < 1100 nm conversion to λ_{vac} according to Elden's formula (3.1)	7000<ν_{vac}<5000 cm^{-1} measurements with evacuated FTS, $\nu_{instrumental} = \nu_{vac}$
Acquisition time	Fast (minutes)	Slow (tens of minutes)	Slow (hours)
Wavelength calibration	Excellent (agrees with NIST Hg line at 253 nm better than 0.001 nm)	Excellent (auto calibration with He-Ne laser) ~ 0.00005 nm	~ 0.0003 cm^{-1}
Optical path	5 cm, 135 cm – 20 m	135 cm and 270 cm	135 cm
Cooling	Double jacketed quartz cell, pre-cooler, cryogenic cooling down to 193 K		

3.4. Summary

Improvement of the spectroscopic parameters, required for the radiative transfer algorithms processing the data from remote sensing instruments, begins with thorough laboratory measurements of the absorption spectra of the atmospheric species of interest.

Absorption cross-sections of ozone demonstrate the temperature dependence in various spectral ranges relevant for remote sensing applications (Section 2.5.1).

Observed characteristic profile of the pressure-broadened absorption lines in the methane spectrum, among other things, also depends on temperature (Sections 2.2 and 2.6.2).

Available experimental setups allow to perform the measurements of ozone and methane absorption spectra in the broad range of conditions necessary to investigate the line-broadening and temperature effects on the absorption parameters.

Corresponding measurements routines, evaluation procedures and uncertainties budges will be given separately for ozone and methane in the following sections together with the analysis of the quality of the obtained spectroscopic data.

4. Investigation of the ozone absorption cross-sections

This section is dedicated to the methodology used to perform the broadband measurements of the ozone absorption cross-sections, estimation of uncertainty budget, experimental approach details, and methods and results of analysis of the acquired data.

The following requirements on the new reference data were summarized after careful consideration of the existing cross-section data (Section 2.6):

- wavelength coverage: 212–1000 nm, at 0.02 nm FWHM spectral resolution or better, with a sampling step of 0.01 nm,
- absolute values: accurate to at least 2% through the Hartley–Huggins and Chappuis bands,
- vacuum wavelength accuracy: better than 0.001 nm, corresponding to the accuracy to which atmospheric spectra can be calibrated using the correlation with the Fraunhofer spectrum,
- atmospherically-relevant temperature range of 193 K – 293 K in steps of 10 K.

The necessary measurements were performed using a combination of the Fourier transform and Echelle spectrometers and the experimental setup described in Section 3.

The assessment of the resulting data quality was performed using several approaches: direct comparisons with other datasets, comparisons of the band-integrated cross sections, polynomial temperature parameterization and calculation of the scaling factors and wavelength shifts between the different datasets.

4.1. Experimental methods and routine

4.1.1. Measurement technique

Measurements of the ozone absorption were based on the Beer-Lambert law (Section 2.3). Some important equations will be repeated below for convenience.

Beer-Lambert law describes the light intensity $I(\lambda)$ transmitted through the cell containing the absorbing gas:

$$I(\lambda) = I_0(\lambda) \int_0^L e^{(-n(T,p,l)*\sigma(\lambda,T))} dl \qquad (4.1)$$

Here I_0 is the initial light intensity in absence of ozone (background), n is the ozone number density (which is a function of temperature T, pressure p, and the position l), σ is the absorption cross-section.

In the laboratory conditions it is possible to create the controlled environment where homogeneity of sample parameters (*T(l)=const*, *n(l)=const*) is assumed sufficient so that the equation (4.1) can be simplified:

$$I(\lambda) = I_0(\lambda) * exp\{-n(T,p) * \sigma(\lambda,T) * \mathrm{L}\} \qquad (4.2)$$

where *L* is the length of the absorption path [cm].

The product of cross-section, gas concentration and absorption length is the optical density *OD*:

$$OD(\lambda) = \ln\left\{\frac{I_0(\lambda)}{I(\lambda)}\right\} = n(T,p) * \sigma(\lambda,T) * \mathrm{L} \qquad (4.3)$$

From the optical density the ozone concentration can be found if both σ and *L* are known. Therefore, precise information on the cross-sections is important for the high quality remote sensing ozone measurements in the atmosphere. Relative cross-sections are defined as:

$$\sigma(\lambda,T) = \frac{1}{A(T,p)} \ln\left\{\frac{I_0(\lambda)}{I(\lambda)}\right\} \qquad (4.4)$$

Here *A* is a scaling factor, which is the product of the ozone number density *n* and the absorption path length *L*. In *relative* ozone cross-section experiments the ozone number density is not known (e. g. flow experiment) so that the scaling factors have to be determined in other ways, e. g. from comparisons to reference values.

Absolute values of the ozone absorption cross-sections span over almost 7 orders of magnitude in the 200-1100 nm wavelength range (Figure 4.1.a).

The 250-340 nm region (Hartley and Huggins bands) and the UV-visible side of the Chappuis band demonstrate steep slopes of the absorption spectrum, often changing as fast as an order of magnitude per 20 nm.

Under these circumstances, laboratory measurements of broadband absorption spectra become very challenging. First of all, modern detectors, like the ICCD installed in the Echelle spectrometer or photodiodes in the FTS, are not capable of reliably registering signals of high dynamic range: non-linearities and cross-talk limit the span between maximal and minimal intensities that can be measured simultaneously. Large difference in cross-sections within the narrow wavelength range results in the observed spectra containing both saturated absorption (signal close to “dark” baseline) and unattenuated intensities of light source (signal close to maximum of detector sensitivity range, where non-linearities are expected).

As a result, the broadband measurements have to be divided in series, so that the optical density span covered in a single acquisition fits the optimal sensitivity window of an instrument (an example is provided in Figure 4.1.b). This is achieved by varying the absorption path and the ozone concentration in the sample.

In this study, to achieve the required dynamic range, seven or more absorption measurements at different experimental conditions were combined for every temperature.

Two approaches to the ozone sample preparation were utilized (Section 3.2.1): flow regime for the relative-calibrated measurements (constant flow rate of ozone-oxygen mixture) and static regime for the absolute-calibrated measurements (absorption cell filled with initially pure ozone), see Section 4.1.2 on the calibration and scaling methods.

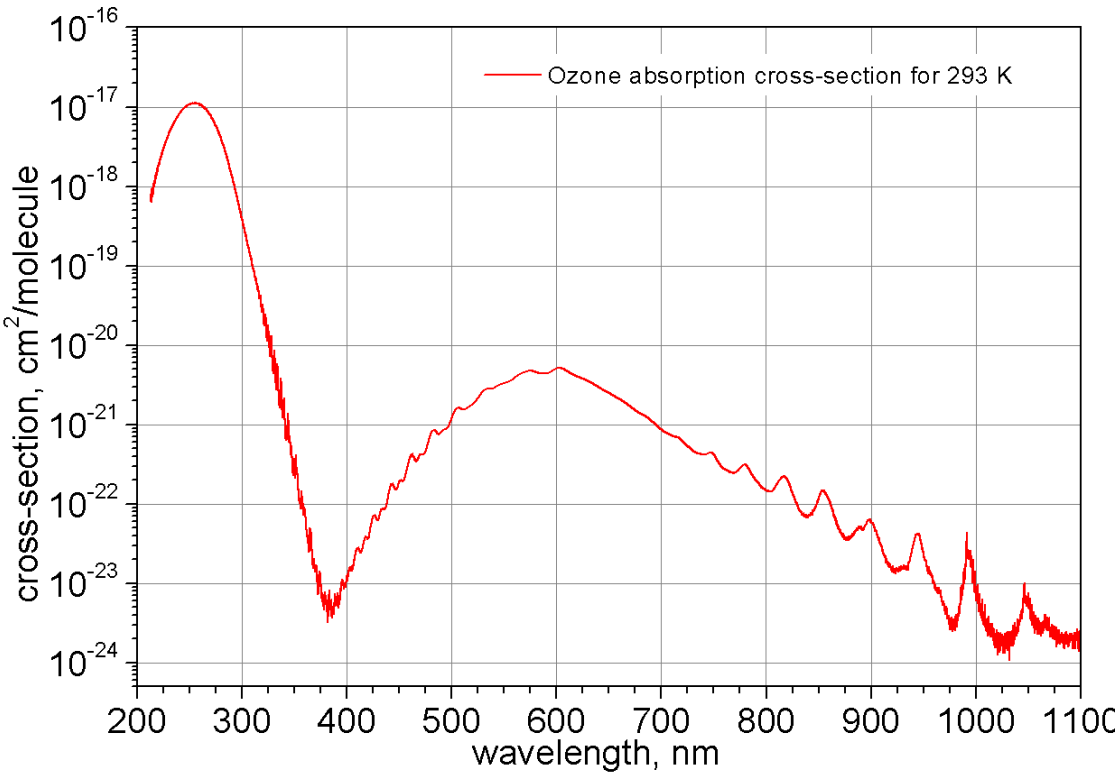

Figure 4.1.a *Ozone absorption cross-sections as a function of wavelength.*

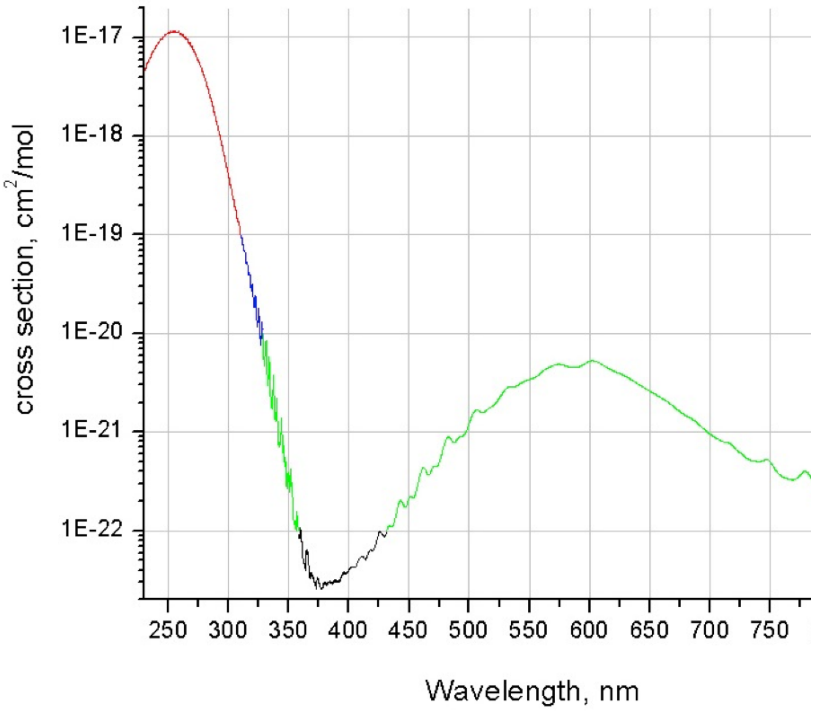

Figure 4.1.b *Ozone absorption cross-sections as a function of wavelength. Example of regions that can be covered in a single measurement*

Both Echelle and Bruker FT spectrometers were used for the absorption spectra acquisition. The wavelength coverage and other experimental parameters are presented in Figure 4.2 and in Table 4.1.

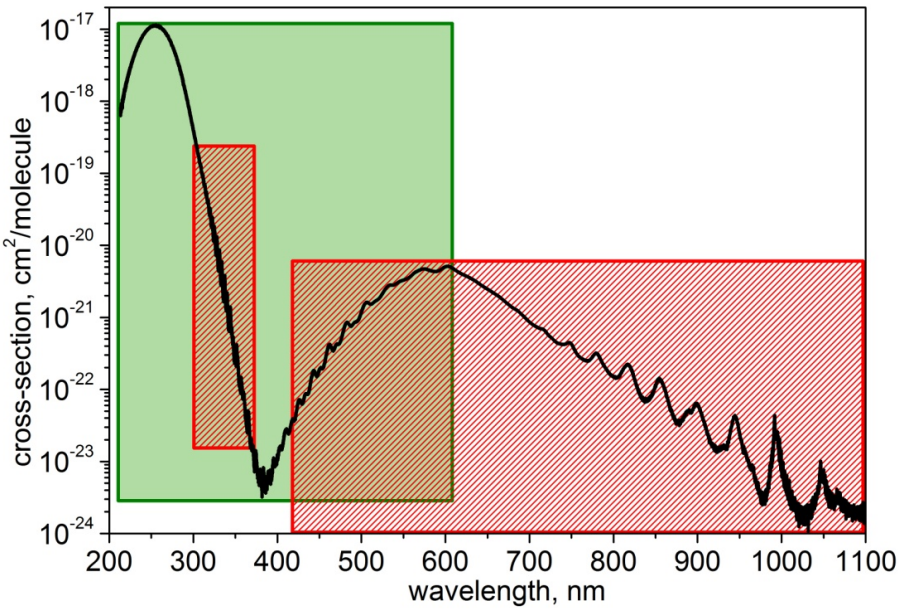

Figure 4.2. *Spectral regions covered by FT (red box) and Echelle spectrometers (green box).*

Table 4.1. *Experimental setups for different spectral regions.*

Spectral region, nm	Spectrometer, detector	Resolution	Calibration	Absorption path, cm	Lamp drift, %[1]	Optical density
213–310	Echelle, ICCD	0.018 nm	Relative	5	D_2, 0.5	0.5–2
310–335	FTS, GaP	1 cm^{-1}	Absolute	135	Xe, 2	0.1–2
335–350	FTS, GaP	1 cm^{-1}	Relative	270	Xe, 1	0.1–1
350–450	Echelle, ICCD	0.02 nm	Relative	~2000	Xe, 1	0.05–1
450–780	FTS, Si	1 cm^{-1}	Absolute	270	Tungsten, 0.2	0.05–2
780–1100	FTS, Si	2 cm^{-1}	Relative	270	Tungsten, 0.2	0.001–0.1

[1] during typical measurement time

4.1.2. Cross-section evaluation

To evaluate the values of the ozone absorption cross-section, calibration of relative optical density spectra obtained at different conditions listed in the Table 4.1 was performed.

Absolute calibration method

For the absolute calibration of the relative optical density spectra, a method based on the pure O_3 pressure measurements (as the most independent and straightforward technique) has been chosen.

To avoid the confusion, note that the optical density spectra calibrated using this approach are referred to as "absolute measurements" or "absolute cross-sections", in contrast to the "relative measurements" or "relative cross-sections" associated with the optical density spectra scaled otherwise.

Absolute broadband measurements in spectral regions of relatively large cross-sections in the Huggins and Chappuis bands were performed using the absorption path lengths of 135 and 270 cm respectively. In this case, sufficiently strong absorption was achieved with a pure O_3 pressure of about 50 mbar.

Due to the instability of the ozone molecules, the absolute measurements were carried out under very careful control of the temperature and pressure. Ozone decay during the absolute measurements can be taken into account by means of various methods. Two different spectra (I_1, I_2) can be used, each recorded over a short time within which O_3 decay can be assumed negligible and separated by a time interval needed to obtain a measurable O_3 pressure difference p_1 - p_2 (**/Griggs, 1968/**; **/Molina and Molina, 1986/**; **/Yoshino, 1988/**):

$$\sigma(I_1, I_2, p_1, p_2, k, T, L) = \ln\left\{\frac{I_2}{I_1}\right\} \cdot \frac{kT}{(p_1 - p_2) \cdot L} \qquad (4.5)$$

In this way, the absolute value of the absorption cross-section depends only on the pressure difference observed in the cell. However, only very limited number of the accumulated spectra and poor signal-to-noise ratio are possible at temperatures above 243 K because of the rapid O_3 decay. For temperatures below 243 K, the O_3 decay slows down and a measurable pressure difference is achieved only after a fairly long time (more than four hours). Unfortunately, such prolonged measurements suffer from the lamp intensity drifts, resulting in an insufficient signal-to-noise ratio of recorder spectra.

Therefore, similar to other studies (e.g. **/El Helou et al., 2005/**) the actual O_3 pressure $p(t)$ in available leak-tight cell was obtained by observation of the change in the total pressure $p_{total}(t)$, i.e. the pressure change Δp after the initial O_3 pressure p_i, the latter measured immediately after the cell was filled:

$$p(t) = p_i - 2\,\Delta p = 3p_i - 2p_{total}(t) \qquad (4.6)$$

Acquisition of the background spectra, defined as having negligible O_3 absorption, and the absorption spectra of O_3 (I_0 and I, respectively) were separated by the time needed i) to fill the evacuated cell with ozone, typically

several minutes, and ii) to accumulate spectra for sufficient signal-to-noise ratio, typically about 30 minutes. To control the lamp intensity drifts, two background spectra were measured: prior to filling the cell with ozone and after evacuating the cell. Background spectra were averaged from about 800 spectral scans, O_3 spectra were recorded in 50 separate files, each being an average of 20 scans collected during several minutes. Every file was assigned the actual O_3 pressure *p(t)* in the cell, whereby O_3 decay on timescale of several minutes was taken into account:

$$\sigma(t, I, I_o, p, k, T, L) = \ln\left\{\frac{I_0}{I(t)}\right\} \cdot \frac{kT}{p(t) \cdot L} \qquad (4.7)$$

This method yields low-noise optical densities, since the absorption spectra at a particular pressure are referenced to the stable background spectrum and results are averaged. Unfortunately, the method does not control for any ozone decay prior to start of the measurements. Overestimation of the O_3 concentration would lead to an underestimation of cross-sections. Ozone pressure p_i at the beginning of the measurements was corrected for the amount decayed during filling the cell. Correction was done by means of the extrapolation of long time (an hour and more) observations of the total pressure changes in the cell. Depending on the gas temperature in the cell, it was up to several percent. Based on the numerous repeated measurements and the quality of extrapolation, an estimate of uncertainty of about 1% in the initial ozone purity at room temperature was made.

Scaling and concatenation of relative measurements

Some O_3 absorption at 255 nm was observed after the cell was evacuated, which is probably due to the O_3 layer of unknown depth remaining attached to the optical surfaces. This effect could not be neglected during the measurements in the Hartley band performed using the short 5 cm absorption path; therefore, in this spectral region the relative cross-sections were measured using the oxygen-ozone mixture.

Oxygen-ozone mixtures were also used for weak O_3 absorption measurements in the minimum between the Huggins and the Chappuis bands and in the Wulf band to avoid the risk of explosions. Concatenation of the absolute and relative spectra obtained from the series of experiments using different combinations of cell lengths and gas mixtures (pure ozone and oxygen-ozone mixtures) was performed, as listed in Table 4.1. Relative cross-sections were concatenated with the absolute ones using scaling and offset coefficients, introduced to compensate for small drifts of the lamp intensity. Only those parts of the spectra with optical density between 0.1 and 2 were taken for concatenation in order to obtain the best possible signal-to-noise ratio and to avoid saturation. Optical densities as low as 0.01 were only used at the O_3 absorption minimum around 380 nm and in the NIR region.

The spectral resolution of the spectrometers was significantly and sufficiently higher than that of the spectral features observed. As a result, smooth spectral matching between the spectra from both spectrometers was possible when needed for the ozone cross-section evaluation.

Cross-sections were calibrated individually at each temperature, using the absolute broadband measurements at 310–335 nm and 450–780 nm, recorded with the FTS at 1 cm^{-1} spectral resolution. This way, the new data are independent for every temperature and free from uncertainties of previous studies.

4.1.3. Analysis of uncertainties

The assessment of the uncertainty budget for the absorption cross-sections is a complex task. The total uncertainty of the absolute measurements consists of uncertainties of the optical density and absolute scaling parameters: temperature, ozone pressure and cell length.

Information on the total uncertainty is very important, particularly when comparing different datasets. The ozone cross-sections are derived from the optical density spectra and suitable scaling factors, which in the case of absolute measurement are the product of ozone concentrations and path length (as described in Section 4.1.2):

$$\sigma(OD, p, k, T, L) = \frac{OD}{pL} kT \tag{4.8}$$

For calculation of the total uncertainty of complicated functions of several variables, the formula for error propagation which includes the systematic and statistical uncertainty states that:

$$\delta F(x_i) = \sqrt{\sum \left(\frac{\partial F}{\partial x_i} \delta x_i\right)^2} = \sqrt{\sigma_{stat}^2 + \sigma_{syst}^2} \tag{4.9}$$

As it is common in error analysis, the systematic error characterizes the accuracy of the method and instruments, whereas the statistical (random) error characterizes the precision (reproducibility) of the measurements.

4.1.3.1. Statistical uncertainty

Statistical uncertainty arises from the instability of the light source, influencing the intensities with and without ozone (I and I_0, respectively).

Uncertainty of the baseline δI_0 (measurement without ozone) is a result of a trade-off between the white noise reduction (lower for long integration) and source intensity drift (lower for fast measurements). The accumulation of spectra leads to improved signal-to-noise ratio, but needs time during which intensity of the lamp might vary. This uncertainty can be found in the standard deviation δI from averaging N spectra:

$$\delta I_0 = \sqrt{\frac{\sum_i^N (I_{0mean} - I_{0i})^2}{N(N-1)}} \tag{4.10}$$

Here I_{0mean} is the mean value, I_{0i} the intensity of a single spectrum, and N the number of obtained spectra.

The intensity uncertainty, δI, during absorption measurement depends on the stability of the lamp and white noise as well. However, it additionally depends on the absorption fluctuations caused by the temperature and pressure fluctuations. Since absorption is wavelength dependent, the uncertainty is wavelength dependent as well. It can be found from the Beer-Lambert law (4.2) using the formula for error propagation (4.9):

$$\delta I(I_0,p,T,L,\sigma) = \sqrt{\sum\left(\frac{\partial I_0 exp(-\sigma L p/kT)}{\partial x_i}\delta x_i\right)^2} =$$

$$\sqrt{\left(I_0 exp(-\sigma L\, p/kT)\right)^2\left(\frac{\delta I_0}{I_0}\right)^2 + \left(I_0 exp(-\sigma L\, p/kT)\right)^2(-\sigma L\, p/kT)^2\left[\left(\frac{\delta p}{p}\right)^2 + \left(\frac{\delta T}{T}\right)^2 + \left(\frac{\delta L}{L}\right)^2 + \left(\frac{\delta \sigma}{\sigma}\right)^2\right]} =$$

$$I_0 exp(-\sigma L\, p/kT)\sqrt{\left(\frac{\delta I_0}{I_0}\right)^2 + OD^2\left[\left(\frac{\delta p}{p}\right)^2 + \left(\frac{\delta T}{T}\right)^2 + \left(\frac{\delta L}{L}\right)^2 + \left(\frac{\delta \sigma}{\sigma}\right)^2\right]} =$$

$$I\sqrt{\left(\frac{\delta I_0}{I_0}\right)^2 + OD^2\left[\left(\frac{\delta p}{p}\right)^2 + \left(\frac{\delta T}{T}\right)^2 + \left(\frac{\delta L}{L}\right)^2 + \left(\frac{\delta \sigma}{\sigma}\right)^2\right]} \qquad (4.11)$$

The relative uncertainty of intensity is then:

$$\frac{\delta I(I_0,p,T)}{I} = \sqrt{\left(\frac{\delta I_0}{I_0}\right)^2 + OD^2\left[\left(\frac{\delta p}{p}\right)^2 + \left(\frac{\delta T}{T}\right)^2\right]} \qquad (4.12)$$

since the path length and cross-section do not fluctuate during the measurements.

The uncertainty of the optical density can be found from the uncertainties of the intensities without and with ozone:

$$\delta OD(I_0,I) = \sqrt{\left(\frac{\delta I_0}{I_0}\right)^2 + \left(\frac{\delta I}{I}\right)^2} \qquad (4.13)$$

Taking into account the uncertainty of the intensities, the optical density uncertainty is then

$$\delta OD(I_0,I,p,T,OD) = \sqrt{2\left(\frac{\delta I_0}{I_0}\right)^2 + OD^2\left[\left(\frac{\delta p}{p}\right)^2 + \left(\frac{\delta T}{T}\right)^2\right]} = OD\sqrt{\frac{2}{OD^2}\left(\frac{\delta I_0}{I_0}\right)^2 + \left(\frac{\delta p}{p}\right)^2 + \left(\frac{\delta T}{T}\right)^2} \qquad (4.14)$$

and the relative uncertainty

$$\frac{\delta OD}{OD} = \sqrt{\frac{2}{OD^2}\left(\frac{\delta I_0}{I_0}\right)^2 + \left(\frac{\delta p}{p}\right)^2 + \left(\frac{\delta T}{T}\right)^2} \qquad (4.15)$$

4.1.3.2. Systematic and total uncertainty

As mentioned above, the systematic error comes from the uncertainty of the scaling factor and depends on the accuracy of p, T and L, which are generally not wavelength dependent (except for T). The total uncertainty for the cross-section is then found using (4.9) for error propagation again:

$$\delta\sigma(p,T,L,OD) = \sqrt{\sum\left(\frac{\partial\frac{OD}{pL}kT}{\partial x_i}\right)^2 \delta x_i^2} = \sqrt{\left(\frac{OD}{pL}kT\frac{\delta p}{p}\right)^2 + \left(\frac{OD}{pL}kT\frac{\delta L}{L}\right)^2 + \left(\frac{OD}{pL}kT\frac{\delta T}{T}\right)^2 + \left(\frac{OD}{pL}kT\frac{\delta OD}{OD}\right)^2} =$$
$$\frac{OD}{pL}kT\sqrt{\left(\frac{\delta p}{p}\right)^2 + \left(\frac{\delta L}{L}\right)^2 + \left(\frac{\delta T}{T}\right)^2 + \left(\frac{\delta OD}{OD}\right)^2} = \sigma\sqrt{\left(\frac{\delta p}{p}\right)^2 + \left(\frac{\delta L}{L}\right)^2 + \left(\frac{\delta T}{T}\right)^2 + \left(\frac{\delta OD}{OD}\right)^2} \quad (4.16)$$

The relative uncertainty is then

$$\Delta\sigma = \frac{\delta\sigma}{\sigma} = \sqrt{\left(\frac{\delta p}{p}\right)^2 + \left(\frac{\delta L}{L}\right)^2 + \left(\frac{\delta T}{T}\right)^2 + \left(\frac{\delta OD}{OD}\right)^2} \quad (4.17)$$

Taking into account the uncertainty of the optical density, the total relative accuracy is expressed as:

$$\Delta\sigma = \frac{\delta\sigma}{\sigma} = \sqrt{\left(\frac{\delta p}{p}\right)^2 + \left(\frac{\delta L}{L}\right)^2 + \left(\frac{\delta T}{T}\right)^2 + \frac{2}{OD^2}\left(\frac{\delta I_0}{I_0}\right)^2} \quad (4.18)$$

Here δp and δT include both fluctuations during measurements and nominal accuracy of the sensors measuring T and p.

The dependence of the relative uncertainty in the wavelength calibration is included in the error part of the optical density and the baseline drift. It inversely depends on the optical density itself.

Table 4.2 summarizes the sources of uncertainties.

Table 4.2. *Sources of uncertainties*

Uncertainty nature	Uncertainty source	Uncertainty
Statistical: optical density	Reproducibility of spectra intensities: • Source intensity drift; • White noise; • Fluctuations of temperature; • Fluctuations of pressure.	Depends on spectral regions
Systematic: scaling factor	Absolute calibration parameters: p, T, L: • Purity of ozone (leaks, ozone decay); • Accuracy of temperature sensors; • Temperature sensors off-set; • Absolute accuracy of the cell length.	Independent of spectral region

4.1.3.3. Uncertainty budget for this study

Absolute calibration was possible for the optical density spectra measured with pure ozone samples in the Huggins band (310-335 nm) and in the 500-800 nm range. OD spectra from other regions were concatenated and scaled to the absolute values using the least squares fit with non-zero offset.

The systematic error, independent on the wavelength, translates on all measured regions. This error needs to be estimated for the uncertainty sources provided in

Table 4.2. In a similar way, uncertainty budgets are typically provided in publications on the ozone absorption cross-sections measurements, as in **/Hearn, 1961/**, **/Malicet et al., 1995/** or **/Daumont et al., 1992/**.

Statistical uncertainty over the different spectral regions

Every spectral region has its own statistical uncertainty which depends on the optical density available and stability of the used light source. The contribution of the statistical uncertainty is usually omitted in other studies.

In this work the relative statistical uncertainty is represented by the following term in (4.18):

$$\Delta\sigma_{stat} = \frac{\sqrt{2}}{OD}\left(\frac{\delta I_0}{I_0}\right) \tag{4.19}$$

The physical meaning of this term is the stability of the source intensity relative to the measured absorption: at the same signal quality $\delta I_0/I_0$ the statistical uncertainty $\Delta\sigma_{stat}$ in the Huggins band can change within one measurement by at least one order of magnitude, resulting from the corresponding drop of the optical density.

Following light sources were used: the deuterium (D_2) lamp in the UV below 300 nm, the xenon lamp (Xe) in the 300–450 nm region and the tungsten lamp (W) in the VIS/IR from 450 nm to 1100 nm. The tungsten and deuterium lamps are more stable than the xenon lamp and they have a stability of $\delta I_0/I_0 \approx 0.1$ and 0.5%, respectively, during the experiment. The stability of the xenon lamp is $\delta I_0/I_0 \approx 1\%$.

When possible, concatenation of the spectra was performed using the saturation-free regions in the optical density range of 0.5–2. However, in the "bottom" region (350–450 nm) and the IR region, spectra with optical densities of 0.1 and lower had to be used. Values for the intensity stability along with measured optical densities and corresponding relative statistical uncertainty are listed in Table 4.3.

Part of the spectrum between 325 nm and 335 nm is referred to as "DOAS window", since it is specifically used for ozone retrievals (see Section 1.4.3).

Note that with optical density falling towards the concatenation regions the corresponding relative statistical uncertainty grows for the same quality of the source signal. Thus relative statistical uncertainty can vary over an order of magnitude for the same wavelength depending on measurement conditions. For example, in the spectral region between the "DOAS" and "bottom" regions the optical density at 340 nm was about 0.1 during the "DOAS" measurement and 1 during the "Bottom" measurement, leading to a statistical error of 1.4% and 14%, respectively.

To make it a bit more simple, the source stability ($\delta I_0/I_0$) is considered as an appropriate estimate of the statistical uncertainty, assuming an optimal optical density OD=1:

$$\Delta\sigma_{stat} \approx \sqrt{2}\left(\frac{\delta I_0}{I_0}\right) \quad (4.20)$$

Equation (4.20) can be safely applied in the 213–350 nm and 450–750 nm regions. It must be added to the reported systematic uncertainty.

For the "Bottom" and "NIR" regions (4.20) leads only to a lower limit of the uncertainty, being higher in reality.

Table 4.3. *Impact on optical density uncertainties for different spectral regions.*

	"Top"	**"UV"**	**"DOAS"**	**"Bottom"**	**"VIS"**	**"IR"**
Wavelength, nm	213 - 290	290 - 310	310 - 340	340 - 450	450 - 750	750-1100
Source stability, % *	0.5 (D_2)	2 (Xe)	1 (Xe)	1 (Xe)	0.2 (W)	0.2 (W)
Optical density limits	0.5 – 2	0.1 – 2	0.1 – 2	0.05 – 1	0.5 – 2	0.01 – 0.1
Relative statistical uncertainty, %	1.4 - 0.4	30 – 1.4	14 – 0.7	28 – 1.4	0.56-0.14	28 – 2.8
Estimation for relative statistical uncertainty (OD=1), %	0.7	2.8	1.4	-	0.4	-
Relative systematic uncertainty, %	≤3					
Estimation of the relative total uncertainty, %	≤3	≤4	≤3.3	-	≤3	-

* the type of lamp is given in brackets, used during measurements:

D_2 – deuterium, Xe – xenon, W – tungsten.

The sufficient length of the absorption cell (more than 1 m) made it possible to measure the absorption path with high accuracy. Thickness of the windows was also taken into account (measured using a caliper). The uncertainties in the temperature and pressure readings contribute to both statistical and systematic uncertainties of cross-sections. The largest uncertainty in the absolute calibration is due to the ozone pressure, corrected for decay as discussed earlier. Pressure fluctuations during the measurements were below the sensitivity of the digital readout of the pressure sensors (0.04 mbar). Accuracy of a calibrated pressure sensor is 0.5% of the reading value (according to the manufacturer specifications). The thermostats maintain the set temperature with a stability of ±0.3 K or better. Calibrations of the internal sensors of the thermostats were checked using several alcohol thermometers; possible offsets were found to be less than 1 K. Readings of the external Pt-sensors installed on both ends of the cells and the internal thermostat sensors agreed to within 1 K or better, confirming the uniformity of the temperature in the setups.

Performance of the optical system (lamps spectra, detector sensitivity curves, etc.) and shape of the absorption spectra lead to a complicated wavelength

dependence of the relative uncertainty of the optical density and were discussed earlier. For simple estimation, the statistical uncertainty related to the source stability at optical density of unity was used. This is valid for almost the entire Hartley and Huggins bands and the 450–750 nm region; however, it strongly underestimates the uncertainties in the spectral regions with weak absorption between Huggins and Chappuis bands and in the NIR Wulf band.

Table 4.4 summarizes the upper estimations for uncertainties from different sources for the O_3 absorption cross-sections absolutely measured in the Huggins and Chappuis bands for room temperature. The systematic uncertainty is about 1%; the statistical uncertainty at optical density of unity is 1–3% in UV and in the visible. In the spectral regions characterized by the weak absorption, statistical uncertainty can reach up to 20% and more due to the very low optical density (Table 4.3). The systematic uncertainty of the absolute measurements propagates into the relative measurements. For relative measurements, additional uncertainties arise from the scaling of these spectra to the absolute calibrated spectra. However, these uncertainties are negligible, because differences between the matched spectra are typically much smaller than the estimated experimental uncertainty.

Table 4.4. *Uncertainty in the absorption cross-section obtained from absolute measurements at 50 mbar and 293 K and path lengths of 135 and 270 cm in the Huggins band and Chappuis band, respectively. Upper estimations are given, real values can be lower.*

Systematic uncertainty	**Statistical uncertainty**
Gas supply system purity: – oxygen purity: 99.995% – leaks: 0.1% Pressure sensors uncertainty: 0.5% (0.25mbar) Temperature sensors uncertainty: 0.3% (1K) Temperature non-uniformity: 0.3% (1K) Cell length[2]: 0.04–0.07% (1 mm) Total: 1.3%	Uncertainty of the correction for ozone decay: 1% Temperature fluctuations: 0.1% (0.3K) Light source stability[1,2]: 0.28–2.8% Total (RMS)[2]: 1–3%

[1] relative to optical density OD=1

[2] depending on spectral region, see Table 4.3.

The uncertainty budget for ozone absorption cross-sections for temperatures below 293 K is provided in Table 4.5. For majority of the spectral regions, the largest contribution to the total uncertainty is due to the determination of the absolute ozone concentration. In the available quartz cell the ozone concentration was found to fall by 10% after 10–12 hours at room temperature, and at temperatures below 243 K the decay rate is lower by at least one order of magnitude. Ozone decay in the cell during gas accumulation before the measurements and during the spectra acquisition had to be taken into account

only for temperatures above 243 K. The uncertainty of the ozone pressure is about 1% and better, improving towards the lower temperatures.

During the absolute measurements, light source stability was 0.2 % and 2% for Chappuis and Huggins bands respectively. The uncertainty of the absolute calibration applies as well into the relative spectra that were concatenated. For the majority of the spectral regions, the statistical uncertainty of the absorption measurements is well below 1%; however, in the spectral regions with weak absorption (350–450 nm and longer than 900 nm) statistical uncertainty can reach up to 30%.

Table 4.5. *Uncertainty associated with the absorption cross-section obtained from absolute measurements at 50 mbar and 193 – 293 K and path lengths of 135 and 270 cm in the Huggins and Chappuis bands.*

Systematic uncertainty	
Ozone impurity:	
oxygen impurity	0.005%
leaks	< 0.1%
Accuracy of pressure sensors	0.04% (0.02 mbar)
Temperature measurements	< 0.3–1.6% (1-3 K)
Temperature non-uniformity in the system	< 0.3% (1 K)
Cell length	< 0.04–0.07% (<1 mm)
Total	< 0.8-2.1%, depending on the temperature
Statistical uncertainty	
Ozone decay	< 1%
Pressure fluctuations	< 0.08% (<0.04 mbar)
Temperature fluctuations	< 0.1–0.16% (<0.3 K)
Light source stability (relative to optical density *OD=1*)	0.2% (VIS) / 2% (UV)
Total:	< 1–2.2%, depending on the spectral region

4.1.3.4. Uncertainties reported for other datasets

Since information on the total uncertainty is particularly important when comparing different datasets, it is reasonable to briefly discuss uncertainties of some published broadband data.

Bass and Paur report 1% noise during their measurements **/Bass and Paur, 1985; Paur and Bass, 1985/**. This random uncertainty needs to be added to the systematic uncertainty arising from their absolute calibration. The data were absolutely calibrated for all temperatures using Hearn's value at the Hg lamp line at 253.65 nm, which is 1147 10^{-20} cm^2/molecule **/Hearn, 1961/**. Hearn himself

states best estimates of the cross-section at 253.65 nm as (1147 ±24) 10^{-20} cm^2/molecule, i.e. 2.1%. Therefore, the total uncertainty of BP data exceeds 2%. At other wavelengths of the Hg lamp lines in the Hartley band, BP data agree with the Hearn's data within 2 – 3 %.

A systematic uncertainty of at least 2% in the SCIAMACHY dataset by **/Bogumil et al., 2003/** arises because the BP data have been used for absolute calibration. The **/Bogumil et al., 2003/** estimated a total uncertainty of about 3% or better, excluding regions with cross-sections below 10^{-23} cm^2/molecule (365–410 nm and longer than 950 nm) and the 305–320 nm spectral region (spectral channel edges). This total uncertainty includes an uncertainty arising from the scaling procedure during concatenation. The **/Bogumil et al., 2003/** dataset was obtained using the concatenation of several spectra performed from UV to NIR covering a broad region from 230 to 1075 nm. Consecutive concatenations starting from the Hartley band towards the longer wavelengths can lead to an accumulated uncertainty towards the Chappuis and Wulf bands, because BP data are only available in the Hartley – Huggins bands.

The other satellite dataset – GOME flight model data - was absolutely calibrated using the titration method **/Burrows et al., 1999a/**. The accuracy stated is 2.6% with less than 2% assigned to the lamp intensity drift. Integrated absorption cross-sections recorded with the GOME-FM instrument were used for the absolute calibration of the FTS dataset by **/Voigt et al., 2001/**. The spectral wavelength accuracy of the **/Voigt et al., 2001/** data is better than 0.5 pm at 230 nm and 7.2 pm at 850 nm.

BMD team states a total systematic uncertainty of 1.5% in the spectral region 420–830 nm and 1.5–4% at 350–420 nm and a statistical uncertainty (RMS) of 0.9–2% **/Brion et al., 1998/**. In the earlier works in the UV region BMD team states a total systematic uncertainty of 1.3% in the Hartley band and 1.3-2.5% in the Huggins band and a statistical uncertainty of 0.9–2.2% **/Daumont et al., 1992/**.

It can be concluded that uncertainty of the new data set (2-3% for most of the spectral regions) is comparable to the other broadband data measured so far. In the ozone retrievals from remote sensing, an additional uncertainty may arise from data convolution with the instrumental slit functions and, therefore, depends on the accurate knowledge of those.

4.2. Results analysis and comparisons

Final data set and analysis approach

The set of the cross-sections, covering the UV-VIS-IR region (212–1100 nm) was obtained for 11 temperatures (from 193 K to 293 K in steps of 10 K). The region of particular interest is in the Huggins band, where the DOAS window between 325-335 nm is located (Section 1.4.3). The UV region and the Hg-line wavelengths (253 nm) were used for control of the data quality, but not for the absolute calibration.

The analysis and comparisons were performed using several approaches. Absorption cross-sections for the entire obtained wavelength range were divided into regions according to the conventional band nomenclature. For those regions where O_3 absorption cross-sections demonstrate pronounced temperature dependence, analysis of parameterization and comparisons with the previously available data were performed.

Review by **/Orphal, 2003/** provided analysis of the broadband data obtained before 2003. Following the similar approach, the analysis of the new absorption cross-sections at the temperature of 293 K was performed:

- scaling factors between the new data and selected published band-integrated cross-sections are determined;
- a comparison between new results with the published datasets at wavelengths of the He-Ne laser, Hg lamp, and spectral channels of various remote sensing instruments is made;
- scaling factors and wavelength shifts are determined with respect to the high spectral resolution datasets (BMD and BP) and the lower spectral resolution datasets (GOME, GOME-2, SCIAMACHY) in the Hartley, Huggins, and Chappuis bands.

As was described in Section 4.1.1, multiple measurements of optical density spectra had to be performed at different conditions to cover the entire dynamic range of absorption cross-section values. The procedure had to be repeated for different temperatures. Table 4.6 summarizes some details on the measurements of individual pieces of spectra.

Table 4.6. *Measurement sequences*

Number of pieces to concatenate	6-7
Temperatures	11
Number of independent measurements	≈5
Total number of measurements:	~390

Figures 4.3 and 4.4 provide the graphical overview of the new data for all temperatures for all measured wavelengths and near the DOAS window.

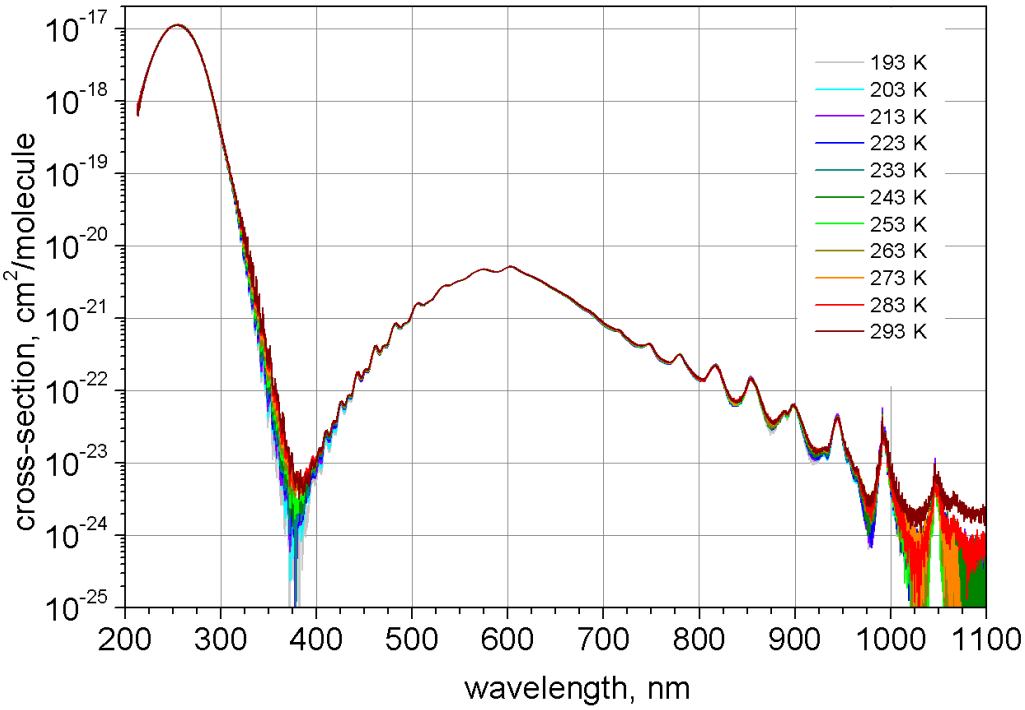

Figure 4.3. *Overview of the new ozone cross-sections data in the UV/VIS/NIR measured at 11 temperatures ranging from 193 K to 293 K*

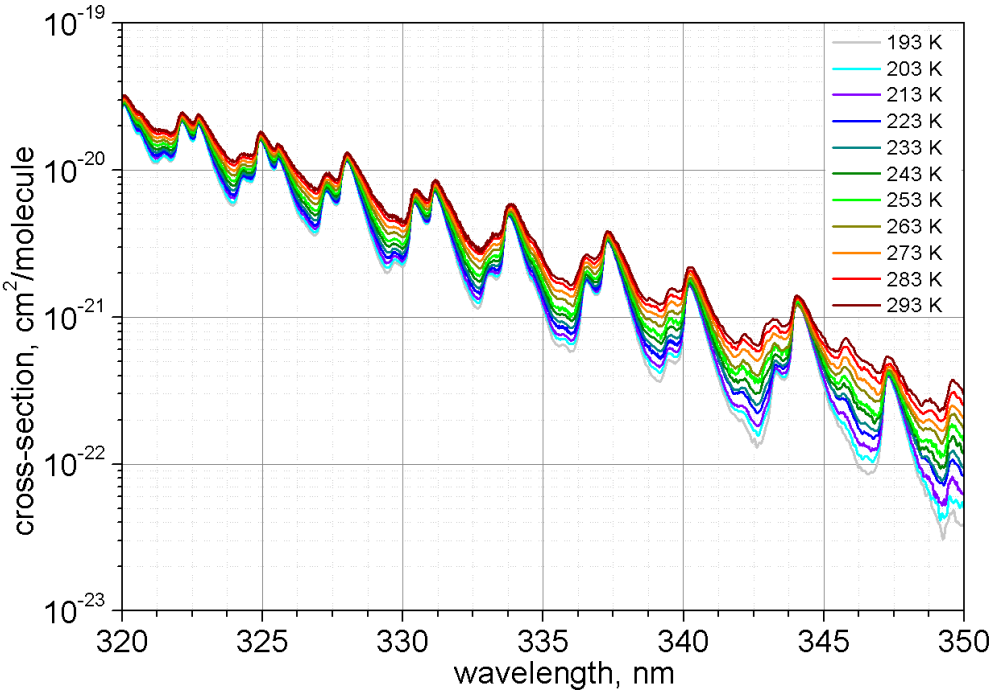

Figure 4.4. *New data near the DOAS window (325-335 nm) for all measured temperatures.*

The new ozone absorption cross-sections for room temperature in the entire measured region are shown in Figure 4.5 together with the high-resolution BMD dataset **/Brion et al., 1998/** and lower resolution satellite spectrometer datasets obtained by **/Burrows et al., 1999a/** and **/Bogumil et al., 2003/**. Figure 4.5 also shows the single wavelengths where cross-section were obtained by **/El Helou et al. (2005)/**, **/Axson et al., 2011/**, and **/Anderson et al., 1993/**.

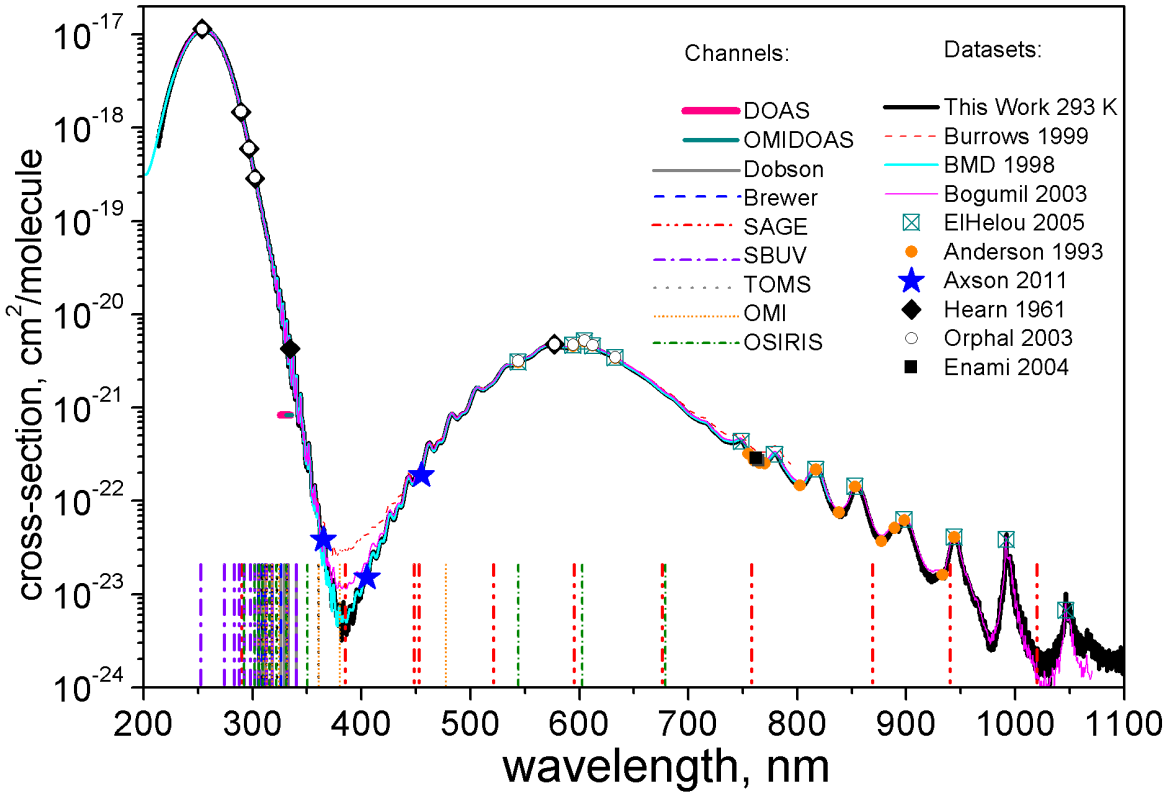

Figure 4.5. *Ozone absorption cross-section at room temperature (293 K).*
Notations for datasets and instruments: see legend.

The vertical drop lines (Figure 4.5) schematically mark the single wavelengths used in retrieval algorithms of the spectra obtained by different ground based and remote sensing instruments for detection of O_3, trace gases, clouds and aerosols (SBUV, OMI, TOMS, OSIRIS, SAGE, Brewer, Dobson). Despite the fact that majority of observations are performed in the UV spectral region, there are important channels in visible and IR as well.

4.2.1. Band-integrated cross-sections at 293 K

The integrated absorption cross-sections over an electronic band are only dependent on the number of molecules in the lower state and the transition probability **/Burrows et al. 1999a/**. Absorption cross-section of ozone rapidly decreases away from the band maximum; therefore the integrated band intensity is weighted to the largest values of the absorption cross-sections.

Consequently, comparisons of the integrated cross-sections reflect mainly the knowledge of the cross-sections close to the maximum of the bands. In addition, the spectral bands overlap (e.g., the high-energy tail of the Huggins band continuously goes over into the Hartley band system). Nevertheless, the method is a valuable test of agreement between the broadband absorption cross-sections datasets having different spectral resolution.

/Orphal, 2003/ proposed integration limits which were found from pragmatic considerations such as the quality of the considered datasets rather than the real band borders, determined by the theoretical studies **/Grebenshchikov et al., 2007; Banichevich et al., 1993/**. For comparison purposes, in this work the same limits were used. In the Wulf band, the integrated absorption cross-sections for the new data and **/Bogumil et al., 2003/** data were calculated using the 663 – 1000 nm range **/Banichevich et al., 1993/**.

Table 4.7 presents the values of the integrated absorption cross-sections obtained from this work, the high spectral resolution BMD dataset, the different satellite instrument datasets and the mean values obtained by **/Orphal, 2003/** from averaging of several data sources (**/Bass and Paur, 1985/**; **/Brion et al., 1998/**; **/Voigt et al., 2001/**; **/Bogumil et al., 2003/**; **/Burrows et al., 1999a/**). The uncertainty of this mean value is the standard deviation from averaging. The new absorption cross-sections agree with all datasets within 1% in the Hartley and Huggins bands, within 1-4% and 6% in the Chappuis and Wulf bands. Agreement with high resolution BMD dataset is about 1% and better.

Table 4.7. *Integrated cross-sections, and their ratios (in brackets) to the new dataset.*

	Temperature				
	295 ± 3 K	273 ± 3 K	243 ± 3 K	221 ± 3 K	203 ± 1 K
Dataset					
Hartley band (245 – 340 nm), x 10^{-16} cm^2/molecule x nm					
BMD, 1993-1998	3.52 (1)	-	3.50 (0.99)	3.49(0.99)	-
Bass and Paur, 1984	3.55 (1.01)	3.54 (1)	3.54 (1)	3.53 (1)	-
Guer et al., 2005, Chehade et al., 2012	3.56 (1.01)	3.56	3.56	3.56	3.56
Bogumil et al., 2003	3.56 (1.01)	3.55 (1.01)	3.54 (1)	3.53 (1)	3.53 (1)
Burrows et al., 1999	3.57 (1.01)	3.57 (1.01)	3.57 (1.01)	3.56 (1.01)	3.56 (1.01)
J. Orphal, 2003	3.55 (1.01)	3.55 (1.01)	3.54 (1)	3.53 (1)	3.53 (1)
This work	*3.53*	*3.53*	*3.53*	*3.54*	*3.52*
Huggins band (325 – 340 nm), x 10^{-20} cm^2/molecule x nm					
BMD, 1993-1998	8.30 (1)	7.12 (0.96)	6.16 (0.98)	5.74 (0.99)	-
Bass and Paur, 1984	8.20 (0.99)	7.27 (0.98)	6.21 (0.99)	5.65 (0.98)	5.44 (1)
Guer et al., 2005	8.40 (1.01)	7.58 (1.02)	6.59 (1.04)	6.15 (1.06)	5.91 (1.06)
Chehade et al., 2012	8.20 (0.99)	7.38 (1)	6.41 (1.02)	5.97 (1.03)	5.73 (1.05)
Bogumil et al., 2003	8.31 (1)	7.46 (1.01)	6.24 (0.99)	5.93 (1.03)	5.58 (1.02)
Burrows et al., 1999	8.33 (1)	7.69 (1.04)	6.38 (1.02)	5.94 (1.03)	5.69 (1.04)
J. Orphal, 2003	8.30 (1)	7.42 (1)	6.30 (1)	5.89 (1.02)	5.64 (1.03)
This work	*8.29*	*7.41*	*6.28*	*5.77*	*5.46*
Chappuis band (410 – 690 nm), x 10^{-19} cm^2/molecule x nm					
BMD, 1998	6.29 (1.01)	-	-	-	-
Guer et al., 2005	6.34 (1.02)	6.33 (1.02)	6.30 (1.02)	6.30 (1.02)	6.28 (1.02)
Chehade et al., 2012	6.34 (1.02)	6.33 (1.02)	6.29 (1.02)	6.23 (1.01)	6.28 (1.02)
Bogumil et al., 2003	6.40 (1.03)	6.42 (1.04)	6.35 (1.03)	6.32 (1.03)	6.41 (1.05)
Burrows et al., 1999	6.45 (1.04)	6.58 (1.06)	6.44 (1.05)	6.54 (1.06)	6.61 (1.08)
J. Orphal, 2003	6.38 (1.03)	6.44 (1.04)	6.35 (1.03)	6.35 (1.03)	6.48 (1.06)
This work	*6.22*	*6.2*	*6.16*	*6.15*	*6.13*
Wulf band (663 – 1000 nm), x 10^{-19} cm^2/molecule x nm					
Bogumil et al., 2003	1.099(1.06)	1.08(1.05)	1.06(1.05)	1.044(1.04)	1.06(1.07)
This work	*1.040*	*1.030*	*1.009*	*1.003*	*0.988*

4.2.2. Hartley and Huggins bands

The Hartley and Huggins bands (Figures 4.6.1, 4.6.2) are especially important for the remote sensing of the atmosphere, since they contain spectral channels used by both the satellites and the ground-based spectrometers.

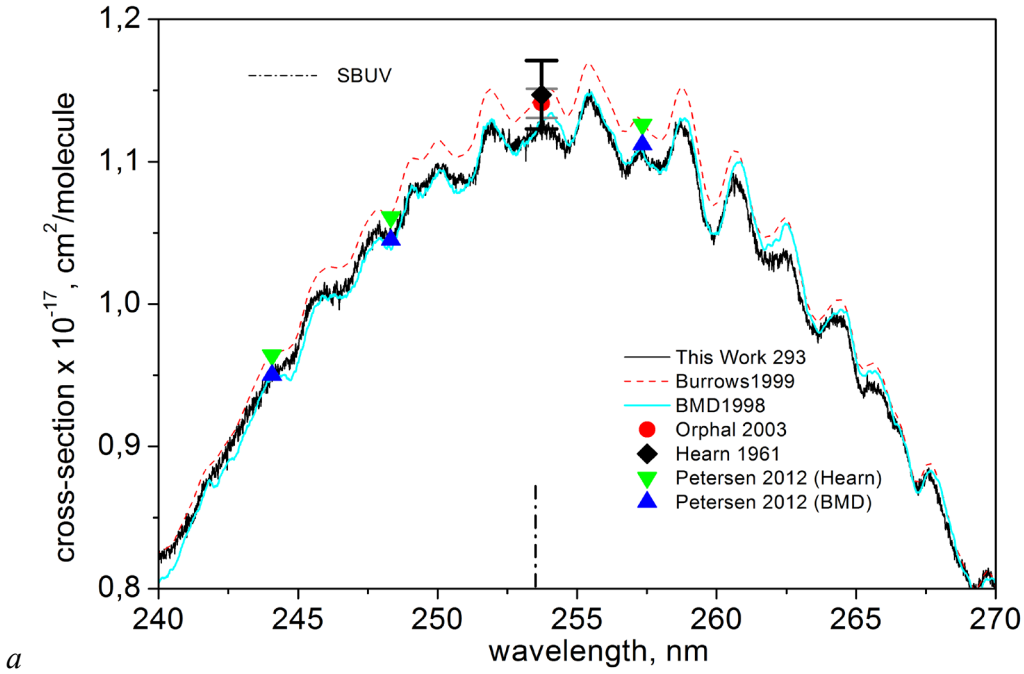

a

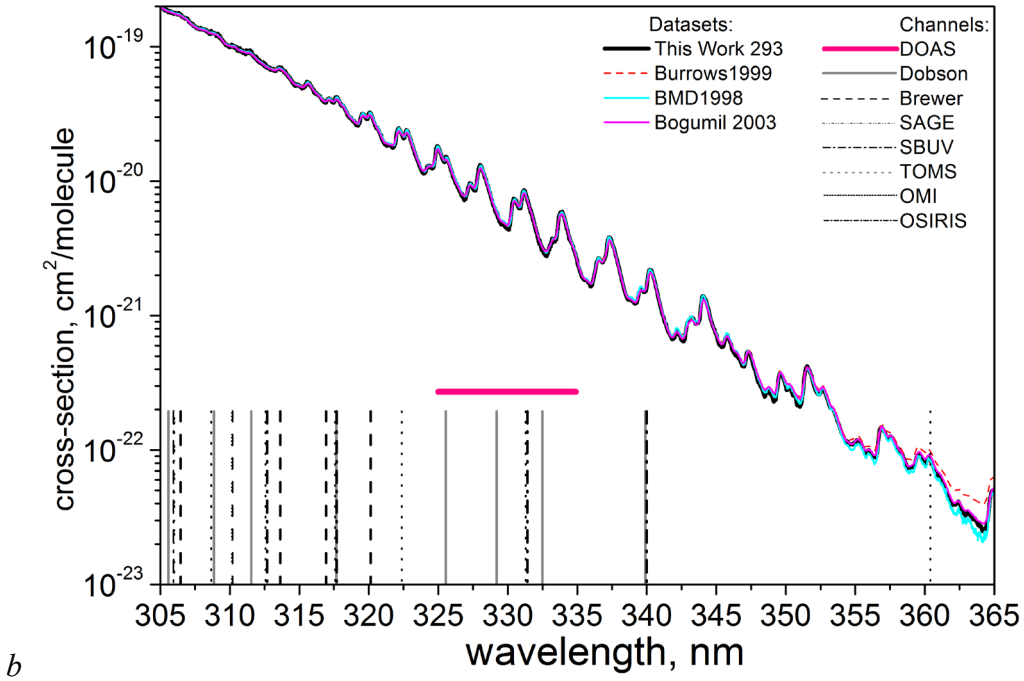

b

Figure 4.6.1. *Ozone absorption cross-sections in the UV region*
(a) *Hartley band, 293 K*
(b) *Huggins band, 293K. Notations for datasets and spectral channels are the same as in Figure 4.5*

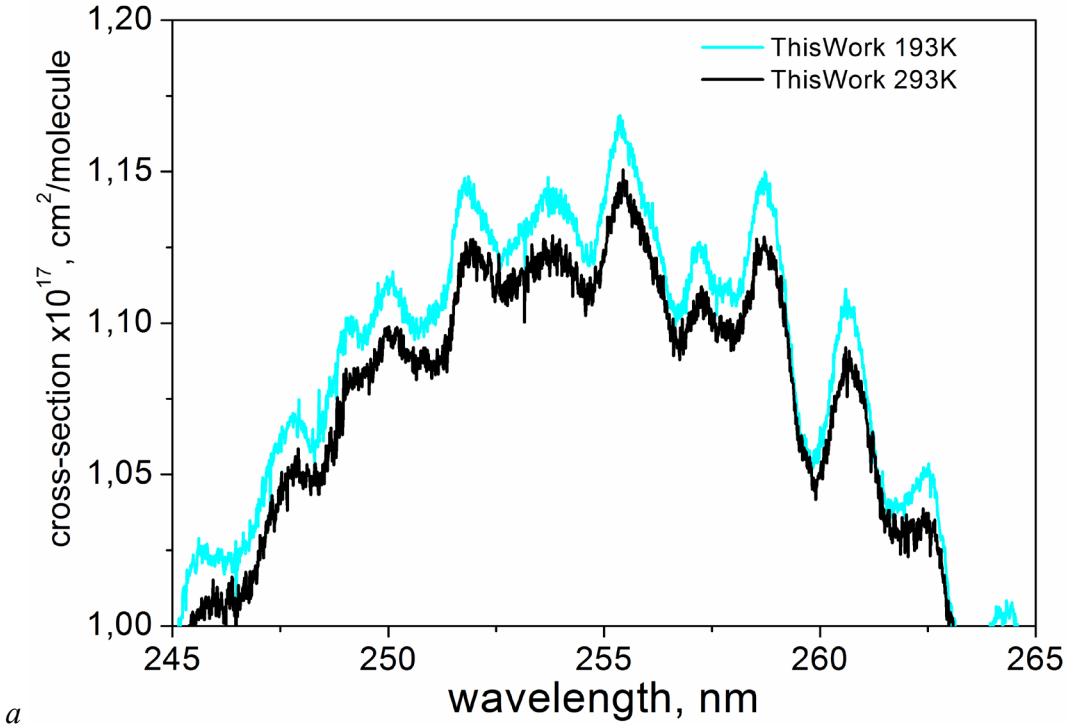

a

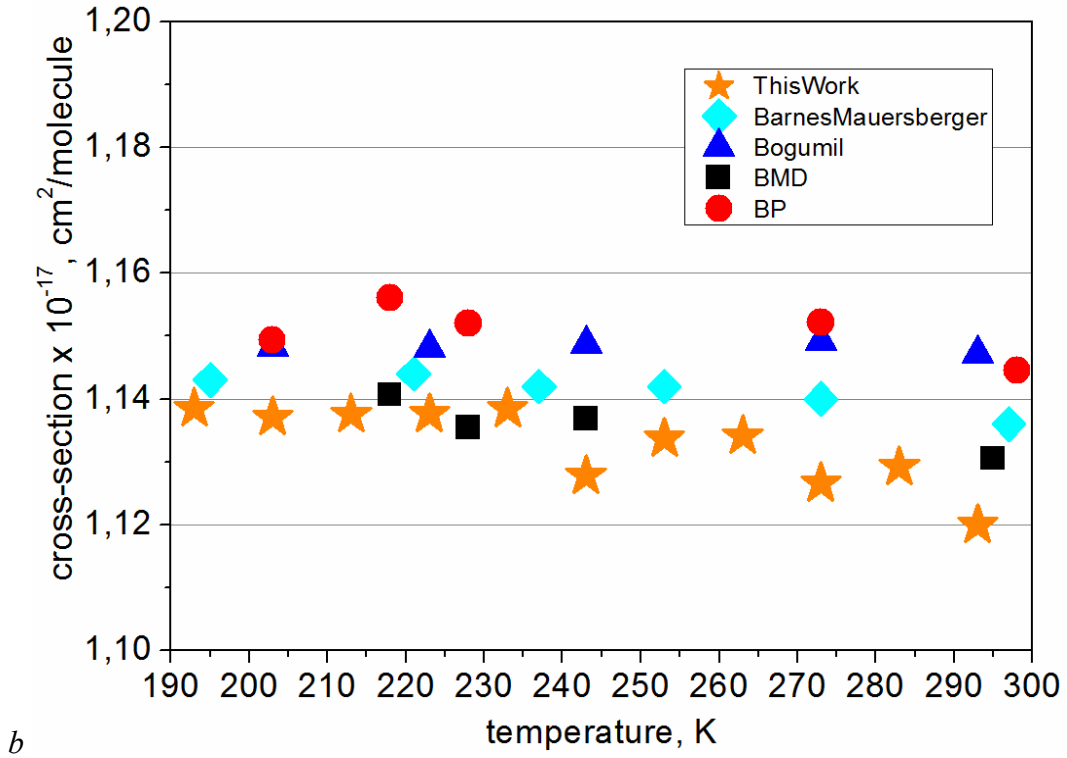

b

Figure 4.6.2. *Ozone absorption cross-section at different temperatures in the UV region*
(a) *cross-sections for 293K (dark line) and 193K (light line);*
(b) *temperature dependence at 253.65 nm. Stars - new data; diamonds - Barnes and Mauersberger (1987); triangles – Bogumil et al. (2003); squares - BMD; circles – BP.*

4.2.2.1. Spectral region near 255 nm

Several datasets in the region around 255 nm are shown in Figure 4.6.1a. The uncertainty reported by Hearn is about 2%. In general, the new absorption cross-sections are lower by several percent compared to the satellites and BP datasets. Agreement with the BMD dataset is within 1%. In Table 4.8, the new data are compared with some published data and the mean values by **/Orphal, 2003/** at selected wavelengths, corresponding to the Hg lamp and the He-Ne lines. Some of the data were interpolated. As mentioned above, the uncertainty of the Orphal's mean data is the standard deviation from averaging over several data sources, each having its own accuracy. Near the 300 nm the new data agree with most of the other datasets within 1–3 %. This is a region of overlap between the spectra obtained with Echelle and FT spectrometers used in this study. Recently, **/Petersen et al., 2012/** measured the cross-sections at three wavelengths using an argon-ion laser with an experimental combined relative uncertainty of 0.085%. For absolute scaling, values at 253.65 nm obtained by BMD and Hearn were used, which, in fact, limit the total accuracy to about 1.5–2%. Agreement between the new absorption cross-sections and those of Petersen et al. obtained by scaling with BMD and Hearn values is within 1% and 2%, respectively.

Table 4.8. *Absolute absorption cross-sections in UV at 295 ± 3K, cm^2/molecule $x10^{-20}$.*

wavelength, nm vacuum (air)	Orphal (2003)	***New data***	Hearn (1961)	BMD (1998)	Burrows et al. (1999)	Bogumil et al. (2003)	Petersen et al. (2012) using Hearn/BMD value
244.06	-	*946*	-	949	964	965	964/950
248.32	-	*105.1*	-	103.8	106.3	106.3	106.1/104.5
253.73 (253.65)	1141 ±0.9%	*1120*	1147	1131	1150	1147	-
257.34	-	*1107*	-	1107	1129	1126	1126/1112
289.44 (289.36)	149 ±2.0%	*151*	147	151	151.6	150	-
296.82 (296.73)	60.3 ±1.6%	*61.1*	59.71	61.5	61.4	60.9	-
302.24 (302.15)	29.2 ±1.8%	*29.6*	28.60	29.8	29.9	29.5	-

4.2.2.2. Spectral region 323 - 340 nm

Analysis of temperature dependence in Huggins band

The new cross-section data at eleven temperatures in the Huggins band are shown in Figure 4.7a.

The analysis of the temperature dependence of the new ozone absorption cross-section was made in the spectral channels of two ground-based instruments: Dobson and Brewer spectrophotometers **/Scarnato et al., 2009/**. The channels

fall on the maxima and minima of the spectral features in the 305–340 nm region (wavelengths are indicated in Figure 4.7a). For a rough resolution matching with the instrumental slit functions, new dataset was convolved to 1 nm and 0.4 nm using a rectangular slit function for analysis at Dobson and Brewer wavelengths, respectively. In addition, the temperature behaviour was investigated at initial spectral resolution of about 0.02 nm at 328 nm and 330 nm, which are local absorption minimum and maximum.

The Bass-Paur parameterization empirically describes the temperature dependence of the cross-sections in the DOAS window as a second order polynomial **/Paur, Bass, 1985/**.

Commonly used equation for the temperature dependence of the cross-section is

$$\sigma(\lambda,T) = 10^{-20} \cdot [C_0(\lambda) + C_1(\lambda)\cdot T + C_2(\lambda)\cdot T^2] \qquad (4.21)$$

where T is the temperature in degrees Celsius and C_0, C_1 and C_2 are wavelength-dependent fitting coefficients.

Using the original BMD data at four temperatures (218, 228, 243, and 295 K), **/Liu et al., 2007/** derived polynomial coefficients for temperature dependence for vacuum wavelength scale (BMD_{calc}), thus making possible the interpolation/extrapolation of the cross-sections to any given temperature.

The deviations of the new cross-sections from the polynomial fits at wavelengths described above are shown in Figure 4.7b (maximal deviations are given in brackets). The quadratic polynomial (4.21) describes the temperature dependence for most wavelengths to within 1.5%, which is within the experimental uncertainty. Generally, wavelengths near the ozone absorption maxima exhibit smaller deviations.

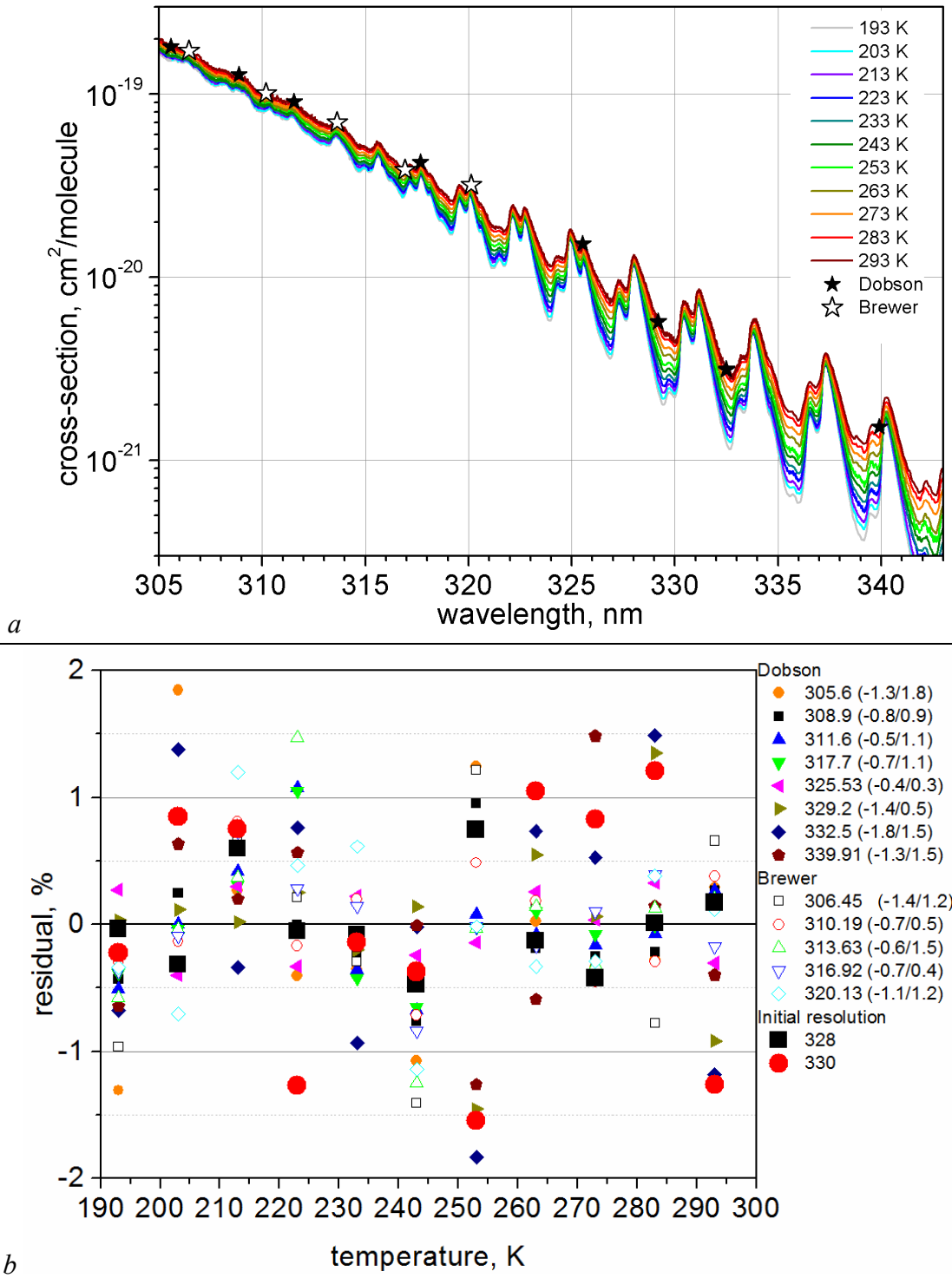

Figure 4.7. *Temperature dependence of the ozone absorption cross-sections:*
(a) *ozone cross-sections data in the Huggins band as measured in this study;*
(b) *residuals from the polynomial fit for the temperature dependence in the Huggins band.*
Small closed and open symbols – Dobson and Brewer spectral channels, respectively; big closed squares and circles – data at 328 nm and 330 nm. Numbers is brackets represent the maximal deviations.

Figure 4.8 (upper panel) demonstrates the difference between the experimental data and calculated data for two temperatures: 193 K and 293 K. Deviations are generally less than 2%. In principle, the calculated data have better signal-to-noise level compared to the experimental ones, as artefacts from measurements at a single temperature are smoothed out.

Differences between the $C_0(\lambda)$ coefficients ($C_0(\lambda)$ effectively being the absorption cross-sections values at 273 K) reported by several researchers are shown in the lower panel in Figure 4.8.

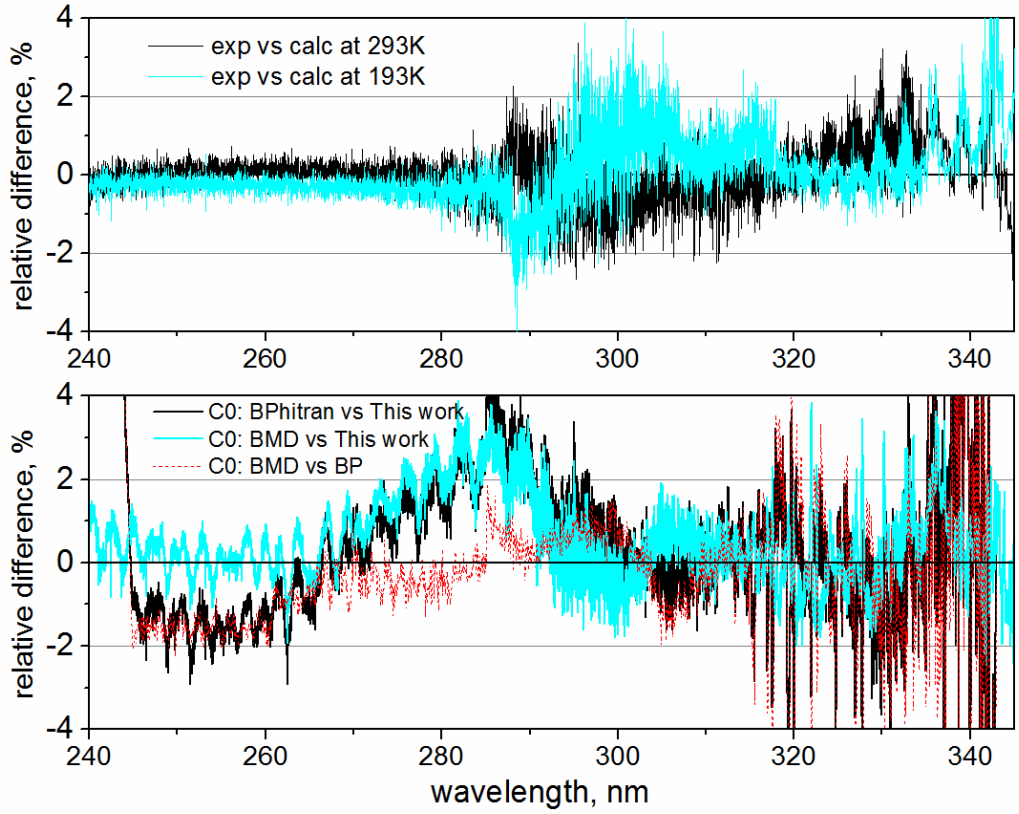

Figure 4.8. *Temperature dependence of the ozone absorption cross-sections.*

Upper panel - difference between the experimental and calculated (4.21) values for 193 K and 293 K (light and dark lines).

Lower panel - difference between fitting coefficients C_0 in (4.21) from this work and BP (dark line) and BMD (light line), and between BP and BMD (dashed line).

Comparison with other datasets at room temperature

Datasets comparison in the Huggins band is complicated due to the sharp structures, which are very sensitive to the spectral resolution of the dataset and temperature. For analysis of the scaling factors and wavelength shifts in the 323–343 nm region, **/Orphal, 2003/** compared different broadband databases convolved assuming a Gaussian profile with a 0.4 nm FWHM using a non-linear least squares fitting algorithm.

/Orphal, 2003/ found that the BP data show systematic wavelength differences compared to the FTS data of **/Voigt et al., 2001/** and need to be shifted to longer wavelengths (+0.029 nm) with a scaling factor of 0.956. **/Orphal, 2003/** also reports the systematic wavelength differences between the BMD and other datasets. He found a jump in the BMD wavelength calibration around 331 nm, making it difficult to determine a single wavelength shift coefficient in the 323–343 nm region. Assuming a linear shift, **/Orphal, 2003/** determines that BMD is shifted towards shorter wavelengths (–0.014 nm) compared to the **/Voigt et al., 2001/** data.

Following a similar approach, a comparison of the new data with the published datasets was made. Note that nowadays several slightly different versions of the datasets are available. Below is a short reference overview and notations used in this study. The MPI online database **/Keller-Rudek and Moortgat, 2013/** contains experimental BP and BMD datasets for different temperatures at air wavelengths (BP_{exp} and BMD_{exp}) obtained in 2000 and in 1998, respectively. The same experimental BMD data can be found on the ACSO homepage **/ACSO/**. **/ACSO/** also provides polynomial coefficients (quadratic fits) BP_{calc} that have been calculated by Bass and Paur for the temperature dependence of the original data excluding the 218 K at air wavelengths, **/Paur, Bass, 1985/**. HITRAN 2008 also contains polynomial coefficients (BP_{HITRAN}); however, a few corrections were made on the original BP data: air/vacuum wavelength conversion according to Edlen's equation **/Edlen, 1966/** and wavelength shift.

Versions of the BP and BMD datasets from the sources mentioned above, as well as **/Voigt et al., 2001/** and **/Bogumil et al., 2003/** datasets from the homepage of the Molecular spectroscopy group of the Institute of Environmental Physics were used for comparison. To avoid alteration of the original data when possible, comparisons were performed with the high-resolution BP, BMD and **/Voigt et al., 2001/** datasets without resolution matching. For the comparison with **/Bogumil et al., 2003/** dataset, the new high-resolution dataset was convolved with the Gaussian profile with FWHM of 0.2 nm. All datasets were compared on the same grid of vacuum wavelengths in steps of 0.01 nm using Edlen's equation and interpolation.

The relative difference $\delta\sigma$ between datasets σ_1 and σ_2 was calculated in percent as a function of a scaling factor F and a linear wavelength shift $\delta\lambda$:

$$\delta\sigma(\lambda) = \frac{[\sigma_1(\lambda) - F\cdot\sigma_2(\lambda+\delta\lambda)]}{F\cdot\sigma_2(\lambda+\delta\lambda)} \cdot 100\% \qquad (4.22)$$

The analysis of the shifts and scalings was performed for three different spectral regions: 323–330 nm, 332–340 nm and the entire 323–340 nm. For every case, the mean was calculated over the region differences $\Delta\sigma$ between the different pairs of datasets and the optimum shifts and scaling factors were found by minimization of these mean differences. For comparisons with the new data, shifts and scaling were applied to the published datasets.

Comparison of the original experimental datasets may be controversial because the 'minima' in absorption features are sensitive to temperature. Even relatively small difference of ±5 K influences the absolute values. New absorption cross-sections and those of **/Voigt et al., 2001/** and **/Bogumil et al., 2003/** were

obtained at 293 K, whereas those of BP_{exp} and BMD_{exp} were made at 298 K and 295 K, respectively. Approximation of the absorption cross-sections by fitting a second order polynomial seems to be a reasonable solution: calculated for 298 K and 295 K, BP_{calc} and BMD_{calc} reproduce corresponding experimental BP_{exp} and BMD_{exp} data very well; mean differences are 0.3% for BP and 0.04% for BMD, scaling factors are 0.998 for BP and 1 for BMD. Using the polynomial coefficients to describe the temperature dependence reduces the differences between the datasets, also due to their smoothing effect.

To test the efficiency of this technique, some results of the analysis done by **/Orphal, 2003/** were reproduced. Similar scaling (0.96) and shift (+0.03±0.005 nm) were obtained between BP_{exp} and **/Voigt et al., 2001/** data. It was found that matching the BP_{calc} calculated for 293K to the **/Voigt et al., 2001/** dataset requires nearly negligible scaling (0.998), but requires the shift of +0.027±0.004 nm. This approach is also capable to reveal the shift of +0.015±0.0005 nm applied to the experimental BP dataset in the HITRAN 2008 version.

The mean relative differences, shifts, and scaling factors, which match the published datasets to the new data, are shown in Figure 4.9a. The uncertainties were obtained from averaging of the shifts over the 323–330 and 332–340 nm regions. The relative differences between the new absorption cross-sections and other relevant datasets are presented in Figure 4.9b. New absorption cross-sections are slightly lower than all the other datasets, but this difference is within the experimental error bar in most cases. Among experimental data, the new absorption cross-sections agree best with the **/Voigt et al., 2001/** and **/Bogumil et al., 2003/** datasets (Figure 4.9a): scaling factors are 0.99 and 0.995 and the mean difference is about 1%. A small wavelength shift of 0.005±0.002 nm was observed between **/Voigt et al., 2001/** and the new data, which exceeds the reported accuracy of the spectral calibration of the FTS (0.001 nm). Both measurements were performed under the similar conditions using the same instrument in the Bremen laboratory; however, the spectral resolution of the **/Voigt et al., 2001/** data is 5 cm^{-1}, whereas that of the new data is 1 cm^{-1}. The shift between **/Bogumil et al., 2003/** data and the new data is 0.006 ±0.004 nm. It was found that BP_{calc} and BP_{HITRAN} datasets agree with the new data within experimental uncertainty and show linear shifts of +0.023±0.003 nm and +0.008±0.003 nm, respectively; the shift of the BP_{exp} is +0.026±0.002 nm, which means that original BP data must be shifted towards longer wavelengths to match the new measurements.

Additionally, a non-linear wavelength calibration of the BMD dataset was observed in the 323–340 nm region: different shifts were found for the 323–330 and 332–340 nm regions. Assuming a mean linear shift, BMD_{calc} is shifted towards longer wavelengths relative to BP, **/Bogumil et al., 2003/** and the new datasets, while absolute values of the cross-sections agree within the experimental uncertainty (excluding BP_{exp}).

Possible biases between the original datasets in Figure 4.9b are masked by the deviations of up to 5%. The scaling and wavelength shifts reduce the relative difference to 0.5–2%. The remaining differences can be attributed to the noise in the measurements, non-linear wavelength differences, differences in the

instrumental slit functions, and slight resolution mismatch between the considered datasets.

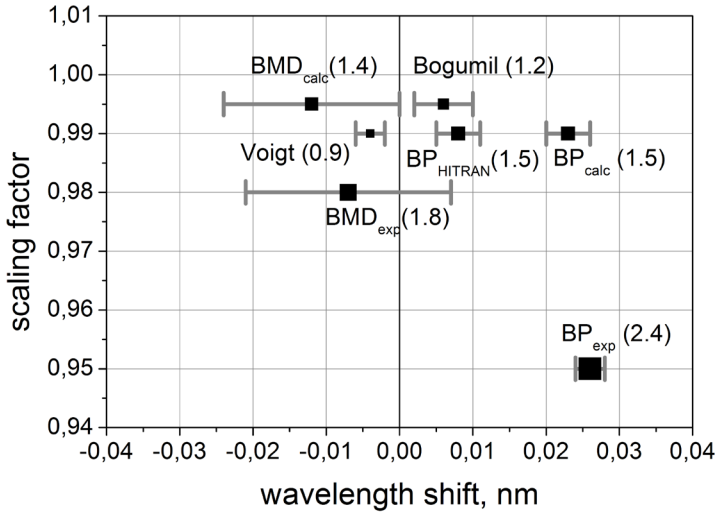

a

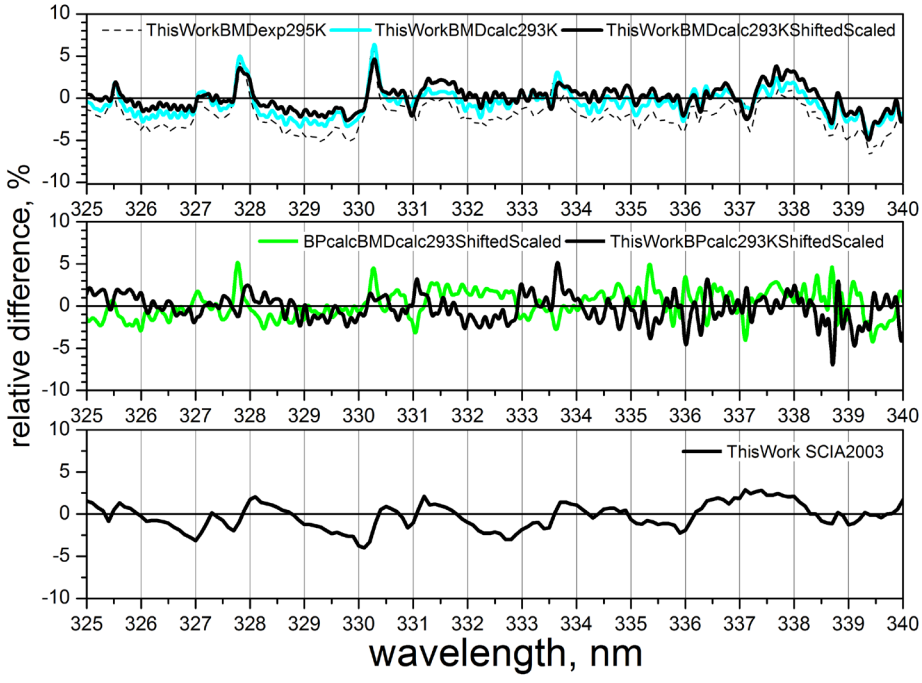

b

Figure 4.9. *Comparison of the absorption cross-sections in Huggins band:*

(a) scaling factors and wavelength shifts between the new data and other datasets, (size of the symbols is proportional to the mean relative difference in percent given in brackets);

(b) Upper panel: relative difference between the new data and BMD in percent.

dashed line – difference with BMD_{exp}, light line – difference with BMD_{calc}, dark line – difference with BMD_{calc} after wavelength shift and scaling.

Middle panel: relative difference between BP_{calc} and BMD_{calc} and BP_{calc} and new data in percent after wavelength shift and scaling.

Lower panel: relative difference between new data and Bogumil et al. (2003) in percent.

Apart from the analysis in the DOAS window, the new dataset was compared with the published datasets at the selected single wavelengths used by different ozone-observing instruments in the UV region. To accomplish that, the BP_{calc} and BMD_{calc} data (calculated for 293 K using the polynomial coefficients) and **/Bogumil et al., 2003/** data were used. Exhaustive comparison involves convolution of the datasets with instruments slit functions, which are not always well documented. For the purposes of resolution matching, the new dataset, **/Bogumil et al., 2003/**, BMD_{calc} and BP_{calc} datasets were convolved to 1 nm using a rectangular slit function for comparisons at SBUV, TOMS and Dobson wavelengths and to 0.4 nm for comparisons with OMI and Brewer wavelengths.

In the pair comparison (new–BMD_{calc}, new–BP_{calc}, and BP_{calc}–BMD_{calc}) it was found that the BMD, BP and the new data agree within the accuracy of the measurements (2%) for wavelengths below 320 nm. In general, the new data are close to the BMD dataset, but slightly lower. At 320–340 nm, the new dataset is lower by 2–3% and 2–7% compared to the BMD and BP, respectively.

Comparison with other datasets at multiple temperatures

In addition to analysis of the temperature dependence at wavelengths of Brewer and Dobson instruments (see above), detailed comparisons of the new cross-sections in the 325–340 nm spectral region with the high-resolution datasets (BMD, BP and **/Voigt et al., 2001/**) and the low-resolution **/Bogumil et al., 2003/** dataset were performed. Cross-sections were analyzed by determining the scaling factors and wavelength shifts between the considered datasets and the mean differences. Spectra were interpolated on a common wavelength grid, converted to vacuum wavelength and then shifted and scaled until the smallest mean difference over the spectral region was reached. For comparison with the low-resolution dataset by **/Bogumil et al., 2003/,** the new data were convolved with the Gaussian profile with FWHM of 0.2 nm. To check the linearity of the shifts and scaling factors, the analysis was performed for three different spectral regions: 323–330 nm, 332–340 nm and 323–340 nm and averaged values to obtain uncertainties.

The experimental BMD data were compared to the temperature parameterized BMD data obtained by **/Liu et al., 2007/** (see above) in order to provide an additional independent check for the uncertainty due to the assumption of the quadratic temperature dependence. The parameterized BMD spectrum deviates from the experimental BMD within the experimental accuracy limits both in absolute values and shifts. The mean difference in the 325–340 nm spectral region is about 1%. Therefore, in the following comparisons both the original and the parameterized cross-sections were used, which is practical in case of missing data at some temperatures. However, since the parameterization itself is a manipulation of the data, an effort was made to use the original BMP and BP datasets as extensively as possible.

Differences were also found between the parameterized BMD and the parameterized BP datasets, which are outside of the accuracy limits reported for both datasets. Wavelength shifts of 0.015–0.02 nm were also detected. Without

the shift corrections and scaling, the differences are up to 20% and more due to the sharp features in this spectral region, the mean over the region difference is 2–5%. After correcting for the wavelength shifts, the mean difference is about 1–3% with larger deviations at low temperatures.

The comparison of the new experimental data with the published datasets is shown in Figure 4.10. Here the wavelength shifts, the scaling factors and the mean differences in the 325–340 nm spectral region are depicted at different temperatures.

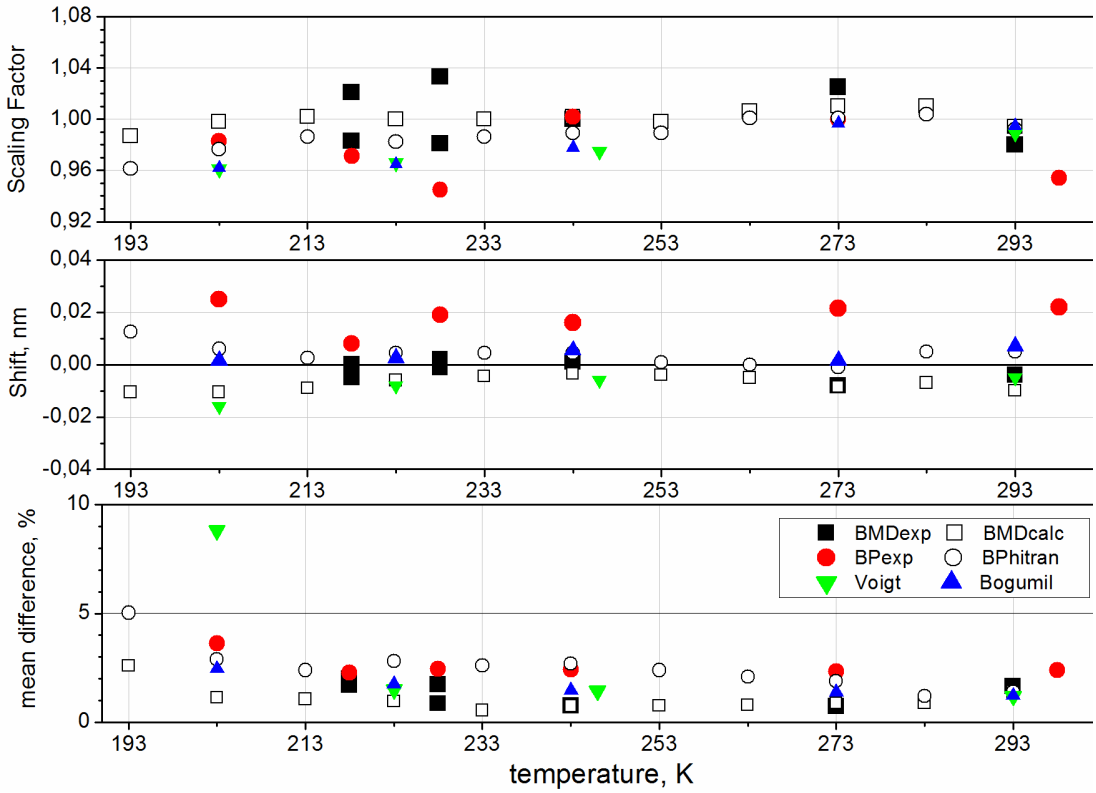

Figure 4.10. *Comparison of the results with BP, BMD, Voigt et al. (2001) and Bogumil et al. (2003) in the 325–340 nm window:*
Upper panel: scaling factors (to match other data to new data);
Middle panel: wavelength shift (to match other data to new data);
Lower panel: relative mean difference (other data after applying corrections for shifts and scaling factors minus new data).
Filled symbols - experimental data; open symbols - data obtained from the polynomial parameterization (4.21) Squares, circles, triangles - BMD, BP, Voigt et al. (2001) and Bogumil et al. (2003) datasets, respectively.

The scaling factors and the wavelength shifts were applied to the published datasets to match the new dataset. The remaining deviations after scaling and shifting are then due to non-linear spectral/wavelength calibration differences, differences in the instrumental slit functions and resolution mismatch between the datasets. In addition, slight mismatch of the temperatures has to be taken

into account when comparing the original experimental data in this region because of the high sensitivity of the Huggins band spectral features to the temperature. All mean differences are positive in Figure 4.10, because the absolute values of differences at every point were taken and averaged. This corresponds to the "worst case scenario" for mean differences, when summands are not compensating each other due to alternating sign (this happens when, for example, within the considered range two cross-section curves are intersecting).

The new data at 213 K were compared with the experimental BP data obtained at 218 K, as well as the new data at 223 K with BP data at 218 and 228 K. As a result, scaling factors were found of up to -6%, needed to minimize the differences which are also due to the temperature mismatch of 5 K. Wavelength shifts of 0.015–0.02 nm were observed between the BP and the new data (similar to that have been seen when comparing the BP to BMD), with the mean difference of about 2–3%, increasing to 4–5% at low temperatures. The HITRAN 2008 version accommodates the polynomial coefficients obtained for the BP data after wavelength correction performed based on the **/Voigt et al., 2001/** measurements. Comparison with the data calculated using these coefficients revealed scaling factors of 1% for most temperatures and a relatively small wavelength shift (0.005–0.01 nm).

Duplicate points in Figure 4.10 for two temperatures (218 K and 228 K) designate the differences between experimental BMD data at those temperatures and the new experimental data at adjacent temperatures of 213 K, 223 K, and 233 K. The new data at 213 and 223 K was compared to the experimental BMD data at 218 K, and the new data at 223 and 233 K to the BMD data at 228 K, and scaling factors of ±2% needed for minimizing the differences were found. Small mean shifts of 0.005 nm and less are observed for the 323–340 nm window between the new data and the experimental BMD. However, real shifts are non-linear because different wavelength shifts were found for smaller regions at 323–330 nm and at 332–340 nm. The same was reported by **/Orphal, 2003/**. The mean relative difference is about 1–2% at 325–340 nm, which is within the experimental accuracy limits. The calculated BMD data agree with the new experimental data within accuracy limits both with respect to the absolute values and the spectral shifts. Small spectral shifts were found between the new data and the **/Voigt et al., 2001/** and **/Bogumil et al., 2003/** data. **/Bogumil et al., 2003/** and **/Voigt et al., 2001/** data exceed the new data by 1–4%.

At wavelengths shorter than 325 nm, the wavelength shift seems to be less important; however, it still influences the agreement between the BP and other data. The BP data at low temperature deviate from both the BMD and the new data. In the 315–325 nm region, the mean difference between the parameterized BMD and BP datasets is 1.4 to 5.7% depending on the temperature. Agreement can be slightly improved (mostly for room temperature) to 0.6–5.4% using the wavelength shifts. The new data differ from the BMD and BP data by 0.9–1.9% and 1.5–5.4%, respectively, with stronger deviations corresponding to the data at low temperature. When wavelength correction is used, only insignificant improvement can be achieved: down to 0.7–1.7 % and 0.7–5% for BMD and BP, correspondingly. During this correction, wavelength shifts of 0.015–0.03 nm (depending on temperature) were applied to the BP to match the new data, and

shift of about 0.008 nm (almost independent of the temperature) applied to the BMD to match the new data. Small scaling correction of about 1.5% further decreases the mean difference between the BMD and the new data down to 0.3–1.4%.

4.2.3. Chappuis and Wulf bands

Satellite retrievals use the Chappuis and Wulf bands and adjoining Huggins and Chappuis bands for the ozone retrieval in limb and occultation experiments. In addition, accurate O_3 absorption cross-sections in this spectral region are necessary for the retrieval of other trace gases, aerosols and clouds. The relative differences between the new absorption cross-sections and published data are shown in Figure 4.11 and discussed in detail below.

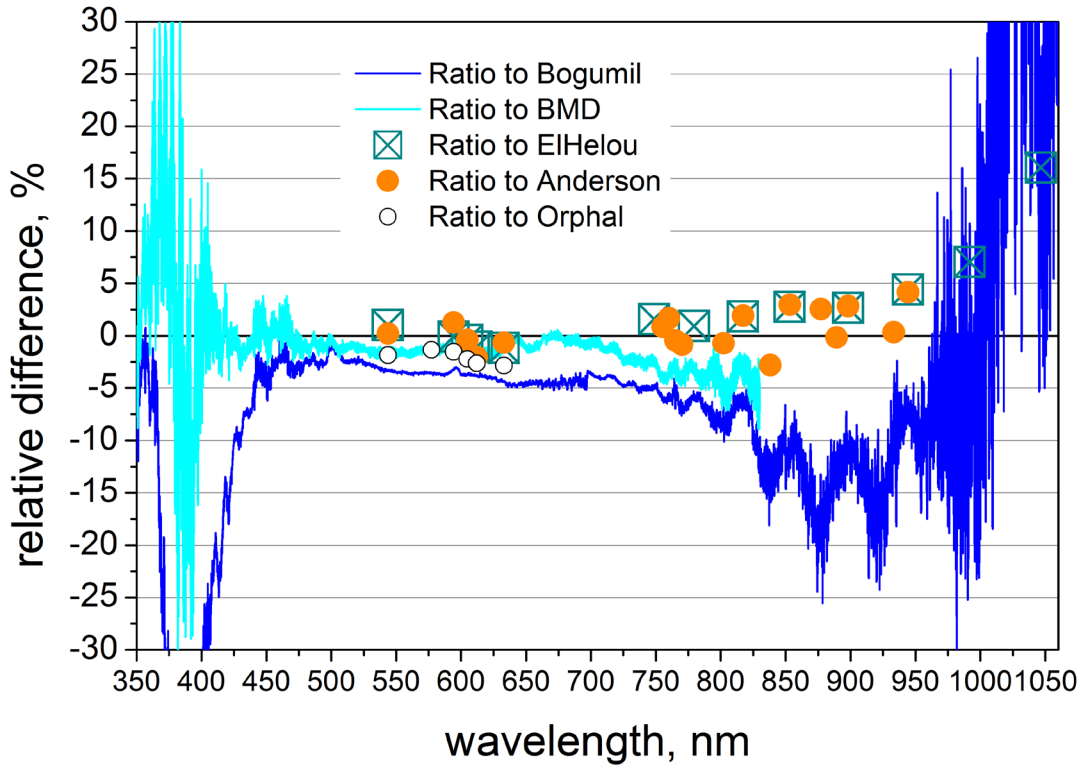

Figure 4.11. *Relative difference between the new cross-sections and published data in the Chappuis and Wulf bands.*

4.2.3.1. Minimum absorption region 350 - 450 nm

Few experimental data are available in the weak absorption region between the Huggins and Chappuis bands near 375 nm. The BP dataset does not cover this region. Figure 4.12 presents the new results along with the BMD and **/Bogumil et al., 2003/** data in this region. The BMD experimental data are only available down to 218 K and for all temperatures below that, the Bass-Paur temperature parameterization must be used. Cross-sections calculated using the temperature

coefficients obtained by **/Liu et al., 2007/** from the BMD experimental data drastically fall at 203 K. The low-resolution dataset by **/Bogumil et al., 2003/** overestimates the minimum absorption. Near the bottom of the weak absorption region (370–390 nm), the new data appears to be noisier than the BMD dataset.

Additional data are available from the measurements at single wavelengths recently performed by **/Axson et al., 2011/** using the incoherent broadband cavity enhanced absorption spectroscopy. These relative measurements scale directly with the choice of the reference cross-section value at 253.65 nm. For absolute calibration, **/Axson et al., 2011/** took the reference value reported by **/Orphal, 2003/** (Table 4.8). The reported accuracy of the **/Axson et al., 2011/** cross-sections is 4–30%, with the greatest uncertainty near the minimum absorption.

Various broadband datasets show large disagreement in the absorption minimum between the Huggins and Chappuis bands at 350–425 nm and especially near 380 nm as shown in Figure 4.11, Figure 4.12a and in Table 4.9. Data given in Table 4.9 were obtained at different spectral resolution as indicated by the numbers in brackets.

Table 4.9. *Absolute absorption cross-sections in minimum absorption region near 380 nm at 295 ± 3K, cm^2/molecule $x10^{-23}$; typical FWHM (nm) is given in brackets.*

wavelength, nm (vacuum)	***New data***	BMD (1998)	Burrows et al. (1999)	Bogumil et al. (2003)	Burkholder et al. (1994)	Axson et al. (2011)
365	*4.9 (0.02)*	4.74 (0.02)	6.26 (0.17)	5.11 (0.21)	-	3.68 (0.27)
405	*1.46 (0.02)*	1.47 (0.02)	4.27 (0.17)	2.12 (0.21)		1.51 (0.29)
455	*20.6 (0.02)*	20.4 (0.02)	22.9 (0.29)	21.4 (0.52)	18.2	18.8 (0.5)

The new absorption cross-section dataset agrees well with the BMD dataset and shows good agreement with the data of **/Axson et al., 2011/** within accuracy limits. There is a significant disagreement between the new dataset and **/Bogumil et al., 2003/** data in the region of the minimum absorption around 385 nm and in the IR region at 1020 nm. In both regions, the uncertainty of measurements is greater than 30% as a result of the very weak absorption measured.

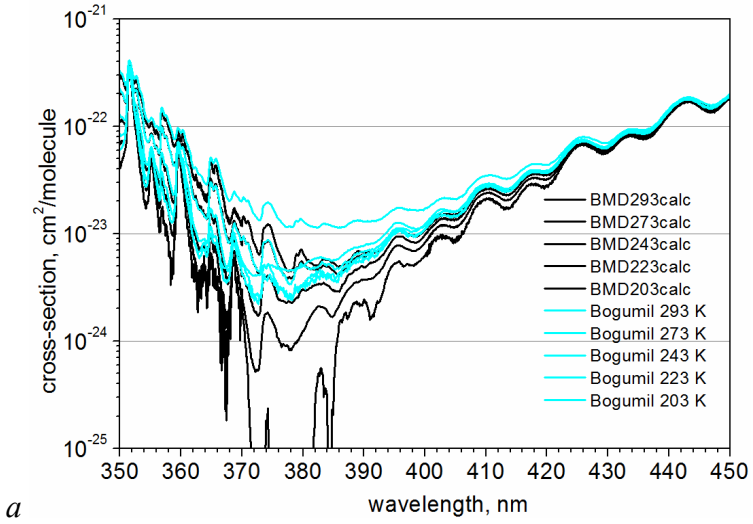

a

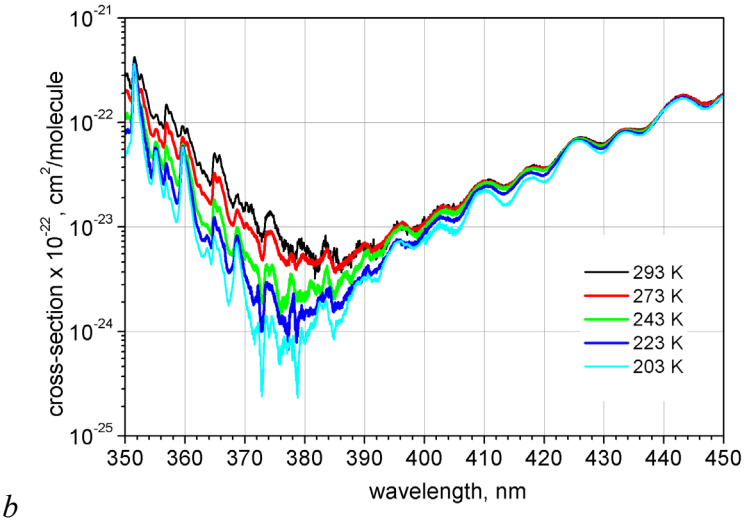

b

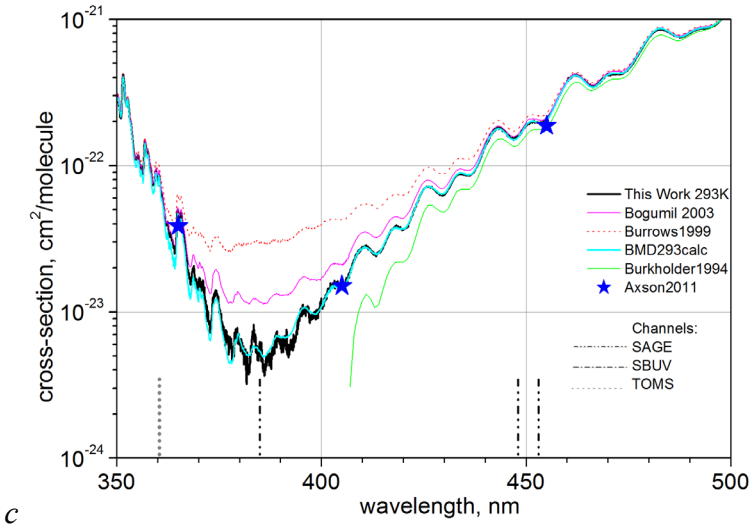

c

Figure 4.12. *Ozone absorption cross-sections near minimum between the Huggins and the Chappuis bands.*

(a) Bogumil et al. (2003) and BMD at different temperatures.

(b) New data at different temperatures.

(c) New data and other data at room temperature.

4.2.3.2. Visible region 450 - 700 nm

Several ozone absorption cross-section datasets are available in the visible region near the maximum of the Chappuis band (Figure 4.13). Absolute calibrated data of **/Anderson and Mauersberger, 1992/** were obtained using a tandem dual-beam spectrometer and pure ozone from the liquid nitrogen trap; reported overall uncertainty of these measurements is below 1%. Very recent absolute measurements performed by **/El Helou et al., 2005/** using a FT spectrometer were calibrated using the pure ozone as well, and have a reported uncertainty of 0.82%.

The values of cross-sections at the selected wavelengths from the different datasets are listed in Table 4.10 (in some cases the data were interpolated). The relative difference in percent between the new data and some published datasets is shown in Figure 4.11.

In general, the new absorption cross-section measurements agree well with those obtained by **/Anderson and Mauersberger, 1992/** and **/El Helou et al., 2005/** at the selected wavelengths (within about 1% or better). The new data agree within 1% or better for the broad 510–680 nm region with those reported by **/Burkholder and Talukdar, 1994/**, which were absolutely scaled using the data of **/Anderson and Mauersberger, 1992/**. Agreement with the BMD is also within the accuracy limits. Difference between the new data and the satellite datasets is about 2–3%, which is almost within their experimental accuracy. It is quite likely that the concatenation performed by **/Bogumil et al., 2003/** might have had an impact on the accuracy of the absolute calibration of this dataset in this spectral region.

Very weak temperature dependence was observed in the new measurements around 600 nm (about 1% between 193 K and 293 K), with a small increase of cross-sections with decreasing temperatures.

Table 4.10. *Absolute absorption cross-sections in Chappuis band at 295±3K, cm^2/molecule $x10^{-21}$.*

wavelength, nm vacuum (air)	J. Orphal, (2003)	***New data***	BMD (1998)	Burrows et al. (1999)	Bogumil et al. (2003)	Anderson et al. (1992)	Burkholder et al. (1994)	El Helou et al. (2005)
543.67 (543.52)	3.14 ±1.3%	*3.08*	3.12	3.17	3.16	3.075	3.11	3.051
577.12 (576.96)	4.77 ±0.8%	*4.70*	4.77	4.83	4.84	-	4.72	-
594.26 (594.10)	4.70 ±1.2%	*4.63*	4.68	4.76	4.74	4.569	4.66	4.631
604.78 (604.61)	5.22 ±1.0%	*5.10*	5.18	5.24	5.25	5.125	5.12	5.125
612.14 (611.97)	4.66 ±0.7%	*4.54*	4.63	4.69	4.68	4.633	4.52	4.586
632.99 (632.82)	3.46 ±1.2%	*3.36*	3.39	3.51	3.48	3.383	3.37	3.401

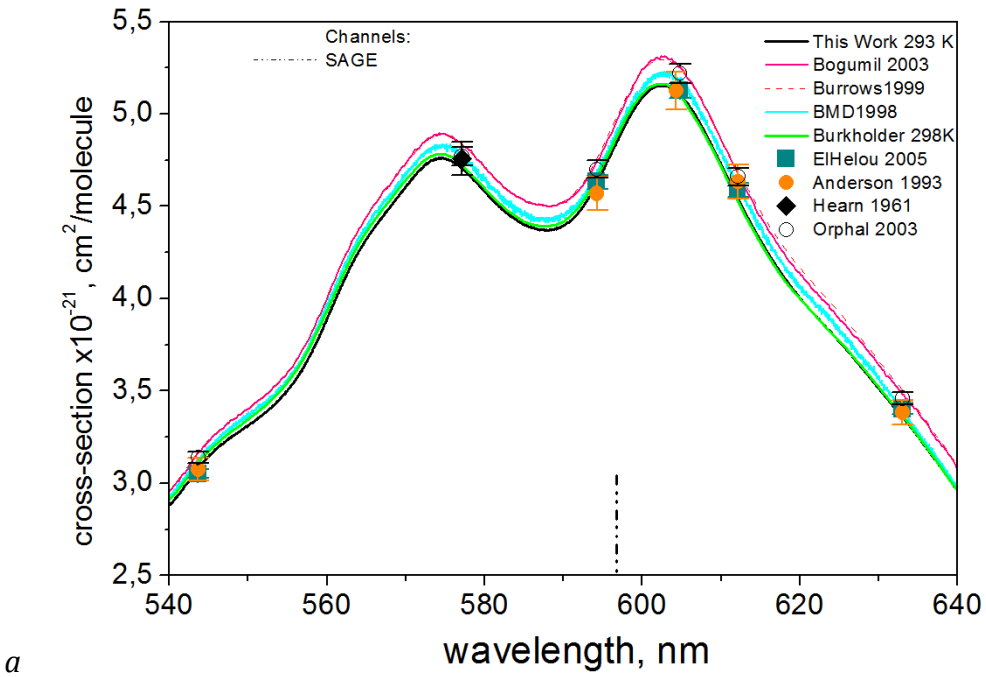

a

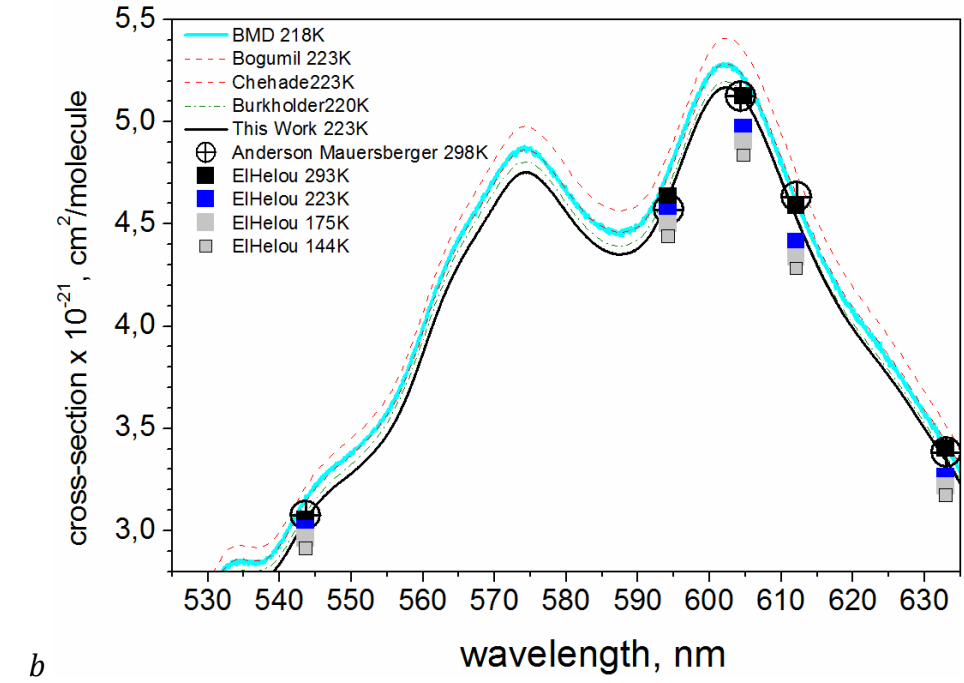

b

Figure 4.13. *Ozone absorption cross-sections near maximum of the Chappuis band.*

(a) Room temperature (293 K).

(b) Low temperatures. Symbols: squares - El Helou et al. (2005), circles – Anderson and Mauersberger (1992); lines: red dashed - Bogumil et al. (2003) and Chehade et al. (2012), light blue solid– BMD, green dash-dot– Burkholder et al. (1994), black solid – new data.

4.2.3.3. NIR region 700 - 1100 nm

Only few studies were performed below 293 K in the Chappuis (Figure 4.13.b) and the Wulf (Figure 4.14.2) bands, especially in the NIR region. The most extensive dataset obtained so far was reported by **/Bogumil et al., 2003/**. In the Chappuis band and NIR, the new data are lower than the **/Bogumil et al., 2003/** dataset (2–4.5% in the 540–850 nm region) and agree very well in the 540–630 nm region with the data of **/Burkholder and Talukdar, 1994/** (0.4–1%) which have reported accuracy of 1% and better for wavelengths longer than 450 nm. There is a good agreement between the new data and the data of **/El Helou et al., 2005/**; however, the latter show a reversed temperature dependence around 600 nm. Several datasets are compared in Table 4.11 at discrete wavelengths taken from **/El Helou et al., 2005/**.

Table 4.11. *Comparison of some ozone cross-sections datasets at low temperatures in the Chappuis band, x 10^{-22} cm^2/molecule.*

Wavelength, nm	El Helou et al., 2005		Burkholder et al., 1994 220 K	Bogumil et al., 2003 223 K	BMD, 1998 218 K	***New data,*** *223 K*
	222-223 K	150 K				
543.667	30.05	-	30.850	31.418	31.573	*30.530*
594.261	45.53	-	46.780	47.376	47.633	*46.335*
604.78	49.7	-	51.301	52.247	52.067	*51.101*
612.14	44.12	-	45.412	46.370	46.126	*45.259*
632.991	32.63	-	33.645	34.314	34.154	*33.462*

High spectral resolution BMD data in the Chappuis band are only available for 218 K. The new data are lower by 2–3%. BMD report a systematic uncertainty of 1.5% and random uncertainty of 0.9–2% in the visible/IR region. Therefore, there is a good agreement between the BMD and the new data.

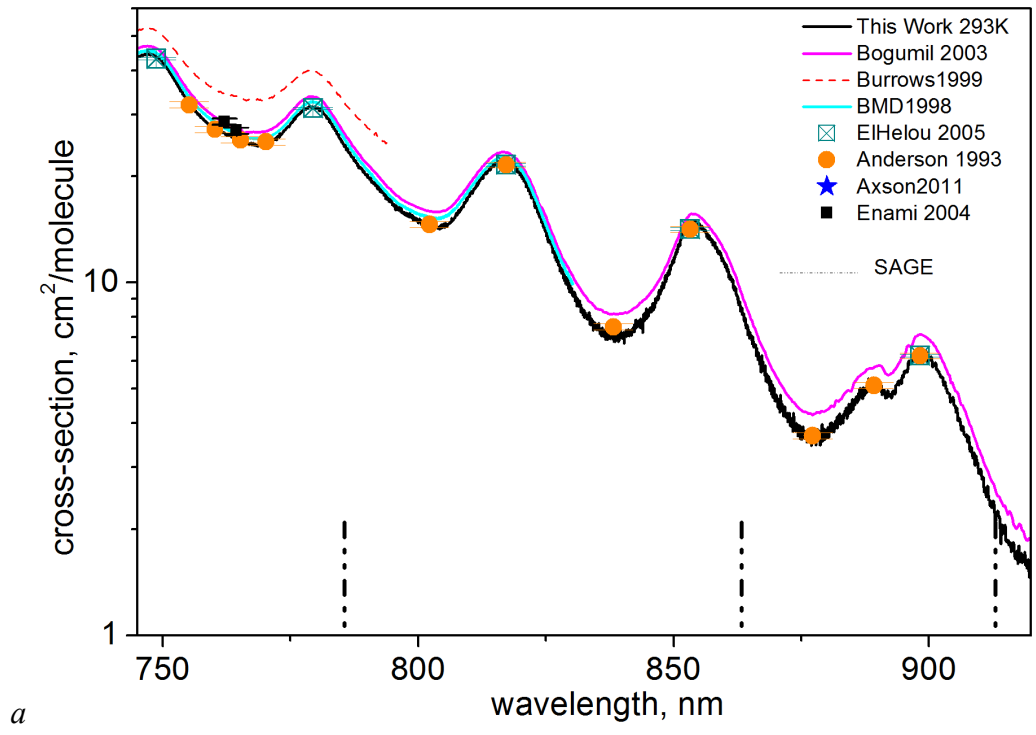

a

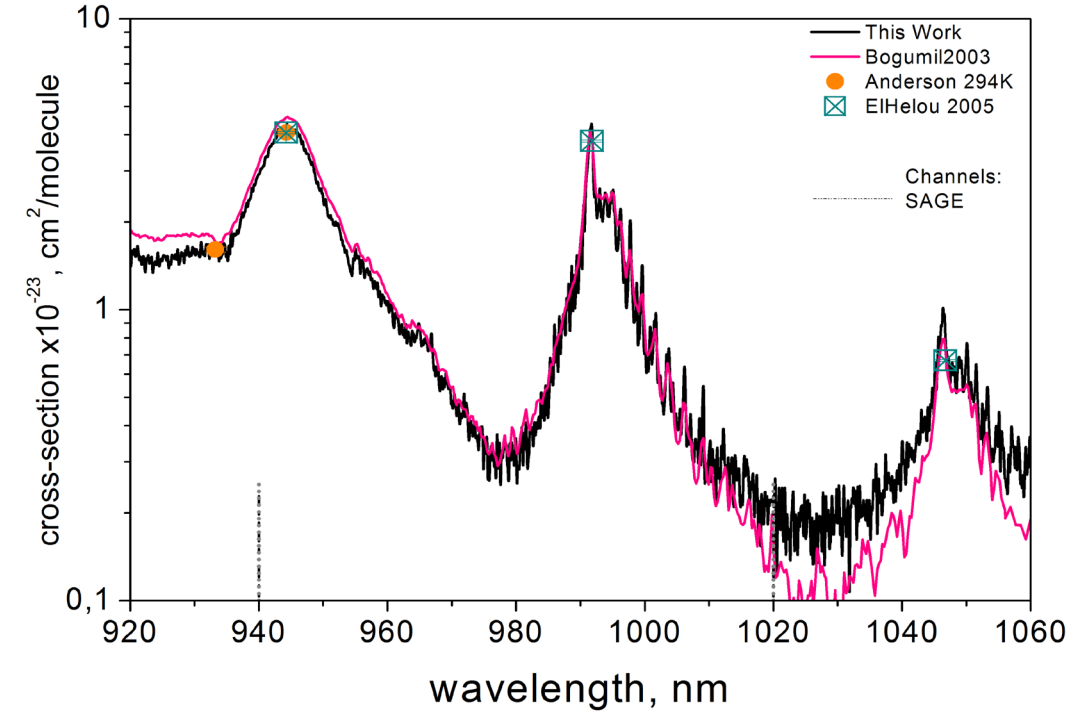

b

Figure 4.14.1. *Ozone absorption cross-sections datasets in the Wulf band:*
(a) *750-900 nm and* ***(b)*** *920-1060 nm ranges at room temperature.*

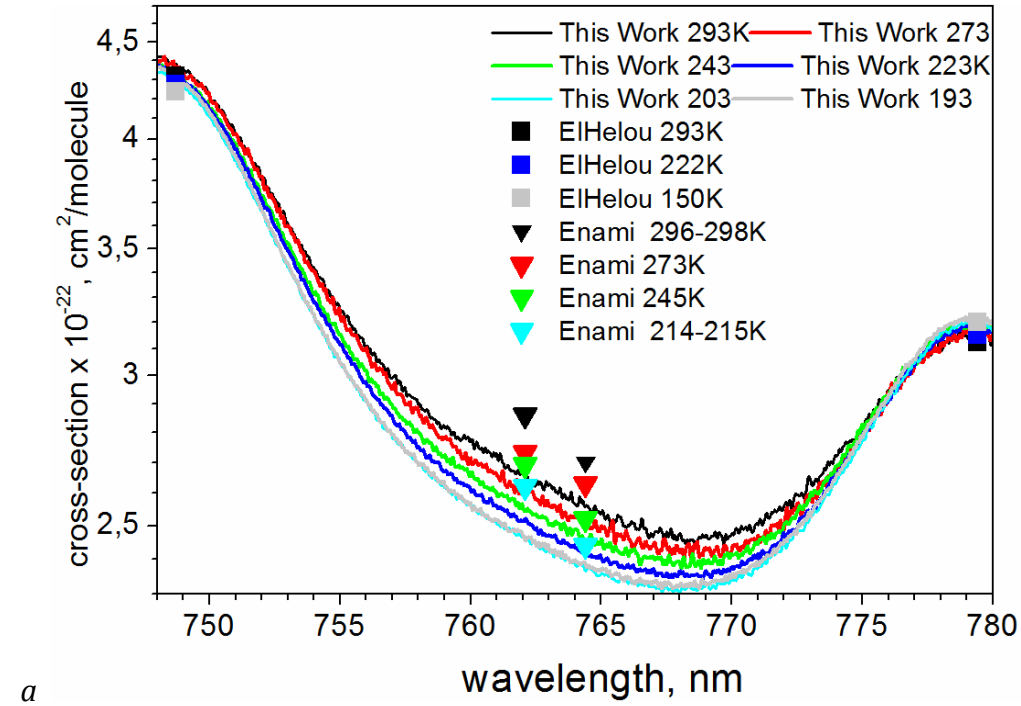

a

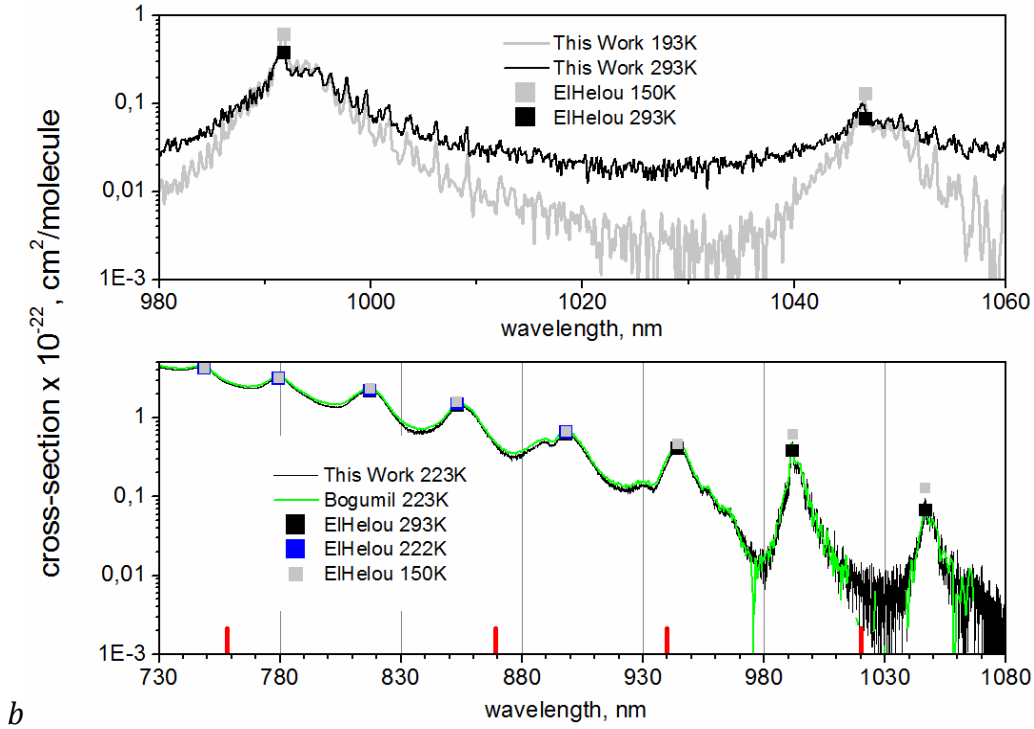

b

Figure 4.14.2 *Ozone absorption cross-sections datasets in the Wulf band:*

(a) *and* ***(b)*** *near 760 nm and 920-1060 nm at different temperatures. Squares -* **/El Helou et al., 2005/***, triangles -* ***/Enami et al., 2004/****, lines - this work and* ***/Bogumil et al., 2003/****.*

The spectral channels from SAGE II are indicated by short vertical lines.

Some of the datasets available in the near IR region are shown in Figures 4.14.1 and 4.14.2b. Data at selected wavelengths are compared in Table 4.12. Data of **/Anderson et al., 1993/** were absolutely calibrated using the absolute cross-section reported by **/Anderson and Mauersberger, 1992/**. In addition to the **/El Helou et al., 2005/** data, there are measurements performed by **/Enami et al., 2004/** at two single wavelengths at 760 nm using the cavity ring-down technique (Figure 4.14.2a). The absorption cross-sections of **/Enami et al., 2004/** were calibrated using the Hearn's value in the UV with the estimated total uncertainty of the O_3 concentration of ±1.5% and the typical overall uncertainty is about ±2%. However, accuracy of the Hearn's value is not included in this uncertainty budget.

At wavelengths longer than 1050 nm the ozone absorption decreases rapidly. Because of the experimental limitations, the measured absorption in this region was weak and sensitive to the baseline stability. The uncertainty of the new measurements around 1000 nm is about 30% and more. Only a few studies on the O_3 absorption cross-sections are available in this region. Results from **/Anderson et al., 1993/** and **/El Helou et al., 2005/** show agreement with the new dataset within 5% at wavelengths below 1000 nm and up to 20% around 1040 nm (Figure 4.11, Figures 4.14.1b and 4.14.2b). Compared with **/Bogumil et al., 2003/**, the new dataset better resolves the rotational structure of the Wulf band. In general, the new dataset in the "valleys" near 970 nm and 1010–1040 nm are lower than the **/Bogumil et al., 2003/** dataset, partly because of the different spectral resolution. Further measurements in this region are of high interest and promising for both O_3 rotational spectra modelling and for use in satellite missions, for example for SAGE II and SAGE III **/SAGE III ATBD Team, 2002/**.

Table 4.12. *Absorption cross-sections in the NIR at 295 ± 3K, [cm^2/molecule $x10^{-22}$]*

Wavelength, nm (vacuum)	***New data***	BMD (1998)	Burrows et al. (1999)	Bogumil et al. (2003)	Anderson et al. (1993)	Burkholder et al. (1994)	El Helou et al. (2005)
748.721	*4.38*	4.48	5.19	4.62	-	4.25	4.314
755.21	*3.22*	3.36	4.04	3.47	3.194	3.26	-
760.21	*2.77*	2.86	3.52	2.95	2.720	2.80	-
765.21	*2.53*	2.62	3.33	2.72	2.539	-	-
770.21	*2.49*	2.58	3.31	2.69	2.509	-	-
779.416	*3.15*	3.25	3.99	3.37	-	-	3.121
802.22	*1.45*	1.53	-	1.60	1.462	-	-
817.224	*2.20*	2.26	-	2.34	2.157	-	2.159
853.234	*1.46*	-	-	1.56	1.417	-	1.420
877.24	*0.377*	-	-	0.422	0.368	-	-
889.24	*0.510*	-	-	0.576	0.511	-	-
898.247	*0.638*	-	-	0.714	0.620	-	0.621
933.256	*0.162*	-	-	0.172	0.161	-	-
944.259	*0.424*	-	-	0.458	0.407	-	0.406
991.841	*0.407*	-	-	0.376	-	-	0.380
1046.766	*0.0773*	-	-	0.0723	-	-	0.067

This region contains an absorption band of oxygen, which is visible, for example, on the **/Bogumil et al., 2003/** dataset, measured in an oxygen/ozone mixture. The **/Bogumil et al., 2003/** data does not show any clear temperature dependence. The new dataset measured using pure ozone is free of oxygen absorption and shows a clear temperature dependence (Figure 4.14.2a). Absolute values are lower by a few percent (3–4%) compared to **/Bogumil et al., 2003/**. The data of **/Enami et al., 2004/** show similar temperature dependence, but the cross-sections are higher than the new data (about 2–3%).

There is good agreement in the NIR spectral region between this study and the data of **/Bogumil et al., 2003/** and **/El Helou et al., 2005/**, both in absolute values and in the temperature dependence. Measurements of **/El Helou et al., 2005/** performed at 150 K are only slightly different from that at 223 K (Table 4.13).

Temperature dependence in the NIR region around 1000 nm is somewhat masked by the low signal-to-noise ratio in the **/Bogumil et al., 2003/** dataset. The new dataset reveals the clear temperature dependence, and resolves the rotational structure (Figures 4.14.1b and 4.14.2b). At wavelengths longer than 1050 nm the new cross-sections drastically drop and have low signal-to-noise ratio, since the FTS setup was not optimized for this spectral region.

Table 4.13 *Comparison of some ozone cross-sections datasets at low temperatures in the Wulf band, x 10^{-22} cm^2/molecule.*

Wavelength, nm	El Helou et al., 2005		Burkholder et al., 1994 220 K	Bogumil et al., 2003 223 K	BMD, 1998 218 K	***New data**, 223 K*
	222-223 K	150 K				
748.721	4.271	4.235	4.037	4.464	-	*4.328*
779.416	3.149	3.199	1.541	3.328	-	*3.181*
817.224	2.211	2.314	-	2.335	-	*2.230*
853.234	1.495	1.577	-	1.573	-	*1.517*
898.247	0.654	0.667	-	0.686	-	*0.611*
944.259	-	0.466	-	0.471	-	*0.420*
991.841	-	0.609	-	0.450	-	*0.469*
1046.766	-	0.128	-	0.0693	-	*0.076*

4.3. Ozone absorption cross-sections: conclusions

Most of the broadband datasets available so far for different temperatures were either limited in terms of the spectral coverage or resolution, or were scaled to the literature data, thus inheriting uncertainties from previous studies.

The experimental setups with two types of spectrometers (Echelle and FTS) were used for measurements necessary to generate the new broadband ozone absorption cross-sections covering the spectral region from the UV to the NIR, which contains spectral channels of the numerous remote sensing instruments. A spectral resolution of at least one order of magnitude better than that of the most remote sensing instruments was achieved. Absolute scaling of relative optical density spectra was performed using the pressure monitoring of pure ozone in the absorption cell. Special attention was paid to ozone decay before and during the absorption measurements for which the corrections were introduced.

Typically, relative datasets are scaled using single reference values in UV region, for example, at 253 nm (the Hg emission line). In this work, the absolute cross-sections were obtained for broad regions in the UV and visible parts of spectra in the Huggins and Chappuis bands. Relative measurements in the Hartley band, in the absorption minimum region between Huggins and Chappuis bands, and in the Wulf band were concatenated by scaling the overlap regions to the absolute cross-sections. Thus, it was possible to avoid the uncertainty accumulation due to the consecutive concatenations across a large spectral range up to the near IR.

The cross-sections data were obtained for various temperatures down to 193 K. The uncertainty of the absolute measurements related to the ozone dissociation practically disappears at temperatures below 243 K due to the very slow decay rate compared to the typical experiment duration. A spectroscopic method using the absorption in the oxygen A-band allowed to independently estimate the mean gas temperature along the experimental cell in addition to the commonly used contact temperature sensors.

The temperature dependence of the new ozone absorption cross-sections was established. Based on the absorption spectra from independent measurements at 11 temperatures in the range from 193 K to 293 K, the new dataset is expected to provide more accurate temperature parameterization compared to that typically derived from 4 to 5 temperature points in other reference databases that are currently used in the ozone retrievals.

The new broadband dataset offers additional information on the temperature dependence of the ozone absorption cross-sections, both inside and outside of the previously available temperatures range. This study confirms that a second order polynomial reproduces the temperature dependence of the experimental data in the Huggins band within the experimental uncertainty limits.

A weak temperature dependence was found for cross-sections near the top of the Hartley and Chappuis bands, which is however within the experimental uncertainties. In the Wulf band, a clear temperature dependence in agreement with the low-resolution measurements reported by **/Bogumil et al., 2003/** was observed.

The new data agree within the experimental uncertainty with the BMD dataset at all temperatures, excluding the region near 380 nm at low temperatures (below 1% in the Hartley band, 1–2% in the Huggins band and about 2–3% in the Chappuis band).

The new ozone cross-sections at room temperature are very close to the high-resolution BMD dataset; the agreement further improves if compared with BMD cross-sections interpolated to 293 K using the quadratic temperature dependence. All considered datasets agree within the reported experimental uncertainty limits for almost the entire spectral region when using conventional methods for data comparison. Part of the disagreement between datasets can be a result of the spectral resolution mismatch (particularly in the Huggins band), wavelength calibration errors, and temperature dependence.

5. Investigation of the methane line parameters

This chapter describes the experimental approach and achievements related to the goal to generate the improved methane spectroscopic line broadening parameters in the 1.6 μm spectral region and to quantify the expected improvements using satellite methane retrievals.

Multiple transmittance spectra were obtained covering a broad range of the experimental conditions, such as different temperatures, pressures, choice of buffer gases and mixing ratios using high-resolution Fourier Transform spectrometer. The obtained spectra have high quality, e.g., high signal-to-noise ratio. The measured spectra have been processed and compiled into the Absorption Spectra Data Base (ASDB), which was used within this study to generate the methane line parameters. The latter has been achieved using analysis software called LPC, which was developed in collaboration with the team from Department of Physics and Astronomy, University of Leicester, United Kingdom. The description of the algorithm is provided in Section 5.2.

The new line parameters have been compared with the HITRAN 2008 and the other datasets and tested on several CH_4 retrieval algorithms used by satellite-borne and ground-based instruments (SCIAMACHY, TANSO-FTS/GOSAT and TCCON).

5.1. Methane spectra measurement campaign

5.1.1. Experimental equipment

To perform the absorption measurements in the near-IR spectral region around 1.6 μm (6000 cm^{-1}) in methane, the experimental setup described in Section 3 was used. It is worth mentioning that spectra were acquired using almost the same apparatus as was used by **/Frankenberg et al., 2008b/**, key difference being the updated electronics and some hardware parts of the Bruker spectrometer. Some other improvements will be considered below. The routine of the cell filling with a gas mixture described in Section 3.2.2 was also inherited form **/Frankenberg et al., 2008b/**, since it was found that uniformity of the mixtures strongly depends on the gas filling sequence.

Overview of the equipment and some relevant settings is summarized in Table 5.1.

Table 5.1. *Details on the experimental setup used in the CH_4 measurement campaign*	
Spectra range	5934-6154 cm^{-1}
Spectrometer	Bruker HR125 FTS
Resolution	0.01 cm^{-1}
Apodization	boxcar
Phase correction	Mertz
Number of interferograms	50
Light source	OSRAM tungsten filament lamp
Beam splitter	CaF_2
Detector	ThorLabs InGaAs diode
Cell length	135 cm
Methane partial pressure,	2 – 10 mbar
Buffer gas kind and partial pressure	O_2, N_2, synthetic air, 0 – 990 mbar
Pressure sensors range	MKS Baratron: 0-100 hPa, 0-1000 hPa
Temperature sensors	PT sensors, internal cryostat sensor

Typical measurements time was about five hours for spectra recording (mixture and background in the empty cell), and additional 1-2 hours for set-up warm-up and parameter stabilization, such as the light source intensity, wavelength of the calibration laser, cell temperature, gas connections and cell evacuation and mixture preparation.

5.1.2. Transmittance model for preliminary data analysis

Experimental data produced in the early stages of the campaign were analyzed by comparison with a simple MatLab-based transmittance model (TM-IUP), which allowed to assess the conformity of observed and expected experimental parameters.

Figure 5.1 outlines the principle scheme of the TM-IUP algorithm. The input spectra are the experimental transmittance spectra of methane, obtained with Fourier transform spectrometer in the laboratory. TM-IUP calculates transmittance spectrum using Beer-Lambert law assuming HITRAN-format line parameters for Voigt line profiles and takes external conditions (total and partial pressure, temperature, path length). Necessary line parameters such as line position, line intensity, broadening coefficients for self- and air-broadening and pressure shift of line position are taken from the HITRAN 2008 database (see Sections 2.2.6 and 2.3.1).

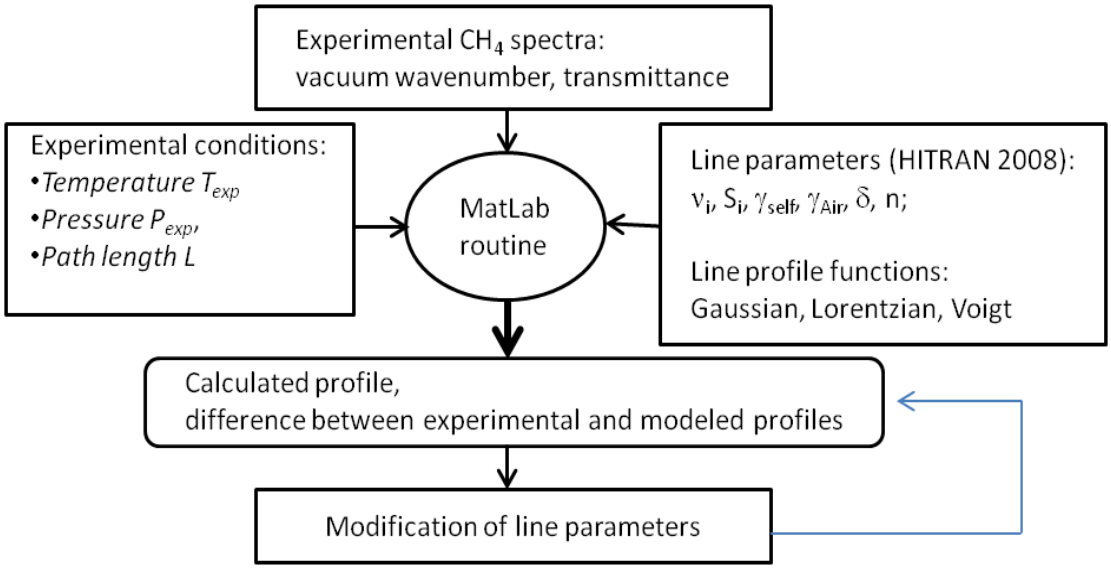

Figure 5.1. *The principle scheme of computation with the TM-IUP.*

The TM-IUP also estimates the difference between the calculated and measured spectra. The discrepancy can be minimized by means of modifications of lines parameters: line positions, air- and self-broadening coefficient, coefficient for temperature dependence and pressure induced wavelength shift. This ability allows to estimate the quality of the used line parameters and to predict modifications of the coefficients leading to the best fit of the experimental spectra.

5.1.3. Experimental conditions and resulting spectra

The choice of the experimental conditions was based on the review of the key publications on the experimental data available around 2011 and which contributed to the HITRAN 2008 version (Section 2.6.2). After this consideration, the measurement campaign was divided in two stages to ensure that the equipment performed as expected and that optimal experimental conditions were chosen.

Selection of experimental conditions is based on several criteria. Spectral lines need to demonstrate dependency of broadening parameters on experimental conditions; therefore, measurements have to be performed for several temperatures and CH_4 partial pressures/total mixture pressures. Limiting factor is the saturation of absorption lines at pressures above 7 mbar of pure methane in the available 135 cm cell, restricting the usable pressure range for direct self-broadening observation. However, self-broadening contribution can still be quantified from the observed line profile, as in equation (2.14)

The following sequence of measurements was established:

- Stage 1: reproduction of former approaches: new measurements under the same conditions as described in **/Frankenberg et al., 2008b/** but using an improved setup and advanced settings to overcome some of the issues described in **/Frankenberg et al., 2008b/.** The goal was to find out if the results from previous publications could be reproduced. The use of the Stage 1 spectra was also a crucial test for the analysis of the developed software.

- Stage 2: measurements in pure CH_4 and in mixtures with the buffer gases - CH_4/N_2, CH_4/O_2 and CH_4/Air at extended set of different pressures and temperatures. Publications of **Lyulin et al., 2009/** and **/Nikitin et al., 2010/** were considered as well.

Stage 1: Frankenberg conditions

New measurements under the same conditions with respect to the buffer gas, pressure and temperature as used by **/Frankenberg et al., 2008b/** have been performed. Table 5.2 provides an overview on these conditions. Not listed are numerous test measurements, which have also been performed as part of this study.

Table 5.2. *Overview of the methane transmittance spectra as measured by IUP using the same conditions as have been used by* ***/Frankenberg et al., 2008b/.***

CH_4 (mbar)	**N_2 (mbar)**	**T (K)**	**Notes**
2.5	123	296	'Frankenberg' mixture, 2% CH_4
5	245	296	'Frankenberg' mixture, 2% CH_4
10	890	296	'Frankenberg' mixture, 1% CH_4
10	490	296	'Frankenberg' mixture, 2% CH_4

The new spectra for four 'Frankenberg mixtures' are shown in Figure 5.2. The upper panel presents transmittance spectra, whereas the lower panel shows the standard deviation of every measurement arising from averaging over 50 interferograms. The new data have very good quality and signal-to-noise ratio.

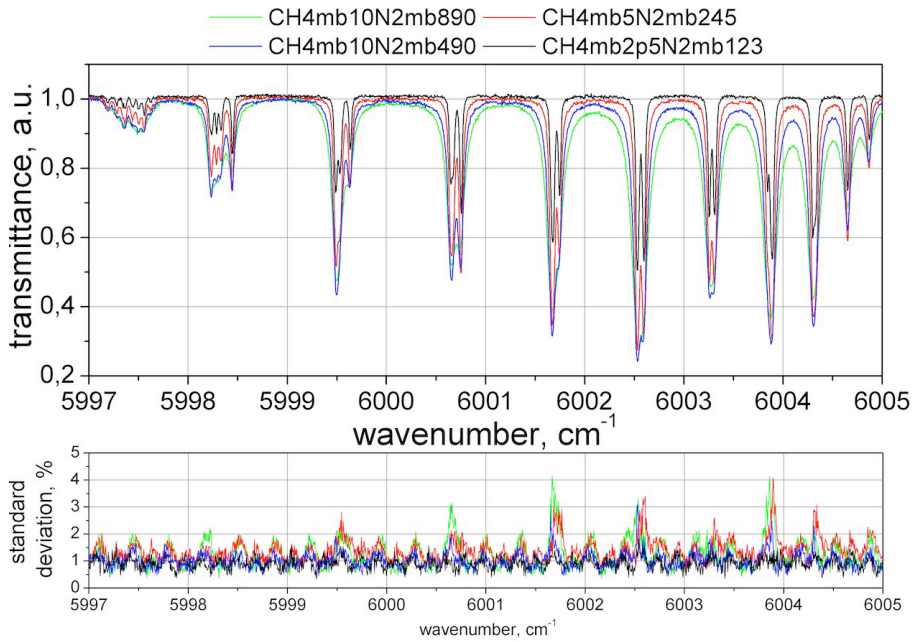

Figure 5.2. *Quality of the new experimental data for different mixtures.*
Upper panel: transmittance spectra, obtained from averaging of multiple scans.
Bottom panel: the ratio of standard deviations of averaged spectra to the average value multiplied by 100 for the following mixtures: Green: 10 mbar CH_4 + 890 mbar N_2, Blue: 10 mbar CH_4 + 490 mbar N_2, Red: 5 mbar CH_4 + 245 mbar N_2, Black: 2.5 mbar CH_4 + 123 mbar N_2.

The new spectra have been analyzed by comparison with the spectra of **/Frankenberg et al., 2008b/,** Figure 5.3. It is important to notice that the conditions of **/Frankenberg et al., 2008b/** were taken as a guideline. Absorption path was decreased from 270 cm, used by **/Frankenberg et al., 2008b/** down to 135 cm to avoid possible saturation of strong lines, therefore absorption is two times smaller in the new measurements.

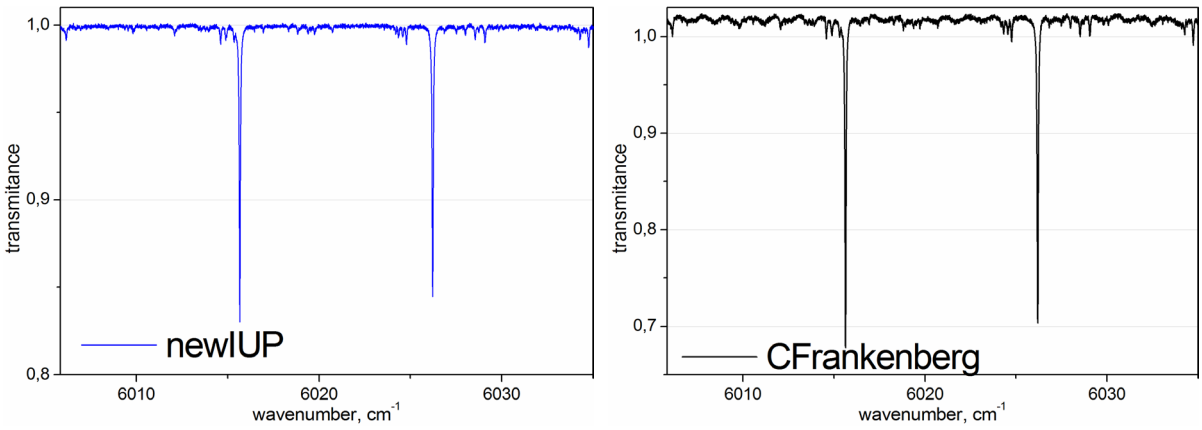

Figure 5.3a. *Comparison between the measured spectra for high total pressure at room temperature for R0 and R1 lines near 6010-6030 cm^{-1}: 10 mbar CH_4 and 490 mbar N_2.*
*Left side graph: new spectra (blue). Right side graph: spectra from **/Frankenberg et al, 2008b/** (black).*

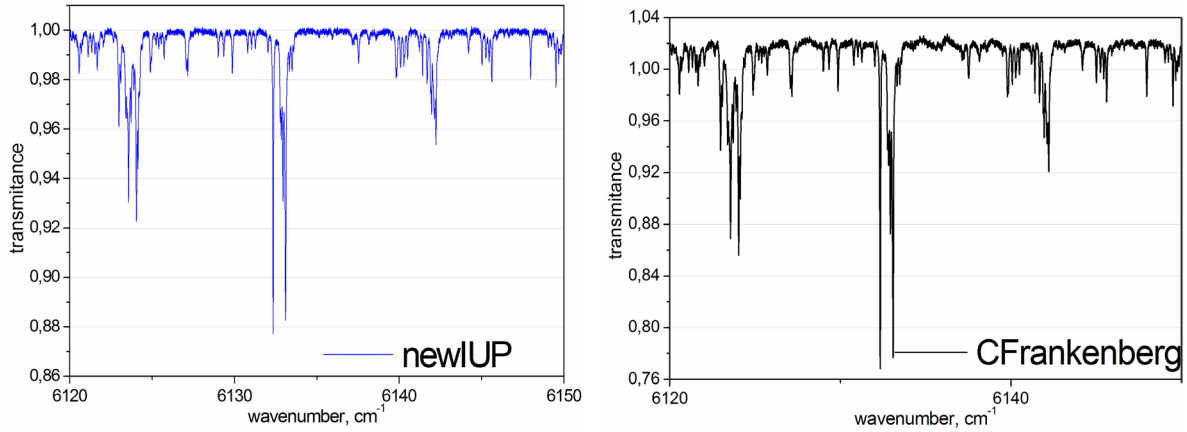

Figure 5.3b. *Comparison between the measured spectra for high total pressure at room temperature for R11-R13 manifolds near 6130 cm^{-1}: 10 mbar CH_4 and 490 mbar N_2.*

Left side graph: new spectra (blue).

Right side graph: spectra from ***/Frankenberg et al, 2008b/*** *(black).*

Several issues were observed on the spectra of **/Frankenberg et al., 2008b/**, (see Figure 5.3c):

- Etalon effect (due to unwedged spectrometer output window);
- Offset (stray light, background measurement resolution mismatch);
- Poor signal-to-noise ratio (small amount of scans, system optimizations);
- Wavelength calibration (FTS instrument was not evacuated);
- Wideband transmission skew present on Frankenberg spectra (non-optimal spectrometer settings)

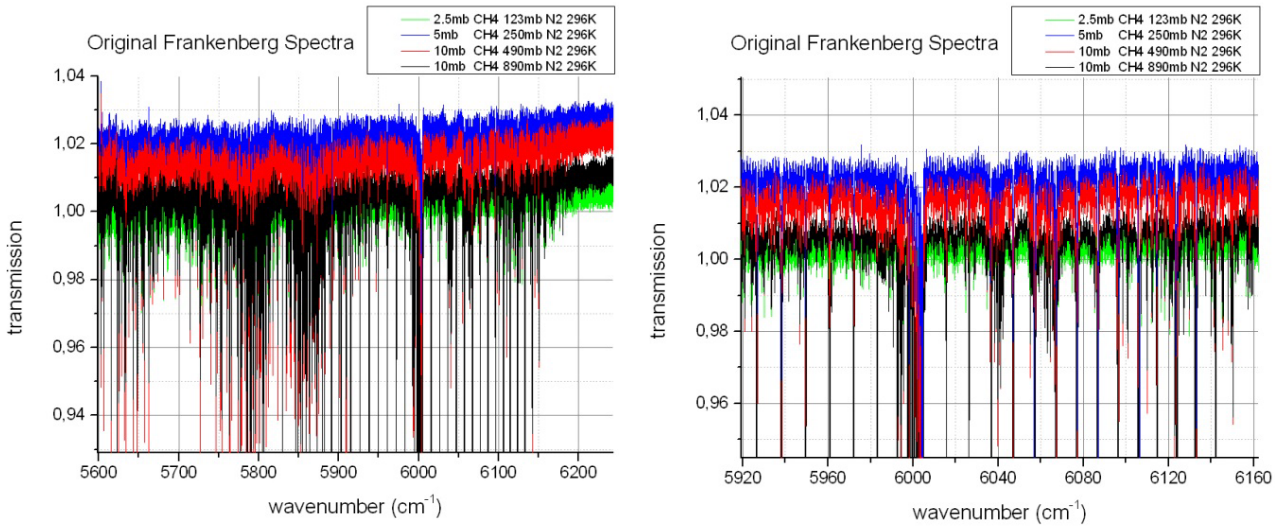

Figure 5.3c. *Original spectra from* ***/Frankenberg et al, 2008b/***

Note the inclination of C. Frankenberg experimental transmittance spectra.

Optimisation of the experimental setup allowed to mitigate the unwanted features mentioned above, allowing to obtain the spectra of significantly higher quality during all measurements (see Figure 5.3d).

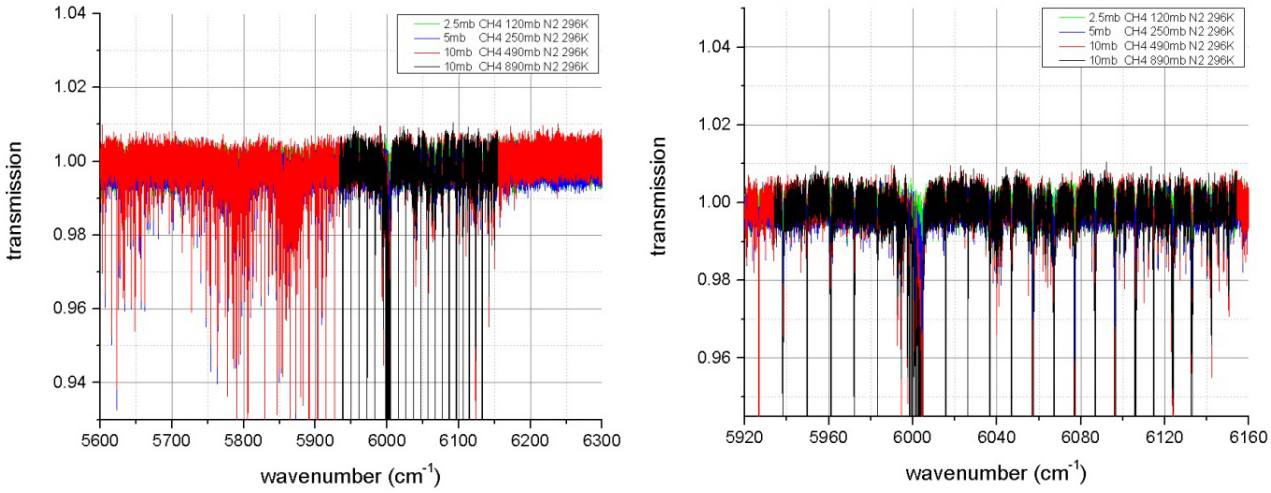

Figure 5.3d. *New spectra for experimental conditions as in* ***/Frankenberg et al, 2008b/***

Stage 2: Extended conditions

As it was mentioned earlier, the goal of the Stage 2 was to perform extended set of measurements with respect to the used buffer gases, pressures and temperatures, extending the conditions listed by **/Frankenberg et al., 2008b/**.

Additional conditions were selected based on the consideration of experimental parameters reported by other research groups (Table 2.7 in Section 2.6.2). As a result, mixtures as used by **/Lyulin et al., 2009/** have been selected. Table 5.3 summarizes the experimental conditions as used by **/Frankenberg et al., 2008b/** and **/Lyulin et al., 2009/.**

Table 5.3. *Experimental conditions reported in relevant publications.*

Lyulin et al. 2009				**Frankenberg et al. 2008b**			
T, K	**CH_4, mbar**	**N_2, mbar**	**O_2, mbar**	**T, K**	**CH_4, mbar (%)**	**N_2, mbar**	**Total, mbar**
296	2.5, 5, 10	-	-	295.65	10 (1%)	890	900
	5	500, 1000	-	295.65	10 (2%)	490	500
	10	500	-	296,15	5 (2%)	235	240
	5	-	500, 1000	297.15	2.5 (2%)	123	126
	10	-	500				
267	2.5, 5, 10	-	-				
	5	500, 1000	-				
	10	500	-				
	5	-	500, 1000				
	10	-	500				
240	2.5, 5, 10	-	-				
	5	500, 760	-				
	10	500	-				
	5	-	500, 1000				
	10	-	500				

Table 5.4 lists the experimental conditions for which the absorption spectra were measured and which have been included in the (ASDB).

Table 5.4. *Experimental conditions for absorption spectra included in ASDB.*

T (K)	CH_4 (mbar)	Buffer gas (mbar)	Notes
195, 223, 243, 263, 296	2	-	Close to 'Lyulin' conditions
195, 223, 243, 263, 296	5	-	Close to 'Lyulin' conditions
195, 223, 243, 263, 296	5	N2, 495	Close to 'Lyulin' conditions
195, 223, 243, 263, 296	5	N2, 995	
195, 223, 243, 263, 296	10	N2, 490	Close to 'Frankenberg' conditions Close to 'Lyulin' conditions
195, 223, 243, 263, 296	10	N2, 990	Close to 'Frankenberg' conditions
195, 223, 243, 263, 296	5	O2, 495	Close to 'Lyulin' conditions
195, 223, 243, 263, 296	5	O2, 995	
195, 223, 243, 263, 296	10	O2, 490	Close to 'Lyulin' conditions
195, 223, 243, 263, 296	10	O2, 990	
195, 223, 243, 263, 296	5	Air, 495, 995	
195, 223, 243, 263, 296	10	Air, 490, 990	

Compared to data from Table 5.3, the spectra were acquired for a broader range of temperatures and include synthetic air as a buffer gas. The content of CH_4 in samples is 1%, 2% and 100%. The total number of mixtures used is about 70.

The measured spectra have a very high quality and therefore are a solid base for the line parameter determination. Data in format of the transmittance spectra are collected in the Absorption Spectra Data Base as ASCII files.

Figures 5.4 - 5.7 provide examples of the spectra for pure CH_4 and CH_4/synthetic air mixtures.

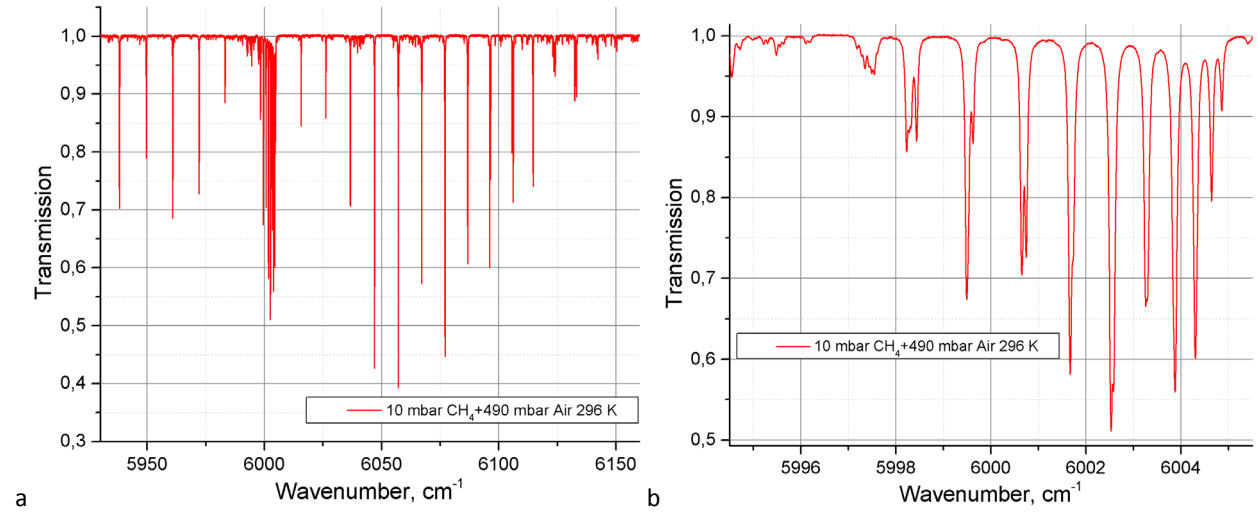

Figure 5.4. ***(a)*** *Transmittance spectrum for the "10 mbar CH_4 + 490 mbar air" mixture at 296 K in the whole considered wavenumber range 5934-6154 cm^{-1} and* ***(b)*** *in the Q-branch of $2\nu_3$ band*

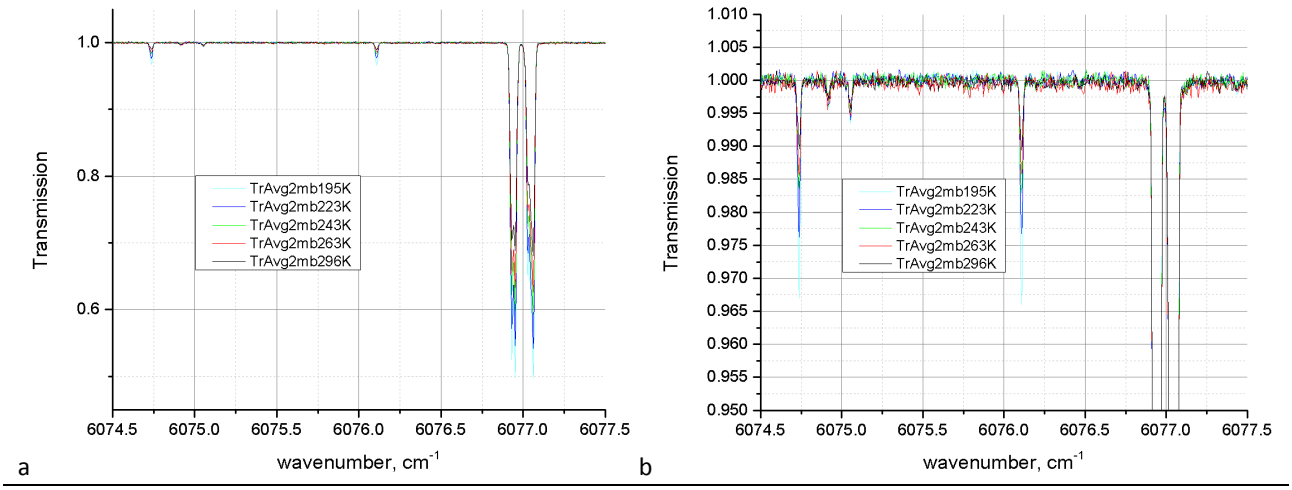

Figure 5.5. ***(a)*** *Transmittance spectra near the R6 manifold of 2v3 band for 2 mbar CH_4.*
(b)*: close up for signal-to-noise estimate*

The resulting spectra have a very good signal-to-noise ratio (Figure 5.5), with the noise level of about 0.015% for typical absorptions of 0.5.

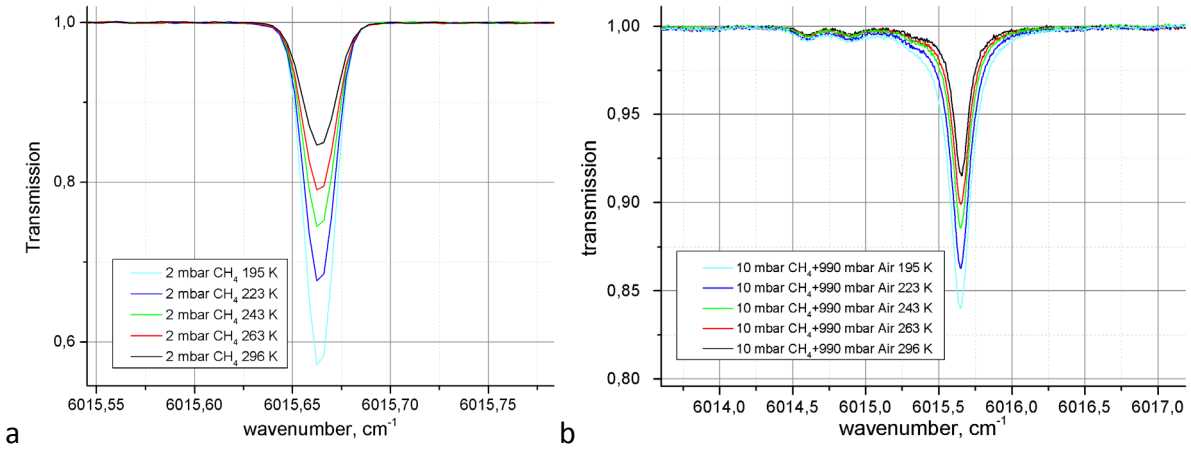

Figure 5.6. *Transmittance spectra near the R0 line of $2v_3$ band for* ***(a)*** *pure CH_4 at 2 mbar at five temperatures and* ***(b)*** *"10 mbar CH_4 + 990 mbar air" mixtures for different temperatures*

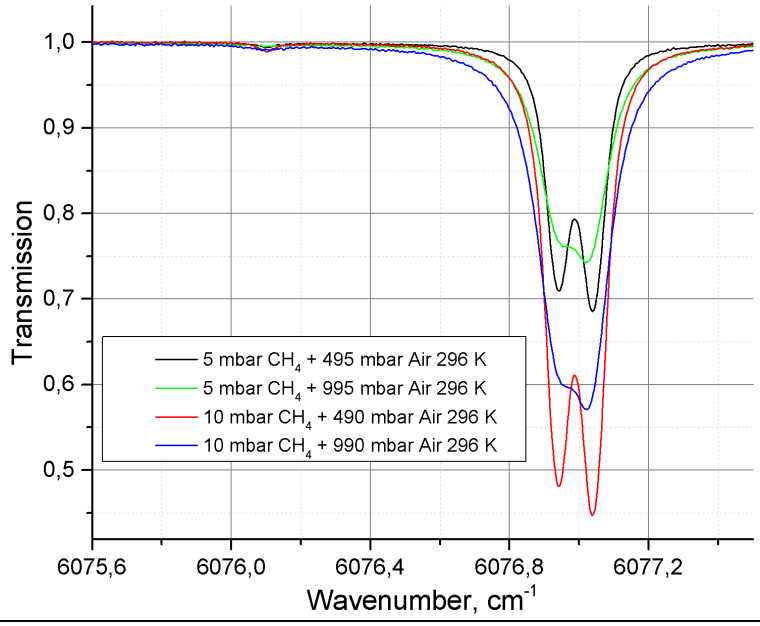

Figure 5.7. *Transmittance spectra near the R6 manifold of $2v_3$ band for different mixtures (see legend)*

5.2. LPC: software used for new line parameters generation

This section contains the review of the analysis software, called *Line Parameter Code* (hereafter LPC), which has been designed in collaboration with the University of Leicester to retrieve line parameters from methane absorption spectra acquired in the laboratory. This software is created for IDL environment and works in parallel with the *University of Oxford Reference Forward Model* (RFM), a radiative transfer code developed by the University of Oxford (see www.atm.ox.ac.uk/RFM for details) written in FORTRAN-77.

The LPC software does not allow investigation of the impact of line mixing on the retrieved parameters. For the purpose of this study, a Voigt line profile is assumed (Section 2.2). As reported by **/Tran et al., 2010/**, this approach - which delivers 'effective' coefficients - is appropriate for satellite remote sensing applications (if the satellite retrievals are also based on the assumption of a Voigt profile, which is typically the case, e.g., for SCIAMACHY methane retrieval). However, due to the line-mixing effects, the 'real' coefficients of interest to those studying molecular spectroscopy, can differ from the 'effective' ones generated within this study.

Optimal estimation method

The line parameter code designed and written for this work uses the optimal estimation method described by **/Rodgers, 2000/**. Optimal estimation is widely used in retrievals of atmospheric profiles from satellite observations, since it provides a way of calculating the most probable atmospheric state for a given measurement, assuming some prior knowledge of the atmospheric state and the measurement uncertainty. In this work, it is the line parameters that represent the *state vector* that are being estimated from the measurements.

The optimal estimation method involved finding the most probable solution for the *state vector* $\mathbf{x}$ given a *measurement vector* $\mathbf{y}$, i.e. finding $\mathbf{x}$ which maximizes the probability $P(\mathbf{x}|\mathbf{y})$. This is achieved by finding $\mathbf{x}$ which minimizes the cost function (see **/Rodgers, 2000/** for its derivation):

$$\chi^2 = (\mathbf{x} - \mathbf{x}_a)^T \mathbf{S}_a^{-1} (\mathbf{x} - \mathbf{x}_a) + (\mathbf{y} - F(\mathbf{x}))^T \mathbf{S}_y^{-1} (\mathbf{y} - F(\mathbf{x})). \qquad (5.1)$$

Here the vector $\mathbf{x}_a$ represents the a priori state (the initial estimate of the line parameters, which is taken from HITRAN 2008), $\mathbf{S}_a$ represents the a priori covariance matrix (the uncertainty in initial estimate), $F(\mathbf{x})$ represents the forward model output (in this case, simulated laboratory spectra assuming line parameters $\mathbf{x}$) and $\mathbf{S}_y$ represents the measurement covariance matrix (the uncertainty in the measured spectra). In minimizing this function, a balance is achieved between a solution like the a priori, which would reduce the first term to zero, and a solution which agrees exactly with the measurements which would reduce the second term to zero.

Levenberg-Marquardt method

There are a number of different methods available for finding the solution depending on the nature of the problem. For this work, the relationship between the spectra and the underlying line parameters is non-linear, so the *Levenberg-Marquardt* method is used. This gives the following iterative solution to the optimal estimation problem:

$$\mathbf{x}_{i+1} = \mathbf{x}_i + [(1+\gamma)\mathbf{S}_a^{-1} + \mathbf{K}_i^T\mathbf{S}_y^{-1}\mathbf{K}_i]^{-1}\{\mathbf{K}_i^T\mathbf{S}_y^{-1}\big(\mathbf{y} - F(\mathbf{x}_i)\big) - \mathbf{S}_a^{-1}(\mathbf{x}_i - \mathbf{x}_a)\} \quad (5.2)$$

Here the Jacobian matrix $\mathbf{K}_i$ describes the sensitivity of the forward model to the different line parameters comprising $\mathbf{x}_i$, and γ is a number chosen at each step to accelerate convergence towards the solution. For the first iteration, $\mathbf{x}_i$ is set equal to $\mathbf{x}_a$ and γ to 0.5. To decide whether γ is increased or reduced for each subsequent step, one should consider the ratio of the change in cost function computed properly to that computed with the linear approximation to the forward model (**/Rodgers, 2000/**). This ratio will be unity if the linear approximation is satisfactory, and negative if χ^2 has increased rather than decreased. The following strategy is applied to changing γ:

- if the ratio is greater than 0.75, then γ is halved;
- if the ratio is less than 0.75, then γ is doubled;
- otherwise, γ is unchanged.

The aim of this strategy is to find a value of γ which restricts the new value of $\mathbf{x}$ to lie within linear range of the previous estimate. The number of iterations is either set to a fixed number, or can be chosen in each case depending on a convergence criterion – this avoids performing unnecessary iterations of the optimal estimation loop after the solution has already converged.

The method employed here also allows estimation of the uncertainty in the retrieved state vector, via the covariance matrix $\hat{\mathbf{S}}$:

$$\hat{\mathbf{S}} = (\mathbf{S}_a^{-1} + \mathbf{K}^T\mathbf{S}_y^{-1}\mathbf{K})^{-1} \quad (5.3)$$

The diagonal elements of $\hat{\mathbf{S}}$ give the variance of each element in the state vector, so the square roots of these elements are taken to find the standard deviation of $\mathbf{x}$.

5.2.1. Algorithm structure

Figure 5.8 shows a schematic overview of the algorithm structure, illustrating the stage of the process at which the various inputs are used. The main iteration loop is denoted by the blue arrows. The number of iterations needed to arrive at a solution depends on the number of spectral points in the wavenumber range being analyzed (i.e. the dimension of the measurement and forward model vectors – this depends on both the wavenumber range and the number of spectra), and the number of spectral lines within the spectral range considered

(the dimension of the state vector). The dimensions of these vectors also have a strong influence on the computation time, with the matrix inversions in the Levenberg-Marquardt method being the most computationally expensive steps in the algorithm.

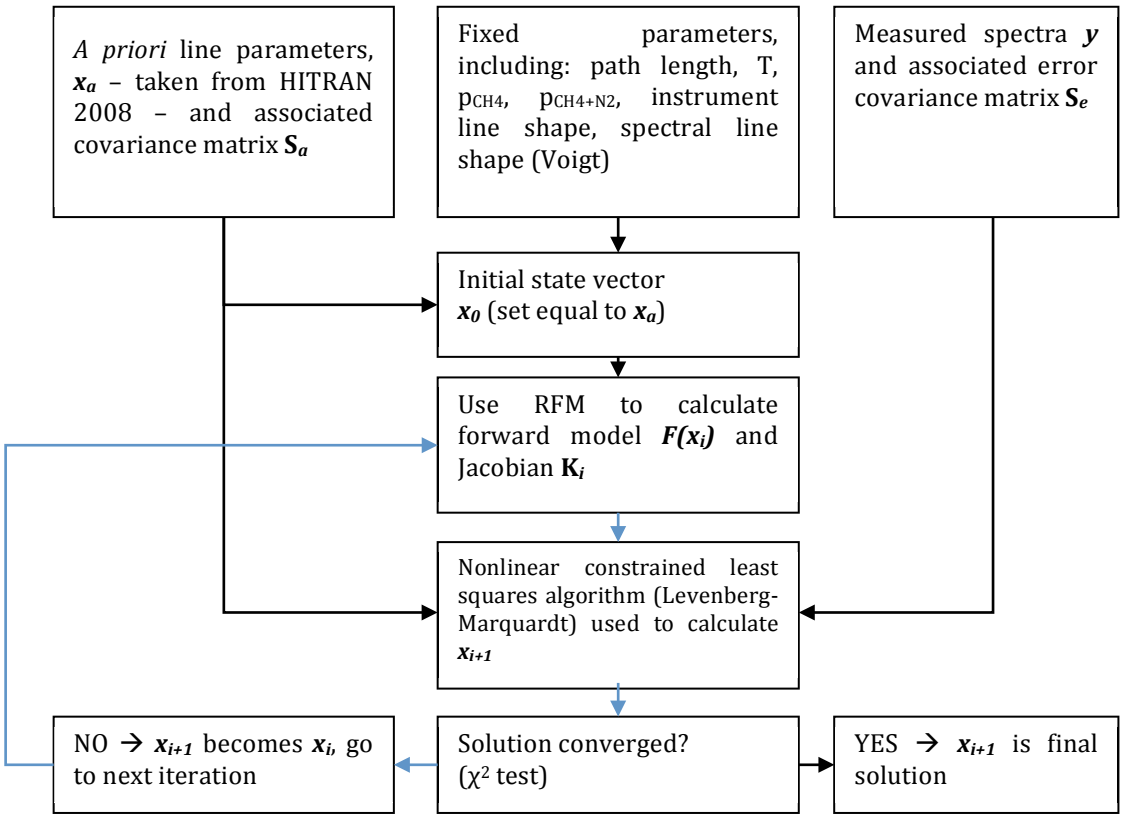

Figure 5.8. *Schematic illustrating the initial design for the line parameter calculation.*

5.2.1.1. Inputs

The a priori line parameters are all taken from the HITRAN 2008 database (**/Rothman et al., 2009/**). Any database in HITRAN format can be used. The a priori state vector contains a number of elements equal to the product of the number of absorption lines within the wavenumber range to be analyzed (according to HITRAN 2008 line positions) and the number of parameters per line. The code has been designed to allow the user to define the a priori covariance matrix, depending on their assessment of the uncertainties for each of the various line parameters.

There are six numbers which describe the a priori uncertainties for each of the six line parameters: line position, intensity, air- and self-broadening, temperature dependence coefficient and pressure induced shift.

The values for line position and pressure shift are absolute uncertainties, i.e. 1.00E-02 means an uncertainty of ±0.01 cm^{-1}.

The values for intensity, air- and self-broadening and temperature dependence coefficients are fractional uncertainties, i.e. 1.00E+00 means an uncertainty of ±100%, 1.00E-01 would mean ±10%, and so on. The uncertainties have to be non-zero for the procedure to function correctly.

The fixed parameters, which remain unchanged after each iteration, are those describing the laboratory conditions for each measured spectrum: absorption path length, cell temperature, total cell pressure, partial pressure due to methane, instrument line shape and assumed absorption line shape function. A preliminary step (not shown in Figure 5.8) estimates the total and partial pressures, along with the cell temperature, by fitting forward modelled spectra to the *R0* and *R1* absorption lines of the $2\nu_3$ band at 6015.66 and 6026.23 cm^{-1}. This step is important, as it is not always possible to measure precisely the composition of the methane mixture being observed. These lines in particular are used as (unlike most methane lines in the NIR region) they are singlets, so their spectral absorption can therefore be easily modelled, whilst their intensities and transition frequencies are also very well known.

The measurement vector contains all of the measurement spectra to be analyzed joined together end-to-end. The spectra do not have to have been measured at the same spectral resolution or under the same conditions, with the exception of the methane mixture which has to include the same broadening gas in each case. There is theoretically no upper limit to the number of spectra that can be analyzed simultaneously, although the impact on processing time is considerable if too many spectra are input at once. The measurement covariance matrix, describing the uncertainty in the spectral measurements, is a diagonal matrix where each diagonal element contains the variance in the measured lab spectra. It is assumed that the variance, estimated from the measurement random noise, is independent of wavenumber (i.e. the same value is used for all of the diagonal elements).

5.2.1.2. Forward model

The forward model used here to calculate spectral radiances and Jacobians given a set of line parameters is the *University of Oxford Reference Forward Model* (RFM, www.atm.ox.ac.uk/RFM/). The RFM is a line-by-line radiative transfer model developed to provide reference spectral calculations for the ENVISAT MIPAS retrieval algorithms. In addition to its primary purpose of calculating the spectral radiance observed from limb or nadir viewing geometries given atmospheric profiles and spectroscopic parameters as input, the RFM may also be used to estimate the transmittance of a laboratory sample cell. The RFM has been chosen as the forward model for this study as it provides both accuracy and flexibility.

To calculate the spectral radiance, RFM uses the line parameters which were described Section 2.2.6. Also see Section 2.6.2 for further details on the various sources of spectroscopic data used in the more recent versions of the database.

These parameters are: $\boldsymbol{\nu}$ - the spectral line transition frequency, $\boldsymbol{S}$ - the spectral line intensity, $\boldsymbol{\gamma_{air}}$ - the air-broadened half width at half maximum (HWHM), $\boldsymbol{\gamma_{self}}$ - the self-broadened HWHM, $\boldsymbol{n}$ - the coefficient of temperature dependence of the air-broadened half width, $\boldsymbol{\delta}$ - the air-broadened pressure shift.

The pressure broadened line half width $\boldsymbol{\gamma(p, T)}$ for a gas at pressure p [atm], temperature T [K] and partial pressure p_s [atm] taking into account both air- and self-broadening is given by equation (2.14) in Section 2.2.6.

Note that the contribution from air-broadening depends only on the total pressure, and is independent of the broadening gas used in the methane mixture. This means that if nitrogen or oxygen is used as the broadening gas, then the LPC algorithm is effectively retrieving γ_{N_2} or γ_{O_2} respectively rather than γ_{air}. The relation (2.15) (Section 2.2.6) can be used (as in **/Lyulin et al. 2009/**) to convert the retrieved nitrogen- and oxygen-broadening parameters into γ_{air}. This relation should also be applied to the coefficient of temperature dependence and the air-broadened pressure shift (e.g. **/Lyulin et al. 2009/**).

The monochromatic absorption coefficient (which is used in the Beer-Lambert law to compute the spectral radiance) is given by:

$$k_{\eta\eta'}(\nu, T, p) = S_{\eta\eta'}(T) f(\nu, \nu_{\eta\eta'}, T, p) \qquad (5.4)$$

Here, $f(\nu, \nu_{\eta\eta'}, T, p)$ is the normalised line shape function. For this work, a Voigt line shape function is assumed. The monochromatic absorption coefficient is expressed in (molecule cm^{-2})$^{-1}$. Multiplying this by the number density of absorbing molecules per unit path length gives the optical depth, $\tau_{\eta\eta'}(\nu, T, p)$.

Figures 5.9 and 5.10 show some examples of spectral residuals obtained comparing RFM calculated transmittances with preliminary test spectra (not included in the ASDB). The forward model spectra are calculated assuming Voigt line shapes and the HITRAN 2008 database of spectroscopic parameters as described above. The initial comparisons made between the RFM calculations and measured spectra illustrate the suitability of the RFM as a forward model for the line parameter retrieval.

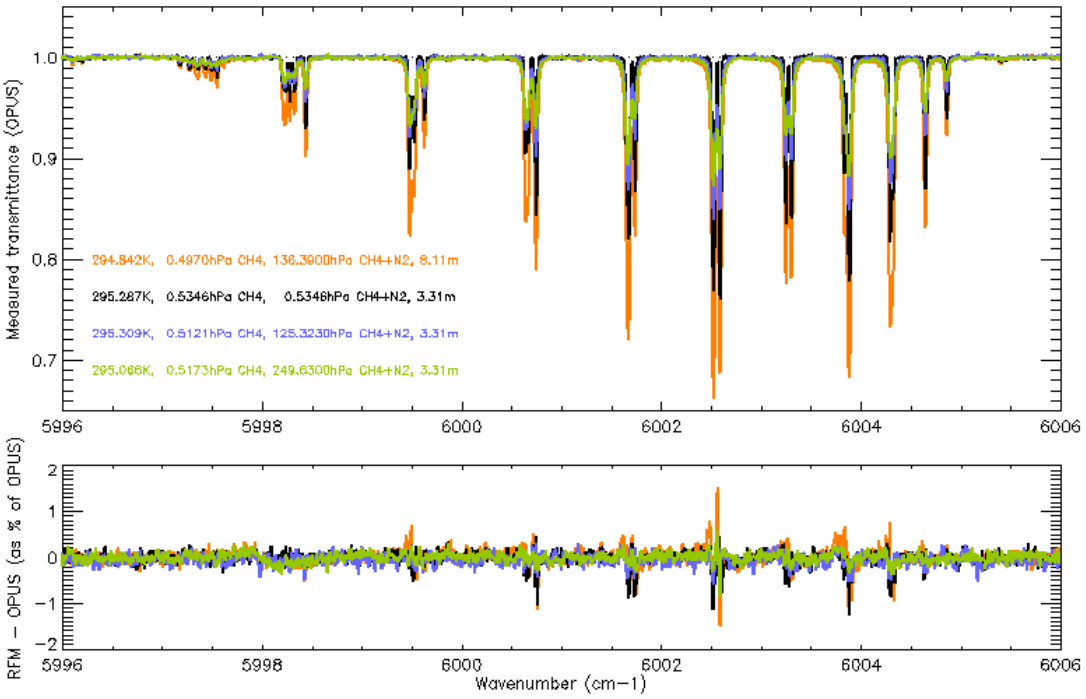

Figure 5.9. *Upper panel: measured 0.005 cm^{-1} resolution transmittances for four different sample conditions, focusing on the CH_4 Q-branch. Lower panel: (RFM-measurement) residual as a percentage of the measurement, assuming HITRAN 2008 line parameters.*

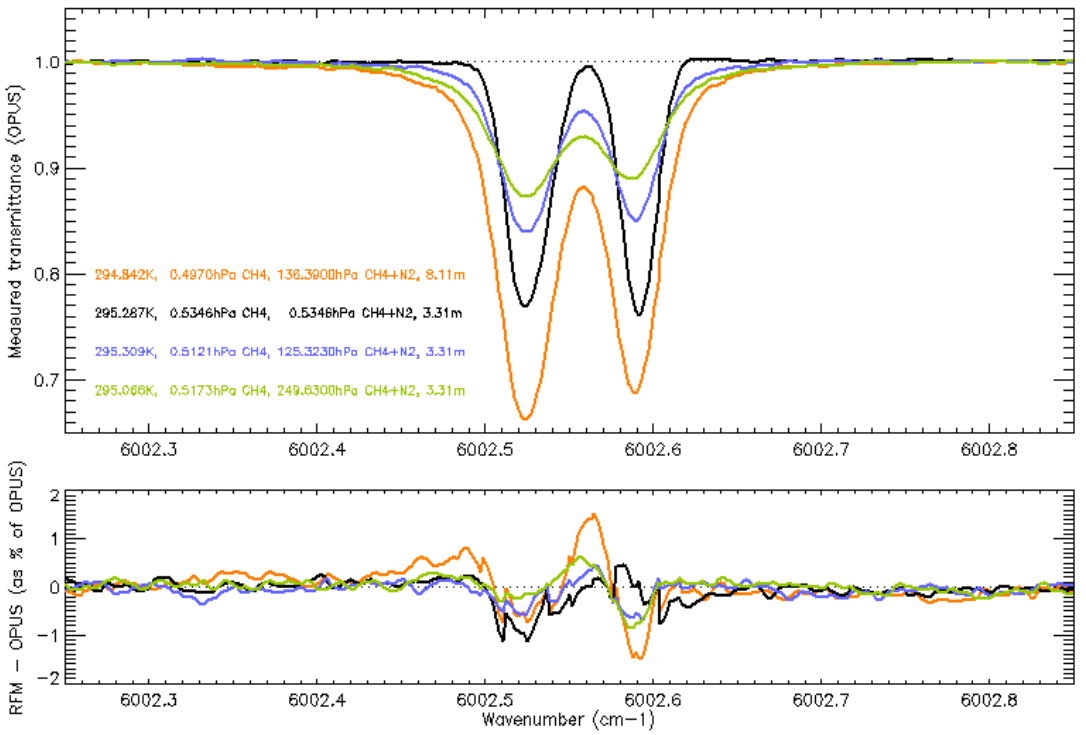

Figure 5.10. *Same as Figure 5.9, but focused on CH_4 Q6 manifold.*

5.2.1.3. Outputs

The final state vector contains updated values for each of the line parameters (number of elements = 6 x number of lines in wavenumber range). The LPC creates a parameter file in the same format as the HITRAN 2008 for use in radiative transfer or retrieval codes, using the values in the final state vector. This includes error codes based on the retrieval uncertainty (see definition of the HITRAN error codes in Section 2.6.2).

The variance for each of the retrieved parameters is given by the diagonal elements of the covariance matrix

$$\hat{\mathbf{S}} = (\mathbf{S}_a^{-1} + \mathbf{K}^T \mathbf{S}_y^{-1} \mathbf{K})^{-1} \quad (5.5)$$

Here, $\mathbf{S}_a$ is the a priori covariance matrix (the uncertainties in initial estimate of the line parameters), $\mathbf{K}$ is the Jacobian and $\mathbf{S}_y$ is the measurement covariance matrix (containing the uncertainties in the measured laboratory spectra). The standard deviation for each parameter, given by the square root of each of the diagonal element, is used to determine the uncertainty index for that parameter.

The LPC provides two further outputs to assist the user in interpretation of the line parameter retrieval results:

- The χ^2 (cost function) values for each wavenumber interval are calculated after the final iteration and written to a text file. These values should be as low as possible, so if any are unusually high then that indicates that there may be an issue with the retrieved line parameters in that particular interval. It is therefore useful for flagging wavenumber intervals which require revisiting in greater detail.

- The code also evaluates the averaging kernel for each wavenumber interval, and from this derives the number of degrees of freedom associated with each retrieved line. The averaging kernel matrix describes the sensitivity of the retrieved line parameters to the 'true' state vector. A perfect retrieval would result in an identity matrix for the averaging kernel matrix. However, in reality some retrieved line parameters are not independent of one another (especially where strong and weak lines are in close proximity), resulting in non-zero off-diagonal elements, whilst in other cases the retrieved parameters are not sensitive to the true state at all (for example, when an absorption line is weaker than the measurement noise). The number of degrees of freedom for a particular line is obtained by taking the sum of the diagonal elements of the averaging kernel for that line. It is a number between 0 and 6, and is equivalent to the number of independent parameters successfully retrieved.

5.2.2. Comparison with software used by other researchers

Comparison of the applied software with the software used by other researchers (Section 2.6.2) is summarized in the Table 5.5, regarding the method, a priory values, constrains and other details of the fitting procedure.

Table 5.5 *Comparison with software used by other researchers*

Frankenberg et al., 2008	**Lyulin et al. 2009** **Nikitin et al. 2011**	**This work**
Method		
Multispectrum nonlinear constrained least squares approach based on optimal estimation; Simultaneously fitting laboratory spectra at different ambient pressures. Each line treated separately, even for multiplets; No cross-correlations between lines assumed; The Jacobian of the transmission with respect to shift and broadening coefficients computed analytically	Multispectrum fitting procedure; a nonlinear least- squares methods; Simultaneously fitting spectra recorded under various experimental conditions (6 spectra recorded at a given temperature).	Line-by-line radiative transfer code used to forward model the measured spectra; Simultaneous fitting of spectra recorded under various experimental conditions (from 4 to 20 spectra at different *p* and *T*); Each line treated separately, even for multiplets; No cross-correlations between lines assumed; Flexibility to retrieve any combination of the six line parameters used to calculate spectral absorption.
Perturbing gases and temperatures		
N_2; room temperature	O_2, N_2; 240K, 267K, 296K	O_2, N_2, synthetic air; 195K, 203, 223K, 243K, 263K, 96K.
Constrains		
Relative line intensities strictly constrained to the /Margolis, 1988/ (HITRAN 2004), permitting only small deviations. Line strengths: linked to the R0 and R1 strengths given in HITRAN 2004 /Margolis, 1988/. The integrated column density of methane was determined using a fit covering the isolated R0 and R1 transitions.	J-manifolds: theoretically predicted line positions and intensities as initial values in the fits. When fitted line intensities differed considerably (15–20%) from the theoretical ones, either a line position or a line intensity of one of the lines of a manifold was fixed. Line intensities: derived from the integrated intensity of a J-manifold. At the end of the fit all intensities were free.	Flexibility to set any uncertainty value between 0.01% and 100% for each of the six line parameters considered. The integrated column density of methane was determined using a fit covering the isolated R0 and R1 transitions. Constraints were applied as described in **Section 5.2.1.1**.
A priory values		
Pressure shifts: –0.011 cm^{-1} atm^{-1} /Kapitanov et al., 2007/ prior broadening coefficients from measurements in the fundamental by /Pine et al, 1992, 1997/ Self-broadening neglected Temperature dependence fixed at 0.85 for the whole obtained region 5860-6184 cm^{-1}.	Initial values of the line positions and line intensities from **/Wegner et al., 1998/** and **/Nikitin et al., 2010/**	HITRAN 2008 – derived from the results of **/Frankenberg et al. 2008/** in the $2v_3$ band considered.
Line shape		
Voigt	Voigt	Voigt
Reported issues		
Unresolved manifolds; temperature dependence of pressure broadening	Temperature dependence of broadening and shifts	Unresolved manifolds; Temperature dependence of broadening and shifts
Line mixing		
No	No	No

5.2.3. LPC verification

Two tests which can be used to determine the success with which the analysis software converges on a solution are summarized here. The sensitivity to the a priori uncertainty chosen by the user is also discussed in this section.

Spectral residual

One criterion for evaluating the success of the algorithm is to look at the spectral residual between the forward model (computed using the retrieved parameters) and the measurement. If the algorithm is performing correctly, then the final spectral residual should be insensitive to the assumed a priori values for the line parameters.

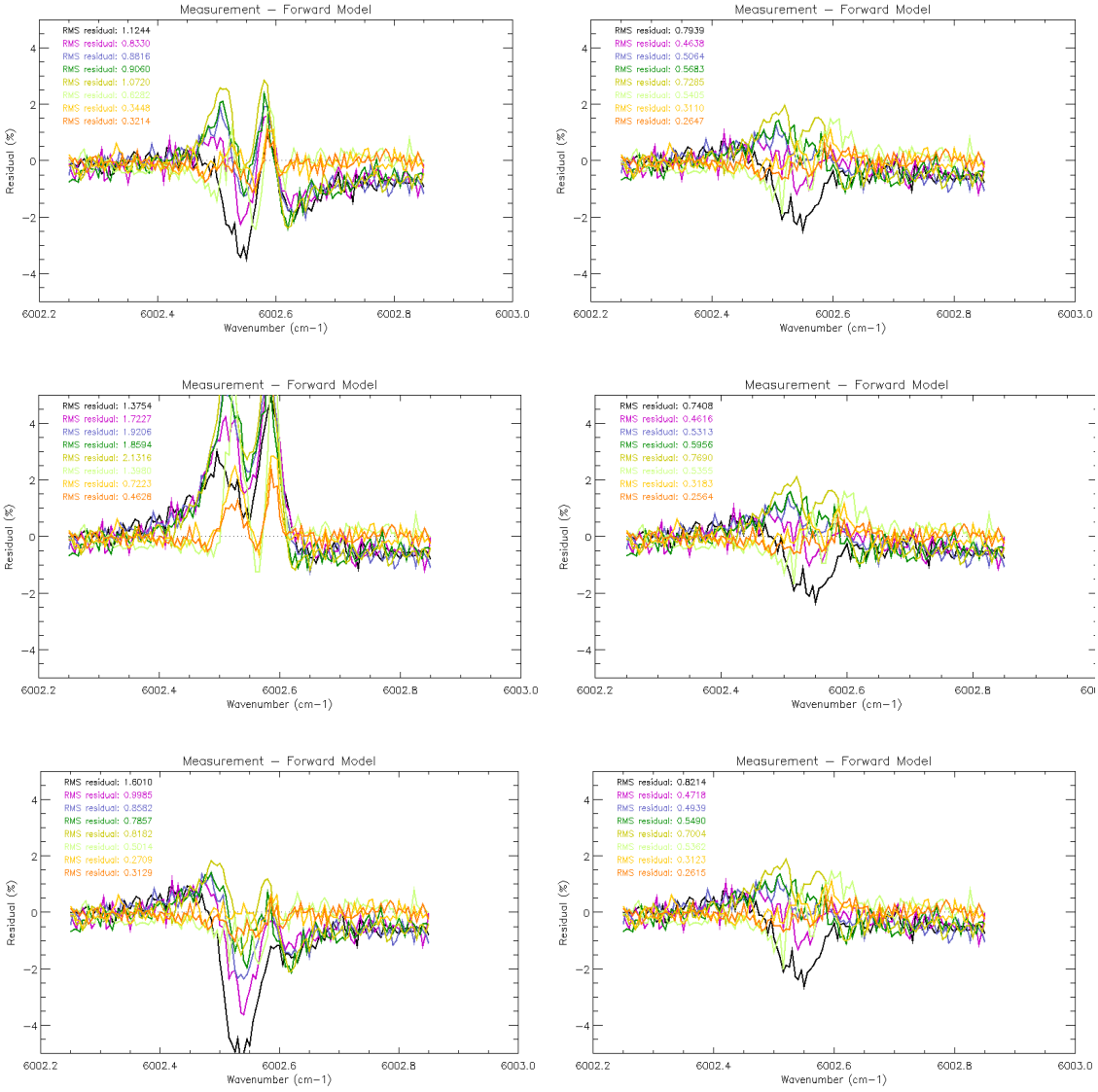

Figure 5.11. *Spectral residuals before (left) and after (right) optimal estimation of line parameters for the Q5 manifold, assuming three different a priori states. Top: HITRAN 2008; middle: HITRAN 2008 with intensity increased by 10%; bottom: HITRAN 2008 with air-broadening increased by 10%*

The examples in Figure 5.11 illustrate the success of the LPC code in this respect. The top row shows the initial and final spectral residuals assuming HITRAN 2008 as the a priori. The second and third rows also use HITRAN 2008, but with the intensity and the air broadening parameters respectively perturbed by 10%. In each case, the solution found using the LPC produces spectral residuals which are very similar to those produced when assuming the unperturbed HITRAN 2008 line parameters as the a priori (compare the right hand panels in Figure 5.11).

Number of iterations

The number of iterations taken for the software to converge is a good indicator of the algorithm's stability. Convergence is typically reached within 10 iterations for a variety of different input conditions. Figure 5.12 shows the change in value of four of the parameters for the six methane lines in the *Q5* manifold from their respective a priori values, as a function of the number of algorithm iterations computed. Each color corresponds to a different line, whilst the four parameters are denoted in the plot by different shapes. The change in each value from its a priori stabilizes quickly, even for a relatively complex case such as this. This plot corresponds to the change in spectral residual observed in the top row of Figure 5.11 (HITRAN 2008 used as the a priori).

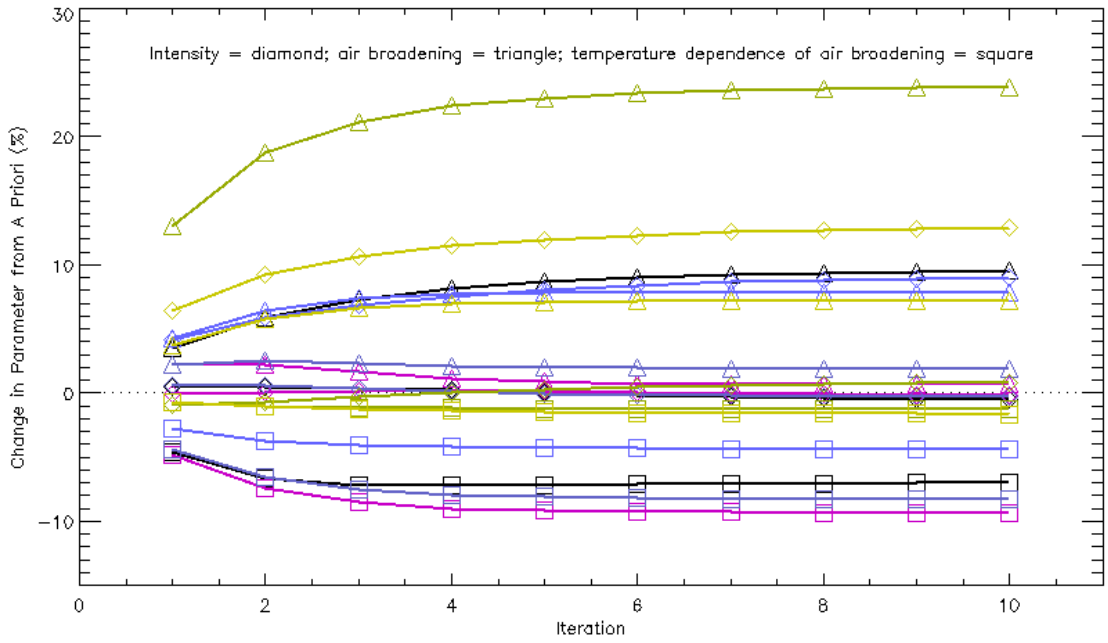

Figure 5.12. *Change in line parameters from their a priori values as a function of algorithm iteration. The colors correspond to different lines in the spectral range considered (in this case the Q5 manifold), whilst the shapes denote the four different parameters plotted here.*

Sensitivity to a priori uncertainties

From equations (2.14) and (2.16) (see Section 2.2.6) one can notice that the broadening parameters are connected. That complicates task of the retrieval of these parameters from the experimental spectra, since, generally, not only one set of the coefficients can be found as a solution. This task becomes especially complicated in case of unresolved manifolds. For example, according to the equation (2.14), increase of the temperature dependence ***n*** might be compensated by decrease of the air-broadened width γ_{air}.

The direction of perturbation depends on the sign of the difference between the measured and forward modelled spectra (forward model based on parameters obtained during previous iteration), and on the sign of the Jacobian (which depends on whether a positive change in the parameter results in a positive or negative change in the spectra). The perturbation can therefore be positive or negative depending on which of these reduces the measurement-model spectral residual. Figure 5.13 shows example transmittance Jacobians for the *R0* line. Some parameters have opposing effects on the spectrum (e.g. intensity and air-broadening), so care needs to be taken in selecting appropriate a priori uncertainties as these determine the magnitude of the Jacobians.

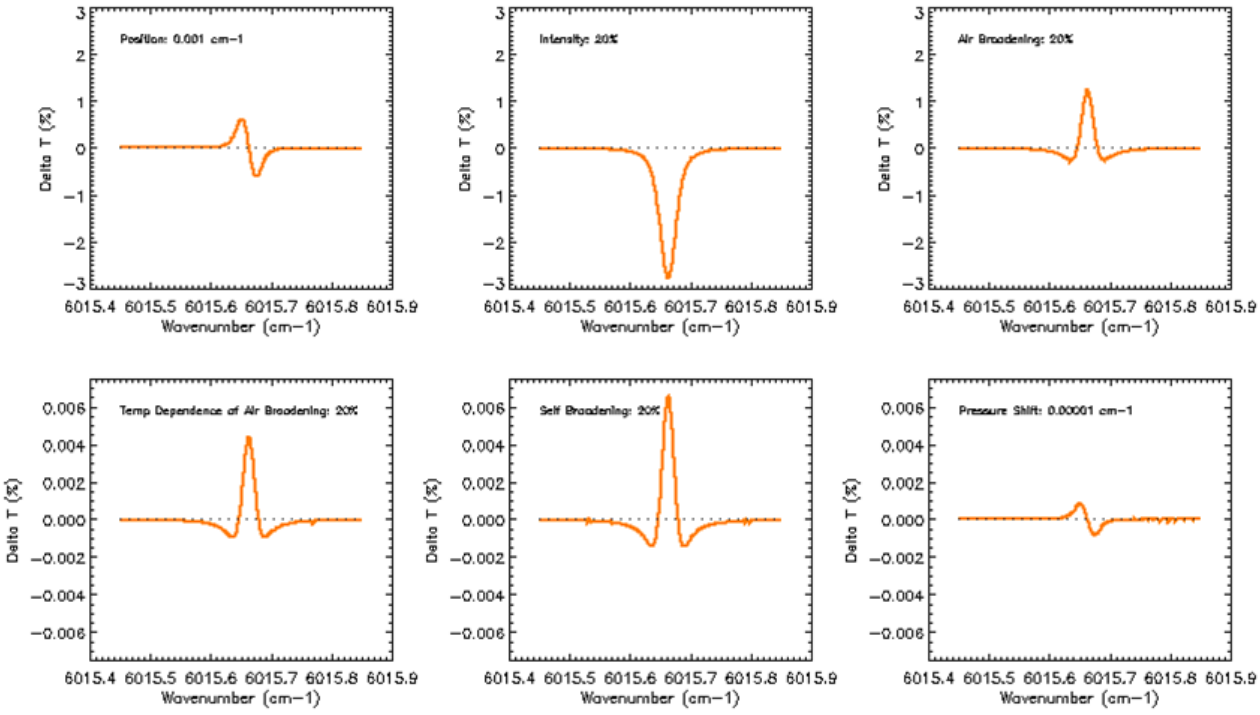

Figure 5.13. *Example Jacobians for the R0 line assuming the following a priori uncertainties: transition frequency 0.001 cm^{-1}; intensity 20%; air-broadening 20%; temperature dependence of air broadening 20%; self-broadening 20%; pressure shift 0.00001cm^{-1}atm^{-1}.*

5.3. Results analysis and comparisons

5.3.1. Selected set of experimental data used for computation

For computation of the line parameters numerous combinations of the experimental and reference data were available (Table 5.4). Reference data are initial line positions and line strength and four broadening parameters. HITRAN 2008 line list was used as reference datasets for initial line parameters assumption in the computation code.

Experimental data can be divided into several groups (Table 5.6).

Table 5.6. *Spectra used for intermediate and final calculations*

	Experimental data	Reference data	Output data
1	All T, all p, N_2	HITRAN 2008, ν, S, γ_{air}, γ_{self}, n_T, δ	γ_{air}, γ_{self}, γ_{N2}, γ_{O2}, n_T, δ, error codes
2	All T, all p, O_2		
3	All T, all p, N_2, O_2		
4	**All T, all p, air**		

The following a priori uncertainties (see Section 5.2.1.1) have been used for generation of the methane line parameters file, referred to as IUP-LP:

- wavenumber: ±0.005 cm-1;
- line intensity: ±10%;
- air broadening coefficient: ±50%;
- temperature dependence exponent: ±50%;
- self broadening coefficient: ±50%;
- pressure shift: ±0.5 cm^{-1}.

Therefore, wavenumber and line intensity were essentially fixed, whereas the other four line parameters were allowed to significantly deviate from the HITRAN 2008 values. This agreed with the objectives to improve the four broadening parameters. Tight constrains on line strengths and positions were especially important for calculations of line parameters for the unresolved manifolds.

Line parameters were obtained from mixtures of methane with air at four concentrations (five temperatures each). The same has been done for mixtures of methane with oxygen and methane with nitrogen. Due to software limitations (the output broadening and pressure shift values in output file correspond to the N_2/O_2 broadening/pressure shift only (i.e. not air broadening/pressure shift) and they need to be added together as described in **/Lyulin et al., 2009/** (*f(air) = 0.79*f(N_2)+ 0.21*f(O_2)* where *f* is the parameter) to obtain the appropriate values for air), i.e., the latter two results do not provide any new information compared to synthetic air/methane spectra processing.

Therefore, IUP-LP file is based on the multispectral analysis of the spectra of methane broadened by air at all temperatures and all pressures with HITRAN 2008 as initial data (group 6, marked red in the Table 5.6) and covers the 5934 - 6154 cm^{-1} spectral range.

As discussed above, the format of the resulting line parameter file is same as used for the HITRAN 2008. It contains the records for 776 lines falling within the 5934 - 6154 cm^{-1} spectral range. For every line, updated values (compared to HITRAN 2008) are given for the air- and self- broadening coefficients, the temperature dependence exponent and the pressure-induced shift. Error codes corresponding to these four parameters are also modified (calculated as described in Section 5.2.1.3). Other parts of the record are left unchanged and coincide with those of HITRAN 2008.

GOSAT line list (Section 2.6.2) is an alternative database, which was partly included in the latest version of HITRAN, i.e., HITRAN 2012. HITRAN 2012 was released in early June 2013. The HITRAN 2012 line list contains significantly more lines (especially week ones, not observed in the measured absorption spectra) than the HITRAN 2008 edition, making computations very time consuming.

Other combinations listed in the Table 5.6 were used for intermediate analysis and to produce selected data for N_2 or O_2 broadened spectra to ensure the stability of the algorithm output. Broadening coefficients for nitrogen and oxygen were also used for comparison with the published data and additional verification of the software.

More details on comparisons of the broadening parameters with broadband datasets, in selected manifolds and narrow-band studies are given in Section 5.3.

5.3.2. Direct evaluation of the new line parameters

This section includes a demonstration of how changes in the pressure broadening parameters (including its temperature dependence) lead to improvements in the spectral residuals between the forward modelled spectra and the laboratory measurements. These improvements are limited, however, since only Voigt line-shapes were considered for calculation of the forward model spectra. Thus, the line parameters retrieved may only be thought of as 'effective' line parameters, suitable only for use when Voigt line-shapes are assumed in spectral calculations (see **/Tran et al., 2010/** for further discussion on this point).

Quality of the data on the pressure broadening coefficients can be analyzed by several approaches:

1. Tests that can be used to determine the success with which the analysis software converges on a solution were described in the Section 5.2.3.
2. Comparison of observed and model spectra based on original HITRAN 2008 and IUP-LP coefficients. This is possible via consideration of residuals between the new experimental data in the wide temperature

and pressure range and corresponding modelled spectra obtained using the IUP-LP coefficients from the LPC software (Section 5.3.2.2).

Failure to reproduce the experimental data reveals:

- imperfection of the pressure broadening coefficients;
- noise in the particular experimental spectra;
- chosen line shape, which might be influenced by line coupling or other effects (see Section 2.2.5).

3. Direct comparison of the new coefficients with the data included in the HITRAN 2008 is a simple and logical step in the analysis of the new data. The comparison between the new data and HITRAN 2008 data will be presented below. Comparison with other recent data (for example, HITRAN 2012, GOSAT line list **/Nikitin et al., 2011/**) in selected wavelengths, and comparison with the data obtained for other bands will also be demonstrated.
4. Testing of the new data in the atmospheric retrievals of the SCIAMACHY, GOSAT instruments and TCCON network, Section 5.3.3.

Overview of the data contained in other datasets.

Table 5.7 contains information on some parameters of the broadband datasets in the region 5934 - 6154 cm^{-1}.

Table 5.7. *Comparison between broadband datasets*

	This work (IUP-LP)	HITRAN 2008	HITRAN 2012	GOSAT-2010
# of lines	776	776	7755	3319
Lowest intensity	10^{-24}	10^{-24}	$4\ 10^{-27}$	10^{-26}
# of lines S>10^{-24}	776	776	1888	1776
# of lines 10^{-25}<S< 10^{-24}	-	-	2940	1376
# of lines 10^{-26}<S<10^{-25}	-	-	2579	165
# of lines S<10^{-26}	-	-	345	-
# of lines: **$^{12}CH_4$** **$^{13}CH_4$**	 710 66	 710 66	 5532 2223	 2857 462
Line positions	/Margolis et al., 1988/ /Margolis et al., 1990/		/Zolot et al., 2013/, 86 lines /Campargue et al., 2012b/, /Campargue et al., 2012a/ Isotope, 6 lines /Lyulin et al., 2010/ Isotope, 2217 lines	/Nikitin et al., 2010/
Line intensity	/Margolis et al., 1988/ /Margolis et al., 1990/ /Frankenberg et al., 2008/		Campargue et al., 2012b/, 5532 lines Campargue et al., 2012a/, Isotope, 6 lines /Lyulin et al., 2010/, Isotope, 2217 lines	/Nikitin et al., 2010/
Air broadening	New	/Rinsland et al., 1988/ /Rinsland et al., 1988/, scaled by 0.95	Averaged widths by J (assigned/estimated from empirical lower-state energy), 6799 lines Updated algorithm described in /Brown et al., 1992/ (averaging by J, C and DJ)	/Nikitin et al., 2010/
Self-broadening	New	HITRAN 1986	Updated algorithm from /Brown et al., 1992/ (averaging by J, C and DJ)	/Lyulin et al., 2011/
Temperature dependence	New	HITRAN 1986	/Brown et al., 2003/	/Nikitin et al., 2010/
Pressure induced shift	New	HITRAN 1986	Calculated using empirically derived approximation: shift = -2×10-6 × (line position).	/Nikitin et al., 2010/

As can be seen from Table 5.7, both the HITRAN 2012 and GOSAT 2010 contain significantly more lines compared to the HITRAN 2008 compilation, which was used for initial values for the line parameters calculations in this work. However, the majority of these new lines have intensity below 10^{-24} cm^{-1}/(molecule x cm^{-2}) and are not relevant for this study. Still, the new compilations are almost three times larger than the old HITRAN 2008 database.

5.3.2.1. Model-based evaluation

In this section, comparisons of experimental and modelled spectra are shown for several different pressures, temperatures and spectral regions together with the relative difference in percent (e.g., Figures 5.14a and b). The figures have been produced by the LPC software. Different colors denote the different experimental conditions. Orange and yellow colors represent measurements done at moderate total pressure of about 125 and 130 mbar, whereas other colors present measurements at 500 mbar at different temperatures.

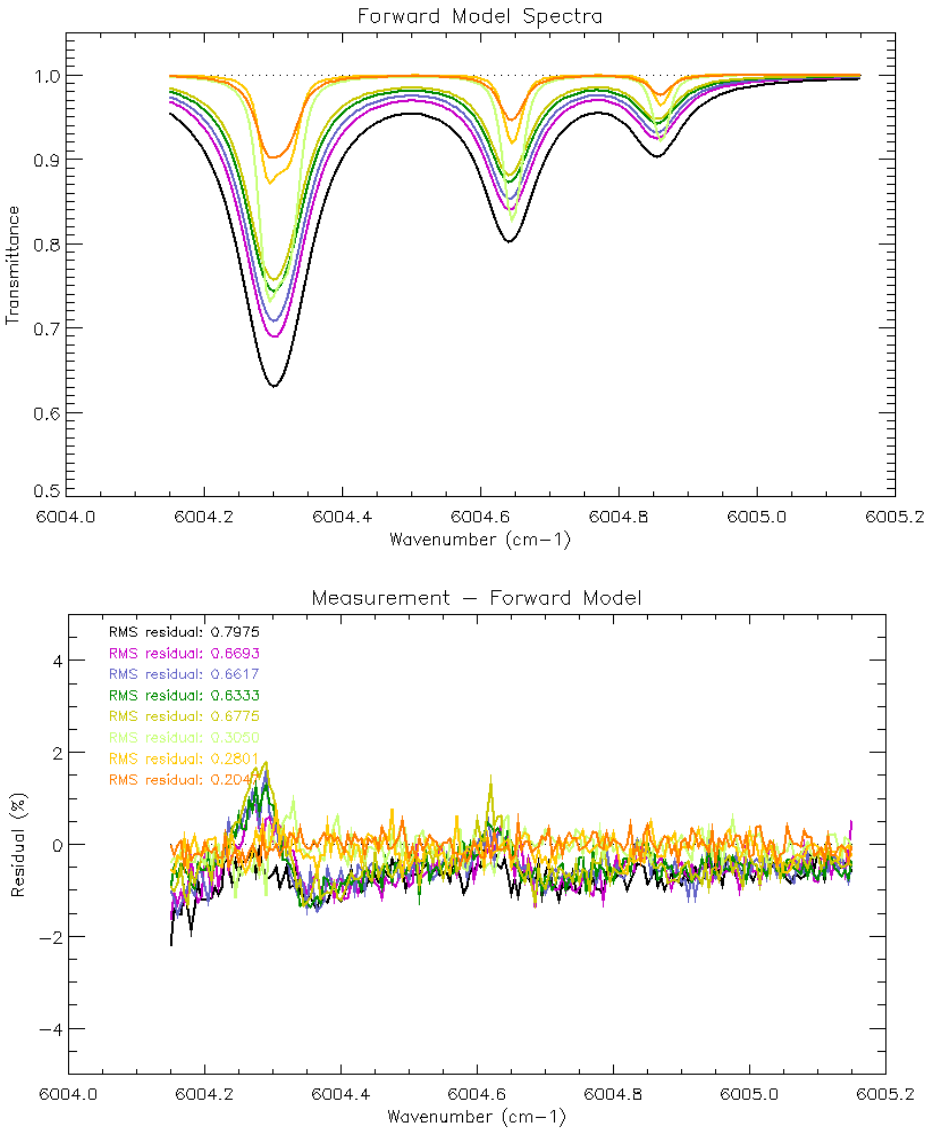

Figure 5.14a. *LPC calculations for part of the Q-branch using "original" HITRAN 2008 line parameters*
Upper panel: synthetic transmittance spectra,
Lower panel: difference between the measured and synthetic spectra

Lower panels demonstrate that use of the new coefficients allows residuals to be reduced significantly in those cases when pressure broadening plays an important role.

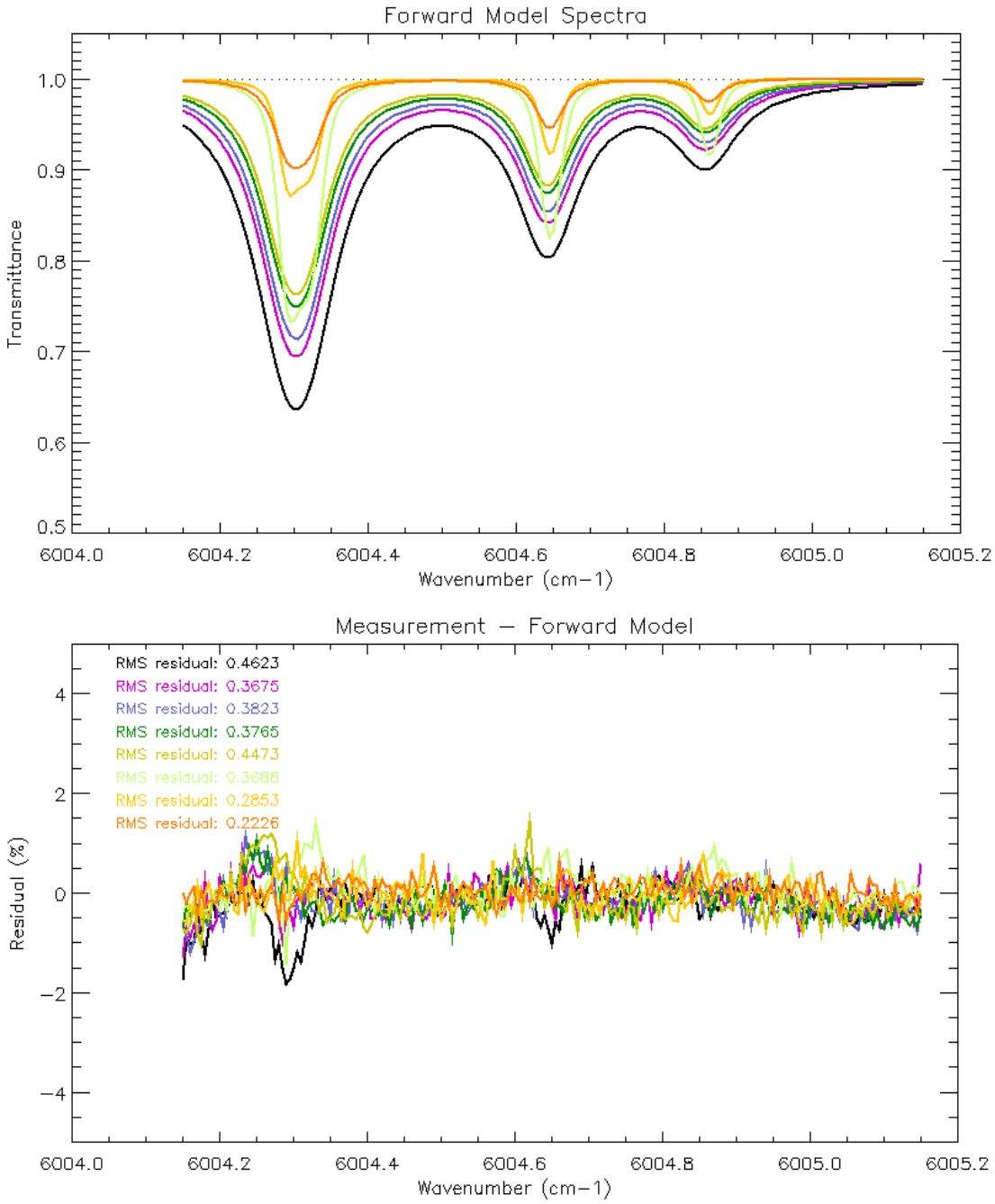

Figure 5.14b. *LPC calculations for part of the Q-branch using IUP-LP line parameters*

Upper panel: synthetic transmittance spectra,

Lower panel: difference between the measured and synthetic spectra

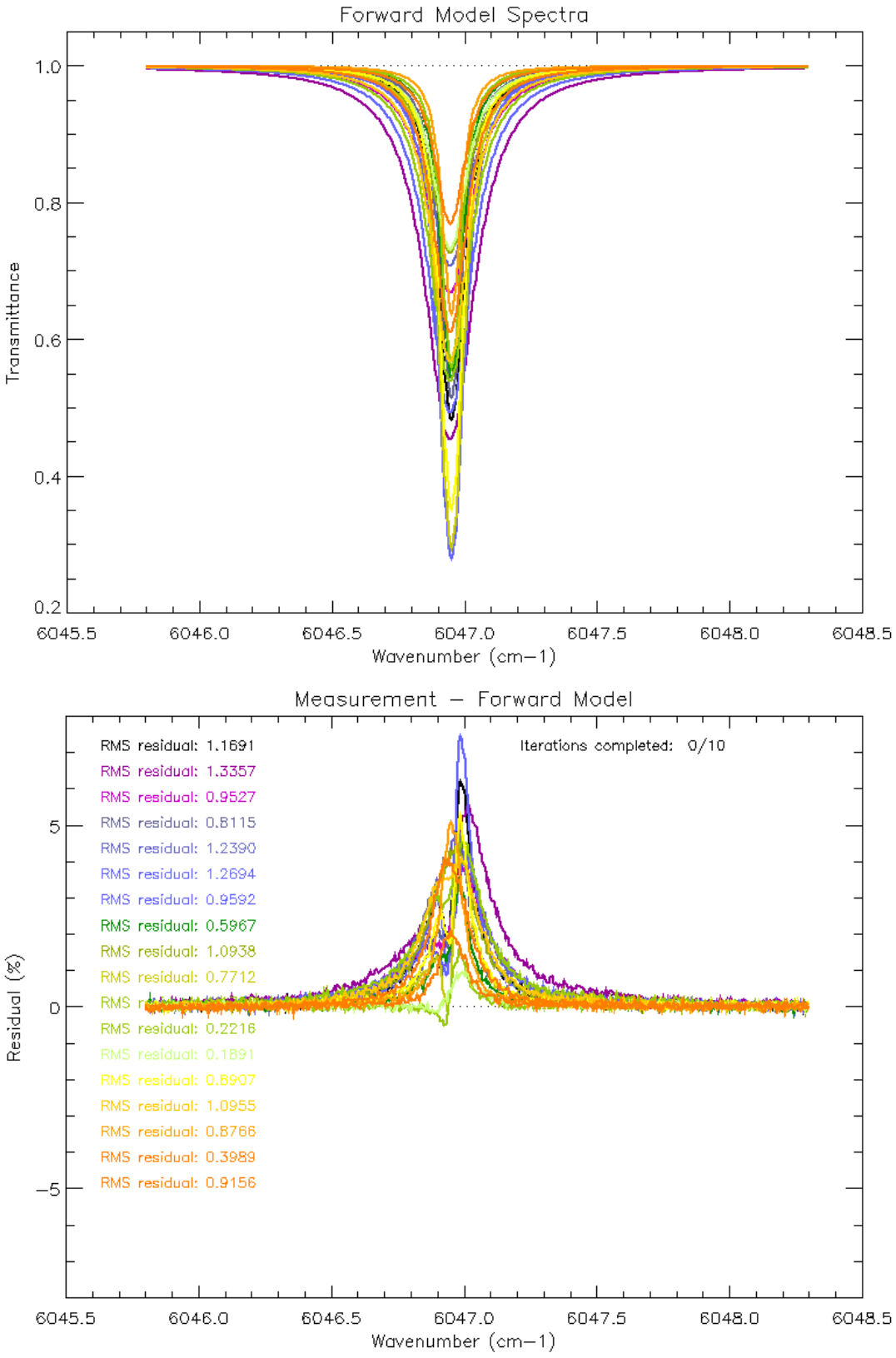

Figure 5.15a. *LPC calculations for R3 manifold using the "original" HITRAN 2008 line parameters*
Upper panel: synthetic transmittance spectra,
Lower panel: difference between the measured and synthetic spectra

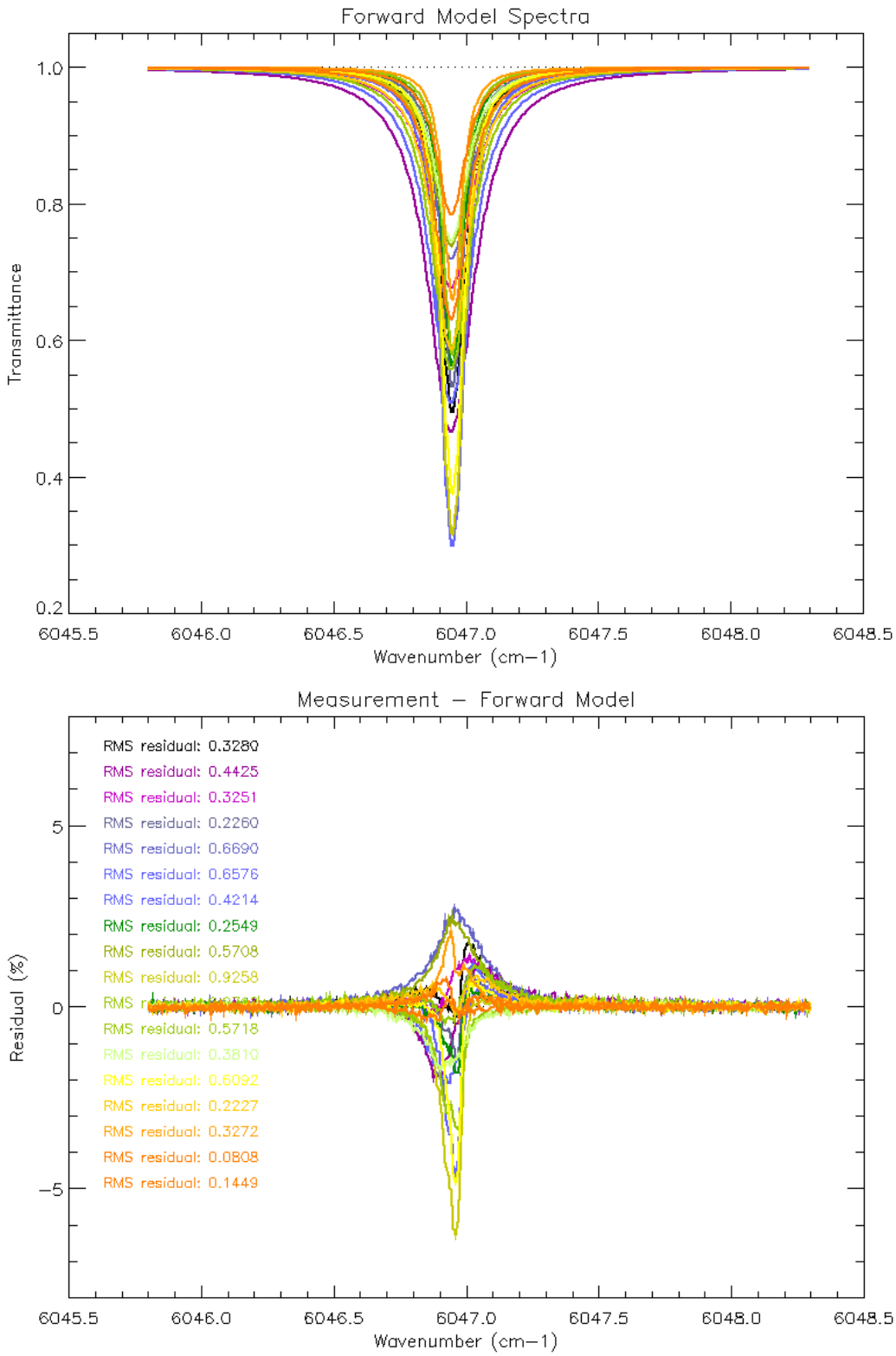

Figure 5.15b. *LPC calculations for R3 manifold using IUP-LP line parameters*
Upper panels: synthetic transmittance spectra,
Lower panels: difference between the measured and synthetic spectra

5.3.2.2. New line parameters vs. HITRAN 2008

Line parameters from generated IUP-LP file were compared with data from HITRAN 2008.

Overview of a broadband value-by-value comparison for four parameters is presented in Figure 5.16.

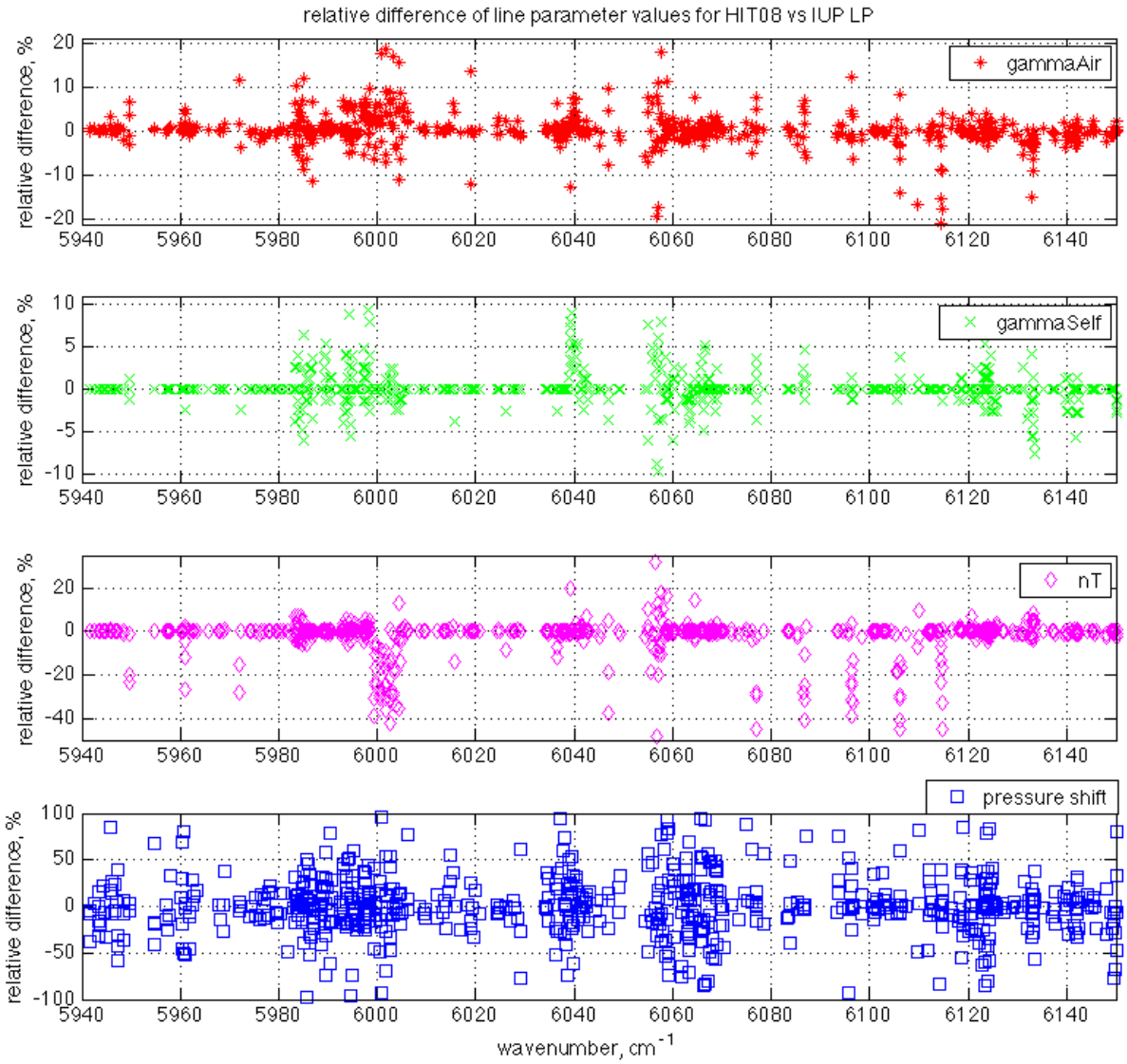

Figure 5.16. *Relative difference, (HITRAN2008 - IUP-LP) / HITRAN2008, between HITRAN 2008 and the IUP-LP data as a function of wavenumber for the investigated parameters.*

More details on new line parameters and difference with the HITRAN 2008 parameters are shown in Figures 5.17-5.20. Difference is given in percent relative to the HITRAN 2008 parameters.

Air- and self-broadening coefficients

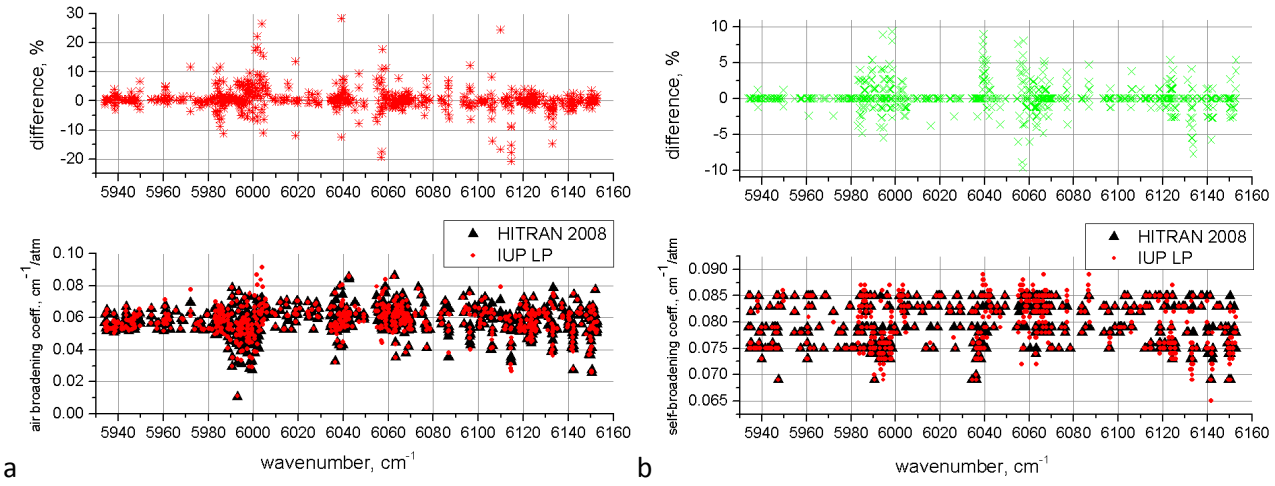

Figure 5.17. ***(a)*** *Air- and* ***(b)*** *self-broadening coefficients*
Upper panel: difference between the IUP-LP data and HITRAN 2008 data
Lower panel: IUP-LP data and HITRAN 2008 data

Temperature dependence and pressure-induced shift coefficients

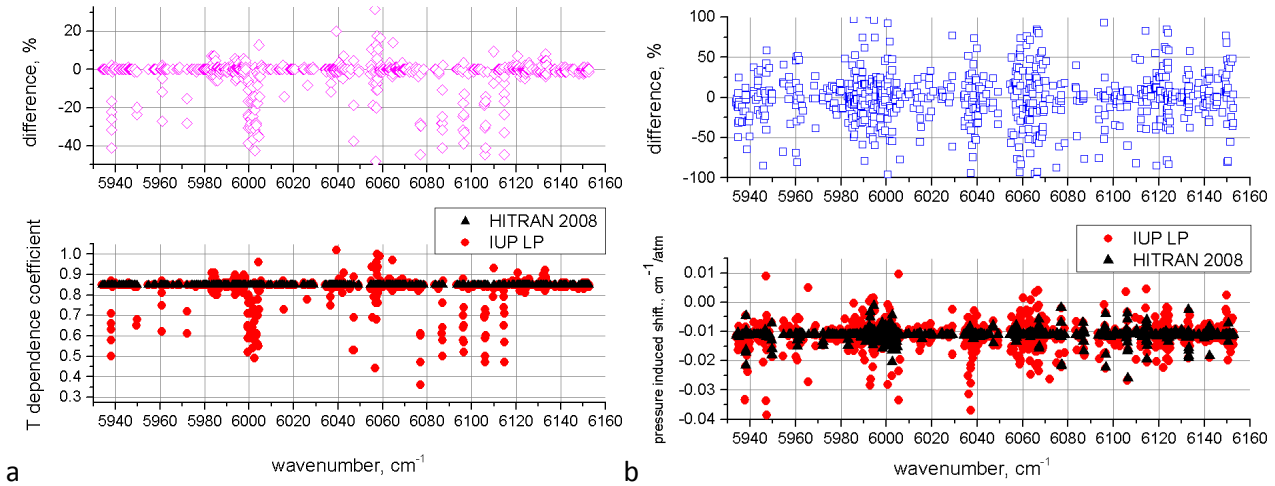

Figure 5.18. ***(a)*** *Temperature dependence and* ***(b)*** *pressure induced shift coefficients*
Upper panel: difference between the IUP-LP data and HITRAN 2008 data
Lower panel: IUP-LP data and HITRAN 2008 data

The new values obtained using the LPC are different for different lines. No apparent trend in deviations is noticeable for air-broadening coefficient (Figure 5.16, 5.17.a).

New self-broadening values also don't seem to follow common deviation trend, being slightly higher in some manifolds and slightly lower in other (Figure 5.16, 5.17.b).

It can be seen from Figures 5.16, 5.18.a that the temperature dependence coefficient as taken from the HITRAN 2008 is constant over broad spectral region. IUP-LP data demonstrates roughly the same pattern, with exception of values at strong lines and in manifolds.

Pressure-induced shift value distribution follows the same pattern as HITRAN 2008. Several outliers having positive values are noticeable. This shouldn't normally happen and might be the result of a trade-off LPC algorithm makes to compensate the variation of width by adjusting temperature dependence and shift.

Another way to analyze and demonstrate the differences between IUP-LP line parameters and ones from HITRAN 2008 is presented in Figures 5.19-5.20.

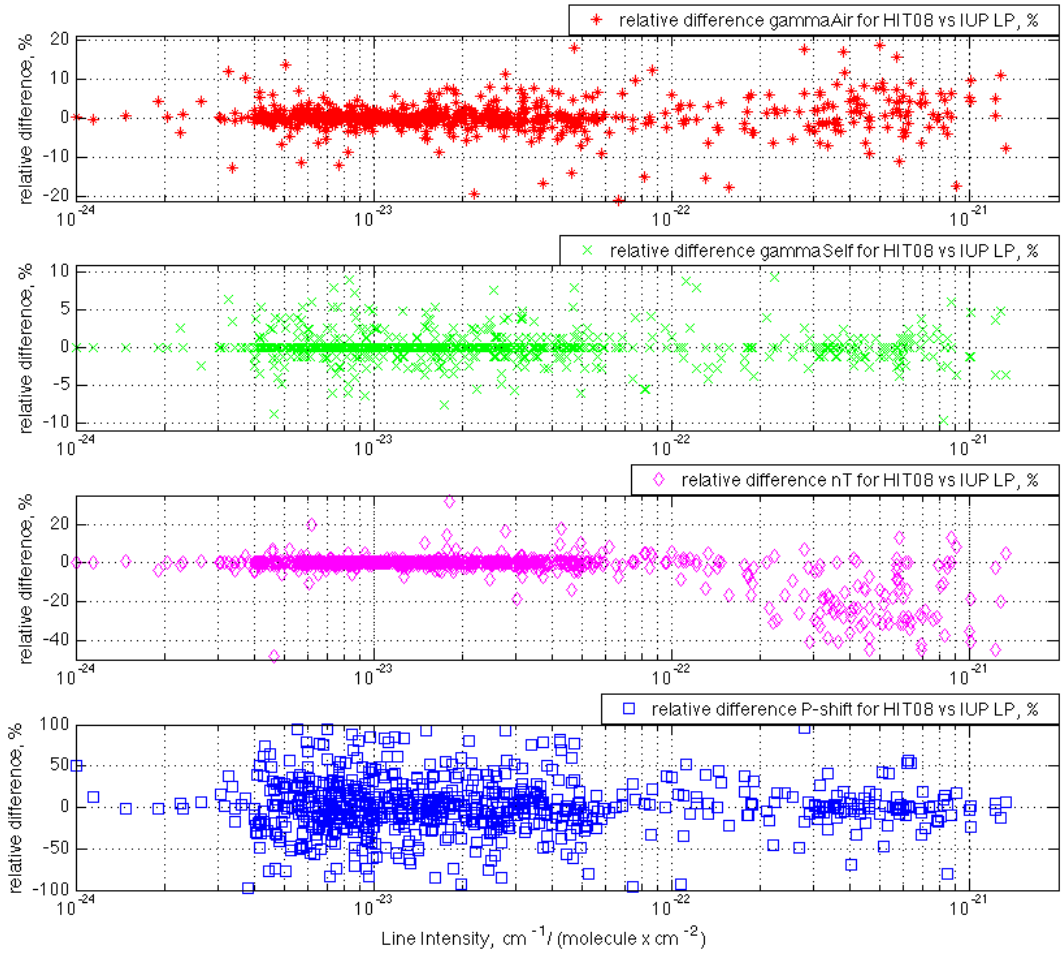

Figure 5.19. *Relative difference [(HITRAN2008 - IUP-LP) / HITRAN2008] between HITRAN 2008 and IUP-LP data as a function of line intensity for investigated parameters.*

Figure 5.19 shows the dependence of parameter value change from the HITRAN 2008 depending on the line intensity. For the broadening coefficients, there is almost no strong correlation between the line intensity and the likelihood for γ_{Self} or γ_{Air} to deviate more or less from HITRAN 2008. Values of temperature dependence n (nT in Figure 5.19) tend to be lower for stronger lines, whereas the pressure shift demonstrates more variability for the weaker lines.

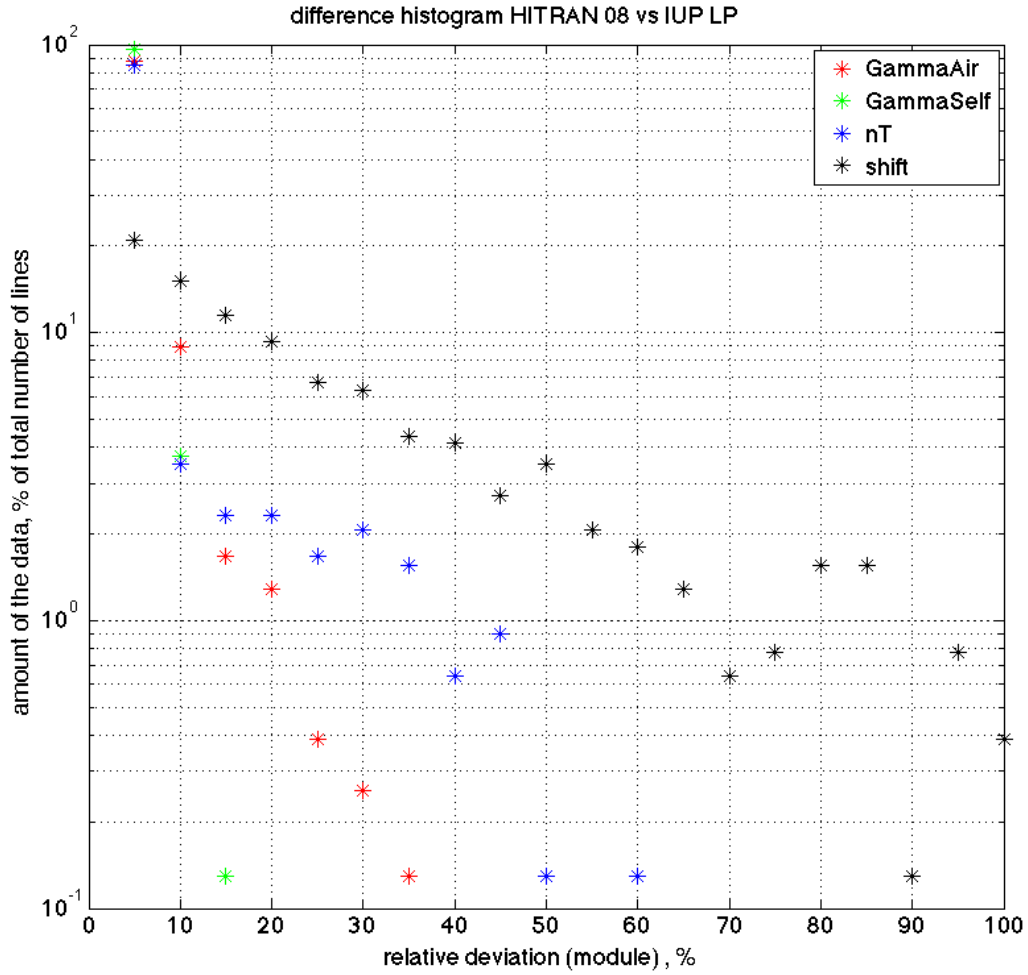

Figure 5.20. *Histogram demonstrating the amount of data within the certain range of relative deviation. Every point marks the percentage of lines for which absolute value of relative difference abs[(HITRAN2008 - IUP-LP)/HITRAN2008] of a certain line parameter falls within particular range.*

5.3.2.3. Comparison with other data in selected manifolds

Lines P1, Q1, R0, R1 and unresolved manifolds R3 and R4

In this section a comparison is given between the shifts, temperature dependence and broadening coefficients for different perturbing gases, as obtained by different researchers for *R0, R1, Q1, P1* isolated lines and *R3* and *R4* manifolds as was described in the Section 2.6.2. Currently, a number of investigations are accumulated, which allows enhanced comparison. Information on the symmetry of energy levels of the considered transitions is given in the Appendix 2.

The isolated lines *R0* at 6015.664 cm^{-1} and *R1* at 6026.227 cm^{-1} were measured by many researchers **/Margolis, 1988, 1990/, /Frankenberg et al., 2008/, /Lyulin et al., 2009/**. Some of them used these lines for precise calibration of the pressure and temperature in the experiments **/Frankenberg et al., 2008/**. Such calibration was performed in this study as well. Analysis of the parameters of the isolated lines is especially advantageous for early tests of the software, since the relatively simple structure provides the direct access to the needed information under the assumption of the Voigt profile.

The *R3* triplet consists of three closely positioned lines *F2, F1,* and *A2* at 6046.965, 6046.953, 6046.942 cm^{-1}. *R4* manifold consists of *A1, F1, E, F2* lines at 6057.08, 6057.09, 6057.10, 6057.13 cm^{-1}. These lines are overlapped even under Doppler broadening. Because of the different intensities, the summarized contour is asymmetrical at a low pressure and the position of triplet absorption maximum changes when the pressure increases only due to the broadening effect. Estimation of the shift coefficients for individual lines, for example, by the Voigt contour fitting is hampered because of a large number of fitted parameters. Besides, interference of lines can appear inside the manifold, which further increases the number of the fitting parameters. Another important circumstance affecting the estimating coefficients of shift and, in particular, broadening is the influence of strong adjacent lines. Some of these issues can be solved using the method based on the measurements of the population relaxation of the particular levels, however, this method can be applied only to a very limited spectral regions **/Menard-Bourcin et al., 2007/**.

Results on the broadening coefficients of methane perturbed by different gases are summarized below in plots and compared with the results of the current study.

Air- and self-broadening coefficients

The broadening coefficients observed by **/Zeninary et al., 2001/** follow the trend:

$$\gamma_{CH_4-Ne} < \gamma_{CH_4-He} < \gamma_{CH_4-Ar} < \gamma_{CH_4-Kr} < \gamma_{CH_4-Xe}$$

The qualitative comparison with a hard-sphere collision model has demonstrated the satisfactory qualitative agreement of this trend with the behavior of the product of the mean velocity and collisional cross-section $v\sigma_{coll}$

/Zeninary et al., 2001/. In the supplemental study by **/Kapitanov et al., 2007/**, the pressure dependence of half-widths on all perturbers was found to be nonlinear and similar to that of the Voigt profile for isolated line.

The results obtained from measurements of rotational relaxation by **/Menard-Bourcin et al., 2007/** compare well with the published line broadening studies (Figure 5.21, 5.22).

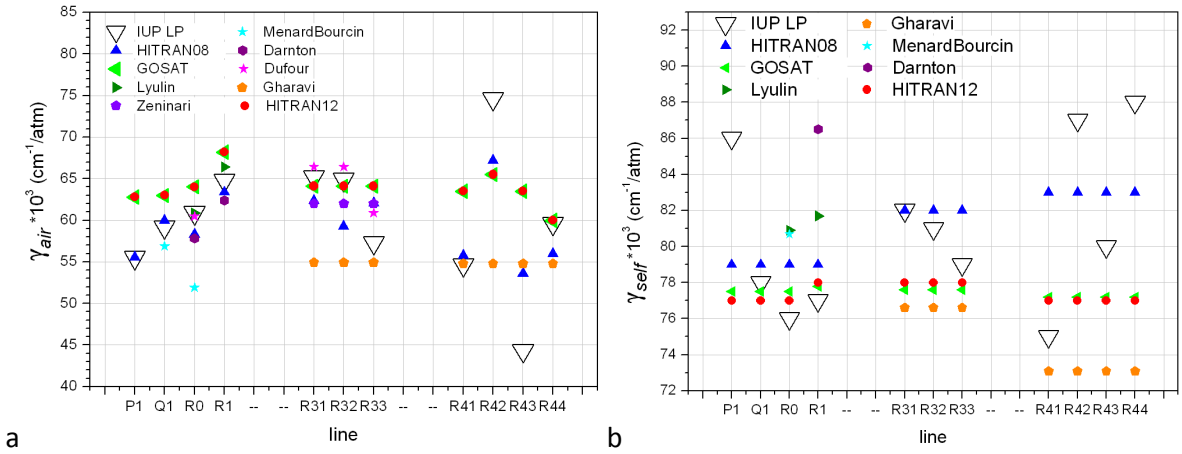

Figure 5.21. *Overview of **(a)** air- and **(b)** self-broadened width coefficients values for P1, Q1, R0, R1 lines and R3, R4 manifolds. See Table 2.7 and Table 5.7 for reference.*

Temperature dependence and pressure-induced shift

The temperature dependence of the data on N_2-broadening by **/Menard-Bourcin et al., 2007/** is particularly well reproduced by the power law deduced from the results on rotational relaxation.

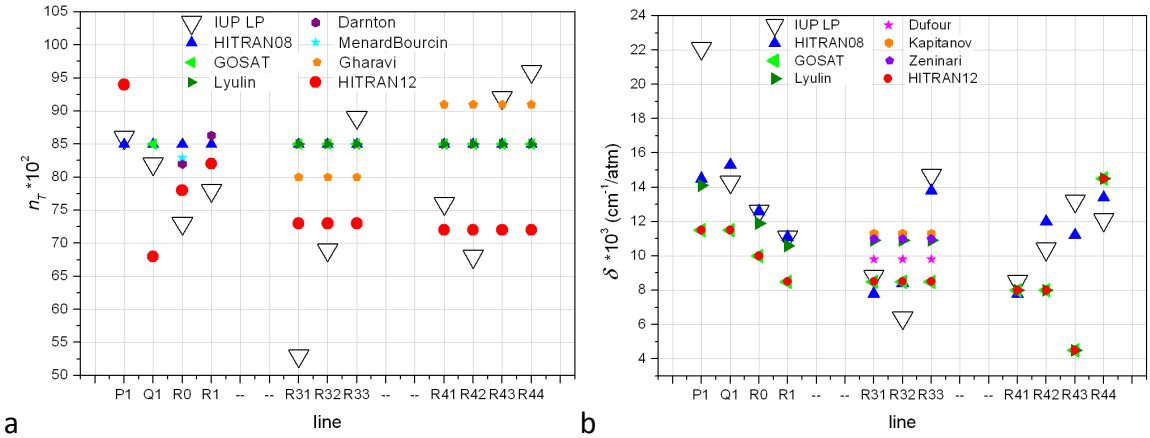

Figure 5.22. *Overview of **(a)** temperature dependence exponent of air-broadened width and **(b)** pressure induced shift coefficients values for P1, Q1, R0, R1 lines and R3, R4 manifolds. See Table 2.7 and Table 5.7 for reference.*

It was also determined by **/Zeninary et al., 2001/** that the shift coefficient of the CH_4 absorption line induced by air linearly increases with the energy of the upper vibrational state. This behavior confirms that the shift value is generally determined by the difference in the polarizabilities of the excited and ground states of the absorbing molecule.

From analysis of the single lines using the Voigt profile, temperature dependence of the shift was found in agreement with the data by **/Lyulin et al., 2011/**. Data are compared in the Tables 5.8a and 5.8b. Dependence is stronger towards higher pressures.

Table 5.8a. *Shift by CH_4*

T, K	*R0*		*R1*		*Q1*	*P1*
	New	**Lyulin**	**New**	**Lyulin**	**New**	**New**
186(6)	-45,8(7)	-23,5	54 (25)	-15,3	41,4(9,3)	35.5(5.7)
223	-34,6(6,8)		35.9 (9)		32,2(10)	28(4)
242(2)	-31(10)	-19	29,6 (10,3)	-18.9	28(7,6)	26,3(5,4)
265(2)	-27(2)		26.8 (1)		26(2,3)	24,6(0,5)
296	-21,9(1,3)	-17,4	20.97(2.2)	-16	22,5(0,5)	21,6(0,4)
All	-30.6(2,8)		-28(3)		30,3(3,1)	28.2 (2.7)
LPC						
Nikitin	-10 (air)		-8.5			
HITRAN08	**-12.562 (air)**		**-11.113**		**-15.295**	**-14.531**

Table 5.8b. *Shift by N_2*

T, K	*R0*		*R1*		*Q1*	*P1*	
	New	**Lyulin**	**New**	**Lyulin**	**New**	**New**	**Lyulin**
193	-17.5 (0.7)		-13.9 (0.5)		23.5 (1.6)	-20 (0.8)	
223	-14.3 (0.4)		-11.9 (0.2)		24.4 (0.2)	-16.1 (0.4)	
242(2)	-13.9 (0.3)	-14.8	-11.1 (0.4)	-12.4	20.5 (1.1)	-16.4 (0.9)	-17.3
265(2)	-12.8 (0.4)	-13.1	-10.5 (0.5)	-11.3	19.5 (0.4)	-13.6 (0.7)	-14.2
296	-12 (0.6)	-12	-10.4 (0.4)	-10.7	16.4 (0.9)	-14.2 (0.5)	-14.2
All	-14.3 (0.8)		-12(0.5)		21.6(1)	-16 (0.9)	
LPC	-15.4 (N2?)		-13.061 (N2?)				
Nikitin	-10 (air)		-8.5		-11.5	-11.5	
HITRAN08	**-12.562 (air)**		**-11.113**		**-15.295**	**-14.531**	

Some data for manifolds from multiple sources (see Table 2.7) is not presented, in particular line parameter coefficients obtained in experiments with N_2, O_2, Ar, He, CO, CO_2, H_2O.

5.3.3. Evaluation using the satellite and ground-based retrievals

In this section, the impact of the new IUP-LP line parameters for satellite and ground-based retrievals of methane is presented and discussed.

Satellite assessment: general approach

Two satellite instruments and corresponding retrieval algorithms were tested:

- the impact on the SCIAMACHY/ENVISAT methane retrievals using the WFM-DOAS (see below) algorithms;
- the impact on the TANSO-FTS/GOSAT methane retrievals using the GOSAT retrieval algorithm.

The general approach is to use the latest versions of these algorithms (including their "default" line parameter data base) and to only replace the used methane line parameters with the new IUP-LP methane line parameters. The impact on the satellite retrieval is assessed by comparison of the data products generated using the new and the current default ("old") line parameters **/ADVANSE2, 2013/**.

5.3.3.1. SCIAMACHY/ENVISAT methane assessment

Retrieval algorithm

The *Weighting Function Modified DOAS* (WFM-DOAS) algorithm (**/Buchwitz et al.,2005a,b/**, **/Schneising et al., 2008, 2009, 2011, 2012/**) is a least-squares method based on scaling pre-selected atmospheric vertical profiles. The column-averaged dry air mole fractions of methane (denoted XCH_4) are obtained from the vertical column amounts of methane by normalizing with the air column, which is determined by simultaneously measured carbon dioxide. CO_2 is used as a proxy for the air column instead of O_2 because of better cancellation of path length related retrieval errors. The corresponding vertical column amounts of CH_4 and CO_2 are retrieved using small spectral fitting windows in the near-infrared/shortwave-infrared (NIR/SWIR) spectral region (1558-1594 nm and 1630-1671 nm, respectively).

Assessment using new line parameters

One year of SCIAMACHY XCH_4 (2004) retrieved using a reference spectra look-up table based on the new line parameters obtained within this project is compared to retrieval results using the HITRAN 2008 spectroscopy in the reference spectra calculation. Except for this difference in the spectroscopic input data, all other settings in both retrieval runs were exactly identical to assess the effect of the new line parameters.

Starting point of the analysis is WFM-DOAS v3.0.2 based on the HITRAN 2008. The data set obtained when changing the spectroscopic data to the new IUP line parameters is referred to WFM-DOAS v3.0.2a. WFMDv3.0.2a is systematically

somewhat smaller than v3.0.2 and is therefore scaled by 1.0075 to be on the same level on average. Monthly means of both runs are compared in Figure 5.23 for April 2004 and Figure 5.24 for September 2004.

As can be seen in these figures, the effect of the new line parameters is small with differences in XCH_4 being of the order of a few ppb. However, the spatial difference patterns are correlated with simultaneously retrieved atmospheric water vapour abundance (r=0.7-0.8), whereby WFMDv3.0.2a systematically exhibits slightly less XCH_4 at locations with enhanced water vapour (e.g. tropics). This can be interpreted as an improvement (albeit small) with regard to the potential methane overestimation in the case of high humidity caused by spectroscopic interference of methane and water vapour **/Frankenberg et al., 2008/**, **/Schneising et al., 2009/**.

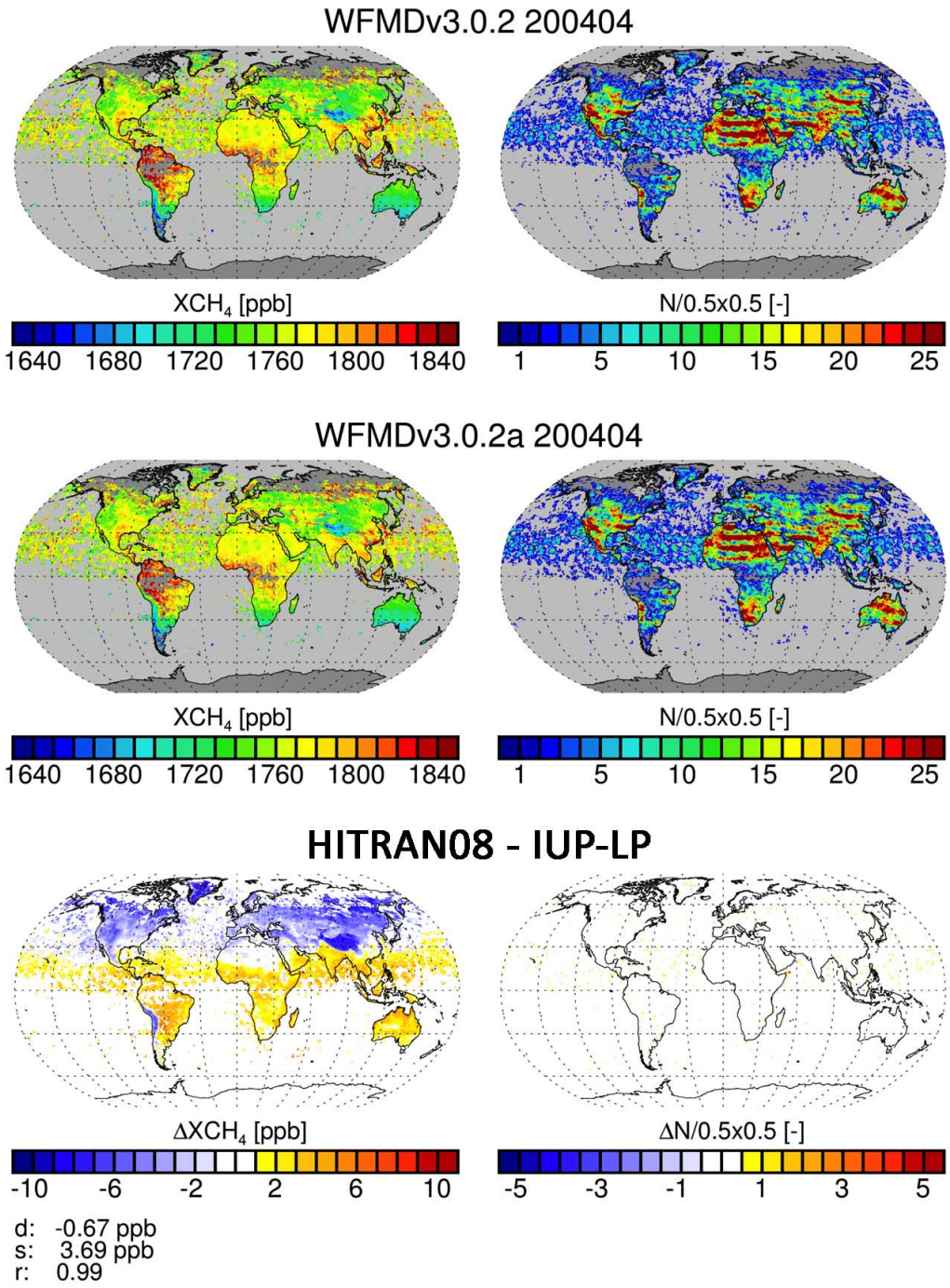

Figure 5.23. *Comparison of WFMDv3.0.2 (based on HITRAN, top panel) and WFMDv3.0.2a (based on IUP-LP spectroscopy, middle panel) for April 2004. Also shown are the differences in the bottom panel as well as following numbers:* ***d*** *is the mean difference of the two datasets,* ***s*** *is the standard deviation of the differences, and* ***r*** *is the correlation coefficient.*

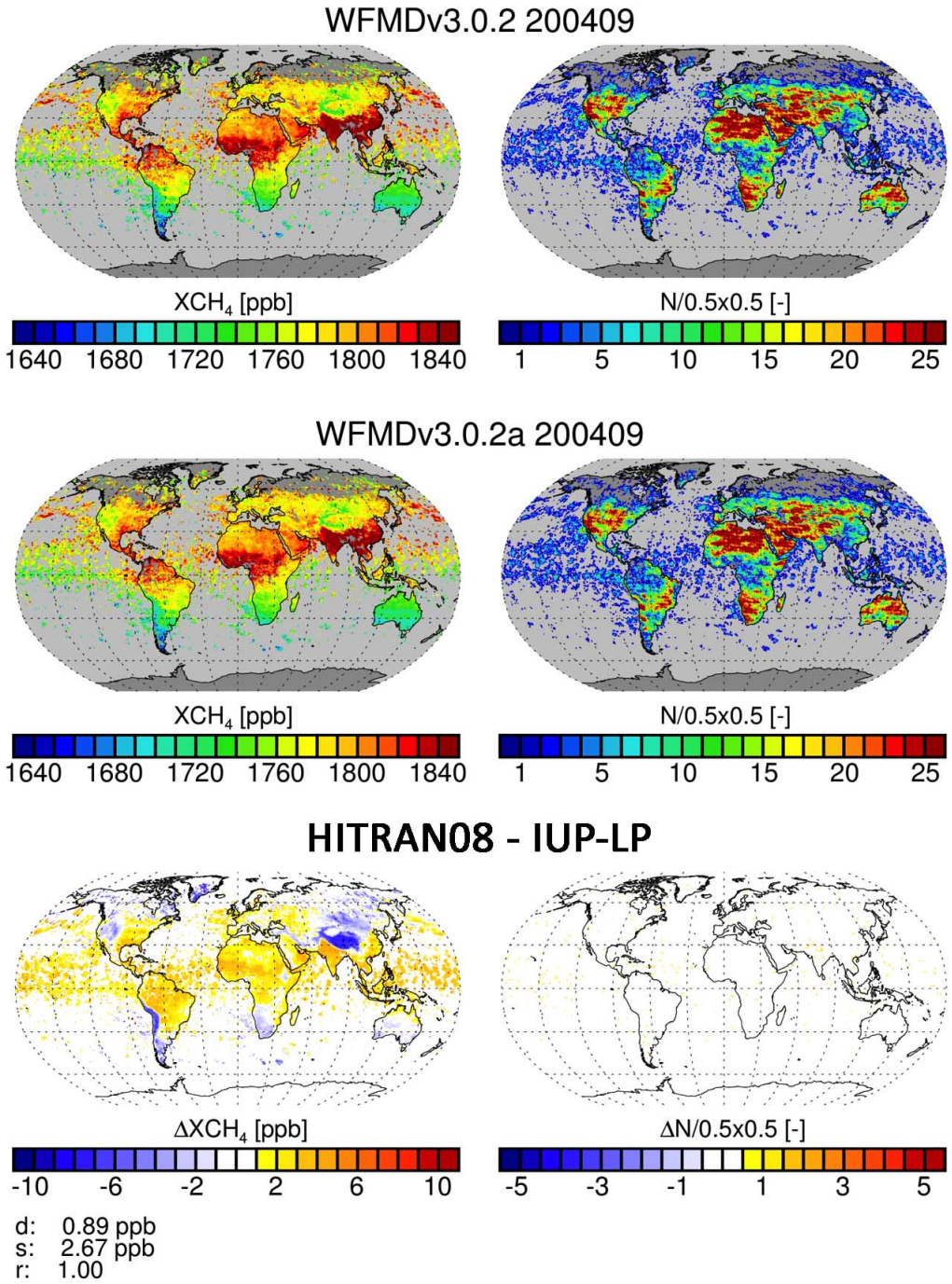

Figure 5.24. *As **Figure 5.23** but for September 2004.*

Figure 5.25 shows the retrieved seasonal cycles of both data sets for both hemispheres. As can be seen, the differences are small with WFMDv3.0.2a exhibiting slightly smaller seasonal cycle amplitudes. As the spatial differences cancel out to some extent for hemispheric means, the effect is typically less than 2 ppb.

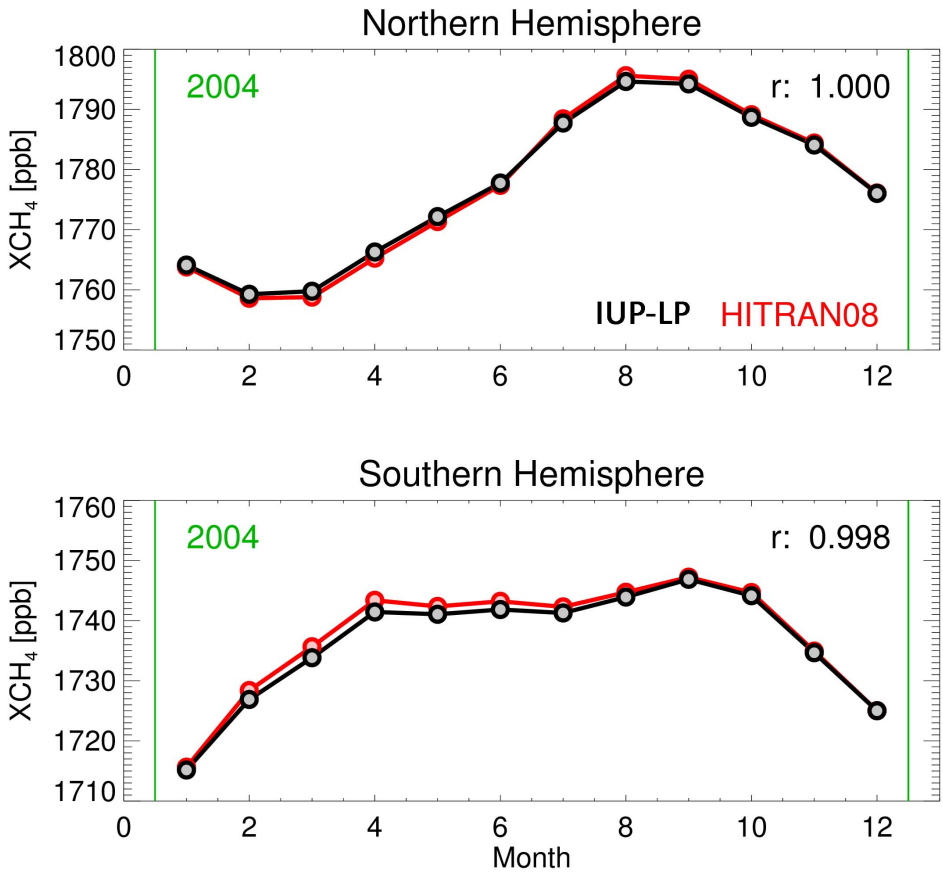

Figure 5.25. *Seasonal cycles for both data sets on the northern and southern hemisphere.*

SCIAMACHY assessment summary

Two SCIAMACHY methane retrieval data sets for the year 2004 have been compared. The only difference between the two retrievals is the spectroscopic input data. The new retrievals have been performed using the new IUP-LP line parameters and by re-processing all SCIAMACHY year 2004 Level 1 files. These retrievals have been compared with an existing data set based on the HITRAN 2008 spectroscopic parameters: WFMDv3.0.2, which is WFMDv3.3 but without a posteriori correction based on simultaneously retrieved water vapour. This approach, which is based on "switching off" the a posteriori bias correction, has been chosen (i) to find out if the currently used a posteriori correction can be avoided in the future and (ii) to avoid possible interpretation issues related to the currently used bias correction **/ADVANSE2, 2013/**.

Initially, the data sets were corrected for a small global offset to better focus on spatio-temporal patterns. Note that this is in line with the user requirements, as relative accuracy is much more important than absolute accuracy. Global monthly maps and hemispheric time series based on monthly means have been compared focusing on relative differences. Only small differences were found. The differences in the time analyzed series are typically much less than 2 ppb. The spatial differences in the monthly maps are on the order of a few ppb (~3 ppb standard deviation of the difference, ~10 ppb max. minus min.). The spatial patterns of the differences HITRAN 2008 - IUP-LP resemble the spatial patterns of atmospheric water vapour (r=0.7-0.8), with higher values in regions with high water vapour abundance, e.g., in the tropics. From this it is concluded that the new IUP-LP methane line parameters are very likely slightly better for SCIAMACHY methane retrieval compared to the currently used HITRAN 2008, because the tropical methane enhancement due to water interference is less pronounced when using the new IUP line parameters. However, due to the smallness of the effect, the a posteriori water vapour bias correction still seems to be advisable.

5.3.3.2. TANSO-FTS/GOSAT methane assessment

This section reviews the result of the GOSAT retrieval algorithm developed by the University of Leicester applied to a large number of GOSAT soundings using the new IUP line parameter list. These retrievals are compared with another set of retrievals which use the 'original' line parameter list **/ADVANSE2, 2013/**. Apart from the different line parameters, the two sets of retrievals are identical. A brief description of the University of Leicester Proxy XCH_4 Product introduces this section. The results are then presented in two parts: retrievals coincident with three of the TCCON sites (Lamont, Bialystok and Darwin) spanning the duration of the GOSAT dataset, and three month-long sets of retrievals covering the whole globe from August to October 2009.

The University of Leicester Proxy XCH_4 Product

The proxy XCH_4 product analysed here is retrieved from GOSAT TANSO-FTS SWIR spectra using the University of Leicester Full-Physics Retrieval Algorithm, based on the original Orbiting Carbon Observatory (OCO) Full Physics Retrieval Algorithm, modified for use on GOSAT spectra.

The retrieval algorithm uses an iterative retrieval scheme based on Bayesian optimal estimation to retrieve a set of atmospheric/surface/instrument parameters, referred to as the state vector, from measured spectral radiances (**/Boesch et al. 2011/**, **/Connor et al. 2008/**). The forward model, used to relate the state vector to the measured radiances, includes the LIDORT radiative transfer model combined with a fast 2-orders-of-scattering vector radiative transfer code (**/Natraj et al. 2008/**).

CO_2 is known to vary in the atmosphere much less than CH_4 and as the CO_2 absorption band is spectrally close to that of CH_4 we can use the CO_2 as a proxy for the light path to minimize common spectral artefacts due to aerosol scattering and instrumental effect. CH_4 and CO_2 retrievals are carried out sequentially with channels at 1.65 μm and 1.61 μm respectively. In order to obtain a volume mixing ratio (VMR) of CH_4, it is necessary to multiply the XCH_4/XCO_2 ratio by a model XCO_2. We obtain the CO_2 VMRs from the LMDZ model (**/Chevallier et al. 2010/**), convolved with scene-dependent instrument averaging kernels obtained from the GOSAT 1.6 µm CO_2 retrieval.

The absorption coefficients used in the University of Leicester Proxy CH_4 Product are based on the same line list as that used in the TCCON retrievals. The CH_4 $2\nu_3$ band uses the line parameters from **/Frankenberg et al. 2008/**, whilst the parameters for the CO_2 lines used are from **/Toth et al. 2008/**. The water vapour line data is taken from **/Toth 2005/** and **/Jenouvrier et al. 2007/**.

GOSAT assessment summary

In order to assess the impact of the IUP-LP line parameters on GOSAT methane retrievals, methane concentrations have been retrieved from the following GOSAT spectral measurements:

- GOSAT measurements from the whole mission duration coincident with three TCCON sites: Lamont, Bialystok and Darwin. These sites represent the full range of different latitudes covered by the GOSAT dataset, and by using the full mission duration it is possible to investigate any seasonality in the effect of using new line parameters.
- GOSAT measurements covering the whole globe for a three-month period in 2009 (August – October inclusive). This dataset has been chosen to provide a global picture of the impact of the new line parameters, and to highlight any regional variations in the impact.

The retrieval is run assuming both the TCCON line parameter dataset (which the University of Leicester use as standard in their proxy methane retrievals) and the new IUP-LP line parameter dataset. All other aspects of the retrieval have been treated identically, including the pre-filtering (e.g. signal to noise ratio > 50), cloud screening and post-filtering (e.g. χ^2 maximum and minimum thresholds).

For the majority of GOSAT observations considered, the retrieved methane concentration is reduced slightly when using the IUP-LP line parameters. Globally, the average reduction is around 0.6 ppbv, though there is some dependence on region and solar zenith angle (at low solar zenith angles the reduction is close to zero (i.e., no change); higher solar zenith angles result in slightly stronger reductions in retrieved methane when using the IUP-LP parameters). Notable exceptions to this overall picture include the Saharan and Arabian desert regions, where using the IUP-LP line parameters in the retrieval leads to an increase in the retrieved methane concentration. Overall, the changes

in retrieved methane are small (within ±2 ppbv) regardless of location, and the quality of the retrievals (as quantified by the χ^2 values) is not changed significantly either **/ADVANSE2, 2013/**.

5.3.3.3. Evaluation using ground-based TCCON retrievals

In this section, results from an assessment of the new methane line parameters are reported based on TCCON retrievals.

TCCON methane retrievals

The Total Carbon Column Observing Network (TCCON) is a global network of ground-based sites measuring near infrared solar absorption spectra (see Section 1.4.1 and **/Wunch et al., 2011/**). Analysis of these spectra allows retrieval of column amounts of CO_2, CH_4, CO, N_2O, H_2O, HDO, HF and O_2. The retrieval of O_2, whose atmospheric abundance is well known, provide a network internal standard as well as calculation of column-average dry-air mole fractions of the other gases. A standardized measurement and retrieval approach allows minimization of inter-site biases, meaning that TCCON is extensively used as the standard for validation of satellite measurements of CO_2 and CH_4. For methane, comparison to coincident profile in situ measurements on board aircraft illustrates that there is a network wide precision of approximately 7 ppb (2-sigma), and a single calibration factor of 0.976 is necessary to bring the xCH_4 into agreement with in situ measurements. The majority of this 2.4% bias is likely due to spectroscopic errors **/ADVANSE2, 2013/**.

Standard spectra acquired within TCCON cover the spectral range from 4000 cm^{-1} to 10 000 cm^{-1} (1 - 2.5 μm) at 0.02 cm^{-1} resolution. Methane is retrieved from these spectra from the 1.6 μm band, using three retrieval windows corresponding to the P-, Q-, and R-branches of this $2\nu_3$ band. The details of the retrieval windows and interfering gases are summarized in Table 5.9.

Table 5.9. *Retrieval windows used for standard TCCON methane fitting*

Microwindow number	Designation/ Central wavenumber (cm^{-1})	Wavenumber range (cm^{-1})	Fitted parameters*	Interfering gases
1	5938	5880.00 – 5996.00	cl, ct, fs, so	CO_2, H_2O, N_2O
2	6002	5996.45 – 6007.55	cl, ct, fs, so	CO_2, H_2O, HDO
3	6076	6007.00 – 6145.00	cl, ct, fs, so	CO_2, H_2O, HDO

cl = continuum level, ct = continuum tilt, fs = frequency shift, so = solar lines

TCCON retrievals are performed using the profile-scaling retrieval routine GFIT. GFIT, developed by Geoffrey Toon at NASA-JPL, is a non-linear least-squares spectral fitting routine that scales an a-priori profile that produce the best match

between a calculated and the measured spectrum. For methane, where three fit windows are used, biases in the retrieved columns between the windows are calculated and corrected, before a weighted-mean vertical column is calculated. All subsequent processing is done using this mean value. Firstly, it is ratioed to the retrieved O_2 vertical column to create an xCH_4. This xCH_4 is calculated for a known airmass-dependent biomass that is at least partly spectroscopic in origin. Following the airmass correction, the final correction is for the calibration factor of 0.976 necessary to make the measurements comparable to the in situ scale.

TCCON uses a spectroscopic line list largely based on the HITRAN 2004 and 2008 **/Rothman et al, 2008/**. For CH_4, the $2v_3$ band on which the TCCON retrievals are based uses **/Frankenberg et al., 2008b/**, with weak CH_4 line from 6180-6220 cm^{-1} provided by Linda Brown. CO_2 lines above 4300 cm^{-1} come from **/Toth et al., 2008a/**, and H_2O from **/Toth, 2005/**, in addition to hundreds of weak H_2O lines identified in humid high airmass spectra, many of which have been subsequently assigned and identified by **/Jenouvrier et al., 2007/**.

The uncertainties reported with individual TCCON xCH_4 values are determined in the following manner: each spectral retrieval has an associated error, determined from the root-mean-square residual to the fit and the continuum level intensity. For the mean column this is again a weighted average between the retrieval windows, but consists of not only a random, but also a systematic component. The systematic component is at least partially removed via the calibration factor, meaning that the error derived from the RMS fits overestimates the measurement reproducibility. To determine the spectrum-to-spectrum variability, the average standard deviation over a Gaussian half-width period of 5 minutes is calculated to derive an "Error Scaling Factor" by which to scale the RMS-derived errors.

To assess the new IUP-LP line parameters using TCCON data, the following six TCCON sites were chosen: Darwin and Wollongong, Australia, Bremen, Germany, Orleans, France, Bialystok, Poland and Ny Alesund, Spitsbergen. These cover a range from southern hemisphere mid-latitudes through the tropics and northern extra-tropics to high polar latitudes. The site details are given in Table 5.10.

Table 5.10. *Sites used for assessment of TCCON retrievals using the IUP-LP CH_4 line parameters*

Site	Latitude	Longitude	Altitude [m]	Operational
Wollongong	34.4°S	150.9°E	30	2008 -
Darwin	12.4°S	130.9°E	30	2005 -
Orleans		2.1°E		2009 -
Bremen	53.1°N	8.9°E	27	2004 -
Bialystok	53.2°N			2009 -
Ny Alesund	78.9°N	11.9°E		2004 -

Spectra for the full year 2010 are used for each site, while the full year 2004 is also used for Ny Alesund and Bremen. This is designed to provide overlap with the reanalyzed GOSAT and SCIAMACHY years. The spectra are fitted with both the standard TCCON line parameters and the IUP-LP CH_4 line parameters. For the

IUP-LP test, all TCCON CH_4 line parameters between 5934 - 6153 cm^{-1} are removed and replaced with the newly generated IUP-LP parameters, while all other gases are unchanged. All other aspects of the retrieval setup are also not varied between the TCCON and IUP-LP fits **/ADVANSE2, 2013/**.

TCCON assessment summary

TCCON spectra from six sites covering southern hemisphere mid-latitudes to high arctic have been used to assess the new IUP-LP line parameters. Comparisons to retrievals using the existing TCCON line parameters show that the differences in retrieved xCH_4 values are small, but up to 5 ppb (0.3%), which is on the order of the precision of the TCCON retrievals. TCCON retrievals fit the *P*-, *Q*- and *R*- branches of the $2\nu_3$ band separately, and the largest differences are seen in the Q-branch, where the different line lists yield retrieved columns that diverge by up to 1%. This behavior is consistent across all sites studied, and each site shows that the differences that occur predominantly track solar zenith angles. Indeed, the IUP-LP parameters appear to exhibit a marginally reduced airmass dependence in comparison to the current TCCON line list. In addition, the IUP-LP parameters show improved consistency between the three fit windows, and a slightly better measurement-to-measurement repeatability **/ADVANSE2, 2013/**.

5.3.3.4. Satellite and ground-based assessments: conclusions

The impact of the new IUP-LP methane line parameters in the 1.6 µm spectral regional for atmospheric methane remote sensing applications has been assessed for the satellite instruments SCIAMACHY and TANSO/GOSAT and using ground-based TCCON FTS retrievals. The latest versions of the corresponding retrieval algorithms and data sets have been used only replacing the default methane line parameters with the IUP-LP line parameters. Overall it has been found that the impact is relatively small, namely on the order of a few ppb (i.e., typically much less than 1%).

For example, for SCIAMACHY monthly maps, the standard deviation of the difference is about 3 ppb, with IUP-LP line parameters compared to HITRAN 2008 line parameters being a few ppb lower in the tropics compared to higher latitudes (or solar zenith angles). The pattern correlates with atmospheric water vapour amounts, which are currently partially a posteriori corrected using a bias correction scheme. The analysis indicates that using the IUP-LP line parameters results in a better methane data product as the need for a bias correction is less relevant if the new IUP-LP line parameters are used.

Similar conclusions can be drawn from the analysis of the GOSAT and TCCON retrievals. Also here the impact is mostly on the order of a few ppb, i.e., relatively small. In contrast to the SCIAMACHY analysis, the solar zenith angle dependence of the difference of the IUP-LP based retrievals and the default retrievals shows an opposite sign: here the methane retrievals based on IUP-LP line parameters

are decreasing with increasing solar zenith angle compared to retrievals using the default line parameters. This is most likely due the fact that both GOSAT and TCCON spectra are at much higher spectral resolution compared to SCIAMACHY (and potential interference issues, e.g., due to atmospheric water vapour, which are relevant for SCIAMACHY, are less important) but probably also due to other reasons such as spectroscopic reference data (note that the default line list for GOSAT and TCCON retrievals are the same ("TCCON line list") but for the SCIAMACHY the HITRAN 2008 is the default line list) and other retrieval algorithm differences.

Overall it can be stated that the new methane line parameters are better for remote sensing of atmospheric methane, compared to the currently used line parameters, but the improvement is relatively small (few ppb) **/ADVANSE2, 2013/**.

5.4. Methane absorption line parameters: conclusions

As a part of the research dedicated to the methane absorption line broadening parameters, numerous transmittance spectra were obtained covering a broad range of the experimental conditions, such as different temperatures, pressures, choice of buffer gases and mixing ratios, using the high resolution Fourier Transform spectrometer. The experimental conditions include those used by former researchers (***/Frankenberg et al., 2008b/, /Lyulin et al., 2009/***).

The experimental methane spectra were obtained for the spectral region from 5934 to 6154 cm^{-1}, covering *P*, *R* and *Q* branches of the $2\nu_3$ methane band. HITRAN 2008 contains 776 lines with intensities ranging from 10^{-24} to 10^{-21} cm^2/molecule (at 296K) for this region.

The obtained spectra have high quality regarding signal-to-noise ratio. The new data reasonably agree with the data of former researchers (e.g., ***/Frankenberg et al., 2008b/***) but are of higher quality with respect to systematic errors and cover more conditions.

The spectra along with the corresponding documentation have been compiled into the Absorption Spectra Data Base (ASDB). The ASDB has been used as input for the line parameters computation code (LPC).

New methane line parameters for remote sensing applications around the 1.6 μm have been generated using the specially developed software. The results are provided in a Line Parameter (IUP-LP) file in HITRAN 2008 format. The following four (HITRAN 2008) methane line parameters related to pressure broadening have been modified / improved (including error codes): air- and self-broadened half widths, exponent for temperature dependence and the pressure shift parameter. All other parameters are identical to HITRAN 2008.

The new IUP-LP line parameters allow the reproduction of experimental spectra across a wide range of pressures and temperatures relevant to atmospheric applications. The spectral residuals are reduced compared to those obtained using the line parameters from HITRAN 2008.

Differences between the new data and the coefficients currently included in HITRAN 2008 are listed in Table 5.11, as a function of the applied degrees of freedom threshold (see Section 5.2). An intensity threshold of $5.0*10^{-23}$ was also applied to filter out very weak lines, for which the parameters are only poorly retrieved.

Table 5.11. *Differences between the new data and the coefficients included in HITRAN 2008*

Degrees of freedom threshold	Number of lines	Mean change in line intensity	Mean change in air broadening	Mean change in T - dependence
0.0	152	1.029	1.034	0.971
0.5	150	1.029	1.035	0.971
1.0	123	1.028	1.041	0.965
1.5	104	1.030	1.046	0.960
2.0	72	1.027	1.051	0.951
2.5	49	1.032	1.058	0.944
3.0	24	1.039	1.064	0.937
3.5	8	1.071	1.103	0.922
4.0	2	1.020	1.072	0.953

The available version of the LPC software, developed and used within this study, does not allow investigation of the impact of line mixing on the retrieved parameters. For the purposes of atmospheric remote sensing applications assuming Voigt profile such 'effective' coefficients are considered appropriate (**/Tran et al., 2010/**). However, due to line-mixing effects, the 'real' coefficients of interest from the standpoint of molecular spectroscopy can differ from the 'effective' ones generated within this study.

The new CH_4 absorption line broadening parameters were tested using the satellite and ground-based retrieval algorithms **/ADVANSE2, 2013/**, demonstrating the relevance for the modern remote-sensing applications.

The ASDB and the methane Line Parameter (IUP-LP) file, derived from the ASDB spectra, are available at the IUP-UB Molecular Spectroscopy Group website http://www.iup.uni-bremen.de/gruppen/molspec/

6. General summary and discussion

Global environmental monitoring is an important activity, which involves collaboration of scientist from all fields of study. Physicist, chemists, biologists, oceanographers, mathematicians and computer scientists, to name a few, are all involved in complex interaction when it comes to understanding such a complicated system as our planet.

Technical advances of the XXth century have taken the capability to perform the instrumental measurements to a whole new level both in terms of coverage (with the beginning of the space exploration era) and accuracy.

However, another by-product of the technical progress is the unprecedented anthropogenic influence on the environment, leading to the change of physical and chemical properties of the atmosphere on a global scale.

The Earth's atmosphere became one of the most important research subjects.

Nowadays, multiple remote sensing methods utilize a wide range of measurement techniques for observation of atmospheric composition.

The character of interaction of molecular species with electromagnetic radiation coming from the sun depends on many parameters. Both the temperature and the pressure influence the absorption pattern, which in turn allows to infer these parameters from the observation data. Modern remote sensing applications rely on the knowledge of the basic spectroscopic properties of species present in the atmosphere.

Uncertainties in the spectroscopic data lead to biases in the retrieved quantities. Therefore, it is crucial to provide the accurate information about the relevant absorption properties of trace gases to remote sensing community.

The demand for the improved spectroscopic data for ozone and methane was main motivational factor for this research.

In course of this study several measurement campaigns and corresponding data processing and analysis have been performed. Laboratory investigations of the absorption properties of methane and ozone were conducted for a wide range of conditions typical for the atmosphere and therefore relevant for remote sensing applications.

Resulting spectroscopic datasets were compared with other published data and, in case of methane, tested on several modern retrieval algorithms.

In comparison with the previously available CH_4 and O_3 datasets, the new data was an improvement for specific applications both in terms of accuracy and coverage of achieved spectral resolutions or temperatures.

The results of the research effort were published in several papers (**/Gorshelev et al., 2014/, /Serdyuchenko et al., 2014/**) and reported on numerous international conferences and symposia.

The new ozone absorption cross-sections and methane line broadening parameters are available for the scientific community.

Multiple researchers have already shown interest for the new spectroscopic data for methane and ozone, meaning that the feedback and further tests on retrieval applications should be expected in the near future.

Acknowledgements.

I would like to express my gratitude to all the colleagues from the Institute of Environmental Physics at the University of Bremen who have helped me to progress with my research.

I would especially like to thank my friend and scientific advisor Anna Serdyuchenko, with whom our team of two was making all the laboratory measurements.

My academic supervisor Professor John Burrows, with his extensive experimental physics background and management skills, provided useful insights for measurement campaigns and facilitated more active interaction in collaborative projects.

I sometimes get too focused on the details, and personal advice from Anna Serdyuchenko and John Burrows, who were always open for discussions, taught me to set the priorities and gave more structure to my work.

Mark Weber and Michael Buchwitz, who were leading the ozone- and methane-related research, provided me with indispensable experience of working on international projects. Their recommendations greatly helped to structure and schedule my activity.

It was a great pleasure to work in collaboration with my colleagues from the Institute of Environmental Physics in Bremen and Department of Physics and Astronomy, University of Leicester, UK, who provided their expertise on analysis of acquired data for the purposes of remote sensing applications. Wissam Chehade, Oliver Schneising, Nicholas Deutscher, Neil Humpage, Hartmut Boesch - made a great contribution to this study.

I would also like to thank the members of IUP FTIR group Thorsten Warneke, Christof Petri and Christine Weinzierl, who helped us with our FTS instrument on many occasions.

This work has been partially funded by the European Space Agency (contracts '"HARMONICS", ESA/ESRIN Contract No. 12160/07/I-LG and "ADVANSE Phase 2", ESA/ESRIN Contract No. 22023/08/I-OL) and the University and the State of Bremen.

References

/ACSO/ Absorption Cross Sections of Ozone (http://igaco o3.fmi.fi/ACSO/cross_sections.html)

/ADVANSE2, 2013/ Serdyuchenko A., Gorshelev V., Buchwitz M., Schneising O., Deutscher N., Notholt J., Burrows J.P. (Institute of Environmental Physics (IUP), University of Bremen (UB), Bremen, Germany), Humpage N., Boesch H., Remedios J. (Department of Physics and Astronomie, University of Leicester (UoL), Leicester, United Kingdom): *"An ADVANced retrieval system for greenhouse gases from SCIAMACHY on Envisat. Phase 2. Final report", 2013*

/Anderson and Mausberger, 1992/ Anderson S.M. and Mauersberger K.: *"Laser measurements of ozone absorption cross-sections in the Chappuis band",* Geophysical Research Letters, 19(9):933-936, 1992

/Anderson et al., 1993/ Anderson S.M., Hupalo P., and Mauersberger K.: *"Ozone absorption cross-section measurements in the Wulf bands",* Geophysical Research Letters, 20:1579-1582, 1993

/Axson et al., 2011/ Axson J.L., Washenfelder R., Kahan T.F., Young C.J., Vaida V. and Brown S.S.: *"Absolute ozone absorption cross section in the Huggins Chappuis minimum (350–470 nm) at 296 K",* Atmospheric Chemistry and Physics, 11:11581-11590, 2011

/Baiamonte et al., 1966/ Baiamonte V.D., Snelling D.R., Bair E.J.: *"Vibrational energy of ozone during photolytic explosion",* Journal of Chemical Physics, 44, 673-682, 1966

/Banichevich et al., 1993/ Banichevich A., Peyerimhoff S.D., and Grein F.: *"Potential energy surfaces of ozone in its ground state and in the lowest-lying eight excited states",* Chemical Physics, 178, 155-188, 1993

/Ballard et al., 1986/ Ballard J. and Johnston W. B.: *"Self-broadened widths and absolute strengths of $^{12}CH_4$ lines in the 1310–1370 cm^{-1} region"*, Journal of Quantitative Spectroscopy & Radiative Transfer, 36:365, 1986

/Barnes et al., 1987/ Barnes J. and Mauersberger K.: *"Temperature dependence of the ozone absorption cross section at the 253.7 nm Mercury line"*, Journal of Geophysical Research, 92(D12), 14861-14864, 1987

/Bass, Paur, 1984/ Bass A.M. and Paur R.J.: *"The Ultraviolet Cross-Sections of Ozone: I. The Measurements."* In: Zerefos, C.S., Ghazi, A., editors. Atmospheric Ozone; Proc. Quadrennial Ozone Symposium. Halkidiki, Greece, 1984. Dordrecht, Reidel, D., 606-610, 1985

/Ben-Reuven et al., 1963/ Ben-Reuven A., Friedmann H., Jaffe J.H.: *"Theory of Pressure-Induced Shifts of Infrared Lines",* Journal of Chemical Physics, 38, 3021, 1963

/Bergamaschi et al., 2007/ Bergamaschi P., Frankenberg C., Meirink J.F., Krol M., Dentener F., Wagner T., Platt U., Kaplan J.O., Körner S., Heimann M., Dlugokencky E.J., and Goede A.: *"Satellite chartography of atmospheric methane from SCIAMACHY onboard ENVISAT: 2. Evaluation based on inverse model simulations"*, Journal of Geophysical Research, 112, D02304, 2007

/Berman, 1972/ Berman P.R.: *"Speed-dependent collisional width and shift parameters in spectral profiles"*, Journal of Quantitative Spectroscopy & Radiative Transfer, 12:1331–1342, 19992, 1972

/Bhartia et al., 2012/ Bhartia P.K., McPeters R.D., Flynn L.E., Taylor S. Kramrova N.A., Frith S., Fisher B., and DeLand M.: *"Solar Backscatter UV (SBUV) total ozone and profile algorithm"*, Atmospheric Measurement Techniques, 6:2533-2548, 2013

/Bobin, 1972/ Bobin B.: *"Interpretation of 2v3 harmonic band of methane CH_4 (from 5890 to 6107cm^{-1})",* Journal de Physique, 33:345, 1972

/Boesch et al. 2011/ Boesch H., Baker D., Connor B., Crisp D., and Miller C.: *"Global characterization of CO_2 column retrievals from shortwave-infrared satellite observations of the orbiting carbon observatory-2 mission"*, Remote Sensing, 3(2):270-304, 2011

/Bogumil et al., 2003/ Bogumil K., Orphal J., Homann T., Voigt S., Spietz P., Fleischmann O.C., Vogel A., Hartmann M., Bovensmann H., Frerick J., and Burrows J.P.: *"Measurements of molecular absorption spectra with the SCIAMACHY pre-flight model: instrument characterization and reference data for atmospheric remote-sensing in the 230–2380 nm region",* Journal of Photochemistry and Photobiology A: Chemistry, 157(2-3):167-184, 2003

/Bovensmann et al., 1999/ Bovensmann H., Burrows J. P., Buchwitz M., Frerick J., Noël S., Rozanov V.V., Chance K.V., and Goede A.H.P.: *"SCIAMACHY - Mission objectives and measurement modes"*, Journal of the Atmospheric Sciences, 56(2):127-150, 1999

/Brault et al., 2003/ Brault J.W., Brown L.R., Chackerian C.Jr., Freedman R., Predoi-Cross A. and Pine A.S.: *"Self-broadened $^{12}C^{16}O$ line shapes in the v = 2←0 band"*, Journal of Molecular Spectroscopy 222:220–239, 2003

/Brion et al., 1993/ Brion J., Chakir A., Daumont D., Malicet J., and Parisse C.: *"High-resolution laboratory absorption cross section of O_3. Temperature effect"*, Chemical Physics Letters, 213:610-612, 1993

/Brion et al., 1998/ Brion J., Chakir A., Charbonnier J., Daumont D., Parisse C., and Malicet J.: *"Absorption spectra measurements for the ozone molecule in the 350–830 nm region"*, Journal of Atmospheric Chemistry, 30:291–299, 1998

/Brown et al., 1992/ Brown L.R., Margolis J.S., Champion J.P., Hilico J.C., Jouvard J.M., Loete M., Chackerian C.Jr., Tarrago G., Benner C.D.: *"Methane and Its Isotopes: Current Status and Prospects for Improvement"*, Journal of Quantitative Spectroscopy & Radiative Transfer, 48(5-6):617-639, 1992

/Brown et al., 2003/ Brown L.R., Benner C.D., Champion J.P., Devi V.M., Fejard L., Gamache R.R., Gabard T., Hilico J.C., Lavorel B., Loete M., Mellau G.Ch., Nikitin A., Pine A.S., Predoi-Cross A., Rinsland C.P., Robert O., Sams R.L., Smith M.A.H., Tashkun S.A., Tyuterev V.G.: *"Methane line parameters in HITRAN"*, Journal of Quantitative Spectroscopy & Radiative Transfer, 82:219 – 238, 2003

/Brown, 2005/ Brown L.R.: *"Empirical line parameters of methane from 1.1 to 2.1 μkm"*, Journal of Quantitative Spectroscopy & Radiative Transfer, 96:251 – 270, 2005

/Brown et al., 2013/ Brown L.R., Sung K., Benner C.D., Devi V.M., Boudon V., Gabard T., Wenger C., Campargue A., Leshchishina O., Kassi S., Mondelain D., Wang L., Daumont L., Régalia L., Rey M., Thomas X., Tyuterev V. G., Lyulin O., Nikitin A.V., Niederer H. M., Albert S., Bauerecker S., Quack M., O'Brien J.J., Gordon I.E., Rothman L. S., Sasada H., Coustenis A., Smith M.A.H., Carrington T.Jr, Wang X. G., Mantz A.W., Spickler P.T.: *"Methane line parameters in the HITRAN 2012 database"*, Journal of Quantitative Spectroscopy & Radiative Transfer, 130:201 – 219, 2013

/Buchwitz et al., 2000a/ Buchwitz M., Rozanov V.V., and Burrows J.P.: *"A correlated-k distribution scheme for overlapping gases suitable for retrieval of atmospheric constituents from moderate resolution radiance measurements in the visible/near-infrared spectral region"*, Journal of Geophysical Research, 105:15247-15262, 2000

/Buchwitz et al., 2000b/ Buchwitz M., Rozanov V. V., and Burrows J. P.: *"A near infrared optimized DOAS method for the fast global retrieval of atmospheric CH_4, CO, CO_2, H_2O, and N_2O total column amounts from SCIAMACHY/ENVISAT-1 nadir radiances"*, Journal of Geophysical Research, 105:15231-15246, 2000

/Buchwitz et al., 2005a/ Buchwitz M., R. de Beek, Burrows J. P., Bovensmann H., Warneke T., Notholt J., Meirink J. F., Goede A.P.H., Bergamaschi P., Körner S., Heimann M., and Schulz A.: *"Atmospheric methane and carbon dioxide from SCIAMACHY satellite data: Initial comparison with chemistry and transport models"*, Atmospheric Chemistry and Physics, 5:941-962, 2005

/Buchwitz et al., 2005b/ Buchwitz M., R. de Beek, Noël S., Burrows J.P., Bovensmann H., Bremer H., Bergamaschi P., Körner S., Heimann M.: *"Carbon monoxide, methane and carbon dioxide columns retrieved from SCIAMACHY by WFM-DOAS: year 2003 initial data set",* Atmospheric Chemistry and Physics, 5:3313-3329, 2005

/**Buchwitz et al., 2006/** Buchwitz M., R. de Beek, Noël S., Burrows J.P., Bovensmann H., Schneising O., Khlystova I., Bruns M., Bremer H., Bergamaschi P., Körner S., Heimann M.: *"Atmospheric carbon gases retrieved from SCIAMACHY by WFM-DOAS: version 0.5 CO and CH_4 and impact of calibration improvements on CO_2 retrieval"*, Atmospheric Chemistry and Physics, 6:2727-2751, 2006

/Buchwitz et al., 2007/ Buchwitz M., Schneising O., Burrows J.P., Bovensmann H., Reuter M., Notholt J.: *"First direct observation of the atmospheric CO_2 year-to-*

year increase from space", Atmospheric Chemistry and Physics, 7:4249-4256, 2007

/Buchwitz et al., 2009/ Buchwitz M., Reuter M., Schneising O., Heymann J., Bovensmann H., and Burrows J. P.: *"Towards an improved CO_2 retrieval algorithm for SCIAMACHY on ENVISAT"*, Proceedings Atmospheric Science Conference, Barcelona, Spain, 7-11 Sept 2009, ESA Special Publication SP-676, 2009

/Boussin et al., 1998/ Boussin C., Regalia L., Plateaux J.J., Barbe A.: *"Line intensities and self-broadening coefficients for methane lines between 5500 and 6180 cm^{-1} retrieved with a multispectrum fitting technique*", Journal of Molecular Spectroscopy, 191:381–383, 1998

/Burkholder, Talukdar, 1994/ Burkholder J.B. and Talukdar R.K.: *"Temperature dependence of the ozone absorption spectrum over the wavelength range 410–760 nm"*, Geophysical Research Letters, 21:581-584, 1994

/Burrows et al, 1999a/ Burrows J.P., Richter A., Dehn A., Deters B., Himmelmann S., Voigt S., and Orphal J.: *"Atmospheric remote-sensing reference data from GOME. 2. Temperature-dependent absorption cross sections of O_3 in the 231 - 794 nm range"*, Journal of Quantitative Spectroscopy & Radiative Transfer, 61:509-517, 1999

/Burrows et al, 1999b/ Burrows J.P., Weber M., Buchwitz M., Rozanov V.V., Ladstätter-Weißenmayer A., Richter A., DeBeek R., Hoogen R., Bramstedt K. and Eichmann K.U.: *"The Global Ozone Monitoring Experiment (GOME): Mission Concept and First Scientific Results"*, Journal of the Atmospheric Sciences, 56:151-174, 1999

/Burrows et al, 2011/ Burrows J.P., Platt U., Borrell P.: *"The Remote Sensing of Tropospheric Composition from Space"*, Springer-Verlag Berlin Heidelberg 2011

/Campargue et al, 2008/ Campargue A., Perevalov B.V.: *"Comment on "Spectroscopic database of CO_2 line parameters: 4300–7000 cm^{-1}""*. Journal of Quantitative Spectroscopy & Radiative Transfer, 109:2261–71, 2008

/Campargue et al., 2012a/ Campargue A., Wang L., Mondelain D., Kassi S., Bézard B., Lellouch E., Coustenis A., C. de Bergh, Hirtzig M., and Drossart P.: *"An empirical line list for methane in the 1.26-1.71µm region for planetary investigations (T=80-300 K). Application to Titan"*, Icarus 219:110-128, 2012

/Campargue et al., 2012b/ Campargue A., Leshchishina O., Wang L., Mondelain D., Kassi S., and Nikitin A.V.: *"Refinements of the WKMC empirical line lists (5852-7919 cm^{-1}) for methane between 80 K and 296 K"*, Journal of Quantitative Spectroscopy & Radiative Transfer, 113:1855-1873, 2012

/Campargue et al., 2013a/ Campargue A., Leshchishina O., Mondelain D., Kassi S., Coustenis A.: *"An improved empirical line list for methane in the region of the*

$2\nu_3$ band at 1.66 μm", Journal of Quantitative Spectroscopy & Radiative Transfer**,** 118:49–59, 2013

/Campargue et al., 2013b/ Campargue A., Leshchishina O Wang L., Mondelain D., Kassi S.: *"The WKLMC empirical line lists (5852–7919 cm^{-1}) for methane between 80 K and 296 K: "Final" lists for atmospheric and planetary applications"*, Journal of Molecular Spectroscopy, 291, 16–22, 2013

/Chehade et al, 2013a/ Chehade W., Gür B., Spietz P., Gorshelev V., Serdyuchenko A., Burrows J.P., and Weber M.: *"Temperature dependent ozone cross-sections spectra measured with the GOME-2 FM3 spectrometer and first application in satellite retrievals"*, Atmospheric Measurement Techniques, 6:1623-1632, 2013

/Chehade et al, 2013b/ Chehade W., Gorshelev V., Serdyuchenko A., Burrows J. P., and Weber M.: *"Revised temperature dependent ozone absorption cross section spectra (Bogumil et al.) measured with the SCIAMACHY satellite spectrometer"*, Atmospheric Measurement Techniques, 6:3055-3065, 2013

/Chevallier et al. 2010/ Chevallier F., P. Ciais, T. J. Conway, T. Aalto, B. E. Anderson, P. Bousquet, E. G. Brunke, L. Ciattaglia, Y. Esaki, M. Fröhlich, A.J. Gomez, A.J. Gomez-Pelaez, L. Haszpra, P. Krummel, R. Langenfelds, M. Leuenberger, T. Machida, F. Maignan, H. Matsueda, J. A. Morguí, H. Mukai, T. Nakazawa, P. Peylin, M. Ramonet, L. Rivier, Y. Sawa, M. Schmidt, P. Steele, S. A. Vay, A. T. Vermeulen, S. Wofsy, D. Worthy: *"CO_2 surface fluxes at grid point scale estimated from a global 21-year reanalysis of atmospheric measurements"*, Journal of Geophysical Research, 115, D21307, 2010

/Ciurylo et al., 2000/ Ciurylo R., Pine A.S.: *"Speed-dependent line mixing profiles"*, Journal of Quantitative Spectroscopy & Radiative Transfer, 67:375–393, 2000

/Ciurylo et al., 2001/ Ciurylo R., R. Jaworski, J. Jurkowski, A.S. Pine, J. Szudy: *"Spectral line shapes modeled by a quadratic speed-dependent Galatry profile"*, Physical Review A, 63:032507–032517, 2001

/Connor et al. 2008/ Connor B. J., H. Boesch, G. Toon, B. Sen, C. Miller, and D. Crisp: *"Orbiting Carbon Observatory: Inverse method and prospective error analysis"*, Journal of Geophysical Research, 113, D05305, 2008

/Crutzen, 1970/ Crutzen P.J.: *"The influence of nitrogen oxides on atmospheric ozone content"*, Quart. J. Roy. Meteorol. Soc. 96:320-325, 1970

/Darnton et al., 1973/ Darnton L. and Margolis, J. S.: *"The temperature dependence of the half widths of some self-and foreign-gas-broadened lines of methane"*, Journal of Quantitative Spectroscopy & Radiative Transfer*,* 13:969–976, 1973

/Daumont et al., 1992/ Daumont D., Brion J., Charbonnier J., and Malicet J.: *"Ozone UV spectroscopy I: Absorption cross-sections at room temperature"*, Journal of Atmospheric Chemistry, 15:145-155, 1992

/Devi et al., 2007a/ Devi V.M., Benner D.C., Brown L.R., Miller C.E., Toth R.A.: *"Line mixing and speed dependence in CO_2 at 6227.9 cm^{-1}: constrained multispectrum analysis of intensities and line shapes in the 30013'00001 band"*, Journal of Molecular Spectroscopy, 245:52–80, 2007

/Devi et al., 2007b/ Devi V.M., Benner D.C., Brown L.R., Miller C.E., Toth R.A.: *"Line mixing and speed dependence in CO_2 at 6348 cm^{-1}: positions, intensities, and air- and self-broadening derived with constrained multispectrum analysis"*, Journal of Molecular Spectroscopy, 242:90–117, 2007

/Dicke, 1953/ Dicke R.H.: *"The effect of collisions upon the Doppler width of spectral lines"*, Physical Review, 89:472, 1953

/Dils et al., 2006a/ Dils B., M. De Mazière, J. F. Müller, T. Blumenstock, M. Buchwitz, R. de Beek, P. Demoulin, P. Duchatelet, H. Fast, C. Frankenberg, A. Gloudemans, D. Griffith, N. Jones, T. Kerzenmacher, E. Mahieu, J. Mellqvist, S. Mikuteit, R. L. Mittermeier, J. Notholt, H. Schrijver, D. Smale, A. Strandberg, W. Stremme, K. Strong, R. Sussmann, J. Taylor, M. van den Broek, T. Warneke, A. Wiacek, S. Wood: *"Comparisons between SCIAMACHY and ground-based FTIR data for total columns of CO, CH_4, CO_2 and N_2O"*, Atmospheric Chemistry and Physics, 6:1953-1967, 2006

/Dils et al., 2006b/ Dils B., De Maziere M., Blumenstock T., Hase F., Kramer I., Mahieu E., Demoulin P., Duchatelet P., Mellqvist J., Strandberg A., Buchwitz M., Khlystova I., Schneising O., Velazco V., Notholt J., Sussmann R., and Stremme W.: *"Validation of WFM-DOAS v0.6 CO and v1.0 CH_4 scientific products using European ground-based FTIR measurements. Proceedings of the Third Workshop on the Atmospheric Chemistry Validation of ENVISAT (ACVE-3)"*, 4-7 Dec. 2006, ESA/ESRIN, Frascati, Italy, ESA Publications Division Special Publication SP-642 (CD), 2006

/Dufour et al., 2003/ Dufour G., Hurtmans, D., Henry, A., Valentin, A., and Lepère, M.: *"Line profile study from diode laser spectroscopy in the $12CH_4$ 2v3 band perturbed by N_2, O_2, Ar, and He"*, Journal of Molecular Spectroscopy, 221:80–92, 2003

/Edlen, 1966/ Edlen B.: *"The refractive index of air"*, Metrologia, 2:71-80, 1966

/El Helou al., 2005/ El Helou, Z., Churassy, S., Wannous, G., Bacis, R., and Boursey, E.: *"Absolute cross sections of ozone at atmospheric temperatures for the Wulf and the Chappuis bands"*, Journal of Chemical Physics, 122:244311, 2005

/Enami et al., 2004/ Enami S., Ueda J., Nakano Y., Hashimoto S., and Kawasaki M.: *"Temperature-dependent absorption cross sections of ozone in the Wulf-Chappuis band at 759-768 nm"*, Journal of Geophysical Research, 109, D05309, 2004

/Farman et al., 1985/ Farman J.C., Gardiner B.G., Shanklin J.D.: *"Large losses of total ozone in Antarctica reveal seasonal ClOx/NOx interaction"*, Nature 315:207 – 210, 1985

/Fox, 1962/ Fox K.: *"Vibration–rotation interactions in infrared active overtone levels of spherical top molecules – 2n3 and 2n4 of CH_4, 2n3 of CD_4"*, Journal of Molecular Spectroscopy, 9:381, 1962

/Fox et al., 1980/ K. Fox, G. W. Halsey, and D. E. Jennings: *"High Resolution Spectrum and Analysis of 2n3 of 13CH4 at 1.67 μkm",* Journal of Molecular Spectroscopy, 83:213, 1980

/Frankenberg et al., 2005a/ Frankenberg C., Platt U., and Wagner T.: *"Iterative maximum a posteriori (IMAP-) DOAS for retrieval of strongly absorbing trace gases: Model studies for CH_4 and CO_2 retrieval from near-infrared spectra of SCIAMACHY onboard ENVISAT"*, Atmospheric Chemistry and Physics, 5:9-22, 2005

/Frankenberg et al., 2005b/ Frankenberg C., Meirink J. F., van Weele M., Platt U., and Wagner T.: *"Assessing methane emissions from global spaceborne observations"*, Science, 308:1010-1014, 2005

/Frankenberg et al., 2006/ Frankenberg C., Meirink J. F., Bergamaschi P., Goede A. P. H., Heimann M., Körner S., Platt U., van Weele M., and Wagner T.: *"Satellite chartography of atmospheric methane from SCIAMACHY onboard ENVISAT: Analysis of the years 2003 and 2004"*, Journal of Geophysical Research, 111, D07303, 2006

/Frankenberg et al., 2008a/ Frankenberg C., Bergamaschi P., Butz A., Houweling S., Meirink J. F., Notholt J., Petersen A. K., Schrijver H., Warneke T., and Aben I.: *"Tropical methane emissions: A revised view from SCIAMACHY onboard ENVISAT",* Geophysical Research Letters, 35, L15881, 2008

/Frankenberg et al., 2008b/ Frankenberg C., Warneke T., Butz A., Aben I., Hase F., Spietz P.: *"Pressure broadening in the $2\nu_3$ band of methane and its implication on atmospheric retrievals"*, Atmospheric Chemistry and Physics, 8:5061–75, 2008

/Galatry, 1961/ Galatry L.: *"Simultaneous effect of Doppler and foreign gas broadening on spectral lines"*, Physical Review, 122:1218–1223, 1961

/Gorshelev et al., 2014/ Gorshelev V., Serdyuchenko A., Weber M., and Burrows J.P.: *"High spectral resolution ozone absorption cross-sections: Part I. Measurements, data analysis and comparison around 293 K"*, Atmospheric Measurement Techniques, 7:609–624, 2014

/Grebenshchikov et al., 2007/ Grebenshchikov S.Y., Zhu H., Schinke R., Qu Z.W.: *"New theoretical investigations of the photodissociation of ozone in the Hartley, Huggins, Chappuis, and Wulf bands"*, Physical Chemistry Chemical Physics, 9:2044-2067, 2007

/Griggs et al., 1968/ Griggs M.: *"Absorption Coefficients of Ozone in the Ultraviolet and Visible Regions"*, Journal of Chemical Physics, 49:857-859, 1968

/Griffiths, Haseth, 2007/ Griffiths P., De Haseth J.A.: "Fourier Transform Infrared Spectrometry", 2007

/Guer et al., 2005/ Guer B., Spietz P., Orphal J., and Burrows J.P.: *"Absorption Spectra Measurements with the GOME-2 FMs using the IUP/IFE-UB's Calibration Apparatus for Trace Gas Absorption Spectroscopy CATGAS. Final Report"*, Contract No. 16007/02/NL/SF, ESA/EUMETSAT, Bremen, 2005

/Gharavi et al., 2005/ Gharavi M. and Buckley S. G.: *"Diode laser absorption spectroscopy measurement of line strengths and pressure broadening coefficients of the methane 2v3 band at elevated temperatures"*, Journal of Molecular Spectroscopy, 229:78–88, 2005

/Gloudemans et al., 2005/ Gloudemans A. M. S., Schrijver H., Kleipool Q., van den Broek M. M. P., Straume A. G., Lichtenberg G., van Hess R. M., Aben I., and Meirink J. F.: *"The impact of SCIAMACHY near-infrared instrument calibration on CH_4 and CO total columns"*, Atmospheric Chemistry and Physics, 5:2369-2383, 2005

/Gordon, et al., 1971/ Gordon R.G., McGinnis R.P.: *"Intermolecular potentials and infrared spectra"*, Journal of Chemical Physics, 55:4898–4906, 1971

/Hartmann et al., 2008/ Hartmann J.M., Boulet C., Robert D.: *"Collisional Effects on Molecular Spectra: Laboratory experiments and models, consequences for applications"*, Elsevier, 2008

/Hamazaki et al., 2004/ Hamazaki T., Kaneko Y., and Kuze A.: *"Carbon dioxide monitoring from the GOSAT satellite"*, Proceedings XXth ISPRS conference, Istanbul, Turkey, July 2004

/Harris et al., 1997/ Harris N.R.P., Ancellet A., Bishop L., Hofmann D.J., Kerr J.B., McPeters R.D., Prendez M., Randel W.J., Staehelin J., and Subbaraya B.H.: *"Trends in stratospheric and tropospheric ozone"*, Journal of Geophysical Research, 102:1571-1588, 1997

/Hearn, 1961/ Hearn A.G.: *"The absorption of ozone in the ultra-violet and visible regions of the spectrum"*, Proceedings of the Physical Society, 78:932-940,1961

/Herman et al., 1997/ Herman J. R., Bhartia P. K., Torres O., Hsu C., Seftor C., and Celarier E.: *"Global distribution of UV absorbing aerosols from Nimbus7/TOMS data"*, Journal of Geophysical Research, 102:16911-16922, 1997

/Herzberg, 1988/ Herzberg G.: *"Molecular Spectra and Molecular Structure. III. Electronic Spectra and Electronic Structure of Polyatomic Molecules",* 1988

/Hollas, 1988/ Hollas J.M.: *"Modern Spectroscopy"*, John Wiley & Sons, 2004

/Houweling et al., 2004/ Houweling S., Breon F.-M., Aben I., Rödenbeck C., Gloor M., Heimann M. and Ciais P.: *"Inverse modeling of CO_2 sources and sinks using satellite data: A synthetic inter-comparison of measurement techniques and their performance as a function of space and time"*, Atmospheric Chemistry and Physics, 4:523-538, 2004

/Houweling et al., 2005/ Houweling S., Hartmann W., Aben I., Schrijver H., Skidmore J., Roelofs G.-J., and Breon F.-M.: *"Evidence of systematic errors in SCIAMACHY-observed CO_2 due to aerosols"*, Atmospheric Chemistry and Physics, 5:3003-3013, 2005

/IPCC, 2007/ Solomon S., Qin D., Manning M., Chen Z., Marquis M., Averyt K. B., Tignor M., and Miller H. L.: *"Climate change 2007: The physical science basis, Contribution of working group I to the Fourth Assessment Report of the Intergovernmental Panel on Climate Change (IPCC)"*, Cambridge University Press, Cambridge (UK), New York (USA), p. 996, 2007

/IPCC, 2013/ Stocker, T.F., D. Qin, G.-K. Plattner, M. Tignor, S.K. Allen, J. Boschung, A. Nauels, Y. Xia, V. Bex and P.M. Midgley (eds.): *"Climate change 2013: The physical science basis, Contribution of working group I to the Fourth Assessment Report of the Intergovernmental Panel on Climate Change (IPCC)"*, Cambridge University Press, Cambridge (UK), New York (USA), 2013

/Janssen et al., 2011/ Janssen C., Simone D., Guinet M.: *"Preparation and accurate measurement of pure ozone"*, C. Janssen et al., Review of Scientific Instruments 82:034102, 2011

/Jenouvrier et al., 2007/ Jenouvrier A., Daumont L., Regalia-Jarlot L., Tyuterev V.G., Carleer M., Vandaele A.M., Mikhailenko S., Fally S.: *"Fourier transform measurements of water vapor line parameters in the 4200-6600 cm^{-1} region"*, Journal of Quantitative Spectroscopy & Radiative Transfer, 105(2):326-355, 2007

/Johnston, **1971/** Johnston H.S.: *"Reduction of Stratospheric Ozone by Nitrogen Oxide Catalysts from Supersonic Transport Exhaust"*, Science, 173:517-522, 1971

/Kapitanov et al., 2007/ Kapitanov V.A., Ponomarev Yu.N., Tyryshkin I.S., Rostov A.P.: *"Two-channel opto-acoustic diode laser spectrometer and fine structure of methane absorption spectra in 6070–6180 cm^{-1} region"*, Spectrochimica Acta Part A: Molecular and Biomolecular Spectroscopy, 66:811–818, 2007

/Keller-Rudek and Moortgat., 2013/ Keller-Rudek, H. and Moortgat G.K.: MPI-Mainz-UV-VIS Spectral Atlas of Gaseous Molecules, available at: http://satellite.mpic.de/spectral_atlas, April 2013

/Komhyr et al., 2013/ Komhyr W.D. and Evans R.D.: *"Operations handbook ozone observations with a Dobson spectrophotometer"*, Geneva: WMO Global Atmosphere Watch; 2008. WMO /Td-No. 1469,

/Kuze et al., 2009/ Kuze A., Suto H., Nakajima M., and Hamazaki T.: *"Thermal and near infrared sensor for carbon observation Fourier-transform spectrometer on the Greenhouse Gases Observing Satellite for greenhouse gases monitoring"*, Applied Optics, 48:6716–6733, 2009

/Liu et al., 2007/ Liu X., Chance K., Sioris C.E., and Kurosu T.P.: *"Impact of using different ozone cross sections on ozone profile retrievals from Global Ozone Monitoring Experiment (GOME) ultraviolet measurements"*, Atmospheric Chemistry and Physics, 7:3571-3578, 2007

/Lyulin et al., 2009/ Lyulin O.M., Nikitin A.V., Perevalov V.I., Morino I., Yokota T., Kumazawa R.: *"Measurements of N_2- and O_2-broadening and –shifting parameters of the methane spectral lines in the 5550–6236 cm^{-1} region"*, Journal of Quantitative Spectroscopy & Radiative Transfer, 110:654–668, 2009

/Lyulin et al., 2010/ Lyulin O.M., Kassi S., Sung K., Brown L.R., and Campargue A.: *"Determination of the low energy values of $^{13}CH_4$ transitions in the $2nu_3$ region near 1.66μm from absorption spectra at 296 and 81 K"*, Journal of Molecular Spectroscopy, 261:91-100, 2010

/Lyulin et al., 2011/ Lyulin O.M., Perevalov V.I., Morino I., Yokoto I., Kumazawa R.: *"Measurements of self-broadening and self-pressure induced shift parameters of the methane spectral lines in the 5550–6236 cm^{-1} region"*, Journal of Quantitative Spectroscopy & Radiative Transfer, 112(3):531-539, 2011

/Maddy et al., 2008/ Maddy E.S., Barnet C.D., Goldberg M., Sweeney C., Liu X.: *"CO_2 retrievals from the Atmospheric Infrared Sounder: Methodology and validation"*, Journal of Geophysical Research, 113 D11, D11301, 2008

/Majcherova et al., 2005/ Majcherova Z., Macko P., Romanini D., Perevalov V. I., Tashkun S.A., Teffo J.L.: *"High-sensitivity CW-cavity ring down spectroscopy of $^{12}CO_2$ near 1.5 mm"*, Journal of Molecular Spectroscopy, 230:1–21, 2005

/Malicet et al., 1989/ Malicet J., Brion J., and Daumont D.: *"Temperature dependence of the absorption cross-section of ozone at 254 nm"*, Chemical Physics Letters, 158(3-4):293-296, 1989

/Malicet et al., 1995/ Malicet J., Daumont D., Charbonnier J., Chakir C., Parisse A., and Brion J.: *"Ozone UV Spectroscopy. II. Absorption cross sections and temperature dependence"*, Journal of Atmospheric Chemistry, 21:263-273, 1995

/Margolis, 1973/ Margolis J.S.: *"Line Strength Measurements of the 2v3 Band of Methane"*, Journal of Quantitative Spectroscopy & Radiative Transfer, 13:1097, 1973

/Margolis, 1988/ Margolis J.S.: *"Measured line positions and strengths of methane between 5500 and 6180 cm^{-1}"*, Applied Optics, 27**:**4038-4051, 1988

/Margolis, 1990/ Margolis J.S.: *"Empirical values of the ground state energies for methane transitions between 5500 and 6150 cm^{-1}"*, Applied Optics 29**:**2295-2302, 1990

/Martin et al., 2010/ Martin B., Lepère M.: *"Temperature dependence of N_2- and O_2-broadening coefficients in the ν_4 band of $^{13}CH_4$"*, Journal of Molecular Spectroscopy, 259(1):46-55, 2010

/Marquardt and Quack, 1998/ Marquardt R. and Quack M.: *"Global analytical potential hypersurfaces for large amplitude nuclear motion and reactions in methane. I. Formulation of the potentials and adjustment of parameters to ab initio data and experimental constraints"*, Journal of Chemical Physics, 109 (24), 10628 – 10643, 1998

/McCormick et al., 1989/ McCormick M.P., Zawodny J.M., Veiga R.E., Larsen J.C., and Wang P.H.: *"An overview of SAGE I and SAGE II ozone measurements"*, Planetary and Space Science, 37:1567-1586, 1989

/McClatchey et al., 1973/ McClatchey R.A., Benedict W.S., Clough S.A., Burch De., Fox K., Rothman L.S., Garing J.S.: *"AFCRL atmospheric absorption line parameters compilation"*, Environmental Research Papers, 434, 1973

/McPeters et al., 2014/ McPeters R.D., Bhartia P.K., Krueger A.J., Herman J.R., Wellemeyer C.G., Seftor C.J., Jaross G., Torres O., Moy L., and Labow G., Byerly W., Taylor S.L., Swissler T., and Cebula R.P.: *"Earth Probe Total Ozone Mapping Spectrometer (TOMS) Data Products User's Guide"*, NASA, 1998

/Meirink et al., 2006/ Meirink J.-F., Eskes H. J., and Goede A.P.H.: *"Sensitivity analysis of methane emissions derived from SCIAMACHY observations through inverse modeling"*, Atmospheric Chemistry and Physics, 6:1275-1292, 2006

/Menard-Bourcin et al., 2007/ Menard-Bourcin F., Menard J., Boursier C.: *"Temperature dependence of rotational relaxation of methane in the $2\nu_3$ vibrational state by self- and nitrogen-collisions and comparison with line broadening measurements"*, Journal of Molecular Spectroscopy, 242:55–63, 2007

/Miller et al., 2007/ Miller C. E., Crisp D., DeCola P.L.: *"Precision requirements for space-based X_{CO2} data"*, Journal of Geophysical Research, 112, D10314, 2007

/Molina and Molina, 1986/ Molina L.T. and Molina M.J.: *"Absolute absorption cross-sections of ozone in the 185- to 350-nm wavelength range"*, Journal of Geophysical Research, 91:14501-14508, 1986

/Mondelain et al., 2007/ Mondelain D., Payan S., Deng W., Camy-Peyret C., Hurtmans D., and Mantz A. W.: *"Measurement of the temperature dependence of line mixing and pressure broadening parameters between 296 and 90 K in the ν3 band of $^{12}CH_4$ and their influence on atmospheric methane retrievals"*, Journal of Molecular Spectroscopy, 244:130 – 137, 2007

/NASA, 2011/ The NASA Panel for Data Evaluation. Chemical Kinetics and Photochemical Data for Use in Atmospheric Studies. 2011. Available from: http://jpldataeval.jpl.nasa.gov/pdf/JPL%2010-6%20Final%2015June2011.pdf

/Natraj et al. 2008/ Natraj V., Boesch H., Spurr R.J.D., and Yung Y. L.: *"Retrieval of XCO_2 from simulated orbiting carbon observatory measurements using the fast linearized r-2os radiative transfer model"*, Journal of Geophysical Research D: Atmospheres, 113(11), 2008

/Nikitin et al., 2009/ Nikitin A.V., Mikhailenko S.N., Morino I., Yokota T., Kumazawa R., Watanabe T.: *"Isotopic substitution shifts in methane and vibrational band assignment in the 5560–6200 cm^{-1} region",* Journal of Quantitative Spectroscopy & Radiative Transfer, 110:964–97, 2009

/Nikitin et al., 2010/ Nikitin A.V., Lyulin O.M., Mikhailenko S.N., Perevalov V.I., Filippov N.N., Grigoriev I.M., Morino I., Yokota T., Kumazawa R., Watanabe T.: *"GOSAT-2009 methane spectral line list in the 5550–6236 cm^{-1} range"*, Journal of Quantitative Spectroscopy & Radiative Transfer, 111(15):2211–2224, 2010

/NOAA/ NOAA. Solar Backscatter Ultraviolet Instrument (SBUV/2) Version 8 Ozone Retrieval Algorithm Theoretical Basis Document (V8 ATBD), 2007

/O'Dell, 2010/ O'Dell C.W.: *"Acceleration of multiple-scattering, hyper-spectral radiative transfer calculations via low-streams interpolation"*, Journal of Geophysical Research D: Atmospheres, 115(10), 2010

/Orphal, 2003/ Orphal, J.: *"A critical review of the absorption cross-sections of O_3 and NO_2 in the ultraviolet and visible"*, Journal of Photochemistry and Photobiology A: Chemistry, 157:185-209, 2003

/OSIRIS/ OSIRIS Level 2 Daily Data Products: Users Guide, available at: http://odin-osiris.usask.ca/sites/default/files/media/pdf/l2dataformat.pdf, April 2013

/Paur, Bass, 1985/ Paur R.J. and Bass A.M.: *"The Ultraviolet Cross-Sections of Ozone: II. Results and temperature dependence"*, in: Zerefos CS, Ghazi A, editors. Atmospheric Ozone; Proc. Quadrennial Ozone Symposium, Halkidiki, Greece, Dordrecht, Reidel, D., 611-615, 1985

/Paynter et al., 2009/ Paynter D.J., Ptashnik I.V., Shine K.P., Smith K.M., McPheat R., Williams R.G.: *"Laboratory measurements of the water vapour continuum in the 1200-8000 cm^{-1} region between 293 and 351 K"*, Journal of Geophysical Research, 114:D21301, 2009

/Petersen et al., 2012/ Petersen M., Viallon J., Moussay P., and Wielgosz R.I.: *"Relative measurements of ozone absorption cross-sections at three wavelengths in the Hartley band using a well-defined UV laser beam"*, Journal of Geophysical Research, 117, D05301, 2012

/Perevalov et al., 1995/ Perevalov V.I., Lobodenko E.I., Lyulin O.M., Teffo J.L.: *"Effective dipole moment and band intensities problem for carbon dioxide"*, Journal of Molecular Spectroscopy, 171:435–52, 1995

/Perevalov et al., 2007/ Perevalov B.V., Kassi S., Romanini D., Perevalov V.I., Tashkun S.A., Campargue A.: *"Global effective Hamiltonians of $^{16}O^{13}C^{17}O$ and $^{16}O^{13}C^{18}O$ improved from CW-CRDS observations in the 5900–7000 cm^{-1} region"*, Journal of Molecular Spectroscopy, 241:90–100, 2007

/Perevalov et al., 2008a/ Perevalov B.V., Campargue A., Gao B., Kassi S., Tashkun S.A., Perevalov V.I.: *"New CW-CRDS measurements and global modeling of $^{12}C^{16}O_2$ absolute line intensities in the 1.6 μm region"*, Journal of Molecular Spectroscopy, 252:190–7, 2008

/Perevalov et al., 2008b/ Perevalov B.V., Kassi S., Perevalov V.I., Tashkun S.A., Campargue A.: *"High sensitivity CW-CRDS spectroscopy of $^{12}C^{16}O_2$, $^{16}O^{12}C^{17}O$ and $^{16}O^{12}C^{18}O$ between 5851 and 7045 cm^{-1}: line positions analysis and critical review of the current databases"*, Journal of Molecular Spectroscopy, 252:143–59, 2008

/Perevalov et al., 2008c/ Perevalov B.V., Deleporte T., Liu A.W., Kassi S., Campargue A., Vander Auwera J.: *"Global modeling of $^{13}C^{16}O_2$ absolute line intensities from CW-CRDS and FTS measurements in the 1.6 and 2.0 μm regions"*, Journal of Quantitative Spectroscopy & Radiative Transfer, 109:2009–26, 2008

/Perevalov et al., 2008d/ Perevalov B.V., Perevalov V.I., Campargue A.A.: *"A (nearly) complete experimental line list for $^{13}C^{16}O_2$, $^{16}O^{13}C^{18}O$, $^{16}O^{13}C^{17}O$, $^{13}C^{18}O_2$ and $^{17}O^{13}C^{18}O$ by high-sensitivity CW-CRDS spectroscopy between 5851 and 7045 cm^{-1}"*, Journal of Quantitative Spectroscopy & Radiative Transfer, 109:2437–62, 2008

/Perevalov et al., 2008e/ Perevalov V.I., Tashkun S.A.: *"CDSD-296 (Carbon Dioxide Spectroscopic Databank): updated and enlarged version for atmospheric applications"*, 10th HITRAN database conference, Cambridge, MA, USA, 2008

/Perner and Platt, 1979/ Perner D., Platt U.: *"Detection of nitrous acid in the atmosphere by differential optical absorption"*, Geophysical Research Letters 6: 917–920, 1979

/Pine, 1992/ Pine A.S.: *"Self-broadening, N_2-broadening, O_2-broadening, H_2-broadening, Ar-broadening, and He-broadening in the ν_3 band Q-branch of CH_4"*, Journal of Chemical Physics, 97:773–785, 1992

/Pine, 1997a/ Pine A.S.: *"Line mixing sum rules for the analysis of multiplet spectra"*, Journal of Quantitative Spectroscopy & Radiative Transfer, 57:145–155, 1997

/Pine, 1997b/ Pine A.S.: *"N_2 and Ar broadening and line mixing in the P and R branches of the v3 band of CH_4"*, Journal of Quantitative Spectroscopy & Radiative Transfer, 57:157–176, 1997

/Pine, et al., 2000/ Pine A.S., Gabard T.: *"Speed-dependent broadening and line mixing in CH_4 perturbed by Ar and N_2 from multispectrum fits"*, Journal of Quantitative Spectroscopy & Radiative Transfer, 66:69–92, 2000

/Pine et al., 2003/ Pine A. S., Gabard T.: *"Multispectrum fits for line mixing in the v3 band Q branch of methane"*, Journal of Molecular Spectroscopy, 217:105–114, 2003

/Pitts, Pitts, 2000/ Pitts B.J., Pitts J.N.: ***"****Chemistry of the Upper and Lower Atmosphere"*, Academic Press, 2000

/Plateaux et al., 2001/ Plateaux J.-J., Regalia L., Boussin C., Barbe A.: *"Multispectrum fitting technique for data recorded by Fourier transform spectrometer: application to N_2O and CH_3D"*, Journal of Quantitative Spectroscopy & Radiative Transfer, 68:507, 2001

/Predoi-Cross et al., 2005/ Predoi-Cross A., Brown L.R., Devi V.M., Brawley-Tremblay M., Benner D.C.: *"Multispectrum analysis of self-broadening and pressure-shifting coefficients of $^{12}CH_4$ from 4100 to 4635 cm^{-1}"*, Journal of Molecular Spectroscopy, 232:231–46, 2005

/Predoi-Cross et al., 2006/ Predoi-Cross A., Brawley-Tremblay M., Brown L.R., Devi V.M., Benner D.C.: *"Multispectrum analysis of $^{12}CH_4$ from 4100 to 4635 cm^{-1}: II. Air-broadening coefficients (widths and shifts)"*, Journal of Molecular Spectroscopy, 236:201–15, 2006

/Predoi-Cross et al., 2007/ Predoi-Cross A., Unni A.V., Heung H., Malathy Devi V., Benner C.D., and Brown L.R.: *"Line mixing effects in the v2+ v3 band of methane"*, Journal of Molecular Spectroscopy, 246:65–76, 2007

/Predoi-Cross et al., 2009/ Predoi-Cross A., McKellar A.R.W., Benner D.C., Malathy Devi V., Gamache R.R., Miller C.E.: *"Temperature dependences for air-broadened Lorentz half width and pressure-shift coefficients in the 30013'00001 and 30012'00001 bands of CO_2 near 1600 nm"*, Canadian Journal of Physics, 87: 517-535, 2009

/Quack, 1990/ Quack M.: *"Spectra and Dynamics of Coupled Vibrations in Polyatomic Molecules"*, Annual Review of Physical Chemistry, 41, 839 – 874, 1990

/Rautian et al., 1967/ Rautian S.G., Sobel'man I.I.: *"The effect of collisions on the Doppler broadening of spectral lines. Simultaneous effect of Doppler and foreign gas broadening on spectral lines"*, Sov. Phys. Uspekhi, 9:701–716, 1967

/Ravishankara et al., 2009/ Ravishankara A.R., Daniel J.S., Portmann R.W.: *"Nitrous Oxide (N_2O): The Dominant Ozone-Depleting Substance Emitted in the 21st Century",* Science 326:123,2009

/Rayner und O'Brian, 2001/ Rayner P. J., O'Brian D.M.: *"The utility of remotely sensed CO_2 concentration data in surface inversions"*, Geophysical Research Letters, 28:175-178, 2001

/Rinsland et al., 1988/ Rinsland C. P., Malathy Devi V., Smith M.A.H., and Benner D.C.: *"Measurements of air-broadened and nitrogen- broadened Lorentz width coefficients and pressure shift coefficients in the ν4 and ν2 bands of $^{12}CH_4$"*, Applied Optics, 27:631, 1988

/Rodgers, 2000/ Rodgers C.D.: *"Inverse methods for atmospheric sounding – Theory and practice"*, World Scientific Series on Atmospheric, Ocean and Planetary Physics Vol. 2, 2000

/Rothman et al., 1987/ Rothman L.S. et al: *"The HITRAN database: 1986 Edition",* Applied Optics, 26, 4058-4097, 1987

/Rothman et al., 1998/ Rothman L.S. et al.: *"The HITRAN Molecular Spectroscopic Database and Hawks (HITRAN Atmospheric Workstation): 1996 Edition"*, Journal of Quantitative Spectroscopy & Radiative Transfer, 60:665-710, 1998

/Rothman et al., 2005/ Rothman, L. S., et al.: *"The HITRAN 2004 molecular spectroscopic database"*, Journal of Quantitative Spectroscopy & Radiative Transfer, 96:139-204, 2005

/**Rothman et al., 2009/** Rothman L. S. et al: *"The HITRAN 2008 molecular spectroscopic database"*, Journal of Quantitative Spectroscopy & Radiative Transfer, 110:533–572, 2009

/Rozanov et al., 2005/ Rozanov A., Rozanov V., Buchwitz M., Kokhanovsky A. and J.P. Burrows: *"SCIATRAN 2.0 - A new radiative transfer model for geophysical applications in the 175-2400 nm spectral region"*, Advances in Space Research, 36(5):1015-1019, 2005

/SAGE III ATBD Team, 2002/ SAGE III Algorithm Theoretical Basis Document (ATBD) Solar and Lunar Algorithm. LaRC 475-00-109, 2002

/Scarnato et al., 2009/ Scarnato B., Staehelin J., Peter T., Groebner J. and Stuebi R.: *"Temperature and slant path effects in Dobson and Brewer total ozone measurements"*, Journal of Geophysical Research, 114, D2430, 2009

/Schinke et al., 2010/ Schinke R. and McBane G.C.: *"Photodissociation of ozone in the Hartley band: Potential energy surfaces, nonadiabatic couplings, and singlet/triplet branching ratio"*, Journal of Chemical Physics, 132, 044305, 2010

/Schneising et al., 2008/ Schneising O., Buchwitz M., Burrows J.P., Bovensmann H., Reuter M., Notholt J., Macatangay R., and Warneke T.: *"Three years of greenhouse gas column-averaged dry air mole fractions retrieved from satellite - Part 1: Carbon dioxide"*, Atmospheric Chemistry and Physics, 8:3827-3853, 2008

/Schneising et al., 2009/ Schneising O., Buchwitz M., Burrows J.P., Bovensmann H., Bergamaschi P., and Peters W.: *"Three years of greenhouse gas column-averaged dry air mole fractions retrieved from satellite - Part 2: Methane"*, Atmospheric Chemistry and Physics, 9:443-465, 2009

/Seinfeld, Pandis, 2006/ Seinfeld J.H., Pandis S.N.: *"Atmospheric Chemistry and Physics. From Air Pollution to Climate Change"*, John Wiley & Sons, Inc., 2006

/Serdyuchenko et al., 2014/ Serdyuchenko A., Gorshelev V., Weber M., Chehade W., and Burrows J.P.: *"New high-resolution ozone absorption cross-sections in UV, visible and near infrared: Part II. Temperature dependence"*, Atmospheric Measurement Techniques, 7:625–636, 2014

/Sussmann et al., 2005/ Sussmann R., Stremme W., Buchwitz M., R. de Beek: *"Validation of ENVISAT/SCIAMACHY columnar methane by solar FTIR spectrometry at the ground-truthing station Zugspitze"*, Atmospheric Chemistry and Physics, 5:2419-2429, 2005

/Tashkun et al., 1998/ Tashkun S.A., Perevalov V.I., Teffo J.L., Rothman L.S., Tyuterev V.G.: *"Global fitting of $^{12}C^{16}O_2$ vibrational-rotational line positions using the effective Hamiltonian approach"*, Journal of Quantitative Spectroscopy & Radiative Transfer, 60:785–801, 1998

/Tashkun et al., 1999/ Tashkun S.A., Perevalov V.I., Teffo J.L., Tyuterev V.G.: *"Global fit of $^{12}C^{16}O_2$ vibrational-rotational line intensities using the effective operator approach"*, Journal of Quantitative Spectroscopy & Radiative Transfer, 62:571–98, 1999

/Teffo et al., 1992/ Teffo J.L., Sulakshina O.N., Perevalov V.I.: *"Effective Hamiltonian for rovibrational energies and line intensities of carbon dioxide"*, Journal of Molecular Spectroscopy, 156:48–64, 1992

/Tejwani and Varanasi, 1971/ Tejwani G. D. T., Varanasi P.: *"Experimental and theoretical studies on collision-broadened lines in the v4-fundamental of methane"*, Journal of Quantitative Spectroscopy & Radiative Transfer, 12:849–855, 1972

/Tejwani et al., 1974a/ G. D. T. Tejwani and K. Fox: *"Calculated Line widths or CH_4 Broadened by N_2 and O_2"*, Journal of Chemical Physics, 60:2021, 1974

/Tejwani et al., 1974b/ G. D. T. Tejwani and K. Fox: *"Calculated Self- and Foreign-Gas Broadened Line widths for CH_3 D"*, Journal of Chemical Physics, 61:759, 1974

/Tran et al., 2006/ Tran H., Flaud P.-M., Gabard T., Hase F., von Clarmann T., Camy-Peyret C., Payan S., Hartmann J.-M.: *"Model, software and database for line-mixing effects in the ν3 and ν4 bands of CH_4 and tests using laboratory and planetary measurements—I: N_2 (and air) broadenings and the earth atmosphere"*, Journal of Quantitative Spectroscopy & Radiative Transfer, 101:284–305, 2006

/Tran et al., 2010/ Tran H., Hartmann J.-M., Toon G., Brown, L. R., Frankenberg C., Warneke T., Spietz P. and Hase F.: *"The $2v_3$ band of CH_4 broadened by N_2 revisited with line-mixing. Consequences for spectroscopic data, laboratory and atmospheric spectra at 1.67 μm"*, Journal of Quantitative Spectroscopy & Radiative Transfer, 111:1344-1356, 2010

/Toth, 2005/ Toth R.A.: *"Measurements of positions, strengths and self-broadened widths of H_2O from 2900 to 8000 cm^{-1}: line strength analysis of the 2nd triad bands"*, Journal of Quantitative Spectroscopy & Radiative Transfer, 94:51-107, 2005

/Toth et al., 2006a/ Toth R.A., Brown L.R., Miller C.E., Devi V.M., Benner D.C.: *"Line strengths of $^{12}C^{16}O_2$: 4550–7000 cm^{-1}"*, Journal of Molecular Spectroscopy, 239:221–42, 2006

/Toth et al., 2006b/ Toth R.A., Brown L.R., Miller C.E., Devi V.M., Benner D.C.: *"Self-broadened widths and shifts of $^{12}C^{16}O_2$: 4750–7000 cm^{-1}"*, Journal of Molecular Spectroscopy, 239:243–71, 2006

/Toth et al., 2007a/ Toth R.A., Miller C.E., Brown L.R., Devi V.M., Benner D.C.: *"Line positions and strengths of $^{16}O^{12}C^{18}O$, $^{18}O^{12}C^{18}O$ and $^{17}O^{12}C^{18}O$ between 2200 and 7000 cm^{-1}"*, Journal of Molecular Spectroscopy, 243:43–61, 2007

/Toth et al., 2007b / Toth R.A., Miller C.E., Malathy Devi V., Benner D.C, Brown L.R.: *"Air-broadened half width and pressure shift coefficients of $^{12}C^{16}O_2$ bands: 4750–7000 cm^{-1}"*, Journal of Molecular Spectroscopy, 246:133–57, 2007

/Toth et al., 2008a/ Toth R.A., Brown L.R., Miller C.E., Malathy Devi V., Benner D. C.: *"Spectroscopic database of CO_2 line parameters: 4300–7000 cm^{-1}"*, Journal of Quantitative Spectroscopy & Radiative Transfer, 109:906–21, 2008

/Toth et al., 2008b/ Toth R. A., Miller C.E., Brown L.R., Devi V.M., Benner D.C.: *"Line strengths of $^{16}O^{13}C^{16}O$, $^{16}O^{13}C^{18}O$, $^{16}O^{13}C^{17}O$ and $^{18}O^{13}C^{18}O$ between 2200 and 6800 cm^{-1}"*, Journal of Molecular Spectroscopy, 251:64–89, 2008

/Varanasi et al., 1983/ Varanasi P., Giver L.P., and Valero F.P.J.: *"Intensity measurements in the v4-Fundamental of $^{13}CH_4$ at planetary atmospheric temperatures"*, Journal of Quantitative Spectroscopy & Radiative Transfer, 30:491-495, 1983

/Varanasi, 1971/ Varanasi P.: *"Collision-broadened half-widths and shapes of methane lines"*, Journal of Quantitative Spectroscopy & Radiative Transfer, 11:1711-1724, 1971

/Veefkind et al., 2014/ Veefkind, J.P. and de Haan, J.F.: *"DOAS Total O_3 Algorithm"*, in: OMI Algorithm Theoretical Basis Document (ATBD), volume II: OMI Ozone Products, 33-52, 2002

/Voigt et al., 2001/ Voigt S., Orphal J., Bogumil K., and Burrows J.P.: *"The temperature dependence (203-293 K) of the absorption cross sections of O_3 in the 230-850 nm region measured by Fourier-Transform spectroscopy"*, Journal of Photochemistry and Photobiology A: Chemistry, 143, 1-9, 2001

/Walrand et al., 1996/ Walrand J., Blanquet G. and Bouanich J.-P.: *"Diode-laser measurements of N_2- and O_2-broadening coefficients in the v_3 band of CH_3D"*,

Spectrochimica Acta Part A: Molecular and Biomolecular Spectroscopy, 52(8):1037-1040, 1996

/Warneke et al., 2005/ Warneke T., de Beek R., Buchwitz M., Notholt J., Schulz A., Velazco V., and Schrems O.: *"Ship borne solar absorption measurements of CO_2, CH_4, N_2O, and CO and comparison the SCIAMACHY WFM-DOAS retrievals"*, Atmospheric Chemistry and Physics, 5:2029-2034, 2005

/Wunch et al., 2011/ Wunch D., Toon G. C., Blavier J.-F. L.: *"The Total Carbon Column Observing Network"*, Philosophical Transactions of the Royal Society A, 369:2087–2112, 2011

/Weber et al., 2013/ Weber M., Chehade W., and Spietz P.: *"Impact of ozone cross-section choice on WFDOAS total ozone retrieval applied to GOME, SCIAMACHY, and GOME2 (1995-present). Technical note"*, Issue 2 Contribution to IGACO Activity: Absorption Cross-Sections for Ozone, available at www.iup.uni-bremen.de/UVSAT_material/manuscripts/weber_acso_201101.pdf, 2013

/Wegner et al., 1998/ Wenger C, Champion J-P.: *"Spherical top data system (STDS) software for the simulation of spherical top spectra"*, Journal of Quantitative Spectroscopy & Radiative Transfer, 59:471–80, 1998

/WMO, 2008/ World Meteorological Organization (WMO): *"Operations Handbook - Ozone Observations with a Dobson Spectrophotometer"*, Revised 2008

/WMO, 2002/ World Meteorological Organization (WMO): *"Scientific Assessment of Ozone Depletion: 2002",* WMO, Geneva, Switzerland, 2002

/White, 1942/ White, J.U.: *"Long optical paths of large aperture"*, Journal of the Optical Society of America, 32:285-288, 1942

/Xiong et al., 2008/ Xiong X.Z., Barnet C., Maddy E., Sweeney C., Liu X.P., Zhou L.H., Goldberg M.: *"Characterization and validation of methane products from the Atmospheric Infrared Sounder (AIRS)"*, Journal of Geophysical Research, 113, G00A01, 2008

/Yoshino, 1988/ Yoshino K., Freeman D.E., Esmond G.R., and Parkinson W.H.: *"Absolute absorption cross-sections measurements of ozone in the wavelength region 238-335 nm and the temperature dependence"*, Planetary and Space Science, 36:395-398, 1988

/Zeninari et al., 2001/ Zeninari V., Parvitte B., Courtois D., Capitanov V.A., Ponomarev Y.N.: *"Measurements of air and noble-gas broadening and shift coefficients of the methane R3 triplet of the $2\nu_3$ band"*, Applied Physics B: Lasers and Optics, 72:953–959, 2001

/Zolot et al., 2013/ Zolot A.M., Giorgetta F.R., Baumann E., Swann W.C., Coddington I. and Newbury N.R.: *"Broad-band frequency references in the near-infrared: Accurate dual comb spectroscopy of methane and acetylene"*, Journal of Quantitative Spectroscopy & Radiative Transfer, 118:26-39, 2013

Appendix

1. Important atmospheric chemical cycles

Table A.1 presents a brief overview of main chemical groups in atmospheric chemistry.

Table A.1. *Chemical groups in stratospheric chemistry*

Acronym	**Name**	**Components**
O_x	Odd oxygen	$O + O_3$
NO_x	Nitrogen oxides	$NO + NO_2$
NO_y	Oxidized nitrogen	$NO + NO_2 + HNO_3 + 2N_2O_5 + ClONO_2 + NO_3 + HOONO_2 + BrONO_2$
HO_x	Hydrogen radicals	$OH + HO_2$
Cl_y	Inorganic chlorine	Chlorine-containing species lacking a carbon atom ($Cl+2Cl_2+ClO+OClO+2Cl_2O_2+HOCl+ClONO_2+HCl+BrCl$)
ClO_x	Reactive chlorine	$Cl + ClO$
CCl_y	Organic chlorine	$CF_2Cl_2+CFCl_3+CCl_4+CH_3CCl_3+CFCl_2CF_2Cl$(CFC-113) + CF_2HCl(CFC-22)
Br_y	Inorganic bromine	Sum of all bromine-containing species that lack a carbon atom ($Br+BrO+ HOBr + BrONO_2$)

Stratospheric source of NO_X from N_2O

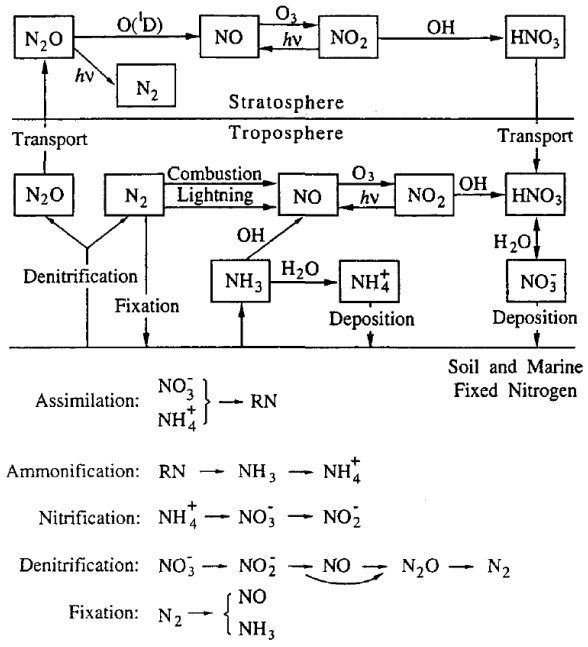

Figure A.1. *The atmospheric nitrogen cycle.*

Processes in the atmospheric cycle of nitrogen compounds. A species written over an arrow signifies reaction with the species from which the arrow originates

HO_X cycles

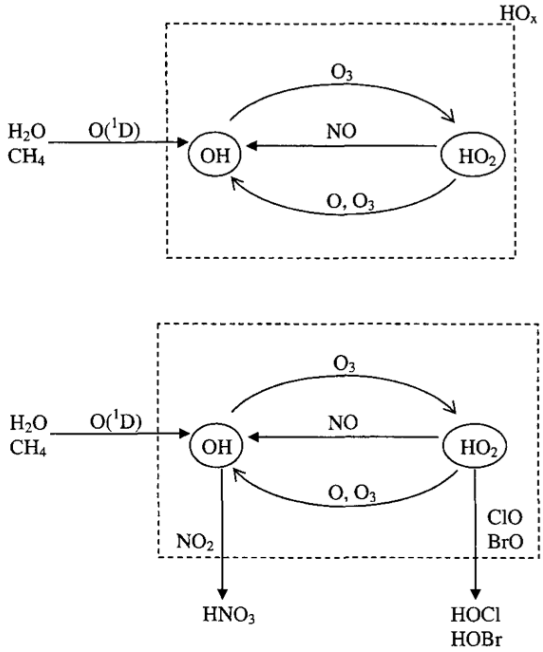

Figure A.2. *The HOx cycles.*

Upper panel: reactions affecting the inner dynamics of the HOx system.

Lower panel: additional reactions that affect OH and HO_2 levels.

Halogen cycles

The quantities of the chlorofluorocarbons in the atmosphere are approximately equal to the total amounts ever manufactured (Figure A.3).

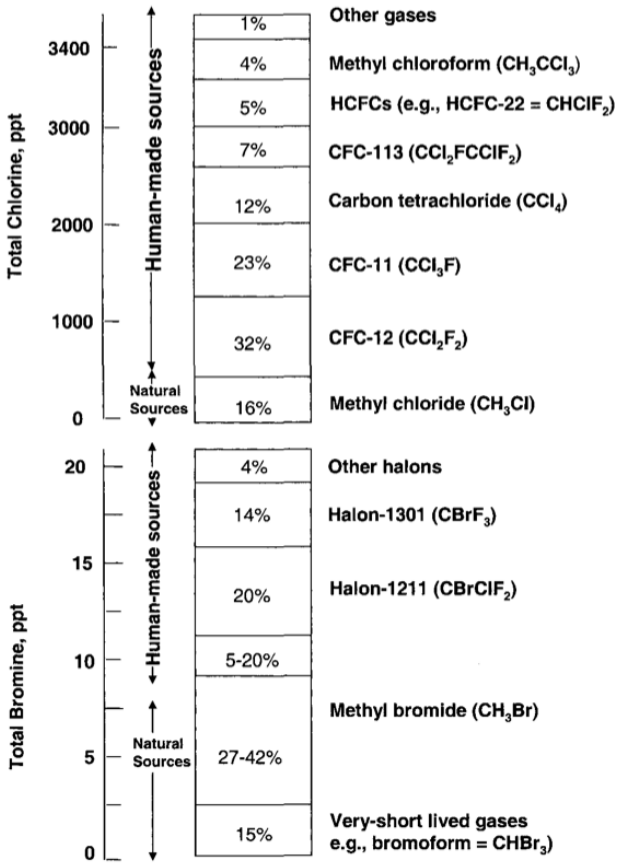

Figure A.3. *Primary sources of chlorine and bromine in the stratosphere in 1999 /WMO, 2002/.*

Chlorine cycles

The chlorine atom is highly reactive toward O_3 and establishes a rapid cycle of O_3 destruction involving the chlorine monoxide (ClO) radical:

ClO_X cycle 1: $Cl + O_3 \rightarrow ClO + O_2$

$ClO + O \rightarrow Cl + O_2$

Total: $O_3 + O \rightarrow O_2 + O_2$

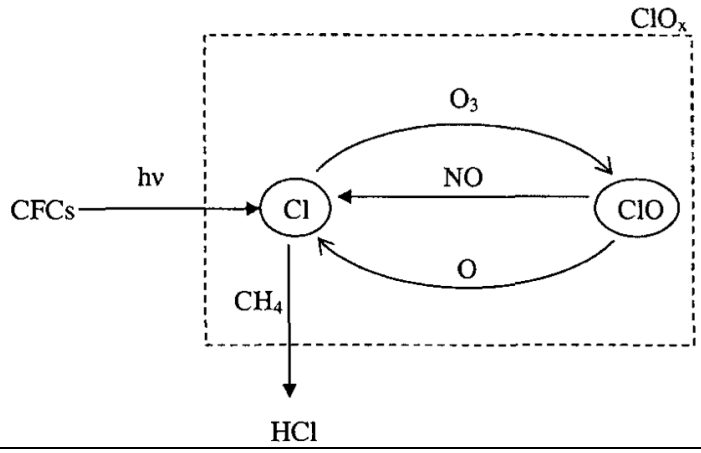

Figure A.4. *The ClO_X cycles.*

ClO/NO cycle:

$$Cl + O_3 \rightarrow ClO + O_2$$

$$ClO + NO \rightarrow Cl + NO_2$$

$$NO_2 + h\nu \rightarrow NO + O$$

$$\text{Net: } O_3 + h\nu \rightarrow O + O_2$$

Because the O atom rapidly reforms O_3, this is a null cycle with respect to O_3 removal. Most of the ClO_X is in the form of ClO; this is a result of the rapidity of the $Cl + O_3$ reaction.

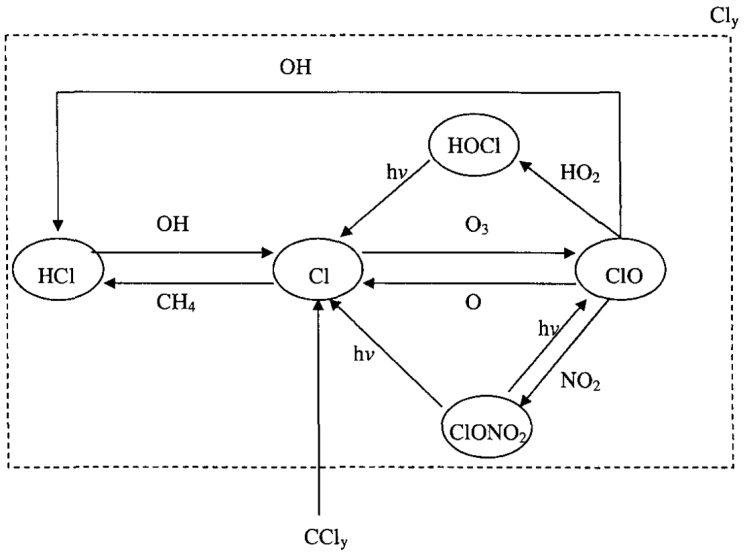

Figure A.5. *The Cl_y cycles.*

HO_X/ClO_X cycle 1: $Cl + O_3 \rightarrow ClO + O_2$

$OH + O_3 \rightarrow HO_2 + O_2$

$ClO + HO_2 \rightarrow HOCl + O_2$

$HOCl + h\nu \rightarrow OH + Cl$

Total: $O_3 + O_3 \rightarrow O_2 + O_2 + O_2$

Bromine Cycles

In addition, the following HO_X/BrO_X and BrO_X/ClO_X cycles are important in the lower stratosphere (~ 20 km):

HO_X/BrO_X cycle 1: $Br + O_3 \rightarrow BrO + O_2$

$OH + O_3 \rightarrow HO_2 + O_2$

$BrO + HO_2 \rightarrow HOBr + O_2$

$HOBr + h\nu \rightarrow OH + Br$

Total: $O_3 + O_3 \rightarrow O_2 + O_2 + O_2$

BrO_X/ClO_X cycle 1: $Br + O_3 \rightarrow BrO + O_2$

$Cl + O_3 \rightarrow ClO + O_2$

$BrO + ClO \rightarrow BrCl + O_2$

$BrCl + h\nu \rightarrow Br + Cl$

Total: $O_3 + O_3 \rightarrow O_2 + O_2 + O_2$

BrO_X/ClO_X cycle 2: $Br + O_3 \rightarrow BrO + O_2$

$Cl + O_3 \rightarrow ClO + O_2$

$BrO + ClO \rightarrow ClOO + Br$

$ClOO + M \rightarrow Cl + O_2$

Total: $O_3 + O_3 \rightarrow O_2 + O_2 + O_2$

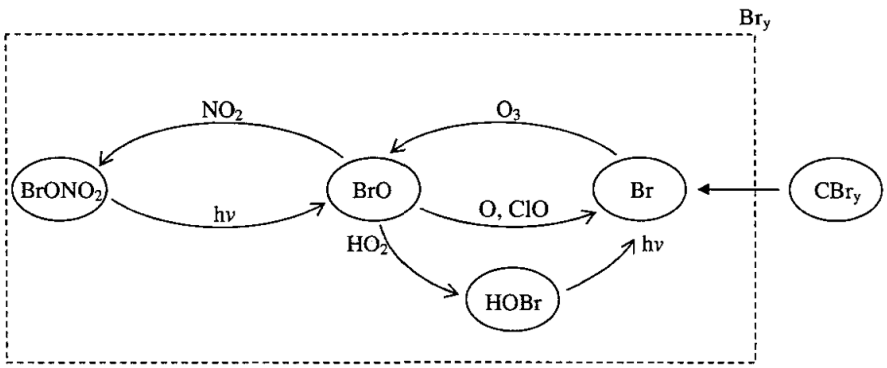

Figure A.6. *The Br_y cycles.*

CO oxidation

Table A.2. *Several important reactions of the CO oxidation mechanism*

Reactions		***Comments***
$CO + OH \rightarrow CO_2 + H$	(C.1)	Oxidation of CO by OH produces the H atom, which reacts rapidly with O_2
$H + O_2 + M \rightarrow HO_2 + M$	(C.2)	HO_2 radical self-reacts to produce hydrogen peroxide (H_2O_2)
$HO_2 + HO_2 \rightarrow H_2O_2 + O_2$	(C.3)	
$H_2O_2 + h\nu \rightarrow 2OH$	(C.4)	H_2O_2 photolyzes or reacts with OH
$H_2O_2 + OH \rightarrow HO_2 + H_2O$	(C.5)	
$HO_2 + NO \rightarrow OH + NO_2$	(C.6)	Alternate reaction for HO_2 in the presence of NO
$NO_2 + h\nu \xrightarrow{O_2} NO + O_3$	(C.7)	NO_2 produced in (C.6) photolyzes
$CO + OH \xrightarrow{O_2} CO_2 + HO_2$	(C.1 + C.2)	(C.7) regenerates NO and produces an O_3, which can then go on to photolyze in Chapman cycle to produce two OH molecules (section 1.3.2.1). (C.6) yields up to three OH molecules, boosting the oxidizing power of the atmosphere. (C.1)+(C.2)+(C.6)+(C.7) sequence is a chain mechanism for O_3 production in which the oxidation of CO by O_2 is catalyzed by the HO_X and NO_X species
$HO_2 + NO \rightarrow OH + NO_2$	(C.6)	
$NO_2 + h\nu \xrightarrow{O_2} NO + O_3$	(C.7)	
net: $CO + 2O_2 \rightarrow CO_2 + O_3$		
$OH + O_3 \rightarrow HO_2 + O_2$	(C.8)	HO_X and NO_X catalyze O_3 production in the troposphere and O_3 destruction in the stratosphere (see HO_X and NO_X cycles).
$HO_2 + O_3 \rightarrow OH + 2O_2$	(C.9)	
and		
$NO + O_3 \rightarrow NO_2 + O_2$	(C.10)	The key difference between the troposphere and the stratosphere is that O_3 and O concentrations are much lower in the troposphere. The difference is particularly large for O atom. In the troposphere, reaction (C.8) is much slower than reaction (C.1), and reaction (C.11) is negligibly slow.
$NO_2 + O \rightarrow NO + O_2$	(C.11)	

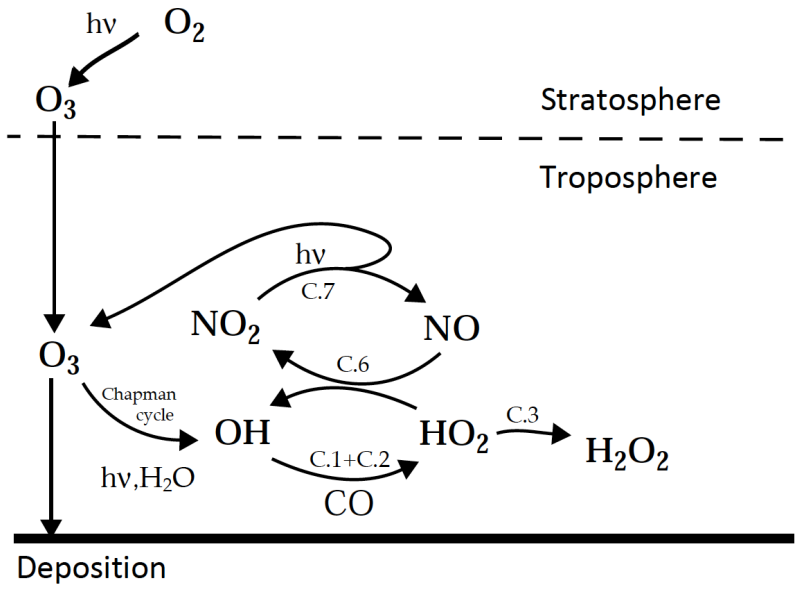

Figure A.7. *Mechanism of O_3 - HO_X - NO_X - CO chemical cycles coupling in the troposphere*

2. Assigned lines in the P, Q, and R branches of the 2v3 band of methane

Table A.3. lists the assigned lines in the *P*-, *Q*-, and *R*-branches of the $2v_3$ band of methane for two most abundant isotopologues $^{12}CH_4$ and $^{13}CH_4$ according to HITRAN 2008.

Table A.3. *Assigned lines of the $^{12}CH_4$ and $^{13}CH_4$ isotopologues*

$^{12}CH_4$ isotopologue				$^{13}CH_4$ isotopologue		
Transition	**Symmetry**		**Line position, cm^{-1}**	**Transition**	**Symmetry**	**Line position, cm^{-1}**
P(10)	9F	10F	5891,0652	**P(10)**		
	9A1	1	5891,0676			
	9E	10E	5891,0695			
	9F	10F	5891,3418			
	9F	10F	5891,3784			
	9F2		5891,5826			
	9E		5891,6159			
	9F1		5891,6452			
P(9)	8F	9F	5902,9488	**P(9)**		
	8F	9F	5902,9645			
	8F	9F	5903,1035			
	8E	9E	5903,1591			
	8F	9F	5903,18			
	8A2	1	5903,2861			
	8F	9F	5903,3376			
	8F	9F	5903,3654			
	8A1	1	5903,3857			
P(8)	7A2		5914,7515	**P(8)**	7F1	5898,2489
	7F2		5914,7651			
	7E		5914,7762			
	7F1		5914,9181			
	7F2		5915,0006			
	7E		5915,0461			
	7F1		5915,0631			
P(7)	6F1		5926,4662	**P(7)**	6F2	5909,3435
	6F2		5926,4837		6F1	5909,3769
	6A1		5926,5755		6A1	5909,52
	6F1		5926,625		6F1	5909,6052
	6E		5926,6482		6E	5909,6455
	6F2		5926,6785		6F2	5909,6957
P(6)	5E		5938,0571	**P(6)**	5	5920,8542
	5F1		5938,0661		5F1	5921,0292
	5A1		5938,0947		5F2	5921,0701
	5F1		5938,1676		5A2	5921,098
	5F2		5938,1901			
	5A2		5938,2086			
P(5)	4F2		5949,5276	**P(5)**	4F2	5932,2274
	4F1		5949,5526		4F1	5932,2964
	4F2		5949,61		4E	5932,3714
	4E		5949,6214		4F2	5932,3911
P(4)	3A2		5960,867	**P(4)**	3A2	5943,4888
	3F2		5960,8837		3F2	5943,5193
	3E		5960,8975		3E	5943,538
	3F1		5960,9339		3F1	5943,607
P(3)	2F2		5972,096	**P(3)**	2F1	5954,6862
	2F1		5972,1136		2A1	5954,7239
	2A1		5972,1347			
P(2)	1E		5983,1839	**P(2)**	1E	5965,665
	1F1		5983,1942		1F1	5965,6853
P(1)	0F2		5994,1451	**P(1)**	0F2	5976,5629

$^{12}CH_4$ isotopologue				$^{13}CH_4$ isotopologue			
Transition	**Symmetry**		**Line position, cm^{-1}**	**Transition**	**Symmetry**		**Line position, cm^{-1}**
Q(10)	10F	10F	5998,2112	**Q(10)**			
		0	5998,2304				
	10F	10F	5998,2426				
		0	5998,2804				
	10F	10F	5998,3198				
		0	5998,3348				
	10A2	1	5998,4396				
		10A1	5998,4419				
	10F	10F	5998,4427				
		0					
	10F	10F					
		0					
	10F	10F					
		0					
	10A1	1					
		10A2					
	10E	2					
		10E					
Q(9)	9F1	2	5999,4743	**Q(9)**			
	9A1	1	5999,481				
	9F2	3	5999,4921				
	9F2	2	5999,5138				
	9A2	1	5999,527				
	9E	1	5999,541				
	9F1	1	5999,6254				
	9F2	1	5999,6343				
Q(8)	8E	1	6000,6368	**Q(8)**		8F1	5982,9644
	8F1	1	6000,6434			8E	5982,9886
	8F2	1	6000,6635			8F2	5983,1352
	8F1	2	6000,6749				
	8E	2	6000,7373			8E	5983,6288
	8A2	1	6000,7484			8E	5983,6288
	8F2	2	6000,7507		8E		5983,6288
Q(7)	7F1	2	6001,6524	**Q(7)**	7F2		5983,9415
	7F2	2	6001,6646		7E		5984,0185
	7A1	1	6001,6752		7F1		5984,0512
	7F2	1	6001,6841		7A1		5984,0889
	7E	1	6001,7389		7F1		5984,3828
	7F1	1	6001,7416				
Q(6)	6A	6A	6002,5172	**Q(6)**	6A2		5984,7976
	6F	6F	6002,5253		6F2		5984,8362
	6F	6F	6002,5367		6	6	5985,0922
	6F	6F	6002,5862		6	6	5985,1154
	6A	6A	6002,5922				
	6E	6E	6002,5969				
Q(5)	5E	1	6003,2472	**Q(5)**	5F2		5985,5529
	5F2	2	6003,254		5E		5985,5743
	5F1	1	6003,2987		5F1		5985,7133
	5F2	1	6003,3111		5F2		5985,7513
Q(4)	4F1	1	6003,837	**Q(4)**	4E		5986,1465
	4F2	1	6003,8714		4F1		5986,2388
	4E	1	6003,883		4F2		5986,2674
	4A2	1	6003,8928		4A2		5986,2963
Q(3)	3A1	1	6004,293	**Q(3)**	3A1		5986,6118
	3F2	1	6004,3133		3F1		5986,6604
	3F1	1	6004,3291				
Q(2)	2F1	1	6004,6435	**Q(2)**	2F1		5986,993
	2E	1	6004,6527				
Q(1)	1F2	1	6004,8632	**Q(1)**	1F2		5987,2184

$^{12}CH_4$ isotopologue			$^{13}CH_4$ isotopologue		
Transition	**Symmetry**	**Line position, cm^{-1}**	**Transition**	**Symmetry**	**Line position, cm^{-1}**
R(0)	1A2	6015,6643	**R(0)**	1A2	5997,9618
R(1)	2F2	6026,2274	**R(1)**	2F2	6008,4684
R(2)	3E - 2E 3F1 – 2F2	6036.653600 6036.658400	**R(2)**	3E 3E	6018,8404 6018,8404
R(3)	4F1 4F2 4A1	6046,942 6046,9527 6046,9647	**R(3)**	4F2 4F1 4A1	6029,0676 6029,0828 6029,1064
R(4)	5E 5A2 5F2 5F1	6057,0778 6057,0861 6057,0998 6057,1273	**R(4)**	5A2 – 4A2 5F2-4F1 5F1 -4F2	6039.153700 6039.1695 6039.2332
R(5)	6F1 6F2 6E 6F2	6067,0816 6067,0997 6067,1485 6067,157	**R(5)**	6F2 6F1 6F2	6049,1235 6049,1582 6049,2448
R(6)	7E 7F1 7A1 7F2 7F1 7A2	6076,928 6076,935 6076,954 6077,0283 6077,0466 6077,0636	**R(6)**	7E 7E 7A1 7F1 7F2 7A2	6058,9526 6058,9526 6059,0037 6059,1183 6059,149 6059,1757
R(7)	8F2 8F1 8A1 8F1 8E 8F2	6086,6229 6086,635 6086,7454 6086,7797 6086,7994 6086,8307	**R(7)**	8A1 8F1 8E 8F2	6068,9151 6068,9873 6069,0215 6069,084
R(8)	9F2 9A2 9E 9F1 9F2 9E 9F1	6096,1665 6096,1743 6096,1809 6096,3727 6096,4244 6096,4856 6096,5015			
R(9)	10F2 9F1 10F1 9F2 10F 9F 10A2 9A1 10E 9E 10F2 9F1 10F1 9F2 10A1 9A2	6105,6259 6105,6261 6106,0402 6106,0505 6106,1943 6106,2205 6106,252 6106,2841			